



# *Towards efficient quantum repeater nodes based on solid-state quantum memories*

**Stefano Duranti**

**ADVERTIMENT** La consulta d'aquesta tesi queda condicionada a l'acceptació de les següents condicions d'ús: La difusió d'aquesta tesi per mitjà del repositori institucional UPCommons (<http://upcommons.upc.edu/tesis>) i el repositori cooperatiu TDX (<http://www.tdx.cat/>) ha estat autoritzada pels titulars dels drets de propietat intel·lectual **únicament per a usos privats** emmarcats en activitats d'investigació i docència. No s'autoritza la seva reproducció amb finalitats de lucre ni la seva difusió i posada a disposició des d'un lloc aliè al servei UPCommons o TDX. No s'autoritza la presentació del seu contingut en una finestra o marc aliè a UPCommons (*framing*). Aquesta reserva de drets afecta tant al resum de presentació de la tesi com als seus continguts. En la utilització o cita de parts de la tesi és obligat indicar el nom de la persona autora.

**ADVERTENCIA** La consulta de esta tesis queda condicionada a la aceptación de las siguientes condiciones de uso: La difusión de esta tesis por medio del repositorio institucional UPCommons (<http://upcommons.upc.edu/tesis>) y el repositorio cooperativo TDR (<http://www.tdx.cat/?locale-attribute=es>) ha sido autorizada por los titulares de los derechos de propiedad intelectual **únicamente para usos privados enmarcados** en actividades de investigación y docencia. No se autoriza su reproducción con finalidades de lucro ni su difusión y puesta a disposición desde un sitio ajeno al servicio UPCommons No se autoriza la presentación de su contenido en una ventana o marco ajeno a UPCommons (*framing*). Esta reserva de derechos afecta tanto al resumen de presentación de la tesis como a sus contenidos. En la utilización o cita de partes de la tesis es obligado indicar el nombre de la persona autora.

**WARNING** On having consulted this thesis you're accepting the following use conditions: Spreading this thesis by the institutional repository UPCommons (<http://upcommons.upc.edu/tesis>) and the cooperative repository TDX (<http://www.tdx.cat/?locale-attribute=en>) has been authorized by the titular of the intellectual property rights **only for private uses** placed in investigation and teaching activities. Reproduction with lucrative aims is not authorized neither its spreading nor availability from a site foreign to the UPCommons service. Introducing its content in a window or frame foreign to the UPCommons service is not authorized (*framing*). These rights affect to the presentation summary of the thesis as well as to its contents. In the using or citation of parts of the thesis it's obliged to indicate the name of the author.

UNIVERSITAT POLITÈCNICA DE CATALUNYA

PHD PROGRAM IN PHOTONICS

---

**Towards efficient quantum repeater nodes  
based on solid-state quantum memories**

---

*Author:*  
Stefano Duranti

*Supervisor:*  
Prof. Dr. Hugues de  
Riedmatten

*A thesis submitted to obtain the title of Doctor by the Universitat  
Politècnica de Catalunya*

*in the*

QPSA - Quantum Photonics with Solids and Atoms *group*,  
ICFO - The Institute of Photonic Sciences

February 2023



UNIVERSITAT POLITÈCNICA  
DE CATALUNYA  
BARCELONATECH





6.52 We feel that even if *all possible* scientific questions be answered, the problems of life have still not been touched at all. Of course there is then no question left, and just this is the answer.

Ludwig Wittgenstein, *Tractatus Logico-Philosophicus*





# *Abstract*

Quantum repeaters are the foundation of future long-distance quantum networks. In most architectures, their functional core is constituted by quantum memories, which are devices that can store and re-emit photonic quantum information on-demand. The goal of this thesis is to progress towards efficient quantum repeater nodes enabling quantum correlations between telecom photons and matter qubits. To these ends, we performed three main experiments.

In our first work, we built a solid-state entanglement photon source with embedded storage capabilities. This emissive quantum memory was implemented in a  $\text{Pr}^{3+}:\text{Y}_2\text{SiO}_5$  crystal, by means of the atomic frequency comb (AFC) protocol. Thanks to the AFC, we were able to adapt the Duan-Lukin-Cirac-Zoller (DLCZ) protocol, initially conceived for cold atoms, to a solid-state ensemble. This experiment proved that we can produce light-matter entanglement between a heralding photon, at 606 nm, and a spin-wave excitation delocalized inside the ensemble. The matter excitation could be read on-demand at a later time with a read pulse, and mapped as a second photon, at 606 nm as well, emitted by the memory. Quantum correlations between the two photons were measured, enabling the violation of a Bell inequality, thus demonstrating the presence of entanglement. The read-out efficiency of this experiment was low, 1.6%, but solutions were identified to increase this value.

In the second experiment, we laid the groundwork for the quantum frequency conversion (QFC) of these photons to the telecom band. The long duration of these photons, up to 1  $\mu\text{s}$ , makes their conversion with high signal-to-noise ratio (SNR) challenging. The conversion from the visible 606 nm wavelength to the telecom regime (1552 nm) was achieved by difference-frequency generation (DFG) in a PPLN waveguide using a strong pump field at 994 nm. A proof of principle with weak coherent pulses showed that we can convert  $\mu\text{s}$ -long photons with the low heralding efficiency of the previous experiment with a SNR around 2.6. This sets the stage for interfacing an AFC-DLCZ memory, working at 606 nm, with the telecom network and with material systems working at a different wave-

length.

Finally, in the last experiment, we implemented an AFC impedance-matched cavity (IMC) storage experiment. It has been demonstrated theoretically and experimentally that the IMC enhances the storage and read-out efficiency of the AFC protocol. We harnessed this cavity to store weak coherent Gaussian pulses with up to 62 % efficiency. Moreover, we stored weak coherent time-bin qubits in the same system, achieving 52 % efficiency and, with an additional analysis carried out by means of an unbalanced Mach-Zehnder AFC-based interferometer, assessing a measured fidelity of 95 % for the retrieved qubit, leading to a quantum memory fidelity compatible with 100 %, within uncertainty. We additionally studied the influence of slow-light effects in our crystal, confirming that they lead to a reduction of cavity bandwidth by two orders of magnitude. Moreover, the AFC storage time was extended up to 50  $\mu\text{s}$ , to certify that the efficiency enhancement holds for different combs.

The achievements of this thesis represent the state of the art in terms of efficiency for AFC memories and for qubit storage in solid-state systems, and pave the way towards efficient quantum memories. In addition, we reported the first demonstration of a solid-state photon pair source of entangled photons with embedded solid-state multimode memory. The results accomplished by this last AFC-DLCZ experiment in terms of heralding efficiency make it possible to interface it with our quantum frequency conversion experiment. Indeed, the QFC experiment, combined with the AFC-DLCZ one, enables to establish a quantum node and to interface it with different kind of nodes via conversion to the telecom band.

# *Resumen*

Los repetidores cuánticos son el fundamento de las futuras redes cuánticas de larga distancia. En la mayoría de las arquitecturas, su núcleo funcional está constituido por memorias cuánticas, dispositivos que pueden almacenar y reemitir información fotónica cuántica bajo demanda. El objetivo de esta tesis es avanzar hacia nodos eficientes de repetidores cuánticos que permitan crear correlaciones cuánticas entre fotones de telecomunicaciones y qubits materiales. Con estos fines, llevamos a cabo tres experimentos principales.

En nuestro primer trabajo, construimos una fuente en estado sólido de fotones entrelazados con capacidades de almacenamiento integradas. Esta memoria cuántica emisiva se implementó en un cristal de  $\text{Pr}^{3+}:\text{Y}_2\text{SiO}_5$ , mediante el protocolo del peine atómico de frecuencia (AFC). Gracias al AFC pudimos adaptar el protocolo Duan-Lukin-Cirac-Zoller (DLCZ), concebido para átomos fríos, a un ensamble de estado sólido. Este experimento demostró que podemos producir entrelazamiento de materia y luz entre un fotón mensajero, a 606 nm, y una excitación de onda de espín dentro del material. En un momento posterior, la excitación de la materia se transfirió a un segundo fotón a 606 nm, emitido por la memoria, a través de un pulso de lectura. Se midieron las correlaciones cuánticas entre los dos fotones, lo que permitió la violación de una desigualdad de Bell, demostrando así la presencia de entrelazamiento. La eficiencia fue baja, un 1,6%, pero se identificaron soluciones para aumentar este valor.

En el segundo experimento, abrimos el camino para la conversión cuántica de frecuencia (QFC) de estos fotones a la banda de telecomunicaciones. La larga duración de estos fotones, de hasta 1  $\mu\text{s}$ , hace que su conversión con una alta relación señal-ruido (SNR) sea un desafío. La conversión desde 606 nm a 1552 nm se logró mediante la generación de diferencia de frecuencia (DFG) en una guía de ondas PPLN utilizando un fuerte campo de bombeo a 994 nm. Una prueba con pulsos coherentes débiles (PCDs) mostró que podemos convertir fotones de unos  $\mu\text{s}$ , dada la eficiencia de anuncio del experimento anterior, con una SNR de 2,6. Esto prepara el escenario para interconectar una memoria AFC-DLCZ, que funciona a 606 nm, con la red

de telecomunicaciones (1530 nm–1565 nm) y con sistemas materiales que funcionan a una longitud de onda diferente.

Finalmente, en el último experimento, implementamos el protocolo AFC asistido por una cavidad con impedancia adaptada (IMC). Ha sido demostrado anteriormente que la IMC mejora la eficiencia del protocolo AFC. Usamos la cavidad para almacenar PCDs con una eficiencia de hasta el 62 %. En el mismo sistema, almacenamos qubits codificados en tiempo constituidos por PCDs, logrando una eficiencia del 52 % y, con un análisis realizado por medio de un interferómetro Mach-Zehnder basado en el AFC, evaluando una fidelidad del 95 % para el qubit emitido, y una fidelidad de la memoria compatible con el 100 %. Además, estudiamos la influencia del efecto de luz lenta en nuestro cristal y concluimos que conlleva una reducción del ancho de banda de la cavidad de dos órdenes de magnitud. Finalmente, el tiempo de almacenamiento del AFC se extendió hasta 50  $\mu$ s, para certificar que la mejora de la eficiencia se mantiene para diferentes AFCs.

Los logros de esta tesis son la vanguardia, en cuanto a eficiencia, para las memorias basadas en el AFC y para el almacenamiento de qubits en sistemas de estado sólido, y abren paso hacia las memorias cuánticas eficientes. Además, hemos hecho la primera demostración de una fuente de estado sólido de parejas de fotones entrelazados que además funciona como memoria multimodo de estado sólido integrada. Los resultados del experimento AFC-DLCZ en términos de eficiencia de anuncio hacen posible conectarlo con nuestro experimento de QFC. La combinación de los dos permite establecer un nodo cuántico y conectarlo con diferentes tipos de nodos mediante la conversión a la banda de telecomunicaciones.

# *Acknowledgements*

People knowing me know that I definitely eschew rhetoric. Therefore, I will try to avoid that as much as possible, keeping in mind that a section devoted to acknowledgements will inevitably be somewhat rhetorical.

I will not deny that my PhD has been a hard journey, and the global pandemic that burst halfway did not make it easier. During it, though, my personal and scientific growths have been enormous. This thesis is the result of 5 years at ICFO. I am very proud of the content of this thesis, and I thank myself for this. However, I would have accomplished absolutely nothing if I had not had brilliant, inspiring, sympathetic and supporting supervisors, colleagues, and friends around me.

So, I would like to thank Hugues for his supervision during this five-year period. He has been a great scientific guide, and always very supporting and very sympathetic, as a supervisor should be. Also, I would like to thank him for his patience, especially at the very beginning of my PhD, when I was still making many mistakes and learning what being a PhD student means.

Then, I would like to thank all the postdocs and PhDs that were my supervisors at some point. Among them, a mention of honor goes to the ones that spent the most time with me and taught me the vast majority of what I know: Bernardo, Alessandro, and Sören. They worked as long or even longer than me (but definitely not Bernardo!) on the experiments contained in this thesis. We shared years together, which were undoubtedly hard but also fun and enjoyable. I take advantage to wish good luck to Leo, which chose to be my successor on the impedance-matched cavity experiment. I hope we laid good bases for new exciting results yet to come.

The QPSA colleagues have been more than colleagues. I found nice and wise people and we spent a lot of time inside and outside ICFO. I will remember a lot of the random Darío-driven conversations arising abruptly in the middle of our lunches. Thank you all for keeping the group so lively.

And speaking of time inside and outside of ICFO, I would like to acknowledge all my friends, for their appreciation, the great time spent together and their support.



# List of publications

## Published papers:

- Kutlu Kutluer, Emanuele Distanto, Bernardo Casabone, Stefano Duranti, Margherita Mazzera, and Hugues de Riedmatten, *Time Entanglement between a Photon and a Spin Wave in a Multimode Solid-State Quantum Memory*. Phys. Rev. Lett. 123, 030501, (2019).

## In preparation:

- Stefano Duranti, Sören Wengerowsky, Leo Feldmann, Alessandro Seri, Bernardo Casabone, and Hugues de Riedmatten, *Highly efficient cavity-assisted storage of qubits in a solid-state quantum memory*
- Sören Wengerowsky<sup>†</sup>, Stefano Duranti<sup>†</sup>, Alessandro Seri, and Hugues de Riedmatten, *Quantum frequency conversion of  $\mu\text{s}$ -long weak coherent pulses from 606 nm to 1552 nm*

<sup>†</sup>These authors contributed equally





# Contents

<b>Abstract</b>	<b>v</b>
<b>Resumen</b>	<b>vii</b>
<b>Acknowledgements</b>	<b>ix</b>
<b>List of publications</b>	<b>xi</b>
<b>Table of contents</b>	<b>xvii</b>
<b>1 Introduction</b>	<b>1</b>
1.1 Quantum communication . . . . .	2
1.2 Quantum repeaters . . . . .	4
1.3 Quantum memories . . . . .	7
1.3.1 State of the art for quantum memories . . . . .	11
1.3.1.1 State of the art of GEM, EIT and emissive protocols . . . . .	11
1.3.1.2 State of the art for the atomic frequency comb protocol . . . . .	13
1.4 Summary of the thesis . . . . .	15
<b>2 Light-matter interaction in rare-earth doped crystals and quantum memory protocols</b>	<b>17</b>
2.1 Rare-earth ions . . . . .	17

2.1.1	Rare earths . . . . .	18
2.1.2	Rare-earth doped crystals . . . . .	20
2.1.2.1	Praseodymium-doped orthosilicate . . . . .	22
2.1.2.2	Homogeneous linewidth . . . . .	23
2.1.2.3	Inhomogeneous linewidth . . . . .	25
2.1.2.4	Classes of ions . . . . .	26
2.1.2.5	Spectral hole-burning . . . . .	27
2.1.2.6	Two-pulse photon echo (TPE) technique . . . . .	30
2.2	Atomic frequency comb (AFC) . . . . .	31
2.2.1	AFC efficiency . . . . .	33
2.2.2	Spin-wave storage . . . . .	36
2.2.2.1	Spin-wave storage efficiency . . . . .	37
2.2.3	AFC-DLCZ protocol . . . . .	37
2.3	Impedance-matched cavity . . . . .	40
2.3.1	Theory of the impedance-matched cavity . . . . .	41
2.3.2	Efficiency of the impedance-matched cavity protocol . . . . .	42
<b>3</b>	<b>Time entanglement with the DLCZ protocol</b>	<b>47</b>
3.1	Introduction . . . . .	48
3.2	Experiment . . . . .	49
3.2.1	Experimental procedure . . . . .	51
3.2.1.1	Creation of Stokes-Anti-Stokes photon pairs . . . . .	51
3.2.1.2	Assessing non-classical correlations between the emitted photons . . . . .	53
3.2.1.3	Time entanglement between a photon and a spin wave . . . . .	56
3.3	Discussion and outlook . . . . .	61
3.3.1	Summary of the work . . . . .	61
3.3.2	Limitations and perspectives . . . . .	62
<b>4</b>	<b>Impedance-matched-cavity-assisted AFC</b>	<b>65</b>
4.1	Introduction . . . . .	66
4.1.1	State of the art . . . . .	67
4.1.2	Challenges . . . . .	68

4.1.2.1	Simulation of the impedance-matched efficiency including losses . . . . .	69
4.2	Experiment . . . . .	72
4.2.1	Storage of weak coherent pulses at the single photon level . . . . .	74
4.2.2	Storage of time-bin qubits and analysis via an AFC interferometer . . . . .	76
4.2.3	Storage efficiency at different storage times . . . . .	84
4.2.4	Pulse bandwidth and slow-light effect . . . . .	86
4.2.4.1	Slow-light effect . . . . .	86
4.2.4.2	Storage efficiency versus pulse bandwidth . . . . .	88
4.2.5	Spin-wave storage in the cavity . . . . .	90
4.3	Discussion and outlook . . . . .	93
<b>5</b>	<b>Quantum frequency conversion</b> . . . . .	<b>99</b>
5.1	Introduction . . . . .	99
5.2	Theoretical background . . . . .	101
5.2.1	Three-wave mixing . . . . .	101
5.2.1.1	Phase-matching . . . . .	103
5.2.1.2	Quasi-phase-matching . . . . .	104
5.2.2	Noise processes . . . . .	105
5.2.3	Measures of efficiency . . . . .	107
5.3	Experimental setup . . . . .	108
5.3.1	First waveguide . . . . .	109
5.3.2	Second waveguide . . . . .	110
5.3.2.1	Filtering stages . . . . .	111
5.4	Experiment . . . . .	112
5.4.1	HC Photonics waveguide . . . . .	112
5.4.1.1	Estimation of $\alpha$ . . . . .	113
5.4.1.2	SNR and $\mu_1$ vs input number of photons . . . . .	114
5.4.1.3	SNR and $\mu_1$ vs pulse length . . . . .	116
5.4.1.4	Internal efficiency and $\mu_1$ vs pump power . . . . .	118
5.4.1.5	Discussion for the HC Photonics waveguide . . . . .	119
5.4.2	NTT waveguide . . . . .	120

5.4.2.1	SNR and $\mu_1$ vs input number of photons . . . . .	120
5.5	Discussion and outlook . . . . .	122
<b>6</b>	<b>Conclusions and outlook</b>	<b>125</b>
6.1	Main results of the thesis . . . . .	125
6.2	Outlook . . . . .	126
<b>A</b>	<b>Theory of two-pulse photon echoes</b>	<b>131</b>
A.1	Optical echoes . . . . .	131
A.1.1	Two-level atom interacting with light . . . . .	132
A.1.2	Free-induction decay . . . . .	134
A.1.3	Rephasing and echo emission . . . . .	138
<b>B</b>	<b>Experimental tools and techniques</b>	<b>143</b>
B.1	Lasers . . . . .	143
B.1.1	606 nm laser . . . . .	143
B.1.1.1	Modulation of light . . . . .	144
B.1.2	994 nm laser . . . . .	145
B.2	Cryostat . . . . .	146
B.2.1	Cryostat noise . . . . .	148
B.2.2	Crystals and mounts . . . . .	150
B.3	Experimental techniques . . . . .	151
B.3.1	Two-pulse photon echo measurement . . . . .	151
B.3.2	AFC preparation . . . . .	154
B.3.2.1	Pit preparation . . . . .	156
B.3.2.2	Broad spectral feature preparation . . . . .	156
B.3.2.3	Comb preparation . . . . .	158
<b>C</b>	<b>Further details for Chapter 4</b>	<b>163</b>
C.1	Details of the setup . . . . .	163
C.1.1	Crystals . . . . .	163
C.1.2	Laser beams . . . . .	164
C.1.3	Cavity . . . . .	168
C.1.4	Cryostation and noise . . . . .	169

C.1.5	Cavity alignment and stabilization . . . . .	170
C.1.5.1	Aligning the cavity . . . . .	170
C.1.5.2	Stabilizing the cavity . . . . .	172
C.2	Analysis of the AFC interferometer . . . . .	176
<b>D</b>	<b>Further details for Chapter 5</b>	<b>179</b>
D.1	Details of the setup . . . . .	179
D.1.1	Filtering cavity . . . . .	179



# Chapter 1

## Introduction

Since the dawn of mankind, transmission of information has been a crucial feature in human societies. Messages at far distances have been transmitted at the speed of horses or even humans, in case of couriers. Legend has it that, during the battle of Marathon, the Greek messenger Pheidippides ran the 40 km between Marathon, where the Athenian forces had defeated the Persian army, to Athens to bring the good news about the victory, and he died immediately after conveying his message. This legend was probably a mix of different stories, and it is unlikely to be accurate, but perfectly depicts the importance of information transmission in ancient societies.

Even in old times, though, messages could be transmitted at the speed of light, through fires, smoke signals or reflecting mirrors. These primitive methods could carry only simple information (like one bit at a time), and relied heavily on the environmental conditions, since they could not be used when it was foggy or cloudy, for instance. With the development of telegraph and wireless communication, it has become customary to send complex messages reliably at speeds close to or equal to the speed of light.

Until recent times, all the information generated and distributed by mankind has been classical information. Classical information in the digital era is encoded into bits, and it is the common kind of information we are used to. In the last decades, as our ability of manipulating atoms



and photons increased, we have got able to send, process and storage a different kind of information, encoded into quantum bits (qubits): quantum information.

## 1.1 Quantum communication

Quantum communication consists in the distribution of quantum states between remote parties. It is part of the broader field of quantum information. The field of quantum information emerged forty years ago, but only in the last decades has it been possible to realize the first experimental trials in order to implement its concepts. In particular, it has been shown theoretically that the quantum counterparts of digital protocols could outperform their classical analogues: while classical encryption methods base their security on the difficulty of specific computational problems, which therefore depends on the computational power of a possible eavesdropper, quantum cryptography security is rooted in the laws of quantum mechanics instead [1, 2]. Quantum cryptography has already found the first commercial implementations [3].

Quantum computation is another technology that bears promises of carrying out tasks for which current classical algorithm are not suited in a reasonable time; nonetheless, it has not reached the level of technological maturity of quantum cryptography. In general, quantum cryptography is one of the most mature technologies inside the realm of quantum information-based technologies.

Quantum sensing is another example of a mature quantum technology. It takes advantage of quantum objects and their quantum properties to measure small quantities that would not be measurable classically or to improve the precision and sensitivity of measurement of quantities beyond the classical limits. These quantities include magnetic and electric fields, masses, gravitational fields [4, 5].

In the rest of this section, I am going to define some basic concepts from the field of quantum information that will be necessary to describe our experiments.

**Qubits** The equivalent of digital bits in the quantum realm are quantum bits, also known as qubits. Like bits, qubits can exist in the familiar states  $|0\rangle$  and  $|1\rangle$ . But quantum bits can take advantage of the features of quantum mechanics, and can be in a superposition of states. Defining  $|\psi\rangle$  as the state of a qubit, we can write it as a superposition of the two basic states that we defined earlier, which form the so-called computational basis:

$$|\psi\rangle = \alpha |0\rangle + \beta |1\rangle \quad (1.1)$$

where for the coefficients  $(\alpha, \beta) \in \mathbb{C}$ , the normalization condition holds:  $|\alpha|^2 + |\beta|^2 = 1$ .

While the value of a bit can be unveiled simply by measuring it, we cannot do the same with a qubit due to quantum mechanical laws. In other words, if we were to measure the state expressed by definition 1.1, we would obtain the outcome  $|0\rangle$  with probability  $|\alpha|^2$  and the other outcome with probability  $|\beta|^2$ , and the superposed state will collapse [6].

A crucial difference between qubits and classical bits is the state of a qubit cannot be perfectly cloned. This is clearly stated by the no-cloning theorem [7]. This means that, given an arbitrary unknown qubit state  $|\Phi\rangle$ , there is no way of copying this state and writing it onto another qubit with perfect fidelity. The existence of this no-go theorem has profound consequences on the way quantum information is distributed. As we will see in section 1.2, a quantum repeater works in a completely different way with respect to a classical one: while the latter amplifies signals travelling from one point to another to compensate for losses in fiber, the former is meant to distribute entanglement between the two points, which is the real resource we want to harness.

**Entanglement** Qubits can also be entangled: namely, considering two qubits, the state of one of them might be impossible to describe without considering the state of the other one. As an example, for two photons with two different states of polarization  $|H\rangle$  (horizontal) and  $|V\rangle$  (vertical), it is possible to build a joint state of the kind

$$|\psi\rangle_{ent} = \frac{1}{\sqrt{2}}(|H\rangle_1 |V\rangle_2 + e^{i\phi} |V\rangle_1 |H\rangle_2), \quad (1.2)$$

with 1 (2) being the first (second) photon and  $\phi$  arbitrary phase, where the individual state of each single particle is not defined. Once we measure the state of the first qubit, and obtain randomly—in this case, with equal 50 % probability—one of the two possible outcomes  $\{|H\rangle, |V\rangle\}_1$ , the state of the other qubit is immediately projected into the opposite state  $\{|V\rangle, |H\rangle\}_2$ , in theory no matter how far away the two qubits are.

Entanglement is a universal resource of utmost importance when dealing with quantum communication. As a matter of fact, the main challenge that we want to tackle is the distribution of entanglement over large distances. I will show in the next section that one of the most relevant inventions in order to accomplish this task are quantum repeaters.

## 1.2 Quantum repeaters

The task of distributing quantum states between distant locations can be carried out by photons. Photons can encode a quantum state in different degrees of freedom: polarization is the most straightforward one, but other kinds of encoding will be mentioned throughout this thesis, such as path, time-bin or energy-time ones.

In the modern Internet infrastructures, pulses with billions of photons are travelling through optical fibers and used as carriers of information. They experience losses around 0.2 dB/km in common telecom fibers, but these losses can be compensated thanks to erbium-doped fiber amplifiers (EDFAs), which use stimulated emission as a way of amplifying signals. These amplifiers are scattered all along the fiber network at distances of 50 km–100 km between each other, and they make distribution of information possible, enabling signals to reach points as far as tens of thousands of km.

However, as I stated in section 1.1, quantum information cannot be perfectly duplicated. This means that we cannot simply apply the same approach to flying qubits and clone them. One might be tempted to argue that, using the EDFAs I have just mentioned, photons could be copied through stimulated emission. In fact, the subtlety is that spontaneous

emission is preventing the achievement of a fidelity higher than  $5/6$  for the final state with respect to the original one, thus making this option unfeasible [1, 8].

In addition, trying direct transmission without amplification to overcome the distances needed to connect a country is unaffordable, as losses become prohibitive after only hundreds of km [9]. Therefore, quantum repeaters need to circumvent this hurdle. As it was suggested previously, what we need to distribute between two distant parties A and Z is entanglement, which can be used to then perform communication protocols between them. Indeed, operations like quantum teleportation or some cryptography protocols are based on having an entangled pair of qubits. The first proposal of a quantum repeater capable of generating entanglement efficiently over large distance was proposed by Briegel *et al.* [10], and it is the one I am going to focus on in this section.

To explain the protocol of reference [10], I will be referring to figure 1.1. The protocol is fully based on the concept that, if two pairs of qubits (A,B) and (C,D) are entangled, then by performing entanglement-swapping operations between B and C, one can get the pair (A,D) entangled. Taking this concept into account, we can suppose now to have two quantum nodes, A and Z, and to divide their distance  $L$  into two segments of length  $L/2$ , with two extremes B and Y that are respectively entangled with A and Z. These segments are called quantum repeater links. If the distance  $L/2$  is short enough to allow direct communication between B and Y, then entangling this pair of stations through direct exchange of photons automatically entangles A and Z.

In real contexts, A and Z are separated by a very large distance  $L$ , which prevents any forms of direct transmission in fiber<sup>1</sup>. Hence, the aforementioned operation of splitting this distance in smaller intervals must be repeated  $n$  times, in order to get  $n$  elementary links whose length  $L/n$  enables direct transmission between the two ends. From here, the protocol

---

<sup>1</sup>This is true for distances of the order of  $10^2$  km. Also, in free-space, using satellites, direct transmission becomes possible, but it is affected by other issues and it will not be treated in this thesis.

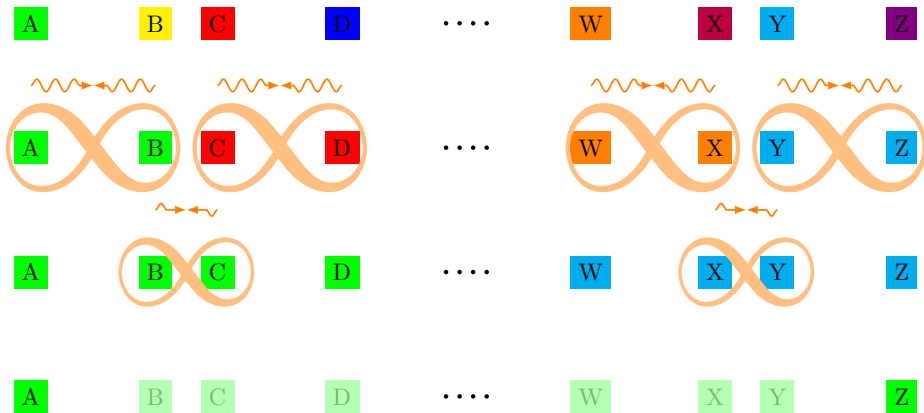


Figure 1.1: Quantum repeater scheme. The convention is that nodes with the same color are entangled. The initial stage of the A ... Z nodes displays no entanglement between them (all different colors). At some point, entangling operations (big  $\infty$ ) are performed between pairs of stations inside a quantum elementary link along the whole chain through photon exchange (orange wavy arrows). The final result is shown in the second row of nodes, with pairs that have become entangled. Finally, the same entangling procedure is repeated on yet non-entangled nodes, such to get the final row where A and Z are eventually entangled, with all the other nodes having no entanglement left and playing no role anymore (transparent filling).

proceeds as described earlier, with pairs of nodes that get entangled at a time until the final result is the entanglement of A and Z, as explained in figure 1.1.

In the practical case, these quantum nodes are quantum memories which store entangled photons. Hence, the protocol goes as follows: pairs of quantum memories are storing entangled photons. At some point, they are released and sent to a beamsplitter for a Bell state measurement. If we managed to erase the path information associated to these photons, they are indistinguishable and they will interfere at the BS. This operation projects the state of the two quantum memories that fired those photons in

an entangled state; but, since they were entangled with the other partner of the pair, these means that the two “external partner memories” are now entangled. It is crucial that classical information heralding the outcome of the BS measurement is exchanged between the stations: if it is not the case, the joint state of the quantum memories will be a perfectly mixed state, and the protocol will fail. This sets a precise boundary on the communication time of the repeater: calling  $L_0$  the distance between a quantum node and a measurement station, the minimum time required to create entanglement in a link is  $2L_0/c$ . Repeating this entangling procedure along the chain makes it possible to entangle the two ends of the chain.

These operations are not deterministic, so the probability of  $N$  nodes being entangled at the same time would decrease exponentially with  $N$ . Quantum memories enable overcoming this necessity by storing entanglement for the time required for the entanglement-swapping operations to succeed, making the links independent. In any case, the scaling is always better than direct transmission [11]. In particular, the use of a quantum repeater enables beating direct transmission at achievable transmission rates after a few hundred km—typically, around 600 km [12].

As we have seen, quantum memories enable the synchronization of entanglement-swapping. So far, the concept of quantum memory has been used without a proper definition. In the next section, I am going to address this topic.

### 1.3 Quantum memories

Quantum memories are devices that can store quantum information for a certain time and output it on demand. In this thesis, I will focus on optical quantum memories. For this kind of memories, in general, the way to achieve this storage capability lies in the light-matter interaction: a photon (or more than one) is mapped onto an internal degree of freedom of a physical system. In our case, as will be treated in section 2.2, light is stored as delocalized atomic excitation in an ensemble of ions in a doped crystal, but quantum memories can also be implemented with single atoms

[13, 14], cold atomic clouds [15–18], warm vapours [19–22], vacancy centers in diamonds [23, 24], single trapped ions [25–27].

Apart from quantum repeaters, quantum memories could be employed in other applications, such as in implementing deterministic single photon sources [28, 29], performing linear quantum computation [30] or synchronizing probabilistic quantum gates for quantum computation [31].

During the last decades, different quantum memory protocols have been devised for different physical systems and harnessing the most disparate physical effects. Examples include the gradient echo memory protocol (GEM) [32, 33], the controlled reversible inhomogeneous broadening (CRIB) protocol [34, 35] and protocols based on the electromagnetic-induced transparency (EIT) [36, 37]. Another protocol for quantum memories this thesis is based on is the atomic frequency comb (AFC) protocol, which I will treat extensively in chapters 2 and 4.

Photonic quantum memories can be divided into two different families: emissive memories and absorptive memories [38].

An emissive memory is a memory where the quantum information is both created and stored. An example of emissive memory can be found in chapter 3. An absorptive memory, on the other hand, can store externally generated quantum states and release them. An experiment employing an absorptive memory is reported in chapter 4.

The main characteristics to look for in a quantum memory for quantum repeater applications are:

- **Efficiency:** it is a crucial figure of merit for quantum memories. The definition of efficiency I will use throughout this thesis change depending on whether we are dealing with absorptive or emissive quantum memories. For the former, the efficiency is given by the ratio between the intensity of the retrieved light and the intensity of the input light. In emissive memories, where the memory can only emit pairs of correlated photons, the efficiency is more correctly defined as *read-out* efficiency, that is, the probability of reading-out a photon when shining a read pulse, conditioned on the fact that an excitation is already present in the memory. Highly efficient quantum mem-

ories enormously facilitate the task of distributing entanglement by speeding up the entanglement-swapping operations. In this thesis, an experiment aimed at achieving very high efficiency in a solid-state quantum memory is reported in chapter 4;

- **Storage time:** this is the time the quantum memory can store a qubit before losing coherence and therefore the capability of re-emitting it<sup>2</sup>. Quantum memories should maintain the entanglement long enough to allow the entangling operations to succeed in the whole chain. To create entanglement between two nodes, the minimum time taken for each node is at least the time the photons take to travel until the measuring station plus the time needed to communicate back the outcome of the measurement. For more complex repeater chains including several links, the storage time should be longer than the time to distribute the entanglement over the full chain.
- **Multimodality:** multimodality (or multiplexing) is defined as the capability of storing more than one mode. Different modes can be created in frequency [39–42], in space [43–46], in time [42, 47–54]. This enhances the probability of entangling processes to succeed because, if we manage to fit a larger number of entanglement attempts in the same communication time, the likelihood that at least one Bell measurement has a positive outcome increases. In particular, it can be shown that, calling  $N$  the number of stored modes, the probability increases, to first order, by this factor  $N$  compared to the single-mode case [55].
- **Fidelity:** the fidelity is a quantitative estimation of how similar a quantum state is to another given one. In particular, for atomic ensembles, the *conditional fidelity* is defined as the fidelity of the

---

<sup>2</sup>Note that this is true for ensemble-based quantum memories, where decoherence decreases the efficiency but the fidelity of re-emitted qubits can still be good. Conversely, in single atoms, decoherence will not affect as much the efficiency but will have a detrimental effect on the fidelity.



output state with respect to the input state:

$$F^c = \text{Tr}(\rho_{in}\rho_{out}) \quad (1.3)$$

The fidelity of a retrieved quantum state must be higher than a certain lower bound in order to claim that the storage is a quantum process. If we consider a measure-and-prepare approach, where, instead of storing the photons in a memory, we measure the state of  $N$  photons and prepare new photons according to the measurement results, we cannot get any fidelity better than  $(N + 1)/(N + 2)$  [56]. A corollary of that is, for a single photon ( $N=1$ ), this lower bound equals  $2/3$ .

In reality, the limit on the fidelity is much more stringent when entanglement is involved. In order to guarantee that the non-locality of a photon belonging to an entangled pair is preserved after storage, i.e. the output entangled state can violate a Bell inequality, the threshold increases to 85.4% [31].

- **Potential of working at telecom wavelengths:** as mentioned in section 1.2, modern telecommunications are based on the telecom fiber network. To transmit signals at long distances, then, we need them to be at telecom wavelength, because losses in fibers at this wavelength are minimal (0.2 dB/km) compared to other sections of the electromagnetic spectrum. The ideal case would be to have a quantum memory naturally working at this wavelengths, that is, a material with a transition absorbing in this part of the electromagnetic spectrum. Despite erbium seems like the perfect element to implement this kind of memory thanks to its transition close to 1550 nm [57], it has displayed inefficient optical pumping and noise processes that could affect quantum-level storage [38]; in this sense, other rare-earth ions have shown better capabilities as quantum memory candidate materials.

The capability of being interfaced with the telecom band is not intrinsic in our photonic memories, because they all work at visible wavelengths. Nonetheless, via the so-called quantum frequency conversion, we can convert coherently photons from visible to telecom,

and we are currently employing it in our labs. In chapter 5, a quantum frequency conversion experiment is reported. Quantum frequency conversion has been devised in order to convert photons to and from the telecom band. It is based on difference- and sum-frequency generations, two non-linear effects that will be explained in chapter 5. For the moment, it suffices to say that this technique enables shifting photon wavelengths in order to either let them interact with matter or to travel through optical fibers.

Another strategy for absorptive quantum memory is using non-degenerate photon pair sources, where one of the photons is at telecom wavelength, whereas the other one is at a different wavelength compatible with storage in a quantum memory, typically working in the visible regime in our case. This technique is largely employed in the field [49, 58–61] and in our group [42, 62–64].

It should be pointed out that, as of now, there is no system ensuring good performances for all of these figures of merit at the same time.

### 1.3.1 State of the art for quantum memories

As just discussed, an efficient quantum memory with long storage time, high multiplex capability and working in the telecom regime does not exist yet. So, it is useful to review the state of the art on quantum memories, focusing on two crucial figures of merit: storage time and efficiency. The review will deal with different storing techniques, implemented in different materials, and treat the atomic frequency comb protocol in a dedicated section, to give a deeper overview about it. A summary of the current records is reported in table 1.2.

#### 1.3.1.1 State of the art of GEM, EIT and emissive protocols

**Gradient echo memory** The gradient echo memory (GEM) protocol [32, 33] is one of the most promising techniques to attain the high storage efficiency regime: a storage efficiency above 87% at a quantum level (but

not with qubits) was achieved in  $^{87}\text{Rb}$  cold atoms [15] and in warm vapours [65], while its application to  $\text{Pr}^{3+}:\text{Y}_2\text{SiO}_5$  yielded the most efficient solid-state quantum memory up-to-date, with 69 % efficiency for weak coherent state storage [33].

**Electromagnetic-induced transparency** Another protocol often used for quantum memories is the EIT protocol [36, 37]. Polarization single photon qubits have been stored into a cold ensemble of rubidium atoms with 85 % retrieval efficiency and average fidelity above 99 % for the retrieved qubits [16]. In a similar work, storage of single photons with 87 % efficiency and storage of heralded single-photon entanglement with 85 % efficiency were performed in two cesium-based quantum memories [66]. For classical pulses, 92 % efficiency was demonstrated in an ensemble of cesium atoms [17].

In addition, long storage times are enabled by this protocol: with the help of dynamical decoupling techniques [67], a coherent state was trapped for 16 s in  $^{87}\text{Rb}$  [68]; in  $\text{Pr}^{3+}:\text{Y}_2\text{SiO}_5$ , classical light was stored coherently for 1 min [69]. It is worth remarking that EIT experiments at the single photon level in a solid-state environment are challenging because of the presence of the coupling laser during the photon read-out. Nevertheless, recently, weak coherent pulses with a few photons inside were slowed down in  $\text{Pr}^{3+}:\text{Y}_2\text{SiO}_5$  for up to 10 s, with the help of advanced spin-echo techniques and heavy filtering [70]. A similar protocol to EIT based on spectral holes and spin-wave storage was implemented in our group and yielded 31 % efficiency for  $\mu\text{s}$ -long weak coherent states with a  $\mu_1 < 0.04^3$ , a very promising value for potential single photon storage [71].

**DLCZ protocol** The protocol proposed by Duan, Lukin, Cirac and Zoller, named DLCZ after the initials of the proposers [11], is the most famous protocol for ensemble-based emissive quantum memories. The first demon-

---

<sup>3</sup> $\mu_1$  is defined as the mean photon number required in order to achieve a SNR of 1. We can write its definition as  $\mu_1 = \frac{\mu_{\text{in}}}{\text{SNR}}$ , where  $\mu_{\text{in}}$  is the mean photon number per pulse. A more extended treatment about this quantity can be found in section 5.4.1.2.

stration of DLCZ in cold atoms happened in 2003, when non-classical correlations were demonstrated between the emitted photons from a cloud of cesium atoms addressed with the DLCZ scheme [72], at Caltech; at the same time, in Harvard, a similar experiment was performed with rubidium atoms in a vapour cell [73]. Later, the DLCZ technique found its first demonstrations in a network scheme, with distribution of entanglement between two distant parties [74–76]. At present, this protocol holds the record for one of the longest storage time at the single-photon level in cold atoms and, generally, in quantum memories: the presence of entanglement, via a CHSH violation, between a photon and an atomic ensemble was detected after 1 s storage in a DLCZ memory [77]. DLCZ memories also hold promises for the generation of highly tunable photons: by tuning the read pulse, photons as long as 10  $\mu$ s were generated in our group in a  $^{87}\text{Rb}$  ensemble of atoms [78], which represents a landmark in terms of temporal waveform tailoring.

**Rephased amplified spontaneous emission** A similar protocol to DLCZ is the rephased amplified spontaneous emission (RASE) [79, 80]. Both techniques are emissive ones and are based on the creation of entanglement between a heralding photon and a spin-wave. RASE achieves that by means of multiple  $\pi$ -pulses, which are meant to invert population initially and to reverse ion dephasing later. A RASE-based memory was able to generate continuous variable entanglement between a photon and a spin-wave, successively converted into a heralded photon, for delay times up to 5  $\mu$ s [81].

### 1.3.1.2 State of the art for the atomic frequency comb protocol

The first demonstration of the atomic frequency comb (AFC) protocol, which will be detailed in section 2.2, happened in 2008, when storage of weak coherent states in a neodymium-doped crystal was carried out [82]. The AFC constituted the first demonstration of a solid-state light-matter interface that could work at the single photon level.

The full AFC protocol [83], where the excitation stored in the comb is coherently transferred to the spin levels for on-demand readout, was

implemented classically in 2010 [84] and extended to the single photon level 5 years later [50, 85].

Nowadays, the new frontier for improving further the AFC efficiency is represented by the impedance-matched cavity-assisted AFC [86]. In the last decades, several experiments employing this protocol have been carried out [87–89], all achieving remarkable efficiencies with respect to the single-pass AFC efficiencies observed in the respective materials. The highest AFC efficiency achieved so far is being reported in this work, with a 62 % with weak coherent states and 52 % with time-bin qubits (paper in preparation).

In addition, the AFC protocol displayed its potentiality in terms of multi-modality and storage time [90]. Temporal multiplexing in the two-level AFC was shown for 62 modes in  $\text{Pr}^{3+}:\text{Y}_2\text{SiO}_5$  by our group [63] and for 1250 modes in  $^{171}\text{Yb}^{3+}:\text{Y}_2\text{SiO}_5$  in a very recent work [91]. Frequency multi-modality was demonstrated as well: 26 spectral modes for weak-coherent time-bin qubits [39] and, in our group, 15 spectral modes for heralded single photons [42]. Spatial multi-modality was implemented to store 51 orbital angular momentum weak coherent states [92] and, lastly, these last three kinds of multiplexing were combined in the same system to store the same kind of orbital angular momentum states [40]. The AFC protocol shows promising storage times as well. In  $^{151}\text{Eu}^{3+}:\text{Y}_2\text{SiO}_5$ , storage up to 20 ms was achieved for time-bin qubits [93]; classical pulses were stored for 53 min in the same material by means of spin-wave storage merged with dynamical decoupling technique [94].

To conclude this section, it is worth mentioning the state of the art for experiments with light-matter and matter-matter entanglement in solid state. A few years after the first AFC demonstration, coherent transfer of entanglement from a photon pair to a photon-matter excitation (and back) was proved in two back-to-back AFC experiments [49, 95]. Some years later, heralded entanglement between two separated neodymium-doped crystals [58] and post-selected entanglement between two solid-state quantum memories at different wavelengths, a thulium-based and a fiber-based memories [96] was shown in two different experiments. In our group, matter-matter entanglement heralded by a photon at telecom wavelength between remote solid-state multimode quantum memories was recently demonstrated for

the first time [63], as well as light-matter entanglement between a photon at telecom wavelength and a delocalized spin excitation in a solid-state quantum memory, using a non-degenerate photonic entanglement source [64]. A fiber-integrated quantum memory for light-matter entanglement was also demonstrated [97].

Protocol	Kind of storage	Efficiency	Storage time
GEM (solid state)	WCS	69 % [33]	1.3 $\mu$ s [33]
GEM (atoms)	WCS	87 % [65]	0.6 ms [15]
EIT	Classical pulses	92 % [17]	1 min [69]
	WCS	68 % [98]	10 s [70]*
	Single photons	87 % [66]	100 ms [77]**
Two-level AFC	Classical pulses	56 % [87]	51 $\mu$ s [51], 100 $\mu$ s [60]***
	WCS	62 % [this thesis]	15 $\mu$ s [99]
	Single photons	30 % [18]	25 $\mu$ s [63]
Three-level AFC	Classical pulses	14 % [100]	53 min [94]
	WCS	8.5 % [100]	20 ms [93]
	Single photons	6.2 % [64]	47.7 $\mu$ s [64]
DLCZ-AFC		3.2 % [52]	1.02 ms [54]
RASE		3 % [81]	5 $\mu$ s [81]

Figure 1.2: List of records in efficiency and storage times in quantum memories for different protocols and different kinds of input: classical pulses, weak coherent states (WCS) and single photons.

\*This experiment was not at the single-photon level but with a few photons per pulse.

\*\*This experiment is actually a cavity-assisted DLCZ experiment, but the dephasing experienced by spin-waves in the spin levels is the same in both techniques.

\*\*\*The  $1/e$  decay time was 27.5  $\mu$ s for reference [51] and 13.11  $\mu$ s for reference [60].

## 1.4 Summary of the thesis

In this thesis, I will report about three experiments I performed during my PhD. After a theoretical introduction (chapter 2) mainly focused on

light-matter interaction, on the bulk crystal we use,  $\text{Pr}^{3+}:\text{Y}_2\text{SiO}_5$ , and on its properties, I will describe, in chapter 3, an experiment combining the AFC and the DLCZ schemes, where we demonstrated the presence of entanglement between a photon emitted by our AFC-DLCZ emissive memory and a spin excitation inside the crystal [53].

In chapter 4, I will present the main results of the first impedance-matched-cavity experiment we performed in our group (paper in preparation). In particular, I will report about the highest efficiency achieved so far with the AFC protocol (62 % device efficiency) by storing weak coherent states in our memory. Another remarkable result from the same experiment is the most efficient storage of qubits in a solid-state quantum memory: we demonstrated a 52 % storage efficiency for weak-coherent time-bin qubits, and we analyzed the memory fidelity by using a filter crystal, where we optically pumped an AFC-based Mach-Zehnder interferometer to interfere the two qubit components.

In the last experimental chapter 5, I will treat a quantum frequency conversion experiment. Within the framework of interfacing different material systems, we converted  $\mu\text{s}$ -long photons from the visible (606 nm) to the telecom wavelength (1550 nm) with a  $\text{SNR} > 2$ , with room for improving this value. This is of paramount importance to interface an AFC-DLCZ memory emitting in the visible regime—whose emitted photons can be as long as tens of  $\mu\text{s}$  in time [72, 78] and hence spectrally narrow—with trapped ions, which have narrow bandwidths [101].

Finally, I will summarize all the reported results in chapter 6, and I will give an outlook for the experiments I presented, in particular in a perspective of a new generation of highly efficient quantum repeater nodes.

## Chapter 2

# Light-matter interaction in rare-earth doped crystals and quantum memory protocols

In this chapter, I will speak about rare-earth ions, provide a few notions about their spectroscopic properties and, eventually, introduce our quantum memory protocols.

### 2.1 Rare-earth ions

In this section, I am going to introduce the element we use for implementing our quantum memory protocols: praseodymium. Praseodymium is an element of the periodic table with atomic number 59; it belongs to the series of lanthanoids<sup>1</sup> and therefore is classified among the so-called rare-earth

---

<sup>1</sup>Throughout this chapter, I will adopt IUPAC's recommendation of using the name "lanthanoids" to refer to these elements, rather than the old one "lanthanides". Instead, I will use the term "rare earths" to refer to set of lanthanoids plus yttrium and scandium, despite it is deprecated by IUPAC, due to the large use of this term in our field.



elements. Praseodymium possesses many isotopes [102], but only a stable one,  $^{141}\text{Pr}$ , which is the one we employ. In this section, I will focus on the spectroscopic properties of rare earths, analyzing then the praseodymium level structure. I will show how this structure is affected by the interaction with its host crystal, yttrium orthosilicate ( $\text{Y}_2\text{SiO}_5$ ), where  $\text{Pr}^{3+}$  ions replace a fraction of yttrium ions (typically of the order of 0.05%).

The treatment of this section is based on several book chapters [103–108] and PhD theses [100, 109–111], alongside several papers that will be cited throughout this chapter.

### 2.1.1 Rare earths

Seventeen elements of the periodic table are classified under the name of “rare earths”. This definition encompasses the 15 elements belonging to the lanthanoids, plus yttrium and scandium. These last two elements have chemical properties very similar to the lanthanoid ones. Lanthanoid atomic numbers range from 57 (lanthanum) to 71 (lutetium), while scandium and yttrium are lighter (respectively 21 and 39 atomic numbers). All these elements are visible in the periodic table in figure 2.1, where rare earths are highlighted with light green color.

Rare-earth ions (REI) exhibit peculiar features due to the fact that their electronic level 4f is more energetic than the 5s and 5p subshells, but it is spatially more internal than this last two orbitals (see figure 2.2 where the case for gadolinium is showed). Therefore, in filling the orbitals, electrons occupy 5s and 5p subshells first: this provides the 4f level with a screening effect from these external shells. This shielding effect yields extremely narrow homogeneous linewidths for the 4f-4f transitions [113] and coherence properties which are beneficial for quantum memory applications, especially when REIs are embedded in crystals.

REIs can be divided into two main categories: Kramers ions and non-Kramers ions [103]. Kramers ions have odd number of electrons, whereas non-Kramers have an even number of electrons. Praseodymium 3+ ion belongs to the latter category, since it has two electrons on the 4f level. The behaviors of these two categories differ a lot, especially when embedded in

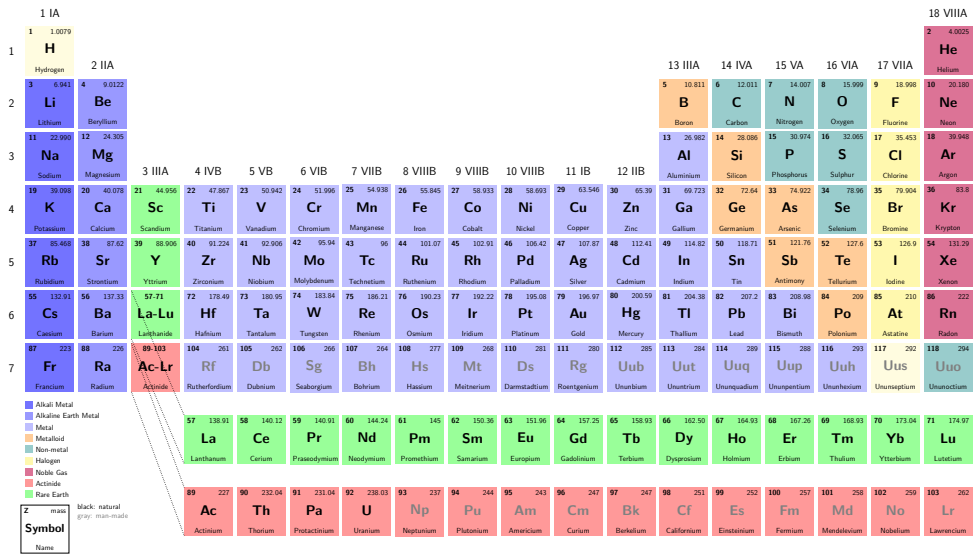


Figure 2.1: Periodic table of elements. In light green, rare earths are shown. The elements from lanthanum (La) to lutetium (Lu) constitute the lanthanoids series.

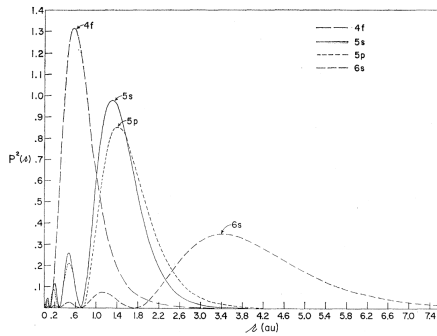


Figure 2.2: The radial charge density,  $P^2(r)$  as a function of radius  $r$ , for the 4f, 5s, 5p, 6s orbitals of Gd<sup>+</sup>. This picture is taken from reference [112].

a crystal lattice: indeed, the magnetic moment of the unpaired electron of Kramers ions is not quenched by its partner, causing a stronger magnetic moment and hence increased reaction to external magnetic fields. I will speak more in detail about their interactions in a lattice in the next section.

### 2.1.2 Rare-earth doped crystals

A rare earth ion embedded in a lattice can be described by an Hamiltonian of the kind:

$$\mathcal{H}_{\text{TOT}} = [\mathcal{H}_{\text{FI}} + \mathcal{H}_{\text{CF}}] + [\mathcal{H}_{\text{HF}} + \mathcal{H}_{\text{Q}} + \mathcal{H}_{\text{Z}} + \mathcal{H}_{\text{z}}] \quad (2.1)$$

where  $\mathcal{H}_{\text{FI}}$  is the free-ion Hamiltonian,  $\mathcal{H}_{\text{CF}}$  represents the crystal field Hamiltonian,  $\mathcal{H}_{\text{HF}}$  accounts for hyperfine interaction,  $\mathcal{H}_{\text{Q}}$  for the quadrupolar one, and  $\mathcal{H}_{\text{Z}}$  and  $\mathcal{H}_{\text{z}}$  describe respectively the Zeeman electronic and Zeeman nuclear interactions [104]. The Hamiltonian is structured in two parts (between square brackets), as the first part is giving rise to the large splitting between the levels, while small hyperfine splittings arise from the second part. I will not treat into detail the whole Hamiltonian, but just discuss the contribution of each of the terms to the level structure. Full treatments can be found in references [100, 104–106, 109].

The first Hamiltonian  $\mathcal{H}_{\text{FI}}$  is a sum of three contributions:  $\mathcal{H}_0$ , the central field Hamiltonian;  $\mathcal{H}_{\text{C}}$ , the Coulomb Hamiltonian for electrons, describing repulsion between them; and  $\mathcal{H}_{\text{LS}}$ , the spin-orbit Hamiltonian. In first approximation, the interaction between REIs and the surrounding environment is not particularly strong: hence, we can consider only the first term, which is describing the ion alone, and treat later the crystal field term as a perturbation.

The first contribution is a central field approximation, which is customary in lanthanoids for solving the Schrödinger equation. Nevertheless, all the eigenstates of the first Hamiltonian are degenerate.

From now on, we will focus on our kind of dopant,  $\text{Pr}^{3+}$ . The first splitting occurs when the Coulomb interaction between electrons lifts this degeneracy and, as a consequence, levels are split between ground and excited ones. L and S become the relevant quantum numbers, and each

level can be described by  $2^{s+1}L$ . The lowest energy ground level emerging from the 4f is the  ${}^3H$  level, where  $L = 0, 1, 2, 3, 4, 5, \dots \equiv S, P, D, F, G, H, \dots$

Another symmetry is broken when we consider the interaction between the electron spin and the magnetic field they create by orbiting around the nucleus, the so-called spin-orbit interaction. The number of sub-levels originating from each level is  $j$ , which is the quantum number associated to the operator  $\mathbf{J} = \mathbf{L} + \mathbf{S}$ .  $j$  can take all the values ranging from  $l + s$  to  $|l - s|$ . These three quantum number are used to define univocally the new levels through the notation  $2^{s+1}L_j$ . Following this definition, the lowest lying level emerging from the 4f can be written as  ${}^3H_4$ .

The crystal field Hamiltonian represents the first of the minor corrections to the main level structure. This interaction with the crystal field generated by the crystal is much weaker than the previous correction, so it represents a simple perturbation within the manifolds. Despite its low intensity, this perturbation makes the 4f-4f transitions weakly allowed. The notation for labeling these levels is  ${}^3H_4(n)$ , with  $n = 0, 1, 2, 3, \dots, 2j$ . For this specific term of equation 2.1, the final configuration changes drastically whether we are considering Kramers or non-Kramers ions. At cryogenic temperatures, we are confined to the  $n = 0$  crystal field level, since all the other levels are accessible only via phononic excitations.

$\text{Pr}^{3+}$  is a non-Kramers ion and, when embedded in a  $\text{Y}_2\text{SiO}_5$  crystal matrix, it occupies a low symmetry site [106, 110]. As a consequence, the electronic angular momentum is quenched and the hyperfine interaction between it and the nuclear spin appears only with second-order corrections [105]. This perturbation splits further every crystal field singlet of praseodymium into  $\pm 1/2, \pm 3/2, \pm 5/2$ .

This degeneracy can be further removed by the last two terms of equation 2.1—the Zeeman effect for nucleus and electrons—when a magnetic field is applied. This is not the case for our experiments, so it will not be treated. Figure 2.3 shows the incremental splittings of the levels due to the contributions discussed. The levels I will focus on in the next sections are the ones enclosed by the green dashed rectangle; figure 2.4 shows a zoom of them.

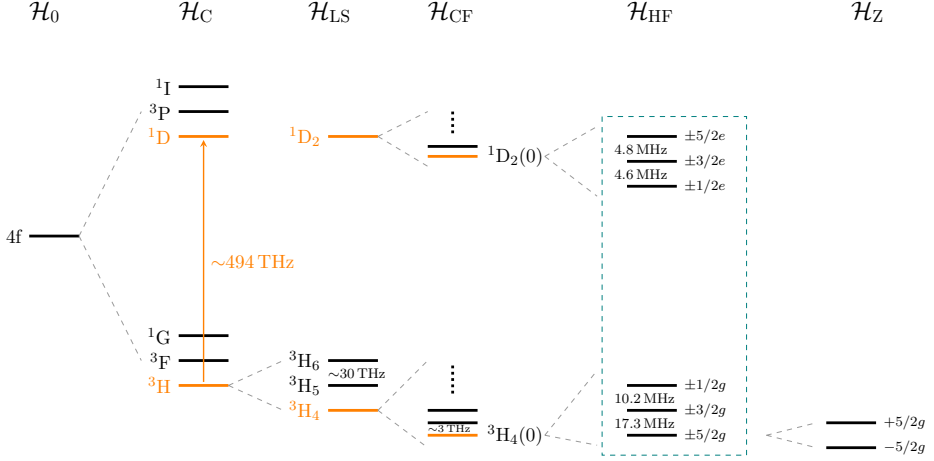


Figure 2.3: Incremental splitting of the  $\text{Pr}^{3+}$  electronic levels as all the contributions of equation 2.1 are progressively considered. The green dashed rectangle surrounds the levels of interest when dealing with the quantum memory protocols used in this thesis. The contribution given by  $\mathcal{H}_Z$  arises only when an external magnetic field is applied, which is not the case in all the experiments that will be presented throughout this thesis. This figure is a reproduction of figure 2.3 from reference [100].

### 2.1.2.1 Praseodymium-doped orthosilicate

The level structure of praseodymium has already been discussed in the previous section. The transition we address in our experiments is  ${}^3\text{H}_4(0) \rightarrow {}^1\text{D}_2(0)$ . The  $\text{Y}_2\text{SiO}_5$  crystal has a monoclinic cell ( $\text{C}_{2h}^6$ ) structure, and it has three optical axes, perpendicular between each other: the crystallographic direction  $b$ ,  $\text{D}_1$  and  $\text{D}_2$  [107]. The absorption of yttrium ions is maximum along this last axis, which is the one we usually address in our experiments by polarizing the light along its direction. Inside the unit cell, the yttrium ions can take two different positions, site 1 and site 2. Typically, 0.05% of the yttrium ions are replaced by  $\text{Pr}^{3+}$  ions. In site 1, the transition  ${}^3\text{H}_4(0) \rightarrow {}^1\text{D}_2(0)$  is at 605.977 nm, corresponding to orange light in the visible

Ground \ Excited	$\pm 1/2$	$\pm 3/2$	$\pm 5/2$
$\pm 1/2$	0.55	0.38	0.07
$\pm 3/2$	0.40	0.60	0.01
$\pm 5/2$	0.05	0.02	0.93

Table 2.1: Oscillator strength for the transitions between the ground states of  ${}^3\text{H}_4(0)$  and the excited states of  ${}^1\text{D}_2(0)$ . This table is taken from reference [114].

regime. Site 1 is usually the most populated between the two sites by  $\text{Pr}^{3+}$  ions. Furthermore, the transition 4f - 4f of ions sitting in site 1 have stronger dipole moments with respect to the 4f - 4f of the ones in site 2. As already discussed, considering all the contributions to the total Hamiltonian of equation 2.1 leads to the splittings shown in figure 2.3. Focusing on the level structure arising from the last contribution  $\mathcal{H}_{\text{HF}}$ , at zero magnetic field, the level structure of figure 2.4 emerges. We can see three ground level doublets  $|\pm \frac{1}{2}g\rangle$ ,  $|\pm \frac{3}{2}g\rangle$  and  $|\pm \frac{5}{2}g\rangle$ , and three excited level doublets  $|\pm \frac{1}{2}e\rangle$ ,  $|\pm \frac{3}{2}e\rangle$  and  $|\pm \frac{5}{2}e\rangle$ . The main transition I will be addressing in my considerations is the  $|\pm \frac{1}{2}g\rangle - |\pm \frac{3}{2}e\rangle$  one. The dipole moments of this level scheme are listed in table 2.1.

Further details about  $\text{Pr}^{3+}:\text{Y}_2\text{SiO}_5$  can be found in books [105–107] and in PhD theses of former members of my group [100, 109, 110].

### 2.1.2.2 Homogeneous linewidth

All the atomic transitions have an homogeneous linewidth  $\Gamma_{\text{hom}}$ , that is, a broadening of their absorption spectrum centered around the main frequency of absorption. This broadening has a Lorentzian shape.

In  $\text{Pr}^{3+}:\text{Y}_2\text{SiO}_5$ , the transitions 4f - 4f have a very narrow homogeneous linewidth (of the order of 2 kHz) since, as it has been discussed in section 2.1, the lower energy levels are also the outer ones and shield the 4f from external fields.

Starting from the homogeneous linewidth  $\Gamma_{\text{hom}}$ , we can define the coherence

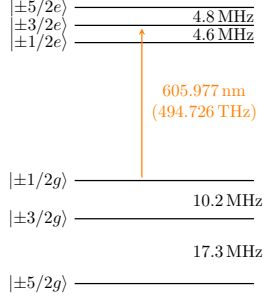


Figure 2.4: Hyperfine levels of  $\text{Pr}^{3+}$  in  $\text{Y}_2\text{SiO}_5$  of the manifolds  ${}^3\text{H}_4$  (ground) and  ${}^1\text{D}_2$  (excited).

time of the transition,  $T_2$ , as:

$$T_2 = \frac{1}{\pi\Gamma_{\text{hom}}} \quad (2.2)$$

Another time quantity associated with a given transition is its population lifetime  $T_1$ , which is the lifetime of the excited state.

In the absence of further mechanisms of line-broadening, we have that  $T_2=2T_1$ <sup>2</sup> [108]. Unfortunately, many dephasing mechanisms affect the ions, such that the homogeneous line gets broadened further:

$$\Gamma_{\text{hom}} = \frac{1}{2\pi T_1} + \frac{1}{\pi T_2^*} = \frac{1}{\pi T_2} \quad (2.3)$$

where the factor  $T_2^*$  accounts for all the dephasing mechanisms that will be explained later.

Broadening effects that vary inside the host material will be treated in the next section. The homogeneous line can be broadened by several effects,

<sup>2</sup>In reference [108], this is not stated explicitly. Nevertheless, in reference [115], this result is inferred from equation 3.29 of reference [108] (the two solutions for  $a$  and  $b$  at page 65 for the exact resonance case of equation 3.27) by putting  $\frac{1}{b} = T_2$ . Note that this does not lead to equation 9.54 from reference [115] nor to equation 2.3 because the author has purposely changed the notation to have  $T_2 = T_2^*$  (rather than  $T_2 = 2T_2^*$ ) in the limit  $T_2^* \ll T_1$ .

which are thoroughly described in references [105, 116]. Equation (2) in reference [116] displays all the four main contributions:

$$\Gamma_{\text{hom}} = \Gamma_{\text{pop}} + \Gamma_{\text{ion-spin}} + \Gamma_{\text{ion-ion}} + \Gamma_{\text{phonon}}$$

The last term  $\Gamma_{\text{phonon}}$  describes the phononic scattering, but it is negligible at the cryogenic temperatures the crystal is at—around 3 K—and we can neglect it.

$\Gamma_{\text{pop}}$  contains both the spontaneous phonon emission contribution, which, like  $\Gamma_{\text{phonon}}$ , can be disregarded at 3 K for low-lying crystal field levels, and the radiative contribution. Its value sets the minimum achievable  $\Gamma_{\text{hom}}$ , which in this specific case<sup>3</sup> is  $(970 \pm 30)$  Hz.

$\Gamma_{\text{ion-spin}}$  depends on the magnetic properties of the crystal.  $\text{Y}_2\text{SiO}_5$  has very low magnetic moments of the constituent elements, therefore this contribution does not play an important role.

$\Gamma_{\text{ion-ion}}$  represents the so called instantaneous spectral diffusion. It arises from the fact that, when probing the material with a laser pulse,  $\text{Pr}^{3+}$  ions get excited and can influence the transitions of neighbouring ions. This issue is often addressed by doping the crystal with less dopants, thus preventing the ions to interact with each other.

### 2.1.2.3 Inhomogeneous linewidth

Real spectral lines of rare-earth ions in crystals are much broader than the values that were reported in the previous section. These lines, indeed, experience an additional broadening due to the strain of the crystal matrix. This effect is called inhomogeneous broadening because it is different for every ion, as the strain depends on the spatial position of the ions. The strain is intrinsic but it can be enhanced by chemical impurities or point defects. The total effect of the spectral shift on the  $\text{Pr}^{3+}$  ions is an absorption line with a width that can be several orders of magnitude larger than their homogeneous line. Figure 2.5 depicts a visual representation of the inhomogeneous broadening. In appendix C, in figure C.1, a measurement of the inhomogeneous broadening of one of our crystals is shown.

---

<sup>3</sup> $\text{Pr}^{3+}:\text{Y}_2\text{SiO}_5$ ,  $^3\text{H}_4(1)^{-1}\text{D}_2(1)$  transition in site 1



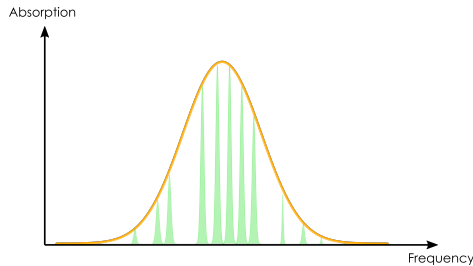


Figure 2.5: Graphical visualization of the inhomogeneously broadened line. The green spectra are the homogeneous broadened lines of the single ions.

The inhomogeneous broadening prevents any input pulse from maintaining any coherence when absorbed: indeed, if a pulse is absorbed by the ensemble of ions, ions at different frequencies will experience different dephasings and the pulse will be re-emitted incoherently at random directions.

Nevertheless it is possible to harness atomic coherences and to apply rephasing mechanisms that undo this inhomogeneous dephasing, allowing the stored photons to be re-emitted collectively by the ions in a well defined spatio-temporal mode. One of this rephasing mechanisms is the atomic frequency comb scheme, which will be introduced in section 2.2, whereas another one is the two-pulse photon echo (TPE) technique, which will be treated in section 2.1.2.6 and in appendix A. Before introducing the AFC protocol, it is necessary to investigate the consequences of the inhomogeneous broadening on the  $\text{Pr}^{3+}:\text{Y}_2\text{SiO}_5$  ion spectrum and the concept of optical pumping, which enables shaping this spectrum in a controlled way. In the next sections, I will treat these topics, starting from the ion classes of  $\text{Pr}^{3+}:\text{Y}_2\text{SiO}_5$ .

#### 2.1.2.4 Classes of ions

As introduced in section 2.1.2.3, accounting for inhomogeneous broadening implies that a pulse is able to excite ions in more than one of the transitions displayed in section 2.1.2.1. This gives rise to classes of ions, i.e., ions

resonating with a specific transition at the same frequency. Since in the considered case, 3 ground levels and 3 excited levels are involved,  $3 \cdot 3 = 9$  possible classes can be defined. These 9 classes span around 37 MHz in the inhomogeneous spectrum, that is, the maximum distance between the  $\pm 5/2g$  and  $\pm 5/2e$ , and they are displayed in figure 2.6. Obviously, these classes form a continuum inside the spectral line, but the discrete picture is useful to understand the hole-burning technique, which is the method we use to tailor this line and that it will be explained in the next section.

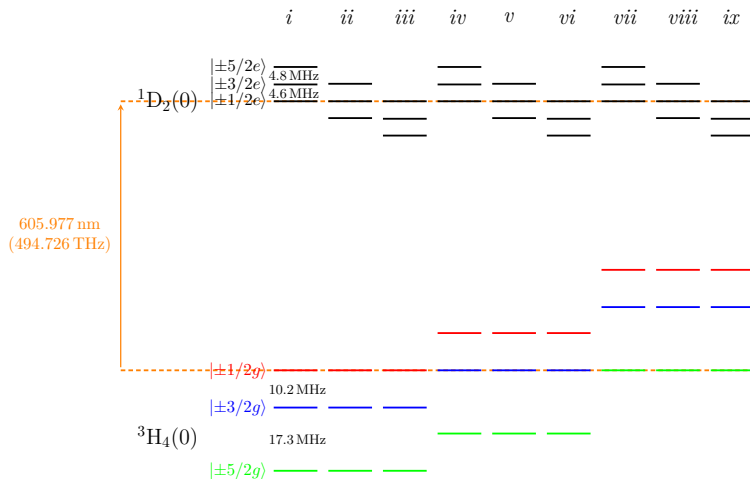


Figure 2.6: Sketch of the 9 classes of ions originating from the inhomogeneous broadening in a  $\text{Pr}^{3+}:\text{Y}_2\text{SiO}_5$  crystal.

### 2.1.2.5 Spectral hole-burning

We have seen the level structure of  $\text{Pr}^{3+}:\text{Y}_2\text{SiO}_5$  and how a pulse resonant with one of the transitions is in fact resonant with 9 transitions of 9 different classes of ions at the same time. Provided that this pulse is shone for long enough, we can actually deplete the population of a ground level and create a transparency window in the material spectrum. This procedure is called

optical pumping for spectral hole-burning [105, 114].

For the sake of simplicity, the complicated classes structure of figure 2.6 will be ignored and I will focus on the single class transitions of figure 2.4.

If a transition of the 9 showed in the picture—for instance, the  $\pm 1/2g - \pm 1/2e$ —is addressed with a strong enough laser pulse, part<sup>4</sup> of the population of the ground state will be excited to the excited state. Then, ions will spontaneously decay to the ground levels, with transition probabilities given in the table 2.1. In order to empty completely a level, the procedure must be repeated to excite away ions that are decaying back to the starting ground state. This is possible only when the population lifetime of the reservoir states (the ground spin states) is much longer than the optical lifetime; otherwise, the initial ground level will be partially filled up again.

In the final configuration, a ground level will have been emptied of its population, while some other ground states will show an excess of population with respect to their starting conditions. Therefore, by probing the transitions with a chirped weak laser pulse, transparency regions—called spectral holes—will be observed on all the transitions driven from the same ground level, whereas increased absorption regions—so called anti-holes—will be present on all the transitions driven from overpopulated levels. Figure 2.7 shows the spectrum of the transitions of figure 2.4 after the ground level  $\pm 1/2g$  has been emptied of its population, causing  $\pm 3/2g$  and  $\pm 5/2g$  to be filled up. This simulation accounts for the multi-class structure detailed in figure 2.6. For details about the software simulator, I refer to appendix section B.3.2.

---

<sup>4</sup>The whole population can be removed if the pulse is shorter than the coherence time of the transition; otherwise, only half of it can be removed.

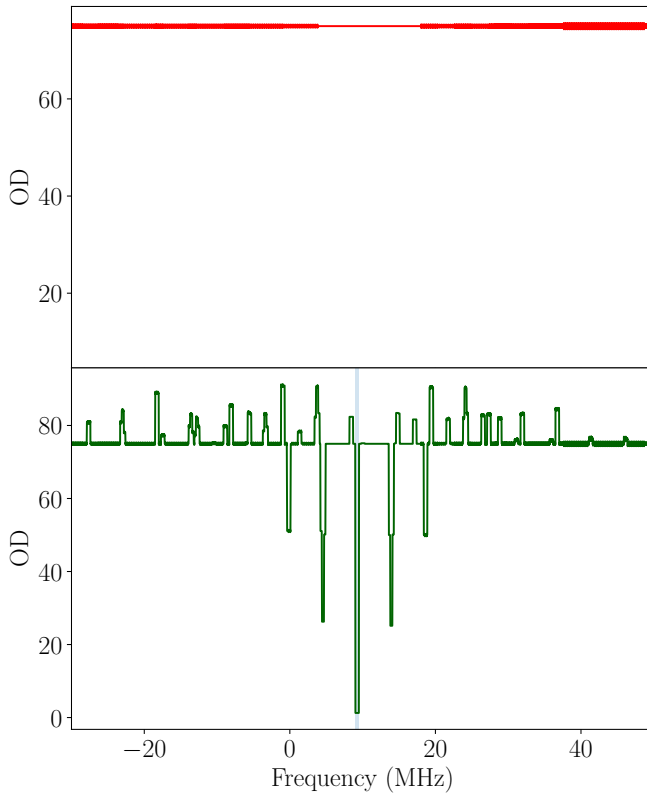


Figure 2.7: Simulation of the effect on a strong pulse (blue shaded area in the bottom graph) addressing and emptying the  $\pm 1/2g$  level (situated at around 9 MHz) on a 80 MHz section of the inhomogeneous broadening. We can see that, compared to the unperturbed inhomogeneously broadened line (red plot at the top), holes and anti-holes appears in all the involved levels. In particular, holes appear in all the transitions starting from the  $\pm 1/2g$  of the first class and all the transitions of other classes resonant with this pulse, while anti-holes are present in all the transitions starting from  $\pm 3/2g$  and  $\pm 5/2g$  of first class and other resonant transitions from other classes. The optical depths (see section 2.2) shown on the y-axes are purely arbitrary and not realistic.

The linewidth of the narrowest hole that can be burnt is limited to twice the homogeneous linewidth of our transition [117]. As stated in section 2.1.2.2, this means that holes narrower than 2 kHz cannot be attained in  $\text{Pr}^{3+}:\text{Y}_2\text{SiO}_5$  (slightly narrower holes are achievable with a magnetic field [116]). Nonetheless, it is extremely challenging to reach this limit, mainly because the laser linewidth can be broader than the homogeneous linewidth. If this is the case, the narrowest hole we can create will at most be as narrow as the laser light we are employing. Furthermore, the hole width is enlarged by power broadening [117–119]. The dependency of the width on the laser power  $P$  scales as  $\sqrt{P}$ .

The hole-burning procedure is the basis for the protocol that is going to be discussed in section 2.2, the atomic frequency comb or AFC protocol.

### 2.1.2.6 Two-pulse photon echo (TPE) technique

The two-pulse photon echo (TPE) technique is a method for inverting the dephasing of a previously excited ensemble, leading to a coherent rephasing of the excitation. It can be used to measure the homogeneous linewidth of the optical transition of interest. A detailed theoretical treatment of this procedure is provided in appendix A, and here I will summarize the salient points. The starting point is a two-level system, where the atoms are polarized in the ground level  $|g\rangle$ . We assume that, at an initial time  $t_1$ , a  $\pi/2$ -pulse (appendix section A.1.3) is shone resonantly with this transition, exciting the atoms to the excited level  $|e\rangle$ . As explained in section 2.1.2.3, the ions will experience different dephasings because of the inhomogeneously broadened line, and thus would normally re-emit incoherently. Nonetheless, it is possible to rephase coherently the absorbed pulse by means of a second  $\pi$ -pulse shone at a time  $t_2 = t_1 + \tau$ . What happens is that now the dephasing reverses and at a time  $t_{12} = t_2 + \tau = t_1 + 2\tau$ , an echo pulse is emitted from the ensemble. The echo intensity provides useful information about the decay and decoherence mechanisms of the ensemble of atoms we are addressing: as a matter of fact, every process occurring between  $t_1$  and  $t_2$  or  $t_2$  and  $t_{12}$  leading to a decrease of the number of atoms that are rephasing diminishes the echo intensity. In appendix section B.3.1,

I will explain our method of extracting the  $T_2$  of our atoms by varying the time  $\tau$  between the two pulses.

## 2.2 Atomic frequency comb (AFC)

The atomic frequency comb memory protocol (AFC) [83] relies on tailoring the inhomogeneously broadened line with a periodic pattern. Shaping this structure is possible thanks to a precise scheme of optical pumping on the level structure that was introduced in section 2.1.2.4. The structure we tailor inside the inhomogeneously broadened line has the shape of a comb, whose teeth have a fixed frequency separation  $\Delta$ ; the storage time of the AFC is given by  $\tau = \frac{1}{\Delta}$ . When an external photon of linewidth  $\gamma > \Delta$  reaches the frequency comb and gets absorbed, it gets mapped into a collective excitation of ions. Since a single photon can excite at most one ion, and the specific ion that absorbs it is unknown, the state of the  $N$  ions involved has the form

$$\sum_{j=1}^N c_j e^{2i\pi\delta_j t} e^{ikz_j} |g_1 \dots e_j \dots g_N\rangle \quad (2.4)$$

This equation is describing the absorption of a photon with wavevector  $k$  by the  $j$ -th ion, which is undetermined, so the sum runs over the index  $j$ . All the other ions remain in the ground state. The  $j$ -th ion is at the spatial position  $z_j$  and spectrally detuned by  $\delta_j$  with respect to the center of the comb; the coefficient  $c_j$  is a function of  $z_j$  and  $\delta_j$ .

Mathematically, to tailor an AFC is equivalent to say that  $\delta_j = m_j \Delta$ , with  $m_j$  integer. As described by equation 2.4, whenever the photon is absorbed, atoms start to inhomogeneously dephase. However, thanks to the periodicity of the comb, this process is controlled, such that after a time  $\tau$  all the atoms get in phase again, collective emission happens and the original photon leaves the crystal in the same spatial mode.

In figure 2.8, we can see an example of an AFC with 4 Gaussian-shaped teeth. The plot shows the optical depth OD of this comb. The optical

depth (OD) is a quantity related to the number of ions interacting with the light. It is defined as  $OD = \alpha L$ , where  $\alpha$  is the absorption coefficient (which typically is around  $20 \text{ cm}^{-1}$  for our crystals described in appendix section B.2.2) and  $L$  is the length of the crystal. Usually, the OD that can be experimentally achieved in an AFC is lower than the maximum OD exhibited by the crystal. Three relevant parameters are highlighted in the figure: the maximum comb optical depth (called simply OD here), the separation  $\Delta$  between the AFC peaks and the full-width-at-half-maximum (FWHM) linewidth  $\gamma$  of the AFC peaks. From these quantities, two more crucial quantities can be calculated: the finesse  $\mathcal{F}_{\text{AFC}}$ , defined as  $\mathcal{F}_{\text{AFC}} = \frac{\Delta}{\gamma}$ , and the average optical depth  $\tilde{d}$ , related to the finesse through  $\tilde{d} = \frac{OD}{\mathcal{F}_{\text{AFC}}}$  for an AFC with square peaks.

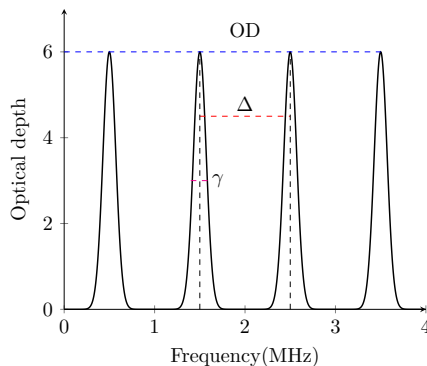


Figure 2.8: Sketch of an atomic frequency comb with 4 teeth in a 4 MHz interval. In the plot, the comb optical depth  $OD$ , the peak width  $\gamma$  and the separation  $\Delta$  between the teeth are highlighted. From these quantities, we can define the comb finesse  $\mathcal{F}_{\text{AFC}}$  as  $\mathcal{F}_{\text{AFC}} = \Delta/\gamma$  and the average OD  $\tilde{d}$  as  $\tilde{d} = OD/\mathcal{F}_{\text{AFC}}$ .

As just discussed, the AFC protocol is not “on-demand”, since the storage time is given by the separation between the peaks and cannot be decided by the user. However, it is possible to transfer the excitation from the excited levels to the spin levels: this is the spin-wave storage protocol that

will be explained in section 2.2.2 [83]. A remarkable feature of the AFC protocol is its temporal multimodality, namely the possibility of storing and retrieving many temporal modes at the same time. This means that, provided that the input modes are distinguishable, they all rephase independently of each other and will all be re-emitted in the same order they were stored. The maximum duration a pulse stored in the AFC can have is dictated by the storage time, so  $T = 2\pi/\Delta$ , while the minimum duration  $\tau$  is limited by the total spectrum of the comb:  $\tau \sim 1/(N_p \Delta)$ , where  $N_p$  is the number of peaks of the comb. Thus, the maximum number of storable temporal modes is given by  $T/\tau \sim N_p$ : increasing the number of peaks yields a larger number of temporal modes that can be stored [83]. This exclusive dependence of the temporal multimodality on the number of peaks is not a trivial characteristic, since storage protocols like EIT or controlled reversible inhomogeneous broadening (CRIB) display a clear dependence on the OD [120].

### 2.2.1 AFC efficiency

The AFC efficiency in the forward direction is limited to the theoretical limit of 54%, reached for a  $\tilde{d}$  of 2 [83]. The single-pass efficiency formula for the AFC with forward retrieval is:

$$\eta_{\text{sp}}^{\text{forw}} = \tilde{d}^2 e^{-\tilde{d}} e^{-d_0} \eta_{\text{deph}} \quad (2.5)$$

where  $d_0$  is the background absorption, that is, the part of the AFC that is absorbing but not leading to coherent rephasing (typically, the absorption pedestal below the peaks);  $\eta_{\text{deph}}$  is the dephasing term arising from the finite width of the peaks.  $\eta_{\text{deph}}$  can have different expressions depending on their shape of the peaks, but I will report only the two most common cases: for Gaussian peaks,  $\eta_{\text{deph}}^{\text{Gauss}} = \exp(-7/\mathcal{F}_{\text{AFC}}^2)$ ; for square peaks (the best shape in terms of efficiency [121]), it is  $\eta_{\text{deph}}^{\text{square}} = \text{sinc}^2(\pi/\mathcal{F}_{\text{AFC}})$ . The behavior of  $\eta_{\text{deph}}$  as a function of  $\mathcal{F}_{\text{AFC}}$  for both cases is shown in figure 2.9. For a given comb OD, an optimal finesse  $\mathcal{F}_{\text{AFC}}^{\text{opt}}$  yielding the maximum efficiency



for that OD can be calculated through the formula [88, 121]

$$\mathcal{F}_{\text{AFC}}^{\text{opt}} = \frac{\pi}{\arctan \frac{2\pi}{OD}}. \quad (2.6)$$

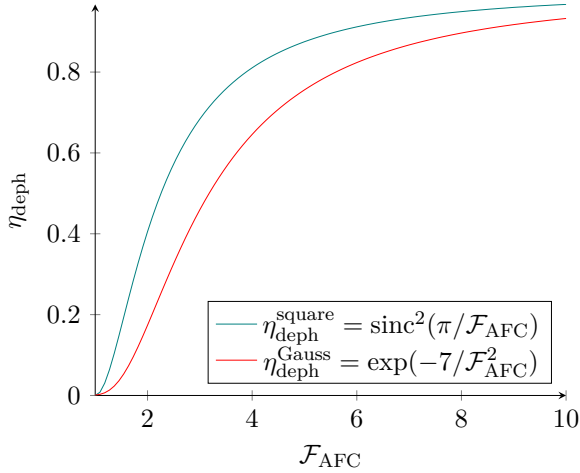


Figure 2.9: Dephasing factor vs AFC finesse for square-shaped peaks (blue curve) and Gaussian-shaped peaks (red curve).

Focusing on equation 2.5, and disregarding for the moment the dephasing term  $\eta_{\text{deph}}$  and the background absorption  $e^{-d_0}$  that appear in it, it can be easily calculated that the maximum of this function in terms of  $\tilde{d}$  is reached for  $\tilde{d} = 2$ , where it takes the value  $4/e^2 = 0.54134\dots$ . This limit arises from a trade-off between the two opposite regimes. In the low OD regime ( $\tilde{d} \ll 1$ ),  $\eta_{\text{sp}} \sim \tilde{d}^2$ : this means that the increase in OD is favoring the absorption, and hence the storage in the AFC. The increase in efficiency is quadratic with the increase in OD.

In the high OD regime ( $\tilde{d} \gg 1$ ),  $\eta_{\text{sp}} \sim e^{-\tilde{d}}$ : in this regime, increasing the OD is in fact counter-productive, because the efficiency exponentially decreases with  $\tilde{d}$ . The physical reason behind that lies in the re-absorption of the AFC echo: the OD is, as a matter of fact, enhancing the light-matter

interaction in the form of absorption from the AFC, but it is also leading to the multiple re-absorptions of the echo inside the ensemble, thus diminishing the overall efficiency. Therefore, the OD must be tuned to an intermediate value, at the expense of efficiency.

This does not hold for the retrieval in backward direction, because the interference between all the possible paths the photon can follow in the medium leads to constructive interference when the direction of emission is changed [83, 122]. The backward retrieval single-pass efficiency is given by:

$$\eta_{\text{sp}}^{\text{back}} = \left(1 - e^{-\tilde{d}}\right)^2 e^{-d_0} \eta_{\text{deph}} \quad (2.7)$$

Backward retrieval is possible in the case of spin-wave storage, which will be treated in the next section: with two counterpropagating control pulses, the phase-matching condition can be changed in such a way to have backward re-emission. Another method for overcoming this strict limit is embedding the AFC in an impedance-matched cavity [86]. I will deal extensively with this topic in section 2.3 and I will present an impedance-matched-cavity-assisted AFC experiment in chapter 4.

An additional limitation that becomes more relevant for long storage times is set by the limited  $T_2$  of our considered transition [51]. The AFC experiences a loss of efficiency due to the limited linewidth  $\gamma_{\text{hole}}$  of the holes, which is  $2\Gamma_{\text{hom}}$  (as stated in section 2.1.2.2), and this is related to the  $T_2$  of the transition through equation 2.2. In order to follow the same notation as reference [51],  $\gamma_{\text{hole}}$  will be the hole width in Hz, while  $\omega_{\text{hole}} = 2\pi\gamma_{\text{hole}}$  will be expressed in  $\text{rad s}^{-1}$ , so to have  $\omega_{\text{hole}} = 4\pi\Gamma_{\text{hom}}$ . Hence, calling  $\eta_0$  the extrapolated efficiency at  $\tau = 0$ , a new factor for the efficiency can be defined:

$$\eta_{\text{h}} = \eta_0 \exp\left(-\frac{\omega_{\text{hole}}}{\Delta}\right) = \eta_0 \exp\left(-\frac{4\pi\Gamma_{\text{hom}}}{\Delta}\right) = \eta_0 \exp\left(-\frac{4\tau}{T_2}\right) \quad (2.8)$$

where equation 2.2 and  $\Delta = 1/\tau$  have been used. Therefore, we can see that the efficiency of the AFC echo strongly depends on the storage time. In section 4.2.3, we will see an AFC experiment with long storage times where this factor plays a crucial role.

So far, I have spoken about the AFC theoretically, without detailing its experimental preparation. This is treated in detail in the appendix section [B.3.2](#).

### 2.2.2 Spin-wave storage

As said at the beginning of section [2.2](#), the AFC itself does not possess any on-demand capability. Its storage time is limited by the coherence time of the excited state, which is of the order of hundred  $\mu\text{s}$  [[100](#)]. Nevertheless, the spin state coherence time is much longer—around 500  $\mu\text{s}$  at zero field [[123](#)] and several ms with magnetic fields [[124–126](#)] up to 900 ms [[127](#)], with a  $T_1$  around 100 s [[128](#)]<sup>—</sup>and can be improved to up to 1 min by means of protocols like dynamical decoupling [[129](#)]. This long coherence time makes it possible to store the excitation in the AFC in a storage spin level (like  $\pm 3/2g$  in figure [2.4](#)) of the  $\text{Pr}^{3+}$  ions for a longer time. The dephasing experienced in this spin level is much slower than the one of the excited level. The protocol works in the following way: at a time  $t' < \tau_{\text{AFC}}$ , a first control pulse CP1 is shone on the transition  $\pm 3/2e \rightarrow \pm 3/2g$ . This coherently transfers the rephasing excitation from the  $\pm 3/2e$  level to the spin level  $\pm 3/2g$ . After a time  $T_S$ , a second control pulse can be sent on the  $\pm 3/2g \rightarrow \pm 3/2e$  transition, to restore the excitation in the excited state. Thanks to the coherence of the process and of the AFC, the rephasing resumes and, after a time  $t''$ , the echo is re-emitted. The whole storage time is then  $t' + T_S + t'' = \tau_{\text{AFC}} + T_S$ . This protocol goes under the name of spin-wave storage, three-level AFC or full AFC protocol.

Excitations stored in spin levels are not immune to decoherence. The inhomogeneous broadening of the spin levels—also called spin inhomogeneity— affects the coherence of the transferred excitations, and limits the spin storage time to some tens of  $\mu\text{s}$ . In  $\text{Pr}^{3+}:\text{Y}_2\text{SiO}_5$  with a similar doping concentration than the one of our samples, this broadening is around 25 kHz [[84](#), [130](#)]. In section [4.2.5](#), we measured a value of 17.1 kHz for our crystal.

Techniques have been adapted from nuclear magnetic resonance [[67](#)] in order to cope with this decoherence. Dynamical decoupling techniques are commonly applied in spin-wave storage, and storage times of the order

of 20 ms at the single-photon level have been achieved [93], whereas, with classical pulses, time spans of seconds [131], minutes [69] or even hours [94] have been reached.

### 2.2.2.1 Spin-wave storage efficiency

Spin-wave storage allows backward re-emission, in that control pulses can change the phase matching condition and make it possible for the echo to be emitted in the backward direction, as I mentioned in section 2.2.1. Therefore, in calculating the spin-wave storage efficiency, we consider the backward AFC efficiency 2.7, and we account for two factors that have not been discussed yet: the transfer efficiency of the control pulses  $\eta_T$ , which describes how well control pulses are able to transfer population to the spin level, and the dephasing factor describing the loss of coherence in the spin level  $\eta_C$  [109]. Assembling together all these factors, the spin-wave storage efficiency is given by:

$$\eta_{\text{SW}} = \eta_{\text{sp}}^{\text{back}} \eta_T^2 \eta_C \quad (2.9)$$

### 2.2.3 AFC-DLCZ protocol

Another interesting application of the AFC concerns the DLCZ protocol implemented in solid-state systems [79, 132].

The DLCZ protocol, which is named after the proposers (Duan, Lukin, Cirac and Zoller) [11], has been elaborated in order to generate pairs of entangled photons with a controllable delay between each other from atomic systems with a  $\Lambda$ -level structure. The first steps consists in addressing off-resonantly a transition between a ground state and an excited one with an off-resonant Raman write pulse between  $|g\rangle$  and  $|e\rangle$ . Stokes photons are emitted by Raman scattering on the transition  $|e\rangle$ - $|s\rangle$ . On average, there will be many photons emitted in all directions, but we experimentally focus on a particular angular direction; therefore, on average, only a low number of Stokes photons will be detected. Each Stokes photon is heralding the storage of an excitation in a spin level of the ensemble. If we define the

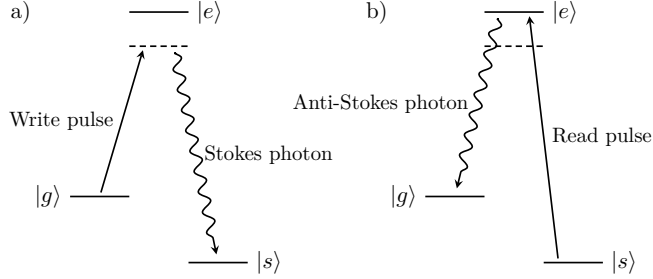


Figure 2.10: The  $\Lambda$ -scheme involved in the DLCZ protocol in atoms. In figure a), a red-detuned write pulse shone on the  $|g\rangle - |e\rangle$  transition stimulates Raman emission of a Stokes photon on the  $|e\rangle - |s\rangle$  transition, which heralds a spin-wave stored in level  $|s\rangle$ .

In figure b), a strong resonant read pulse shone on the  $|s\rangle - |e\rangle$  transition leads to the re-emission of the spin-wave as an Anti-Stokes photon on the  $|e\rangle - |g\rangle$  transition.

spin-wave annihilation operator [133] as:

$$S = \frac{1}{\sqrt{N}} \sum_{j=1}^N e^{-i(\mathbf{k}_W - \mathbf{k}_S) \cdot \mathbf{r}_j} |g_j\rangle \langle s| \quad (2.10)$$

with  $\mathbf{k}_W$  ( $\mathbf{k}_S$ ) wavevector of the write pulse (Stokes photon) and  $r_j$  position of the  $j$ -th atom, then the detection of a Stokes photon on the  $|e\rangle - |s\rangle$  transition ideally projects the state of the ensemble into:

$$|\Psi_{SW}\rangle = S^\dagger |G\rangle = \frac{1}{\sqrt{N}} \sum_{j=1}^N e^{-i(\mathbf{k}_W - \mathbf{k}_S) \cdot \mathbf{r}_j} |g_1 \dots s_j \dots g_N\rangle \quad (2.11)$$

where  $|G\rangle = |g_1 \dots g_N\rangle$  is the initial ground state with all the ions polarized in the ground state. It must be remarked that the initial write pulse intensity should be low: this is to prevent multiple spin-wave excitations in the ensemble. Indeed, the light-matter can be described by the two-mode

squeezed state:

$$|\Phi\rangle = \sqrt{1-p} \sum_{n=1}^{\infty} p^{n/2} \frac{(a^\dagger S^\dagger)^n}{n!} |0\rangle_s |G\rangle \quad (2.12)$$

where  $p$  is the excitation probability,  $a^\dagger$  is the photon creation operator which acts on the vacuum photonic state  $|0\rangle_s$ . It can be seen from this equation that, if the probability  $p$  of creating a spin-wave is increased, then multiple excitations start appearing and the fidelity of the correlations between the Stokes photon and the spin-wave decreases.

At a later time, in order to read out the spin-wave, a strong read pulse resonant with  $|s\rangle$ - $|e\rangle$  permits the emission of an Anti-Stokes photon resonant with the initial transition. The Anti-Stokes detection will be conditioned on the detection of the previous Stokes photon and its direction will be determined by the phase-matching condition: defining  $\mathbf{k}_W, \mathbf{k}_R, \mathbf{k}_S, \mathbf{k}_{AS}$  respectively the wavevectors of the write pulse, the read pulse, the Stokes photon and the Anti-Stokes photon, the phase-matching condition reads  $\mathbf{k}_W + \mathbf{k}_R - \mathbf{k}_S - \mathbf{k}_{AS} = 0$  and implies that this last photon is resonant with  $|g\rangle - |e\rangle$  and counterpropagating with respect to the Stokes photon.

The original DLCZ proposal was concerned with atomic ensembles, but it can be implemented in rare-earth ion doped (REID) materials [132]. The main differences from the atomic implementation lie in the weaker dipole moment of the involved transitions and in the presence of inhomogeneously broadened lines that completely dissipate the coherence of absorption processes. To solve this issue, the optical transition can be addressed resonantly and an AFC can be burned on the broadened transition. Its coherence-preserving properties permit to tackle the inhomogeneous broadening effect. The protocol follows the one described earlier for cold atoms, with some differences. The write pulse is shone resonantly, therefore Stokes photons are emitted by spontaneous emission. A Stokes photon resonant with the  $|e\rangle - |s\rangle$  is selected, detected at a time  $T_S$  after the write pulse, which heralds the presence of a spin-wave on the ground level  $|s\rangle$ . As mentioned before in section 2.2.2, the phase evolution of this spin-wave proceeds

more slowly than in the excited states. At a later time, we can send the strong read pulse, resonant with the same transition as the Stokes photon, to transfer back the spin-wave into an excitation stored in the AFC. What happens now, analogously to what happens with spin-wave storage, is that the excitation resumes the phase evolution inside the AFC, the ion decays back to the original ground level  $|g\rangle$  and an anti-Stokes photon is emitted at a time  $T_{AS}$ , defined as the time interval between the read pulse and the detection of this photon. The times  $T_S$  and  $T_{AS}$  satisfy  $\tau_{AFC} = T_S + T_{AS}$ . The phase matching condition still reads  $\mathbf{k}_W + \mathbf{k}_R - \mathbf{k}_S - \mathbf{k}_{AS} = 0$ , but this time no recoil of atoms is present due to the crystal lattice preventing ions from moving.

A notable difference between the AFC-DLCZ protocol and the original DLCZ protocol lies in its temporal multimodality. Indeed, this feature is inherited from the AFC protocol, which is intrinsically temporally multi-mode, as already stated.

The efficiency of the AFC-DLCZ protocol, as mentioned in section 1.3, is more correctly defined in terms of read-out efficiency, namely the efficiency with which the spin-wave can be converted into an Anti-Stokes photon and detected. In the latest AFC-DLCZ experiment from our group, as we will see in chapter 3, this efficiency was around 1.6% [53], with some figures of merit that could be improved in order to get it higher.

### 2.3 Impedance-matched cavity

The main problem with many REID memories is that their interaction with light is weak. In order to make REID materials absorb light efficiently, high optical depths are necessary, that is, a large number of ions light can interact with. Therefore, to reach high ODs, it is necessary to increase the length of crystals, since the OD is proportional to it, as it was introduced in section 2.2. Even considering this fact, for reasonable crystal length of some millimetres, the OD is still low: for instance, in our praseodymium-doped crystal,  $\alpha=20\text{ cm}^{-1}$ ; hence, for typical crystal lengths of 3 mm–4 mm, we have ODs of 6–8. For these values of ODs, thanks to equation 2.6, we can

define optimal AFC finesses around 3.9–4.7 and so aim at efficiencies of 40%–45%. These values are not even approaching the boundary of 54% for the AFC forward retrieval efficiency mentioned in section 2.2, which is per se a fundamental limitation that cannot be overcome by tuning the OD, thus preventing this bare protocol from being used for highly efficient quantum memories. In the next section, I will introduce a scheme that can bypass these limitations by embedding the crystal in a low-finesse impedance-matched cavity.

### 2.3.1 Theory of the impedance-matched cavity

Increasing the OD of an ensemble of ions is one of the most straightforward methods of increasing the light-matter interaction. Nonetheless, another very effective method is replacing the OD interaction with a cavity interaction. The impedance-matched cavity is a promising approach in this sense to overcome the limitations of the AFC [86].

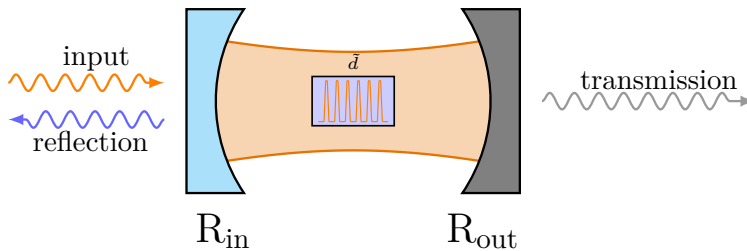


Figure 2.11: A sketch of the impedance-matched cavity. The input, reflection and transmission modes are shown, together with  $R_{\text{in}}$  and  $R_{\text{out}}$ . A comb with average OD  $\tilde{d}$  is prepared inside the crystal embedded in the cavity.

An impedance-matched cavity is a cavity where the absorption from the memory crystal inside the cavity itself is exactly matched to the reflection from the in-coupling mirror. The concept is very similar to the impedance-matching concept in electronics: when the impedance-matched condition



is fulfilled, signal reflection is minimized and the power flux is maximally transmitted. In this case, the cavity in an impedance-matching condition is meant to enhance the absorption of the input pulses by the atomic frequency comb.

Mathematically, the impedance-matching condition can be expressed by establishing a relationship between the reflectivity of the cavity mirrors and the average optical depth of the atomic frequency comb:

$$R_{\text{in}} = R_{\text{out}}e^{-2\tilde{d}} \quad (2.13)$$

with  $R_{\text{in}}$  ( $R_{\text{out}}$ ) reflectivity of the first (second) mirror<sup>5</sup> and  $\tilde{d}$  average optical depth of the AFC. Figure 2.11 shows a sketch of an impedance-matched cavity, where all the quantities of equation 2.13 are reported.

In the next section, I will show the reason why the impedance-matched-cavity-assisted AFC protocol can theoretically attain high storage efficiencies.

### 2.3.2 Efficiency of the impedance-matched cavity protocol

As introduced in section 2.2.1, there is a delicate trade-off between increasing the comb OD to absorb an input pulse more efficiently and decreasing the comb OD to avoid echo re-absorption inside the medium. Since the OD is only needed to force the pulse to interact with matter, one could think of increasing the light-matter interaction in a different way. That is precisely what the impedance-matched cavity is granting: it boosts the interaction with the AFC not by harnessing the OD but by exploiting a cavity effect. It should be noted that not only does the cavity enhance the input absorption, but it does enhance the emission of the echoes as well: indeed, following the treatment in references [86], it can be seen that the whole argument is time-reversible, therefore the emission efficiency is increased as well. This is of paramount importance for emissive memories,

---

<sup>5</sup>I am making the reasonable assumptions that  $R_{\text{in}} < R_{\text{out}}$  and that we are addressing the impedance-matched cavity with an input entering from the mirror with less reflectivity.

like the AFC-DLCZ protocol of section 2.2.3, where the relevant efficiency is the read-out efficiency.

The impedance-matched cavity efficiency can be calculated in the same way as the AFC efficiency [83], but accounting for multiple round-trips inside an optical cavity built around the crystal [86]. It is given by:

$$\eta_{\text{cav}} = \frac{4\tilde{d}^2 e^{-2\tilde{d}} (1 - R_{\text{in}})^2 R_{\text{out}} \eta_{\text{deph}}}{(1 - \sqrt{R_{\text{in}} R_{\text{out}}} e^{-\tilde{d}})^4} \quad (2.14)$$

This formula does not take into consideration the impedance-matching condition 2.13 and it is of general application for a cavity mounted around a crystal. In figure 2.12, a plot of the efficiency as a function of  $R_{\text{in}}$  is shown, for different values of  $\mathcal{F}_{\text{AFC}}$  (which is implicitly contained in  $\eta_{\text{deph}}$ , as treated in section 2.2.1) and  $\tilde{d} = 0.45$ , which is the value that we targeted in our experiment and that will be justified in section 4.1.2.1.

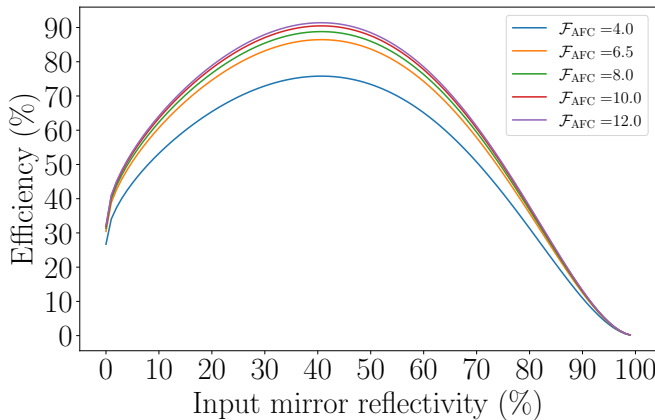


Figure 2.12: Efficiency trends with different  $\mathcal{F}_{\text{AFC}}$  using equation 2.14, assuming square AFC peaks,  $\tilde{d} = 0.45$  and  $R_2 = 1$ . It is apparent that the plots are showing a peak at  $R_{\text{in}} = R_{\text{out}} e^{-2\tilde{d}}$ , which is the impedance-matching condition 2.13.

If we plug the impedance-matching condition 2.13, equation 2.14 reads:

$$\eta_{\text{cav}} = \frac{4\tilde{d}^2 e^{-2\tilde{d}} (1 - R_{\text{out}} e^{-2\tilde{d}})^2 R_{\text{out}} \eta_{\text{deph}}}{(1 - R_{\text{out}} e^{-2\tilde{d}})^4} \quad (2.15)$$

We can make use of this last formula to calculate the ideal lossless efficiency, but, as it will be treated in section 4.1.2.1, it also enables us to calculate the effect of losses. Figure 2.13 displays how the impedance-matched efficiency changes when changing the comb finesse  $\mathcal{F}_{\text{AFC}}$ . The simulation was performed while keeping the value  $\tilde{d}$  fixed and changing  $R_{\text{out}}$  ( $R_2$  in this figure) for each curve; for each point, the impedance-matching condition 2.15 was imposed.

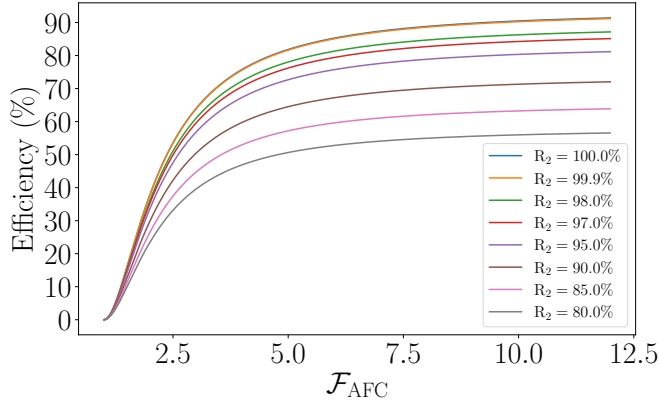


Figure 2.13: Efficiency trends as a function of  $\mathcal{F}_{\text{AFC}}$ , with  $\tilde{d} = 0.45$  and varying the reflectivity of second mirror  $R_2$  while fixing the impedance-matching condition 2.15.

Figure 2.13 and equation 2.15 also elucidate that a value of  $R_{\text{out}}$  lower than 1 leads to a decrease in efficiency. To further highlight this fact, we simulated again a scenario where the outcoupling mirror  $R_{\text{out}}$  value is changed and, once  $\mathcal{F}_{\text{AFC}}$  is fixed (in this case, to  $\mathcal{F}_{\text{AFC}} = 10$ ) and the impedance-matching condition 2.13 is imposed for each point, we search the value of  $\tilde{d}$  yielding the best efficiency. In figure 2.14, this simulation is reported. It is apparent that the efficiency  $\eta_{\text{cav}}$  decreases monotonously

with  $\tilde{d}$  only for the case with perfect reflectivity of the second mirror ( $R_{\text{out}} = 100\%$ ); instead, if  $R_{\text{out}} < 100\%$ , there is an optimal value of  $\tilde{d}$  which yields the maximum efficiency. When we include the intra-cavity losses, the situation changes, as I will show in section 4.1.2.1.

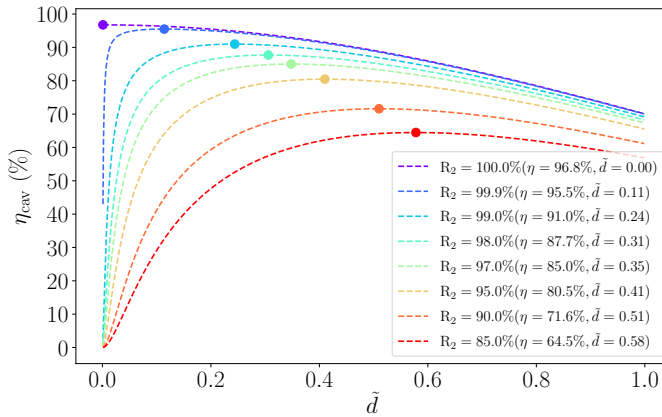


Figure 2.14: Impedance-matched-cavity-assisted efficiency  $\eta_{\text{cav}}$  vs  $\tilde{d}$  changing the value of  $R_2$  (also called  $R_{\text{out}}$ ) and imposing the impedance-match relationship 2.13. This simulation assumes no losses and  $\mathcal{F}_{\text{AFC}} = 10$ .



## Chapter 3

# Time entanglement with the DLCZ protocol

In this chapter, I will be presenting our experiment with an AFC-DLCZ emissive quantum memory protocol. The aim of the experiment is to demonstrate time entanglement between a photon emitted by this memory and a spin excitation stored in it. In a previous experiment by our group [52], they had demonstrated non-classical correlations between this photon and a delocalized spin-excitation inside the same memory. In this experiment, we demonstrate the presence of entanglement between the heralding photon and the spin-wave by mapping the latter into a photon by means of a read pulse, and analyzing their state with an AFC-based unbalanced Mach-Zehnder interferometer.

The theory of this chapter has been introduced in section 2.2.3. I will report on the experimental details and on the results we obtained from this experiment, which was published in Physical Review Letters [53]. Most of the content of this chapter, including most of the reported pictures, will be taken from this publication. The experimental setup was built by the then PhD student Kutlu Kutluer, in collaboration with his supervisor Dr. Margherita Mazzera. They performed a prior DLCZ experiment, published in Physical Review Letters [52]. For this second experiment, Dr. Emanuele

Distante joined the team as an additional supervisor. At some point, I joined the experiment as a PhD student to perform the last measurements, together with my supervisor Dr. Bernardo Casabone.

### 3.1 Introduction

Light-matter entanglement is an important resource in quantum information science. It enables complementing the advantages of using photons as flying qubits in quantum communication schemes with those of matter qubits, which are ideal for quantum storage and processing [12, 134]. It can be achieved, for example, by interfacing quantum sources of entangled photons with long lived quantum memories [49, 55, 95]. But the direct generation of light-matter entanglement, without the use of external photon pair sources, is particularly attractive in view of practical application as it generally features less complexity and can lead to higher efficiency than the so-called read-write memory protocols [135].

A very convenient method to directly generate light-matter entanglement in atomic ensembles is the Duan-Lukin-Cirac-Zoller (DLCZ) protocol [11] that has been widely treated in section 2.2.3. Several types of entanglement have been demonstrated using the DLCZ scheme in atomic gases, such as polarization [136, 137], spatial modes [44, 45, 138], orbital angular momentum [139], and time-bin [140]. The DLCZ scheme has also been demonstrated with nanomechanical resonators [141].

Very few attempts of implementing DLCZ-like schemes in REID crystals have been done, demonstrating continuous variable entanglement [81, 142] and quantum correlation between photons and spin waves [52, 54]. The latter demonstrations combined the DLCZ protocol and the AFC storage scheme [83].

In the experiment I will discuss in this chapter, we used the AFC-DLCZ protocol to create entanglement in time between a single photon and a single collective spin excitation in a REID memory crystal (MC), in the photon counting regime. The matter state is transferred on demand onto a single photon, and the photonic qubits are analyzed in Franson-like

interferometers implemented with another REID crystal. The entanglement is demonstrated by observing high-visibility interference fringes in different bases and by violating a Bell inequality.

## 3.2 Experiment

The cryostat used in that experiment was a closed loop Cryostation from Montana Instruments (see appendix section B.2 for a more detailed description). As far as the laser is concerned, we used the 606 nm laser described in appendix section B.1 and, as mentioned there, we require the light to be modulated very precisely by means of acousto-optic modulators (AOMs). For this experiment, we need three AOM paths: the writing path, to write a spin-wave excitation in the ensemble; the reading path, which permits us to read the spin-wave excitation and to perform the optical pumping of the crystal; and the filter preparation, to optically pump the filter crystal and prepare the AFC interferometer. Additionally, we use a AOM in single-pass for filtering the anti-Stokes photons. The crystals used in this experiment and in the experiment in chapter 4 are described in appendix section B.2.2. We are employing two crystals, a memory crystals (called MC) and a filter crystal (IFC) that we use as an interferometer by burning an AFC interferometer inside it. A sketch of the setup is displayed in figure 3.1(a).

We tailor the  $\pm 1/2g - \pm 3/2e$  transition of the MC as an AFC structure with  $\tau_{MC} = 9 \mu\text{s}$ , while the  $3/2g$  state is emptied to store the single spin excitation. The involved transitions and a sketch of the whole process are pictured in figure 3.1(b). For this experiment, we employed the coherent technique for shaping the comb in the memory and the hole-burning technique for the filter crystal (see section 2.2 for theoretical details about the AFC and appendix section B.3.2 for the experimental implementation).

The write, read and filter preparation pulses applied in the DLCZ protocol are polarized parallel to the  $D_2$  crystal axis (see section 2.1.2.1) to maximize the interaction.



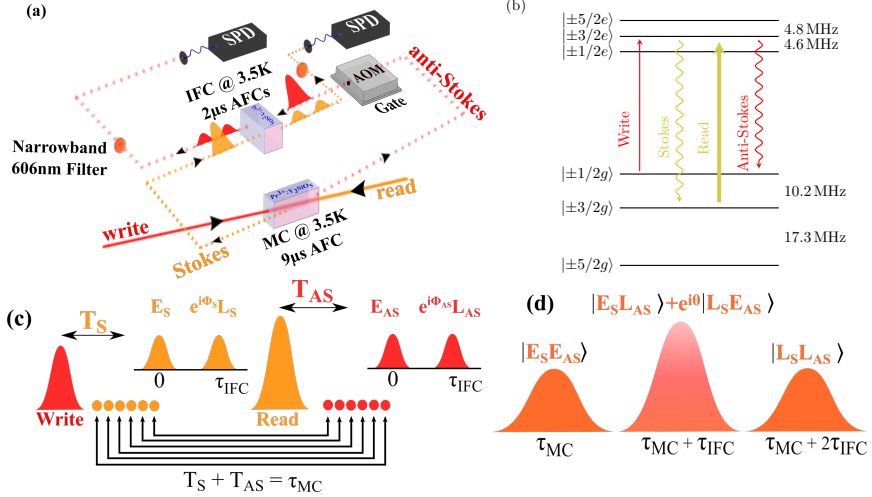


Figure 3.1: (a) Experimental setup. The write and read pulses are polarized parallel to the  $\text{D}_2$  memory crystal (MC) axis to maximize the interaction. Both Stokes and anti-Stokes photons pass through the interferometric filter crystal (IFC), but in different spatial modes, where dedicated laser beams prepare the required spectral features (transparency window or AFC). Spectral filters at 600 nm (width 20 nm) are placed on both arms before the photons are fiber coupled to the single photon detectors (silicon SPD). (b) Hyperfine splitting of the first sub-levels (0) of the ground  $^3\text{H}_4$  and the excited  $^1\text{D}_2$  manifolds of  $\text{Pr}^{3+}$  in  $\text{Y}_2\text{SiO}_5$ . (c) Temporal pulse sequence for the AFC-DLCZ protocol.  $T_S$  ( $T_{AS}$ ) is the time separation between a Stokes (anti-Stokes) photon detection and the write (read) pulse. The insets show the effect of the AFCs in the IFC on the Stokes (orange) and anti-Stokes (red) photons. (d) Sketch of the Stokes-anti-Stokes coincidence histogram vs  $T_S + T_{AS}$  when the IFC is prepared with an AFC in each photon arm, with equal transmission and echo probability. These figures are adapted from reference [53].

### 3.2.1 Experimental procedure

#### 3.2.1.1 Creation of Stokes-Anti-Stokes photon pairs

The experiment starts by preparing an atomic frequency comb on the  $\pm 1/2g - \pm 3/2e$  transition. The AFC is prepared with the read pulse beam with a maximum power of 30 mW. After the comb has been prepared, we wait 145 ms to skip the noisy part of the cryostat cycle.

We then start to send 700 ns FWHM long Gaussian write pulses resonant to the AFC at a rate of 3.7 kHz (1100 pulses per AFC preparation). We detect the Stokes photons in a 4  $\mu$ s window starting 1  $\mu$ s after the write pulse (temporal sequence in figure 3.1(c)). As discussed in reference [52], the number of temporal modes stored is given by the ratio between the Stokes photon detection window (limited by  $\tau_{MC}$ ) and the duration of the Stokes photon itself. The Stokes photon duration is set by the duration of the write pulse, therefore resulting in 5 distinguished temporal Stokes modes ( $5 \cdot 700 \text{ ns} = 3.5 \mu\text{s}$  out of the 4  $\mu$ s window). The Stokes detection mode is set to an angle of about  $3^\circ$  in the backward direction with respect to the write mode, to minimize the leakage noise from the write pulse.

A characterization of the Stokes creation probability,  $P_S$ , as a function of the write pulse power is shown in figure 3.2. The scaling is linear, with the exception of the highest write pulse power investigated where, we believe, the sequence of write pulses might destroy the comb structure. Notably, the linear interpolation of the data points at lower write pulse powers highlights a residual background at  $P_W = 0 \mu\text{W}$ . This corresponds to a  $P_S$  of about 0.5%, which is a remarkable portion of the total Stokes probability, especially at lower write pulse power. We believe that it might be due to stray light reaching the Stokes detector. The fact that a considerable portion of the Stokes detections does not in fact correspond to a spin wave in the crystal largely affects our anti-Stokes read-out efficiency, which has been defined in section 1.3: the read-out efficiency is the probability of actually retrieving an Anti-Stokes photon after shining a strong read pulse, conditioned on the actual presence of a spin-wave in the ensemble.

Directly after the emission, the Stokes photons are steered to the IFC,

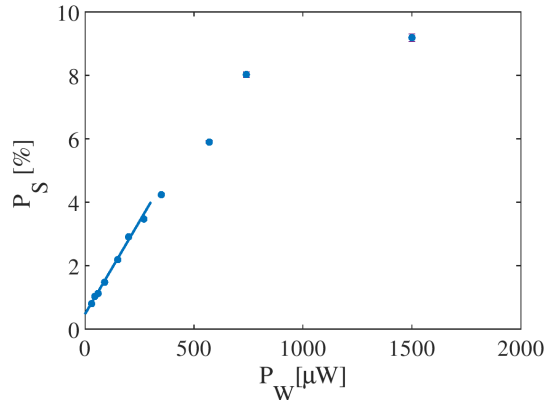


Figure 3.2: Stokes creation probability,  $P_S$ , as a function of the write pulse power,  $P_W$ . A linear fit of the data points at lower  $P_W$  is also shown. The fitting curve intercepts the y axis at  $P_S = 0.5\%$ . This figure is taken from reference [53].

where a 2 MHz-wide transparency window is prepared, to filter the photons emitted through the decay to hyperfine ground levels other than the  $\pm 3/2g$ . Narrow-band filters at 600 nm (width 20 nm) filter the Stokes photons further before they are fiber-coupled to the single photon detectors (silicon SPD, efficiency  $\eta_D = 50\%$ ). The total transmission in the Stokes arm, from the cryostat to the detector, is typically 59%, which includes the passive losses of the optical elements and the residual absorption in the IFC.

Then, conditional on a Stokes photon detection, we send the Gaussian read pulse, counter-propagating to the write mode and delayed by 16  $\mu\text{s}$ . The read pulses have a maximum power of 30 mW. They are 1  $\mu\text{s}$  long and frequency chirped of 800 kHz with a hyperbolic tangent waveform. As a consequence of the phase matching conditions, the Stokes and anti-Stokes photons are emitted in opposite directions. The anti-Stokes detection gate is eventually opened for about 10  $\mu\text{s}$ . The average storage time in the spin state is  $\overline{\tau_S} = 13 \mu\text{s}$ .

The anti-Stokes photons are temporally gated with an AOM before

traveling through the IFC where another transparency window is created in a different spatial mode (about 4 mm apart) to suppress the coherent and incoherent noise deriving from the read pulse [50]. After that, they cross the same spectral filter as the Stokes photons, they are coupled to a SM fiber and sent to a single-photon detector with similar efficiency. The anti-Stokes path from the cryostat to the detector has a typical transmission of 56%. The Stokes and anti-Stokes arrival times are saved to reconstruct coincidence histograms.

### 3.2.1.2 Assessing non-classical correlations between the emitted photons

We first verify that the Stokes and anti-Stokes photons are emitted in pairs, and assess the cross-correlation function:

$$g_{S,AS}^{(2)} = \frac{p_{S,AS}}{p_S \cdot p_{AS}} \quad (3.1)$$

where  $p_{S,AS}$  is the probability to detect a coincidence between a Stokes and an anti-Stokes photon and  $p_S$  ( $p_{AS}$ ) is the probability to detect single Stokes (anti-Stokes) photon. So, after each detection of a Stokes photon, we send 10 unconditional write-read pairs, with 3.8 kHz repetition rate, in order to detect the accidental counts for estimating the second-order cross correlation function between Stokes and anti-Stokes photon. An example of Stokes-anti-Stokes coincidence histogram as a function of the  $T_S + T_{AS}$  time is shown in the plots of figure 3.3, for two different sets of data, taken several months apart. On the left plot, the red bars plot the Stokes-anti-Stokes coincidence counts in the conditional storage trials; for both plots, the solid curve (black on the left, green on the right) is the average of the coincidence counts in the following 10 unconditional trials. The latter represents the accidental counts. We observe a clear peak at  $T_S + T_{AS} = 9 \mu\text{s}$ , which represents the correlated Stokes-anti-Stokes pairs. Besides this main peak, the histogram also includes a broader peak at longer times. This is a leakage of the third AFC echo of the write pulse in the anti-Stokes mode, likely due to scattering in the memory crystal, which cannot be filtered by

the IFC because it is resonant with the transparency window (see figure 2.4). Nevertheless, it is possible to eliminate this peak through a thorough alignment of the setup. As this peak is present in both curves, it is washed out in the calculation of the  $g_{S,AS}^{(2)}$ .

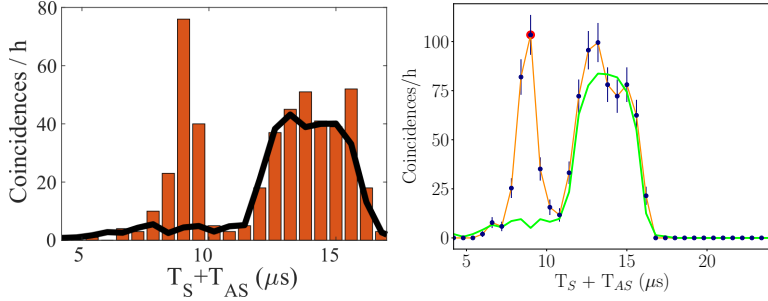


Figure 3.3: **Left:** Time resolved Stokes–anti-Stokes coincidence histogram (red bars) plotted together with the accidental coincidence histogram (solid curve) for  $P_W = 90 \mu W$ , corresponding to  $P_S = 1.6 \%$ . This figure is taken from reference [53].

**Right:** Time resolved Stokes–anti-Stokes coincidence histogram for a set of data taken several months later, with the same parameters as the figure on the left, where histogram bins are not displayed. The orange curve emphasizes the experimental coincidences (blue points), whereas the green curve highlights the accidental counts, similarly to figure 3.3.

The plots in figure 3.4 show the measured  $g_{S,AS}^{(2)}$  histograms fixing the coincidence window time-bin size to  $\Delta t = 600$  ns; in the one on the right, histogram bins are not displayed. Both measurements are taken with a write pulse power of  $P_W = 90 \mu W$ , corresponding to a total Stokes creation probability  $P_S = 1.6 \%$  ( $P_S = 0.4 \%/ \mu s$ ). To calculate the  $g_{S,AS}^{(2)}$ , we take the ratio between coincidences and accidental counts. We again observe the clear correlation peak at  $T_S + T_{AS} = 9 \mu s$  that was visible in figure 3.3. This peak reaches a maximum of  $g_{S,AS}^{(2)} = 17.3 \pm 3.3$  in the left figure, and  $g_{S,AS}^{(2)} = 20.4 \pm 4.9$  in the right one. Both results lie widely above the clas-

sical limit of 2 fixed by the Cauchy-Schwarz inequality, assuming thermal statistics for the Stokes and anti-Stokes fields, as predicted for the DLCZ protocol in the ideal case [72]. The efficiency to retrieve an anti-Stokes photon, conditioned on a Stokes detection, is about 1.6 %.

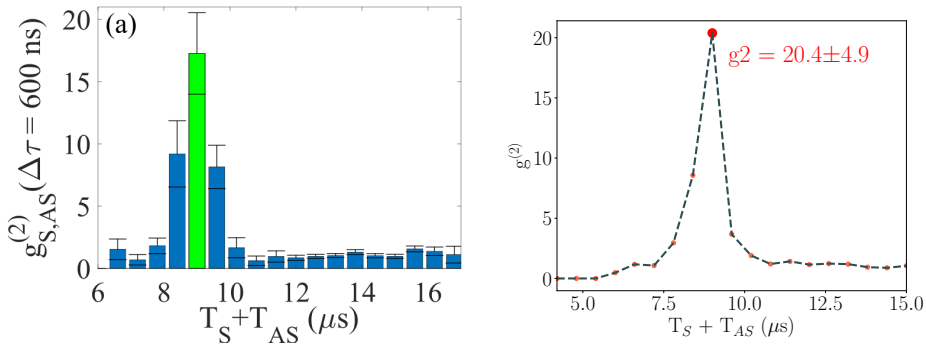


Figure 3.4: **Left:**  $g_{S,AS}^{(2)}$  histogram as a function of the  $T_S + T_{AS}$  time, with a time-bin size of 600 ns. The write pulse power  $P_W$  is  $90 \mu\text{W}$ , corresponding to a Stokes creation probability  $P_S = 0.4 \text{ \%}/\mu\text{s}$ . This  $g_{S,AS}^{(2)}$  histogram corresponds to the coincidence histogram shown on the left in figure 3.3. The  $g_{S,AS}^{(2)}$  calculated in the green bin is  $17.3 \pm 3.3$ .

**Right:**  $g_{S,AS}^{(2)}$  histogram, with the same parameters as the one on the left (including the time-bin size of 600 ns), corresponding to the coincidence histogram shown on the right in figure 3.3. In this plot, histogram bins are not displayed. As anticipated in figure 3.3, the  $g_{S,AS}^{(2)}$  at the big red dot position ( $9 \mu\text{s}$ ) is  $g_{S,AS}^{(2)} = 20.4 \pm 4.9$ .

To further characterize our system, we measured the coincidence count rate and  $g_{S,AS}^{(2)}(\Delta t = 600 \text{ ns})$  as a function of the Stokes probability  $P_S$ , as it is shown in figure 3.5. As expected, the coincidence rate increases with the Stokes probability. Nonetheless, this increases the probability of multiple spin-excitations and creates a noise component proportional to  $P_S$ , therefore reducing the  $g_{S,AS}^{(2)}$ . At the lowest  $P_S$  values, the cross-correlation

decreases because the Stokes photon rate becomes comparable to the noise. The correlation between Stokes and anti-Stokes photons remains largely above the classical limit until  $P_S = 2\%/ \mu\text{s}$ , corresponding to  $P_W$  of almost 1 mW. However, in the presented experiments, we maintain  $P_W = 90\ \mu\text{W}$  to guarantee a good balance between coincidence rate and cross-correlation value.

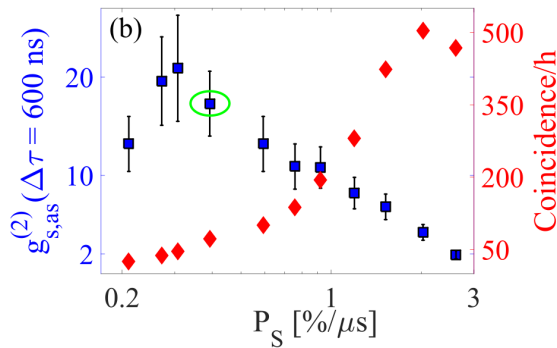


Figure 3.5:  $g_{S,AS}^{(2)}$  (blue squares) and coincidence rate (red diamonds) vs Stokes creation probability. Both quantities refer to a time-bin size of 600 ns. The errorbars are calculated assuming Poissonian statistics. The point circled in green correspond to the data presented on the left plot of figure 3.4 ( $P_W = 90\ \mu\text{W}$ ). This figure is taken from reference [53].

### 3.2.1.3 Time entanglement between a photon and a spin wave

To demonstrate time entanglement, measurements in complementary time bases are required. This can be achieved by sending the photons in unbalanced interferometers serving as time-bin analyzers, as suggested by Franson [143]. In our case, we use the IFC as a time-bin analyzer by preparing an AFC with storage time of  $\tau_{\text{IFC}} = 2\ \mu\text{s}$  in both spatial modes. The AFC structure acts on the single photons as a beam splitter with a delay line in one output, i.e. a part of an unbalanced Mach-Zehnder interferome-

ter [18, 49, 144]. This provides a convenient and robust time-bin analyzer [144], without the need of phase stabilizing interferometers with 200 m path length difference. In the IFC, each Stokes and anti-Stokes photon can be either transmitted (early time bin E) or stored in the AFC and retrieved as an AFC echo after a time  $\tau_{\text{IFC}}$  (late time bin L). The phase  $\Phi_{\text{S}}$  ( $\Phi_{\text{AS}}$ ) between the early and late time-bin can be tuned by changing the center frequency of the AFC with respect to the Stokes (anti-Stokes) photons [83]. A phase shift of  $2\pi$  is achieved with a frequency detuning of  $\Delta$ .

The coincidence histogram between Stokes and anti-Stokes photon detections after the time-bin analyzers, as a function of the  $T_{\text{S}} + T_{\text{AS}}$  time, will thus be composed of three peaks. One corresponds to the coincidences between transmitted Stokes and anti-Stokes (labeled  $|E_{\text{S}}E_{\text{AS}}\rangle$  in figure 3.1(d)) and it thus lays at  $T_{\text{S}} + T_{\text{AS}} = \tau_{\text{MC}}$ . One builds up with the coincidences between Stokes and anti-Stokes photons when both undergo AFC storage in the IFC,  $|L_{\text{S}}L_{\text{AS}}\rangle$ . Consequently, it will appear at  $T_{\text{S}} + T_{\text{AS}} = \tau_{\text{MC}} + 2\tau_{\text{IFC}}$ . The central peak featured in figure 3.1(d) at  $T_{\text{S}} + T_{\text{AS}} = \tau_{\text{MC}} + \tau_{\text{IFC}}$  is the sum of two contributions: the coincidences between transmitted Stokes photons and stored anti-Stokes photons ( $|E_{\text{S}}L_{\text{AS}}\rangle$ ) and those between stored Stokes photons and transmitted anti-Stokes photons ( $|L_{\text{S}}E_{\text{AS}}\rangle$ ). If these two processes are indistinguishable and coherent (which requires e.g. equal AFC echo efficiency in the IFC for both photons), they will be able to interfere. By selecting only the central peak, the correlation between Stokes and anti-Stokes photons can be interpreted as coming from the postselected entangled state  $\frac{1}{\sqrt{2}}(|E_{\text{S}}L_{\text{AS}}\rangle + e^{i\theta}|L_{\text{S}}E_{\text{AS}}\rangle)$ , where  $\theta = \Phi_{\text{S}} - \Phi_{\text{AS}}$  [49]. This photonic state results from the postselected light-matter entangled state  $\frac{1}{\sqrt{2}}(a_{\text{S}}^{\dagger}(T)a_{\text{SW}}^{\dagger}(T) + a_{\text{S}}^{\dagger}(T')a_{\text{SW}}^{\dagger}(T'))|0_{\text{S}}0_{\text{SW}}\rangle$ , where T and T' are separated in time by  $\tau_{\text{IFC}}$ , set by the analyzing interferometer. In our experiments, we tailor the finesse of the AFC structures in the IFC such that the amplitudes of the transmitted and stored pulses are comparable (approximately 30% of the input pulses). All the states that can result as an output from the IFC are illustrated in figure 3.1(d).

The left plot of figure 3.6 shows an example of  $g_{\text{S,AS}}^{(2)}$  between Stokes and anti-Stokes photons when both pass through an AFC in the IFC. In the



figure, the constructive and destructive interference cases are highlighted respectively with dark bars and with light bars. Constructive and destructive interference are obtained by fixing the Stokes phase shift  $\Phi_S = 0^\circ$ , and the anti-Stokes phase shift  $\Phi_{AS}$  to  $0^\circ$  and  $180^\circ$ , respectively. As expected, the two histograms differ in the area around  $T_S + T_{AS} = 11 \mu\text{s}$ . The value of  $g_{S,AS}^{(2)}$  for the constructive interference case of the left plot of figure 3.6 is  $7.6 \pm 0.5$ , which is lower than the value measured before the time-bin analyzers. This is due to the fact that there is an intrinsic loss in the IFC ( $\eta_{IFC} = 30\%$ ), and that the noise from different temporal modes is summed up.

In the right plot of figure 3.6, the results of the interference measurements in different bases are shown, obtained by tuning the anti-Stokes phase shift for two different values of  $\Phi_S$ . The visibility is  $(75.9 \pm 4.6)\%$  for  $\Phi_S = 0^\circ$  and  $(70.1 \pm 4.4)\%$  for  $\Phi_S = 90^\circ$  showing evidence of entanglement.

To further assess quantum entanglement, we perform an experiment probing the violation of the Clauser, Horne, Shimony, and Holt (CHSH) inequality [145]. We measure thus the coincidence histograms in 16 different settings to calculate the S parameter as a function of  $T_S + T_{AS}$  as:

$$S = E(\alpha, \beta) + E(\alpha', \beta) + E(\alpha, \beta') - E(\alpha', \beta'), \quad (3.2)$$

where  $\alpha$  and  $\alpha'$  ( $\beta$  and  $\beta'$ ) are two different phase choices for the Stokes (anti-Stokes) photons arm, and the dependency on  $T_S + T_{AS}$  has been dropped for simplicity. The different terms of equation 3.2 are built from the coincidences  $C$  in a time bin  $\Delta t = 600 \text{ ns}$  as follows:

$$E(\alpha, \beta) = \frac{C(\alpha, \beta) + C(\alpha + \pi, \beta + \pi) - C(\alpha, \beta + \pi) - C(\alpha + \pi, \beta)}{C(\alpha, \beta) + C(\alpha + \pi, \beta + \pi) + C(\alpha, \beta + \pi) + C(\alpha + \pi, \beta)}$$

Figure 3.7 shows the resulting S parameters as function of  $T_S + T_{AS}$  when the phase values are fixed to  $\alpha = 0^\circ$ ,  $\alpha' = 90^\circ$ ,  $\beta = 45^\circ$ , and  $\beta' = 135^\circ$ .

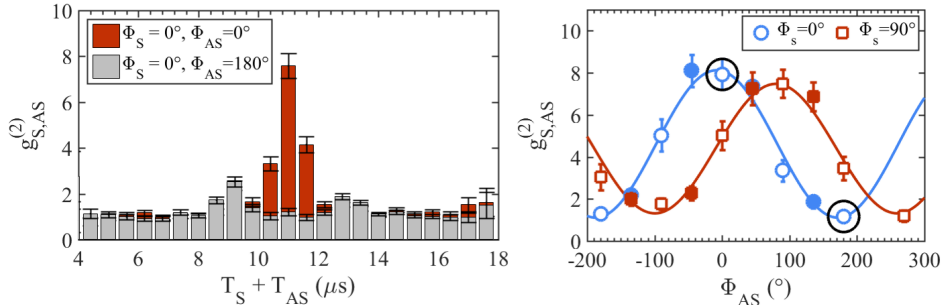


Figure 3.6: **Left:** Examples of  $g_{S,AS}^{(2)}$  between Stokes and anti-Stokes photons when an AFC with  $\tau_{\text{IFC}} = 2 \mu\text{s}$  is prepared in both the Stokes and the anti-Stokes mode in the IFC. The cases of constructive (darker bars) and destructive (lighter bars) interference are shown. For both measurements, the integration time is 10 h, approximately.

**Right:** Interference fringes measured by tuning the frequency of the anti-Stokes filter AFC (i.e. by tuning  $\Phi_{AS}$ ) in two different bases, selected by changing the frequency of the filter AFC for the Stokes photon. The circled points are the ones related to the figure on the left. The filled points are those used to calculate the S parameter (integration time 6.5 h per point). The remaining data points are the result of 5.5 h of integration each. These figures are taken from reference [53].

Once we fix these phases, the  $E(\alpha; \beta)$  terms become:

$$\begin{aligned}
 E(0^\circ, 45^\circ) &= 0.50 \pm 0.03 \\
 E(90^\circ, 45^\circ) &= 0.56 \pm 0.03 \\
 E(0^\circ, 135^\circ) &= -0.59 \pm 0.03 \\
 E(90^\circ, 135^\circ) &= 0.50 \pm 0.04.
 \end{aligned}$$

As expected, the maximum violation is obtained for  $T_S + T_{AS} = \tau_{\text{MC}} + \tau_{\text{IFC}} = 11 \mu\text{s}$ , where we measure  $S = 2.15 \pm 0.07$ , which surpasses the classical bound of 2 by more than 2 standard deviations. If compared to the maximum value of  $2\sqrt{2}$ , we estimate a visibility of  $V_{\text{CHSH}} = 76.5 \pm 2.5$ , com-

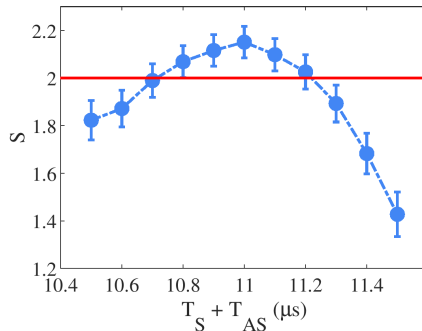


Figure 3.7: Bell inequality  $S$  parameter measured as a function of  $T_S + T_{AS}$ . The red line denotes the threshold  $S = 2$  for violating the CHSH inequality. This figure is taken from reference [53].

patible, within error bars, with the average value of the visibilities measured from the interference fringes of figure 3.6.

We also investigated the  $S$  parameter as a function of the coincidence window  $\Delta t$ , showing that higher violations can be obtained for smaller  $\Delta t$ , at the expense of lower coincidence count rate and read-out efficiency. By doing that, we found out that there is a finite range of positions where the CHSH inequality is clearly violated. To reach this conclusion, we proceeded by fixing the window position at the maximum and analyzing the  $S$  parameter as a function of the time-bin size, as depicted in figure 3.8. As seen in the figure, the  $S$  parameter increases for smaller time-bin sizes at the expense of lower coincidence count rate and read-out efficiency. The inset shows the corresponding violation of the CHSH inequality in terms of standard deviations.

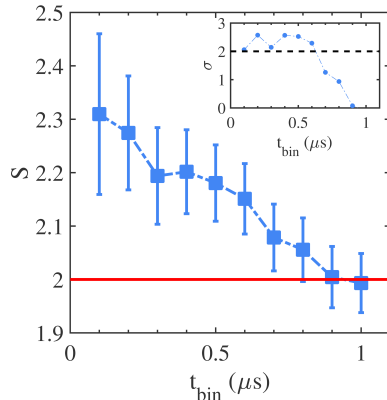


Figure 3.8:  $S$  parameter as a function of the time-bin size. The coincidence window is fixed at  $\tau_{\text{MC}} + \tau_{\text{FC}}$ . Inset: violation of the CHSH in terms of standard deviations vs time-bin size. This figure is taken from reference [53].

### 3.3 Discussion and outlook

#### 3.3.1 Summary of the work

These measurements have clearly shown that the Stokes and anti-Stokes photons are entangled in time. Consequently, as the conversion spin wave to anti-Stokes photon is a local operation, this also demonstrates entanglement between a photon and the spin-wave stored in the crystal. Therefore, we have shown that a solid-state device can emit pairs of entangled photons with an embedded quantum memory for one of the photons. Moreover, the quality of the entanglement is high enough: we achieved a  $g_{\text{S,AS}}^{(2)} = 17.3 \pm 3.3$ , and we violated a Bell inequality with  $S = 2.15 \pm 0.07$ , demonstrating that our device is suitable for applications in quantum communication.

The anti-Stokes retrieval efficiency (conditioned on a Stokes detection) obtained in this experiment was quite low,  $\eta_{\text{R}} = 1.6\%$ , with  $P_{\text{W}} = 90 \mu\text{W}$ , corresponding to a Stokes creation probability of  $P_{\text{S}} = 1.6\%$ . We note that these values are comparable to those reported in our previous realization of the AFC-DLCZ protocol [52]. However, in the present work the average

storage time in the spin state  $\overline{\tau_S}$  is more than twice as long and the coincidence count rate has been increased by a factor 8. Further changes with respect to [52] include the number of trials per comb—increased from 500 to 1100—the wider detection window—enlarged from  $2\ \mu\text{s}$  to  $4\ \mu\text{s}$ —and the better transmission from the memory crystal to the filter crystal, increased from 24 % to 56 % by optimizing the filtering scheme (at the expense of one of the two AOMs used for gating).

### 3.3.2 Limitations and perspectives

This device could be an important resource for the implementation of temporally multiplexed quantum repeaters. Indeed, with the current storage time in our memory—currently limited by the spin-inhomogeneous broadening—we could be able to demonstrate light-matter entanglement over distances of a few kilometers. For the transmission of the photon in optical fibers, quantum frequency conversion to telecom wavelengths would be required, as was recently shown in reference [146] for this wavelength. In chapter 5, an experiment dealing with quantum frequency conversion of long photons coming from AFC-DLCZ will be reported. Hence, with this separate experiment, in principle we have already achieved the capability of interfacing an AFC-DLCZ memory working in the visible regime with telecom wavelengths.

Longer storage times can be readily achieved by implementing spin-echo sequences to overcome the inhomogeneous broadening effect (leading to  $T_2 = 500\ \mu\text{s}$  for our crystal, at zero magnetic field, as reported in section 2.2.2). Ultimately, the application of a suitable magnetic field and of dynamical decoupling techniques [54] may prolong the storage time up to tens of seconds in our crystal [69] and up to a few hours in Europium doped samples [94, 147].

The current coincidence count-rate limitations are mainly due to the low retrieval efficiency and low signal-to-noise ratio and to the repetition rate of the experiment. A higher signal-to-noise ratio would allow increasing  $P_S$ , and thus the coincidence rate, while keeping the same value for the  $g_{S,AS}^{(2)}$ . This can be achieved by increasing the read-out efficiency, which can be

accomplished mainly by improving the read pulse transfer efficiency. Additionally, as stated in reference [52], the read-out efficiency could be further increased by improving the AFC preparation (to the aim of enhancing the rephasing efficiency of the AFC), by a better control of the spin decoherence (section 2.2.2) as well as by using a longer crystal with higher optical depth and/or by embedding the crystal in a low finesse cavity [86]. As far as the latter solution is concerned, in chapter 4 I will show a cavity-assisted AFC experiment where the cavity boosts the absorption and re-emission of external states of light in our absorptive quantum memory. This experiment can also be performed with an AFC-DLCZ memory in order to enhance its read-out efficiency, and we have plans to implement this experiment with our setup in the near future.

Another way of getting higher SNR and higher repetition rate at the same time is by suppressing the background noise, coming mostly from uncorrelated detections in the Stokes mode. Background noise suppression would also allow us to widen the coincidence window, leading to a higher coincidence rate, as show in figure 3.9. Nevertheless, the repetition rate  $R$  for experiments aiming at entangling remote crystals in a heralded fashion is limited by the communication time between the two memories,  $R=L/c$  (e.g. 4 kHz for  $L = 50$  km). The coincidence count rate could however be enhanced by increasing the number of modes. The number of temporal modes can be increased by using longer storage time in the excited state in the memory crystal (several tens of  $\mu$ s are possible in our crystal). Additional multiplexing can be achieved by implementing frequency and spatial mode multiplexing, e.g. using an integrated approach [109].

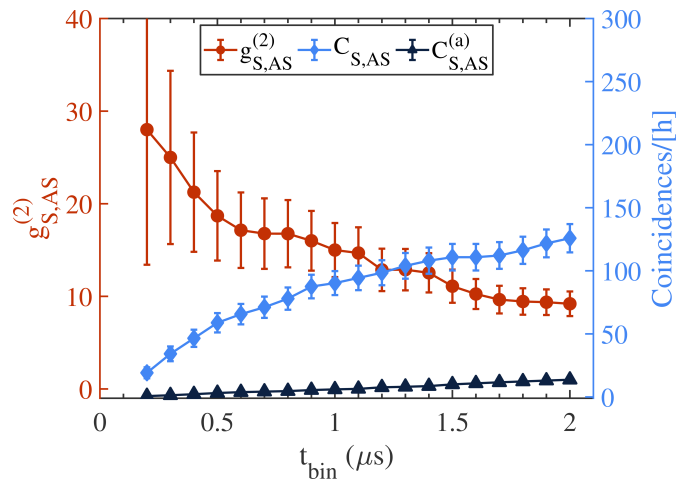


Figure 3.9: The cross-correlation function  $g_{S,AS}^{(2)}$  (red dots), the coincidences per hour  $C_{S,AS}$  (blue diamonds) and the accidental coincidences per hour  $C_{S,AS}^{(a)}$  (black triangles) as a function of the coincidence detection window width  $t_{bin}$ . This figure is taken from reference [53].

## Chapter 4

# Impedance-matched-cavity-assisted AFC

In this chapter, I will report on an AFC storage experiment enhanced by an impedance-matched cavity. The AFC technique has been introduced in section 2.2, while I treated the impedance-matched cavity technique in section 2.3. This experiment consists in embedding the memory crystal that we are using as a quantum memory in a Fabry-Pérot cavity. This optical cavity is made in such a way that the round-trip losses experienced by light inside it are matched to the reflectivities of the two mirrors according to equation 2.13. Satisfying this condition implies that the AFC efficiency can be greatly enhanced with respect to its 54% forward emission limit [83, 86]. By employing this setup, we demonstrated up to 62% storage efficiency for weak coherent pulses in our quantum memory, the highest efficiency recorded with the AFC technique so far. Moreover, we were able to store time-bin qubits with 52% efficiency, which also marks a record for efficiency of qubit storage in a solid-state quantum memory. These qubits were additionally analyzed by an unbalanced Mach-Zehnder interferometer made with the AFC technique in an auxiliary filter crystal sitting inside the same vacuum chamber of our cryostat. By scanning the interferometer and changing the phase between the qubit components, we were able to perform



a measurement in three different bases, confirming the high fidelity (94.8 %, near unity if we correct for the interferometer fidelity) of our quantum storage. Furthermore, we investigated the bandwidth of our cavity and the spectral limitations introduced in our  $\text{Pr}^{3+}:\text{Y}_2\text{SiO}_5$  crystal by slow-light effects [148, 149] in section 4.2.4. We assessed that we can store pulses up to 3.7 MHz bandwidth with efficiencies higher than 30 %. As far as storage time is concerned, we accomplished the storage of single weak coherent pulses up to 50  $\mu\text{s}$ , proving that we can also enhance the efficiency for long storage times. Finally, we are currently performing a spin-wave storage experiment where we are storing bright and weak coherent pulses in the spin levels of our memory crystal, following the procedure described in section 2.2.2. Up to this point, we have achieved an efficiency of 33 % for storage of classical pulses; with weak coherent states, we have obtained an efficiency of 21.7 % for storage of pulses with a mean photon number of 1.14.

A scientific paper describing the results is in preparation. I performed the simulations to assess the feasibility of this experiment and to establish the features of the setup. Later, I assembled the setup and took the measurements shown throughout this chapter. I was assisted by two postdocs, Dr. Bernardo Casabone and Dr. Alessandro Seri. Later, they left and Dr. Sören Wengerowsky joined as new postdoc. A new PhD student, Leo Feldmann, is currently performing the final measurements.

## 4.1 Introduction

As mentioned in section 1.2, highly efficient quantum memories are required in order to distribute entanglement effectively in a quantum network. Given that, in order to perform the Bell state measurements needed to extend entanglement between quantum nodes, we need to interfere photons between each other, higher memory efficiencies correspond to higher likelihood of success. In reference [12], it is reported that, if the efficiency of the quantum memories in a 600 km quantum repeater chain diminishes from 90 % to 89 %, then the time required to share entanglement between the two

ends enlarges up to 10%–14%, depending on the specific protocol used. Therefore, boosting quantum memory efficiencies is crucial for realistic applications. The high efficiency scenario could not be approached with the AFC protocol alone, because of the well-known 54% limit I discussed several times throughout this thesis. Nevertheless, the impedance-matched cavity protocol introduced in section 2.3 serves this purpose, and permits to envision a quantum network where AFC-based quantum memories play a meaningful role.

#### 4.1.1 State of the art

As stated in section 1.3.1, in the last decade there have been the first experimental implementations of the original impedance-matched cavity proposal [86]. The first one was performed in Lund, where they managed to store classical pulses in  $\text{Pr}^{3+}:\text{Y}_2\text{SiO}_5$  with a remarkable 56% storage efficiency [87]. They were the first to observe the enhancement of slow-light effect by the cavity [148, 149]—following the creation of the transparency window, which is usually the first step in the creation of the AFC (appendix section B.3.2).

The second demonstration, from Geneva, included spin-wave storage, and employed a  $^{151}\text{Eu}^{3+}:\text{Y}_2\text{SiO}_5$  crystal [88]. This experiment achieved 53% efficiency for the two-level AFC protocol and 12% for the full spin-wave storage one, both with bright pulses.

The third and last one was accomplished in Delft and was the first one at the single photon level [89]. In this experiment, single photons were stored in  $^{153}\text{Tm}^{3+}:\text{Y}_3\text{Al}_5\text{O}_{12}$  for 25 ns. The estimated internal memory efficiency was 27.5% and was measured at the classical level; the reported storage efficiency for weak coherent states was 7%.

In the next section, we will see the main issues that affected these three experiments.

### 4.1.2 Challenges

The materials used in these three demonstrations changed from case to case, so the problems they faced were different.

Two out of three experiments [87, 89] employed coated crystals as cavities. On the one hand, this diminishes the sources of losses they can have, since, between the crystal facets, there are no additional interfaces that can lead to background absorption. On the other hand, however, it becomes extremely challenging to perform procedures which normally would be easier in single-pass, e.g. reading the spectral structures or characterizing the round-trip losses. Furthermore, extending the two-level AFC to spin-wave storage becomes challenging, because inserting control pulses at a small angle with respect to the input beam while keeping them outside of the cavity is not possible anymore.

Another issue, which will be presented in detail in section 4.2.4, is slow-light effect. This was reported in reference [87] and treated in detail in references [148, 149]. It mostly affects only materials whose OD is high enough, and it reduces enormously the bandwidth of the cavity. As we will see, this was a very detrimental effect for our experiment.

Finally, the last hurdle is common to all the presented experiments, including ours, and it is mode-matching. Mode-matching consists in placing the correct lens, in the correct position and with the correct cavity alignment, such that the beam is adapted to the cavity mode. In general, the degrees of freedom that mode-matching involves are so many that it is experimentally challenging to achieve a perfect match. In our case, the low finesse of the cavity constituted an additional obstacle to that, due to the spectrally broad cavity modes, making it harder to distinguish a proper single mode from a mixture of modes.

For a detailed discussion about the challenges of our experiment, I refer to section 4.3.

#### 4.1.2.1 Simulation of the impedance-matched efficiency including losses

A preliminary part of the work has consisted in simulating the behaviour of our impedance-matched cavity for different  $\tilde{d}$  and intra-cavity losses  $\epsilon$ . As mentioned in reference [88], one of the most important figures to assess the efficiency is the ratio  $\tilde{d}/\epsilon$ . Therefore, we should always stay in a regime where  $\epsilon \ll \tilde{d}$ .

Equation 2.15 does not explicitly contain intra-cavity losses  $\epsilon$  but, following the same treatment as in references [88], we can include them in equation 2.15 by tuning the cavity away from the ideal impedance-matching condition. The first thing to note is that, in equation 2.15, we must plug the impedance-matching condition 2.13 to obtain equation 2.14, which accounts for the fact that the two cavity mirrors have reflectivities matched to the comb absorption. This is the only good “loss” that must be matched with the cavity or, in other words, the only absorption that contributes to the impedance-matching. At this point, we can account for losses by replacing  $R_{\text{out}}$  by the term  $R_{\text{out}-\epsilon}$  in equation 2.14 and obtaining:

$$\eta_{\text{cav}}^{\text{lossy}} = \frac{4\tilde{d}^2 e^{-2\tilde{d}} (1 - (R_{\text{out}} - \epsilon)e^{-2\tilde{d}})^2 (R_{\text{out}} - \epsilon)}{(1 - (R_{\text{out}} - \epsilon)e^{-2\tilde{d}})^4} \eta_{\text{deph}} \quad (4.1)$$

Thanks to this formula, it is possible to simulate different efficiency cases by varying the losses. In our experimental case, our  $R_{\text{out}}$  is 97% and  $\eta_{\text{deph}}$  changes depending on the finesse  $\mathcal{F}_{\text{AFC}}$  of each particular comb, but we can assume a value of  $\mathcal{F}_{\text{AFC}}$  around 6.5 (achieved in the experiment), which yields  $\eta_{\text{deph}} = 92.5\%$  for a square comb. Once we fix these parameters in equation 4.1, we can change  $\tilde{d}$  to observe the change in efficiency. In figure 4.1, we performed a simulation similar to the one shown in figure 2.14, but here we considered the case with  $\mathcal{F}_{\text{AFC}} = 6.5$  and double-pass losses around 3%, which were realistic in our situation. I have already showed in section 2.3.2 that decreasing the value of reflectivity of the out-coupling mirror leads to a decrease in the achievable theoretical efficiency, proving that any transmission through the second mirror is an additional efficiency loss. Therefore, in figure 4.1, I distinguished different scenarios

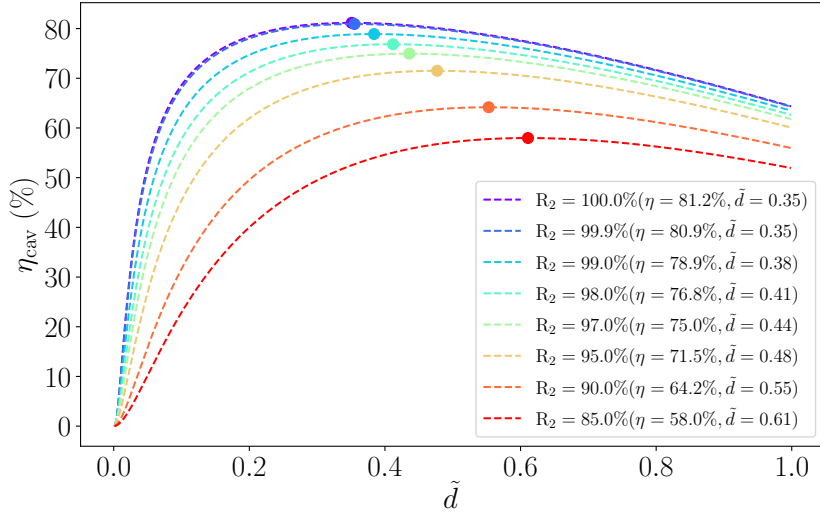


Figure 4.1: Impedance-matched-cavity-assisted efficiency  $\eta_{\text{cav}}$  vs  $\tilde{d}$  changing the value of  $R_2$  (also called  $R_{\text{out}}$ ) and imposing the impedance-match relationship 4.1 that accounts for losses. This simulation assumes 3% intra-cavity double-pass losses and  $\mathcal{F}_{\text{AFC}} = 6.5$ . Compared to the case shown in figure 2.14, the efficiency with  $R_{\text{out}}=97\%$  decreases by 10%.

for different values of reflectivity of the out-coupling mirror, to include these transmission losses as well. Comparing this last figure to figure 2.14 (with no intra-cavity losses and  $\mathcal{F}_{\text{AFC}} = 10$ ), we can see that, by installing a 97% reflecting mirror rather than a 99.9% one (which is available to us), we lose more than 10% in efficiency. Nevertheless, we have opted for the 97% because it facilitated the lock of the cavity in transmission. In addition, we see that the best efficiency in this case is yielded by  $\tilde{d} = 0.44$ , which is the reason why we have chosen  $\tilde{d} = 0.45$  for our experiment.

To investigate further the effect of losses, in figure 4.2, we also simulated the cavity efficiency calculated through equation 4.1 as a function of losses and for different values of  $\tilde{d}$ . Here we fixed the reflectivity of the second mirror  $R_{\text{out}}$  to 97%, and we scanned the intra-cavity losses, imposing the

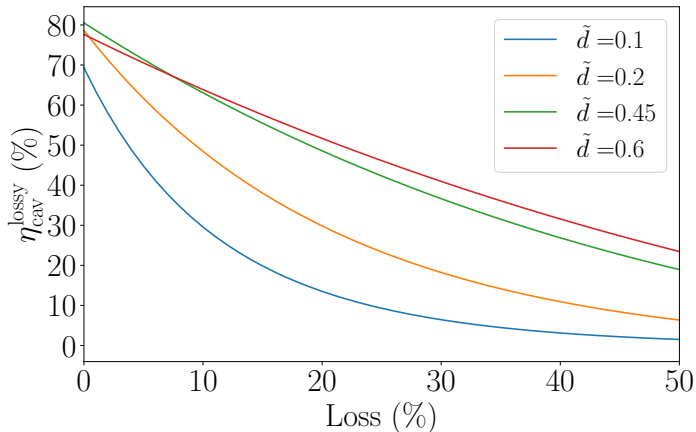


Figure 4.2: Impedance-matched-cavity-assisted efficiency  $\eta_{\text{cav}}^{\text{lossy}}$  vs round-trip losses  $\epsilon$  as predicted from equation 4.1 with  $R_{\text{out}} = 0.97$ ,  $\mathcal{F}_{\text{AFC}} = 6.5$ . Our case is the green one with  $\tilde{d} = 0.45$ .

impedance-matched condition 4.1 for each curve.

Up to this point, I have treated these losses as theoretical losses, not explaining where they stem from. We distinguish between two kind of losses. As mentioned *en passant*, the formula 2.5 defining the efficiency of the AFC protocol in single-pass explicitly contains losses via the term  $e^{-d_0}$ . These losses are background absorption losses from the AFC, as explained in section 2.2.1. Moreover, as it will be shown in the next sections, our cavity is assembled around the vacuum chamber of our cryostat, so—in addition to background absorption losses—it is affected by losses through the vacuum chamber windows and crystal facets as well. This problem is obviously not there in experiments where the cavity is formed by coating the facets of the crystal [87, 88].

## 4.2 Experiment

The setup we have used for our impedance-matched cavity experiment is shown in figure 4.3. All the details about the laser diodes, the beams, the crystals, the cryostatation and the cavity are reported in appendices B and C.

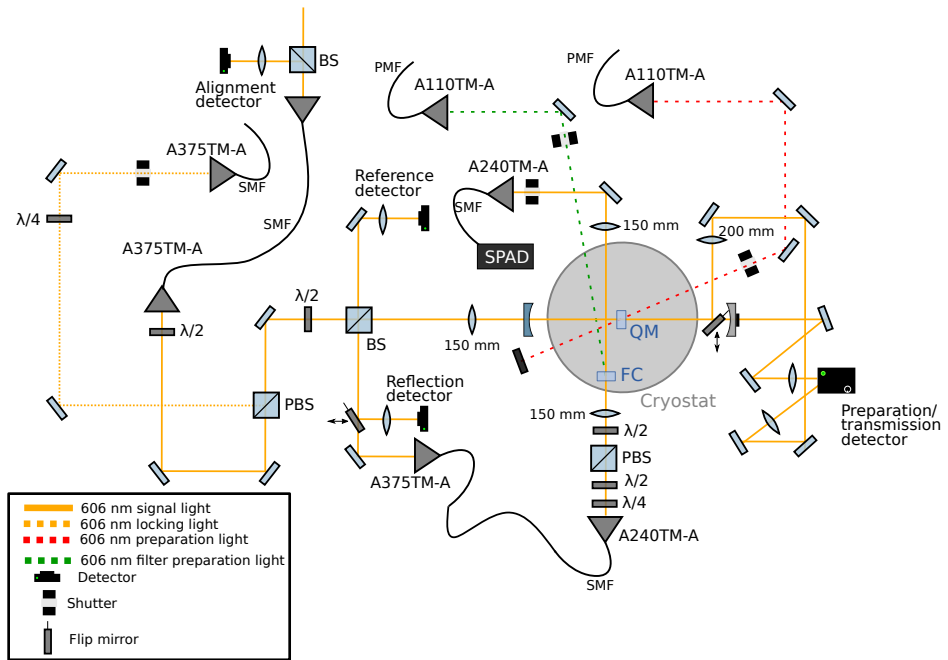


Figure 4.3: Sketch of the setup of our experiment. The control pulse beam is not shown for the sake of simplicity.

In figure 4.3, our full setup is shown. We can sketch the main elements out:

- Four different laser beams, with four different modulations, which are used to address the two crystals (appendix section C.1.2);
- Two crystals, a memory crystal (QM) and a filter crystal (FC), both

sitting inside the cryostat (grey circle in figure 4.3); see appendix section C.1.1 for additional details;

- The impedance-matched cavity mounted around the cryostat (blue mirror and grey mirror). The cavity consists in two curved mirrors mounted on pillars clamped on the optical table. The cavity length is 21 cm, yielding an approximate FSR of 720 MHz. The reflectivity of the second mirror is 97 %, whereas the reflectivity of the first mirror is 40 %, ensuring impedance-matching with a comb with  $\tilde{d} = 0.45$ . The finesse of the cavity is 6.5, hence its linewidth is around 111 MHz. The second mirror has been chosen to be 97 % reflectivity in order to transmit some of the light. Therefore, the cavity is stabilized by maximizing the transmission of the locking light by means of a piezo mounted on the back of this mirror. The piezo is controlled by an Arduino microcontroller, which detects the transmitted signal and drives the piezo to shift the second mirror and ensure maximum transmission. More details about the cavity and its stabilization can be found in appendix section C.1.3.

The experiment was divided in more phases:

1. As a first step, we demonstrated enhancement of the AFC efficiency for the storage of single pulses at the single-photon level (section 4.2.1);
2. Later on, we proved that our cavity-enhanced quantum memory can store time-bin qubits faithfully, and we achieved that by storing weak coherent double-Gaussian pulses in the memory and analyzing them via an AFC-based unbalanced Mach-Zehnder interferometer prepared in an auxiliary filter crystal (section 4.2.2);
3. In a third phase, we changed the storage time of our atomic frequency comb and demonstrated that the efficiency enhancement due to the cavity also worked at different storage times; from this result, we inferred our effective  $T_2$  (section 4.2.3);
4. Then, we investigated the slow-light effect originating from the spectral structures we prepare inside the memory crystal. This effect



virtually elongates the cavity by two orders of magnitude, leading to a shrink in the cavity bandwidth that limits our storage capabilities to narrow ( $\sim$ MHz) pulses (section 4.2.4);

5. Finally, we perform the full spin-wave storage protocol for storing weak coherent pulses in a spin state of our  $\text{Pr}^{3+}:\text{Y}_2\text{SiO}_5$  crystal (section 4.2.5).

#### 4.2.1 Storage of weak coherent pulses at the single photon level

To prove that our cavity is suitable for highly efficient single photon storage, we began by storing attenuated laser pulses and detecting their echoes by means of single photon detectors.

The pulses were  $1\ \mu\text{s}$  FWHM Gaussian pulses, sent at a rate of  $1000\ \text{s}^{-1}$ . These pulses contained less than one photon each: in order to tune this number carefully, we measured first the classical power in CW at a certain AOM voltage, and then we attenuated light with characterized OD filters. In our case, we set powers in the order of  $10\ \mu\text{W}$ , measured in front of the vacuum chamber, and then we used a stack of 3 OD filters, calibrated at  $606\ \text{nm}$ , amounting to  $1.03 + 5.2 + 2.11 = 8.34$  total OD<sup>1</sup>. With this attenuation, each pulse had a number of photons around  $10^{-1}$ .

The experimental time sequence was divided into two phases, described in appendix section C.1.5.2: in a first phase lasting around  $160\ \text{ms}$ , the locking light was enabled and the locking procedure, detailed in the same section, was used to stabilize the length of the cavity. During this phase, all the shutters on the detector path were closed, and the preparation beam was used to tailor the spectral features inside the crystal. This phase had different durations depending on the kind of experiment we performed.

In the second phase, the locking light shutter and preparation shutter closed, and only the single photon light was entering the cavity path. To account for instabilities in power, every other cryostat cycle we prepared

---

<sup>1</sup>When speaking about the OD of neutral density filters, we follow Thorlabs convention of defining the absorption as  $10^{-\text{OD}}$ .

a high OD absorption feature instead of an AFC inside the crystal. This interrupted the cavity and, as a consequence, we only saw the 40 % of the input light that got reflected from the first mirror. The reflected part was halved by the BS and was coupled to a single-mode fiber. To guarantee that the AFC efficiency was not overestimated, the reflected input mode was coupled with 90 % to a SM-fiber, i.e. the spatial mode reflected by the first mirror<sup>2</sup> We detected the reflected pulse, which amounts to 40 % of the input pulse, with a single photon avalanche detector (PerkinElmer SPCM-AQR-16-FC, 25 Hz dark counts), and we normalized the number of counts to 100 % to have an estimation of the original pulse. Note that we do not need to account for losses along the path, since the echo and the reflected input were transmitted through the same path.

During the cycles when we prepared an AFC inside the crystal, echoes were re-emitted by the AFC 2  $\mu$ s after the input pulse. Given the unbalanced reflectivity of the cavity mirrors, they were mostly expelled in reflection from the cavity. We detected those echoes in the same path as the input pulses.

The ratio between the number of counts detected in the echoes and the number of counts in the 40 % input pulses, after they have been normalized to 100 %, yields the AFC efficiency.

In figure 4.4, I am reporting one of the experimental traces we recorded. This efficiency was  $(62.0 \pm 1.3) \%$ , and it is the highest AFC efficiency reported up-to-date. The reflected part of the pulse from the cavity was as low as 6 %, demonstrating a high degree of both mode- and impedance-matching. The average efficiency measured with ten independent measurements taken over a few days was  $(55.8 \pm 1.5) \%$ . For these results, we were sending 1000 pulses per second to the cavity, using only the first 12.2 ms of the measurement phase (see figure C.7 for a sketch of the whole cryostat cycle). The measurement times were ranging between 2 min and 10 min, which ensured a good statistics during all the trials. The detection window for input and echo was 2  $\mu$ s. The histogram time bin we are considering for


---

<sup>2</sup>We assume that the echo mode originating from the cavity is not coupled with a better efficiency to the fiber than the reflected mode that we use for comparison.

the reported results is 10 ns, while figure 4.4 displays a trace with 50 ns time bin for aesthetic purposes. The reliability of our cavity locking system is clearly displayed in figure 4.5, where I plotted the number of counts versus the number of triggers, grouped in bins of 10 000 for convenience, over a whole measurement. In this case, the data recording lasted 5 min.

Figure 4.6 displays a trace of the comb we used to record the efficiency of figure 4.4. From the trace of the comb, using equation 4.1, we can infer the storage efficiency we could expect from it. An analysis of this comb gives  $\tilde{d} = 0.38$ ,  $\mathcal{F}_{\text{AFC}} = 5.77$ ,  $d_0 = 0.006$ . Plugging this parameters inside equation 4.1, and accounting for single-pass intra-cavity losses around 2.5%, which is a reasonable value according to the several loss measurements performed throughout this experiment, we estimated a reachable efficiency of 67.2%<sup>3</sup>. This value is not far from the maximum 62% recorded. For all the other measurements, we imputed the disagreement to the fact that the cavity must be perfectly resonant with the comb position and, if this resonance was not tuned carefully, the echo efficiency decreased considerably.

#### 4.2.2 Storage of time-bin qubits and analysis via an AFC interferometer

To investigate whether we could store quantum information in our memory, we proceeded with storage of time-bin qubits. To generate these qubits, we sent two Gaussian pulses in a row, very close between each other, commonly referred to as early pulse  $|e\rangle$  and late pulse  $|l\rangle$ , to the cavity light AOM (). Both pulses were around 510 ns long (FWHM). When the mean number of photons is reduced to less than one per pulse, then the photon is delocalized between the early ( $|e\rangle$ ) and late ( $|l\rangle$ ) components, thus approximately producing the quantum state:

$$|\psi\rangle = \frac{1}{\sqrt{2}}(|e\rangle + e^{i\Phi} |l\rangle) \quad (4.2)$$

---

<sup>3</sup>Note that this value does not agree with the value displayed in figure 4.2 for similar losses, because in this case we are using different parameters and single-pass losses.

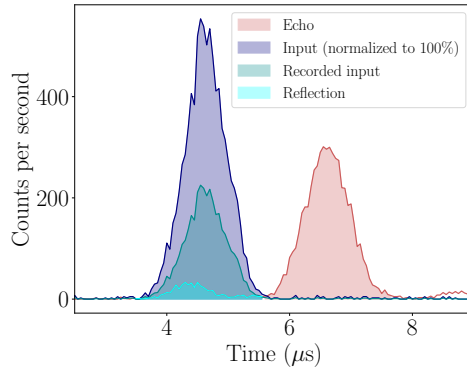


Figure 4.4: Input pulse and its echo (red pulse) after  $2\ \mu\text{s}$ . The recorded input pulse (cyan pulse) is the reflected 40% of the original input pulse, so it is normalized to 100% (dark blue pulse). The ratio between the echo and the original pulse yields  $(62.0 \pm 1.3)\%$  storage efficiency. The reflection from the cavity (light blue pulse) was 6%, indicating that we achieved a good mode-match and a good impedance-match. The time bin considered for plotting this trace is 50 ns.

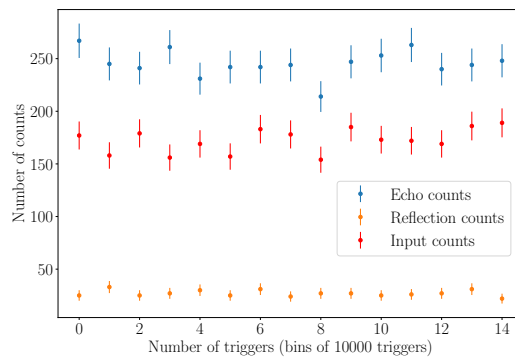


Figure 4.5: Number of counts (for input, echo and reflection) versus number of triggers, grouped by 10 000 (10 s). The number of counts stays approximately constant over the whole duration of the measurement.

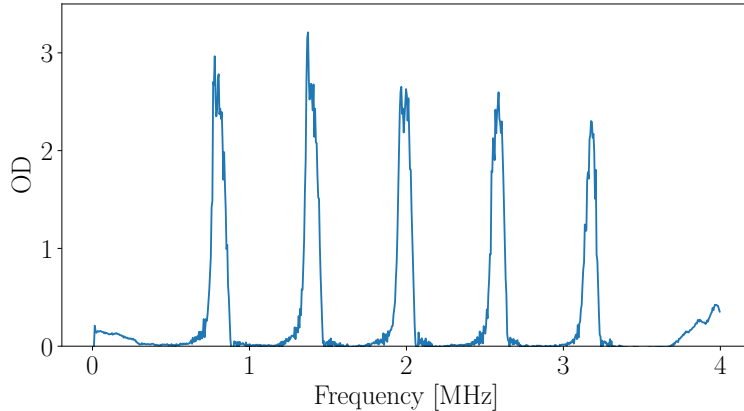


Figure 4.6: Trace of the comb (in absorption) that yielded the efficiency in figure 4.4. The theoretical efficiency achievable with this comb, considering its background absorption of  $d_0 = 0.006$  and our intra-cavity single-pass losses of 2.5%, is 67.2%.

The phase  $\Phi$  between the two components can be controlled by means of the AOM.

The experiment proceeded similarly to the one described in the previous section, with some important differences. First of all, during the locking phase, we addressed the filter crystal by means of the filter preparation beam, which prepared a balanced (transmission = echo intensity) AFC inside it [144]. The purpose of the balanced AFC was acting as an unbalanced Mach-Zehnder interferometer: the two components of the qubit had equal probabilities of being absorbed or transmitted, and they could interfere after the AFC because the comb storage time was set to  $1\ \mu\text{s}$ , which was the time between the early and late pulses that constitute the qubit. We could change the basis of measurement by tuning the phase between the qubits—setting it to  $0^\circ$ ,  $45^\circ$ ,  $90^\circ$  and  $135^\circ$ —and we could change the phase of the interferometer by shifting the AFC spectral position with respect to the central frequency of the qubit [83, 144]. By changing both the bases in which we prepared the input qubit and the AFC positions, we could

obtain interference fringes, infer their visibilities and, as a consequence, the fidelity (see section 1.3) to the original state 4.2. Basically, we used the same technique as in section 3.2.1.3 to analyze the degree of entanglement between the Stokes and Anti-Stokes photons, except with only one qubit and one spatial mode.

We employed similar powers and attenuations with respect to what described in the previous section, the main difference being that in this experiment we sent pairs of 510 ns-long pulses (FWHM). Each qubit contained a mean number of photons of 0.15. These qubits were sent to the cavity and, after a 2  $\mu$ s time, re-emitted by the AFC. The retrieved echoes were coupled into the SM-fiber and sent over to the filter crystal. Before the filter, their polarization was restored to vertical (the polarization that interacts with the ions) by means of a quarter-wave plate, a half-wave plate, and a PBS. After the filter crystal, the photons were coupled back into another fiber and transmitted to the detector.

In a first phase, we prepared a spectral window inside the filter crystal, to assess the pure storage efficiency of our quantum memory. We recorded two sets of data, averaging out to around 52 % efficiency. The first trace is shown in figure 4.7. We imputed the discrepancy with the previous 62 % storage efficiency of single pulses to the mismatch in bandwidth between this double Gaussian shape and the previous single Gaussian shape. I will go into detail in section 4.2.4.

Following this estimation of efficiency, we prepared an interferometric AFC inside the filter and we started changing both the phase between the early and late components of the qubit and the frequency starting position of the AFC, analogously to what described in section 3.2.1.3. In this case, the phase between the early and late components of the qubit was the phase of the qubit, and was changed through the cavity beam AOM. The setting of the analyzer was given by the frequency shift of the comb created in the interferometric filter crystal. We recorded the interference fringes shown in figure 4.8. The detection window for this analysis was 1  $\mu$ s. As it can be seen from this figure, if we change the phase between the early and late parts of the qubit, we measure the visibility of the interferometer fringe for different input qubit states. If this visibility is high for all these input qubit

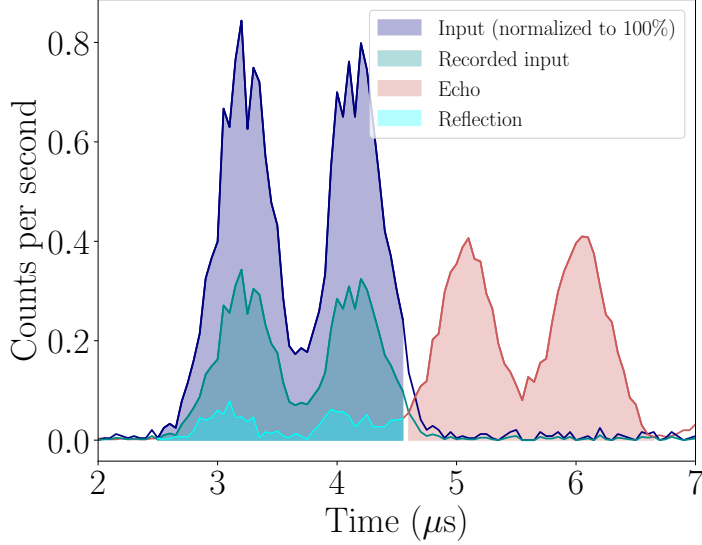


Figure 4.7: Input qubit (cyan double pulse) and its echo (red double pulse) after  $2\ \mu\text{s}$  of storage. The recorded qubit is the reflected 40 % of the original qubit, so it is normalized to 100 % (dark blue double pulse). The ratio between the echo and the original qubit yields  $(52.3 \pm 1.1)\%$  storage efficiency. The mean number of photons per pulse is 0.15, and the number of pulses sent was 2000 per each measurement period (over one cryostat cycle). The histogram time bin considered for plotting this trace is 50 ns, while for the efficiency analysis we considered a 10 ns time bin. The detection window for inputs and echoes is  $2.1\ \mu\text{s}$ .

states, it means that the memory preserves the qubit with a high fidelity. This has to occur in at least two different bases, which is equivalent to say that the same happens when we fix the basis of measurement and we scan the position of the AFC. The resulting pulses after crossing the IFC, in the case of constructive interference, are shown in appendix C, in the upper plot of figure C.9. Constructive and destructive interference histograms for the first and the fifteenth points (from the left) of the  $90^\circ$  phase plot of

figure 4.8 are displayed in figure 4.9.

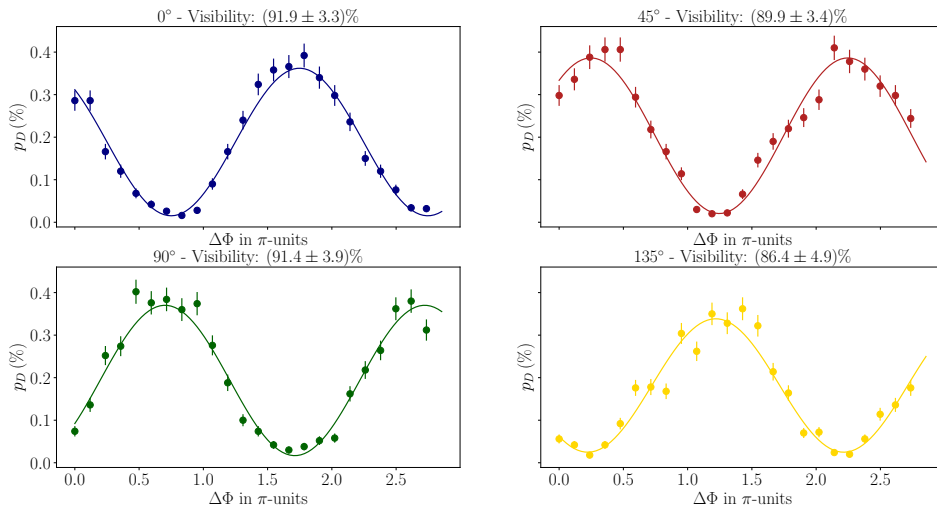


Figure 4.8: Interference fringes for different measurement bases. The plots show the detection probability per trial ( $p_D$ ) versus the interferometric comb phase change, expressed in units of  $\pi$ . All these measurements were recorded with 2000 pulses per second. The detection window was  $1 \mu\text{s}$ .

From these fringes, we could infer the visibility by fitting the experimental data points with the function  $A \sin(B\Delta\Phi + C) + D$ , mimicking the theoretical behavior  $\frac{1}{2}(1 + V \cos \Delta\Phi)$ , and extracting it from the values of  $A$  and  $D$ : for  $0^\circ$  phase between the pulses,  $V_{0^\circ} = (91.9 \pm 3.3)\%$ ; for  $45^\circ$  phase between the pulses,  $V_{45^\circ} = (89.9 \pm 3.4)\%$ ; for  $90^\circ$  phase between the pulses,  $V_{90^\circ} = (91.4 \pm 3.9)\%$ ; and, finally, for  $135^\circ$  phase between the pulses,  $V_{135^\circ} = (86.4 \pm 4.9)\%$ . All these visibilities averaged out to the final value  $V_{\text{avg}} = (89.9 \pm 3.9)\%$ , calculated by first averaging the redundant measurements corresponding to the same basis and then averaging these two equatorial visibilities together.



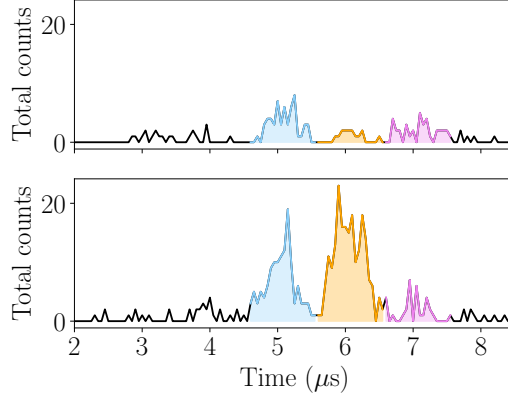


Figure 4.9: Examples of destructive (upper plot) and constructive (bottom plot) interference (in orange), corresponding to the first and fifteenth points (from the left) for  $90^\circ$  phase of figure 4.8. The colors of the time intervals follow the same convention as the ones in figure C.9, and are  $1 \mu\text{s}$  long. The histogram time bin of this figure is  $50 \text{ ns}$ , while the analysis was performed with a  $10 \text{ ns}$  histogram time bin.

To assess the fidelity of our system<sup>4</sup> over the full Bloch sphere, we needed to measure the fidelity of the early (late) component when we sent only one component, that is, the fidelity of the poles of the Bloch sphere. The early and late echoes are shown in figure 4.10. This fidelity is  $F_{\text{poles}} = (94.6 \pm 0.3) \%$ . Finally, from the formula  $F = \frac{1+V_{\text{avg}}}{2}$  [150], we calculated a fidelity of  $F_{\text{equator}} = (94.9 \pm 1.9) \%$ , and a final fidelity of  $F_{\text{total}} = \frac{2}{3}F_{\text{equator}} + \frac{1}{3}F_{\text{poles}} = (94.8 \pm 1.4) \%$ . A similar analysis for the inteferometer without memory (see appendix C for the whole procedure) led to an inteferometer fidelity of  $F^{\text{interf}} = (94.2 \pm 1.0) \%$ . As a consequence, accounting for this last fidelity, the real fidelity of our quantum memory could be estimated as  $F^{\text{memory}} = F_{\text{total}}/F^{\text{interf}} = 100 \%_{-2\%}^{+0\%}$ .

<sup>4</sup>By “system”, I mean the combination of quantum memory and interferometer. We will see later than we can correct this system fidelity with the interferometer fidelity to get the memory fidelity.

As I clearly stated, our qubits were not really single-photon qubits but they were obtained by attenuating a laser to less than one photon per pulse. Therefore, the limit we needed to surpass to prove that our memory is a real quantum memory was not the usual value for Fock states of  $F_{\text{Fock}} = \frac{N+1}{N+2}$  mentioned in the introduction of this thesis, but rather some other bound in which the Poissonian distribution of the photons is accounted for [39, 110, 151]. Moreover, this limit is merely theoretical, as in it does not consider realistic memories with efficiencies lower than 100%. If we consider the thorough analysis performed in the appendix A of reference [110], which accounted for efficiency-limited quantum memories and weak coherent states, we can see that the limit we needed to surpass, with a mean photon number around 0.15 and a memory efficiency of 52% (for qubits), lied slightly below 75%. Our measured fidelity is much higher than this bound, showing that our device behaves as a quantum memory.

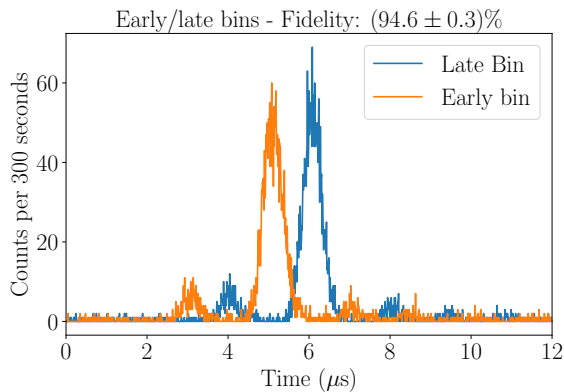


Figure 4.10: Early and late pulse echoes from the memory, and their fidelity, measured by preparing a transparency window in the filter crystal and estimating the overlap between the early (late) echo and the late (echo), and vice versa.

### 4.2.3 Storage efficiency at different storage times

To investigate whether the efficiency enhancement from the cavity held at different storage times, we created different combs with different storage times, and we carefully tuned their finesse and height to achieve approximate impedance-matching to observe the expected enhancements. To do so, we employed both the techniques described in appendix section B.3.2, the hole-burning technique and the coherent technique. The first one was employed to shape the combs with  $1.5\ \mu\text{s}$  and  $2\ \mu\text{s}$ , while the second was used to tailor combs for  $8\ \mu\text{s}$ ,  $12\ \mu\text{s}$ ,  $17\ \mu\text{s}$ ,  $24\ \mu\text{s}$ ,  $35\ \mu\text{s}$  and  $50\ \mu\text{s}$ . The tuning procedure of the various combs to achieve the best possible efficiency slightly changed their storage times, so the ones listed before became  $1.3\ \mu\text{s}$ ,  $1.9\ \mu\text{s}$ ,  $8.3\ \mu\text{s}$ ,  $10.3\ \mu\text{s}$ ,  $17.1\ \mu\text{s}$ ,  $24.1\ \mu\text{s}$ ,  $35.5\ \mu\text{s}$  and  $50.0\ \mu\text{s}$ . For each point, we had to adjust the comb OD and the comb finesse.

Figure 4.11 shows the recorded points. In order to demonstrate the enhancement, we recorded both the cavity efficiencies with weak coherent pulses (we used the same powers and filters used in section 4.2.1) and the single-pass efficiencies with classical pulses. These latter ones were recorded with different combs, whose finesesses and ODs were specifically optimized to yield the maximum single-pass efficiency. From these data, it is apparent that the cavity is improving the AFC efficiency at different times, except for the last point. To extrapolate the  $T_2^{\text{eff}}$  of our AFC and estimate the quantity  $\eta_h$  defined in section 2.2.1 accounting for the decay with time, we performed a fit on the efficiencies with the function  $A \exp\left(-\frac{4\tau}{T_2^{\text{eff}}}\right)$ , where  $A$  is a coefficient and  $\tau$  is the storage time, which is basically the contribution to the AFC efficiency given by equation 2.8. The fit provided us with a  $T_2^{\text{eff}} = (55.5 \pm 2.9)\ \mu\text{s}$ , compatible with the values observed previously in our group, in this cryostat, as reported in the supplemental material of reference [63].

Another interesting result is the  $(60.2 \pm 0.9)\%$  efficiency reached at  $1.3\ \mu\text{s}$ . Since we reached  $62\%$  efficiency for  $2\ \mu\text{s}$  storage time, we expected an even higher efficiency at this storage time, because the detrimental effect of the finite coherence of the ions is smaller here. However, during the time of this experiment, the cryostat was not providing the same performances

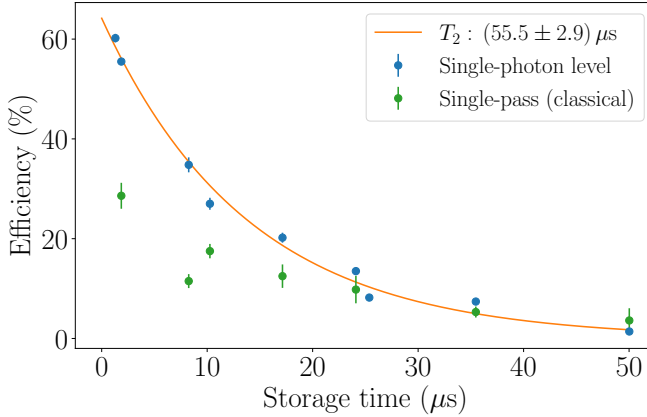


Figure 4.11: Efficiency versus storage time for 9 different storage times. The blue dots represent the efficiencies with weak coherent pulses, the green ones are the efficiencies in single-pass—without cavity—recorded at the classical level. The orange curve is an exponential fit to the blue points yielding the effective  $T_2$  of our atomic frequency comb. The combs for the first 2 efficiencies were shaped through the hole-burning technique, while the remaining 7 combs were prepared through the coherent method (see appendix section B.3.2.3 for an explanation of the two procedures).

as in the experiment in section 4.2.1, thus leading to a warmer crystal; also, the kind of crystal mount we employed in this experiment is stiffer than the previous one, as mentioned in appendix section B.2.2. A consequence of this fact is that more vibrations of the cryostat are transferred to the crystal, which severely limits the parts of the cryostat cycle that can be used for measurement and also reduces the  $T_2$ . Therefore, the efficiency achieved at  $1.3 \mu\text{s}$  is to be compared with the  $2 \mu\text{s}$ -efficiency we got in this experiment,  $(55.5 \pm 0.6) \%$ : the conclusion we can draw from this comparison is that, by going to shorter storage times, we were actually gaining efficiency. Ultimately, storing for very short times requires very short pulses in time, so very frequency-broad pulses, but the pulse bandwidth was limited by

the cavity bandwidth, as we will see in the next section.

#### 4.2.4 Pulse bandwidth and slow-light effect

One of the main limitations for pulse storage in our impedance-matched cavity I have been mentioning in this chapter and throughout this thesis is the slow-light effect. I will give a brief introduction about that, mainly based on references [148, 149].

##### 4.2.4.1 Slow-light effect

The free spectral range (FSR)  $\Delta\nu$  of a Fabry-Perot cavity is given by the formula [149, 152]:

$$\Delta\nu = \frac{c}{2L n_g(\nu)} = \frac{v_g(\nu)}{2L} \quad (4.3)$$

with  $c$  speed of light,  $\nu$  light frequency,  $n_g$  group velocity index of refraction and  $v_g(\nu)$  group velocity. Following reference [87],  $n_g$  can be split into two components:

$$n_g = \frac{c}{v_g} = \frac{\partial(\nu n_r(\nu))}{\partial\nu} = n_r(\nu) + \nu \frac{dn_r(\nu)}{d\nu} \quad (4.4)$$

where  $n_r(\nu)$  is the real part of the phase-velocity refractive index. In a low dispersion regime, when the absorption is low as well, then  $n_r(\nu) \gg \nu \frac{dn_r(\nu)}{d\nu}$ , so equation 4.4 reduces to the equivalence between the group velocity index of refraction and the phase velocity index. In the opposite regime, when absorption starts playing an important role, then  $n_r(\nu) \ll \nu \frac{dn_r(\nu)}{d\nu}$  and the index of refraction for the group velocity is dominated by dispersion. Whenever we prepare a transparency window, also known as pit, inside the crystal, we create a sharp change in absorption inside the medium. In this case, we work in a regime in which absorption plays an important role, therefore it follows that the mode spacing described by equation 4.3 is mainly determined by the dispersion, whereas the changes in frequency is not so relevant.

Another operational definition we can use for understanding this problem is that the FSR of the cavity is the inverse of the round-trip time. We could divide this round-trip time into the free-space round-trip time  $T_{\text{fs}}$  and the crystal round-trip time  $T_{\text{cr}}$ . Also, from references [149, 153, 154], an approximate expression for the group velocity index of refraction is given by<sup>5</sup>  $v_g = \frac{2\pi\Gamma}{\alpha}$ , where  $\Gamma$  is the pit bandwidth and  $\alpha$  is the absorption coefficient defined in section 2.2. Now, calling  $L_{\text{cr}}$  the length of the crystal embedded in the impedance-matched cavity, and  $T_{\text{fs}}$  and  $T_{\text{cr}}$  the times spent by the light respectively in free-space and inside the crystal, we can write:

$$\Delta\nu = \frac{1}{T_{\text{fs}} + T_{\text{cr}}} = \frac{1}{\frac{2(L-L_{\text{cr}})}{c} + \frac{2L_{\text{cr}}}{v_g}} = \frac{1}{\frac{2(L-L_{\text{cr}})}{c} + \frac{\alpha L_{\text{cr}}}{\pi\Gamma}} = \frac{\pi c\Gamma}{2\pi\Gamma(L - L_{\text{cr}}) + \alpha c L_{\text{cr}}} \quad (4.5)$$

which enables us to calculate the new FSR. If we plug into this equation our experimental values ( $\alpha = 20 \text{ cm}^{-1}$ ,  $L = 208 \text{ mm}$ ,  $L_{\text{cr}} = 3 \text{ mm}$ ,  $\Gamma = 18 \text{ MHz}$ ), we obtain  $\Delta\nu = 9.3 \text{ MHz}$ . Therefore, from the original value of  $720 \text{ MHz}$  quoted in section 4.2, we observe a reduction by two orders of magnitude. If we calculate the linewidth of the cavity by considering a finesse of 6.5 from the same section, we get a FWHM linewidth of  $\gamma_{\text{cav}} = 1.4 \text{ MHz}$ .

In our real cavity described in section 4.2, the linewidth was slightly lower than this value. Considering that the linewidth changes depending on the OD and on the spectral position we are centered on, we never observed more than  $1.16 \text{ MHz}$  (FWHM) at the center of the pit, that is, the furthest position from the pit walls: the further we move from the sharp change in OD, the less accentuated the slow-light effect is. In figures 4.12 and 4.13, this situation is shown. This bandwidth decrease has been widely described in another impedance-matched experiment [87, 148, 149]; recently, it has been proposed to harness this narrowing to build laser reference cavities less sensitive to cavity length changes [155].

As I will show in the next section, the slow-light effect has repercussions

---

<sup>5</sup>I am following the convention expressed in reference [149]; in reference [154], a factor 2 is missing in the group velocity expression, as pointed out in reference [149]; in reference [153], instead, there is an additional factor  $\pi$  multiplying this expression.

on the spectrum of light we can store efficiently in our quantum memory.

#### 4.2.4.2 Storage efficiency versus pulse bandwidth

To assess this reduction in linewidth, we performed a storage experiment where we changed the bandwidth of the input pulses and measured the storage efficiency. The setup for the experiment was basically the same as the one presented in section 4.2.1, with the same 2  $\mu\text{s}$  storage time; in this case, we changed the temporal duration of the pulses from 120 ns up to 1  $\mu\text{s}$ , such to get pulse bandwidths ranging from 3.7 MHz to 412 kHz. Since the linewidth of the laser is much smaller than these values, and since the input pulses are not chirped, we can assume that they are Fourier-limited pulses. Thanks to this assumption, we calculated their spectral width through the time-bandwidth product for Gaussians: called  $\Delta\nu_p$  the bandwidth of a pulse, and  $\Delta\tau_p$  its temporal duration, then for a Gaussian pulse it holds that  $\Delta\nu_p\Delta\tau_p \geq 0.441$  [156].

In figure 4.14, I am showing the outcome of this experiment. As expected, the efficiency started dropping considerably as soon as the pulse spectral width exceeded the cavity linewidth threshold of 1.16 MHz. Despite the efficiency decrease, we could still store a 3.7 MHz broad pulse with 31.7% efficiency. Moreover, as it is apparent from the same plot, we could still store 1.8 MHz FWHM single photons from our current single-photon source with an efficiency around 48%. As far as the initial bump is concerned, we attribute that to the fact that, for those bandwidths, the separation of the AFC teeth is comparable to the FWHM of the pulses. Therefore, the pulses did not intercept all the AFC teeth, but only a few, and any inhomogeneity in the teeth preparation was leading to a decrease in efficiency (see also section 2.2 about the temporal multimodality and the minimum frequency width of storable pulses).

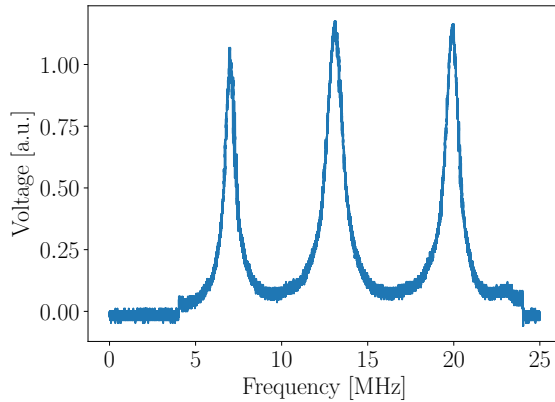


Figure 4.12: Cavity modes obtained by creating a pit in the crystal and chirping the light for 20 MHz for 4 ms inside it. The central mode has a linewidth of 1.16 MHz, which is two orders of magnitude less than the expected value of 111 MHz for the cold case scenario.

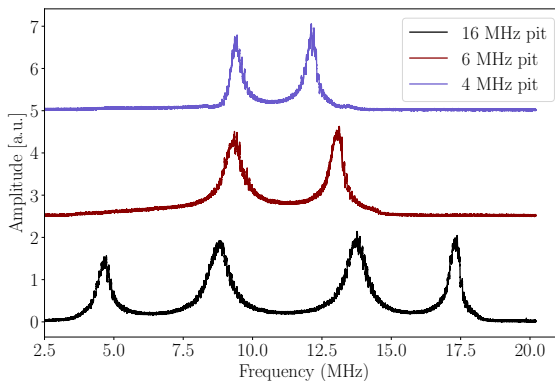


Figure 4.13: Variation in cavity mode linewidth  $\gamma_{\text{cav}}$  and FSR inside pits of different width: inside the usual 16 MHz pit (black), where FSR = 5.8 MHz and  $\gamma_{\text{cav}} = 1.3$  MHz; inside a 6 MHz pit (red), where FSR = 4.5 MHz and  $\gamma_{\text{cav}} = 1$  MHz; and inside a 4 MHz pit (slate blue), where FSR = 3 MHz and  $\gamma_{\text{cav}} = 690$  kHz. The three traces have arbitrary units and have been shifted vertically between each other for the sake of comparison. These data were collected at an early stage of the experiment, when the cavity finesse  $\mathcal{F}_{\text{cav}}$  was 4.4 due to mode-mismatch.



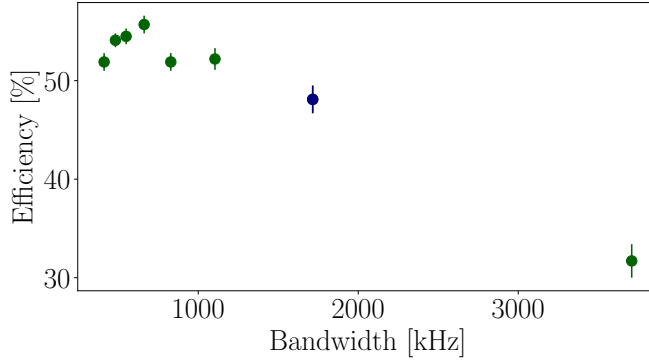


Figure 4.14: Storage efficiency versus pulse bandwidth for Gaussian pulses and  $2\ \mu\text{s}$  storage time. As it is expected, the broader the pulse becomes, the more the storage efficiency decreases, due to the filtering effect of the cavity. We attribute the initial bump to the fact that the separation between the AFC teeth starts being comparable with the pulse bandwidth, leading to a decreased number of peaks absorbing the pulse. The blue point is the one whose x-coordinate is lying the closest to our single-photon bandwidth, 1.8 MHz, and it represents an efficiency of 48 %.

#### 4.2.5 Spin-wave storage in the cavity

As a final step, we are currently performing spin-wave storage in our impedance-matched cavity. The theory behind this technique has been detailed in section 2.2.2. With respect to the setup displayed in figure 4.3, we have an additional strong beam outside of the cavity axis and focusing inside the memory crystal (see appendix section C.1.2 for additional details). The results that will be presented will be most likely improved in the next months.

The spin-wave storage measurements have been performed with a comb designed for  $8\ \mu\text{s}$  storage and a total storage time around  $11.5\ \mu\text{s}$ . In figure 4.15, I am showing the best efficiency, at the classical level, that we obtained with the spin-wave storage protocol. This efficiency is 32.7%, with 6.9% reflection. The first control pulse (CP) is shone at  $3.3\ \mu\text{s}$  from the input pulse, while the second one is sent at  $3.5\ \mu\text{s}$  after the previous one.

The echo appears after  $4.7 \mu\text{s}$  from this second pulse, as it is expected, since  $3.3 \mu\text{s} + 3.5 \mu\text{s} + 4.7 \mu\text{s} = 11.5 \mu\text{s} = \tau_{\text{AFC}} + T_{\text{S}}$ , as stated in section 2.2.2.

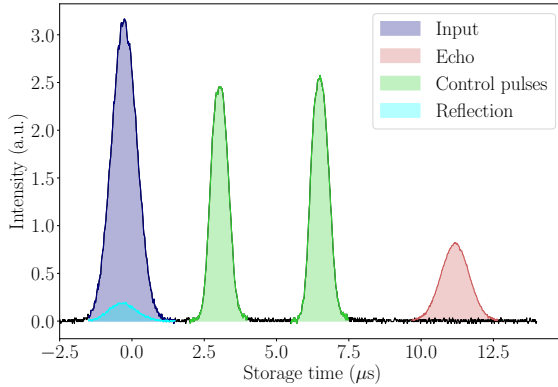


Figure 4.15: Spin-wave storage efficiency for a classical pulse (blue pulse), with  $\tau_{\text{AFC}} = 8 \mu\text{s}$  and  $T_{\text{S}} = 3.5 \mu\text{s}$ . Despite the fact they are not shone inside the cavity mode, the CPs (light green pulses) are leaking into it and are recorded by the photodetector. The efficiency is 32.7%, estimated by dividing the echo area (red pulse) by the input pulse. The reflection (light blue pulse) is 6.9% of the input pulse.

By varying the time  $T_{\text{S}}$  between the two CPs, we can estimate the dephasing induced by the inhomogeneously broadened spin state line  $\gamma_{\text{inh}}$ , by observing the decay of spin-wave efficiency. This is shown in figure 4.16, where the echo efficiency is recorded after scanning the time span between the CPs. The decay follows an exponential law of the form  $\exp(-\frac{\pi^2 \gamma_{\text{inh}}^2 T_{\text{S}}^2}{2 \log(2)})$ . By fitting this function to our data, we found a value of  $\gamma_{\text{inh}}$  of  $(17.1 \pm 0.2) \text{ kHz}$ .

Referring to these values, we can now estimate the transfer efficiency of control pulses, defined in section 2.2.2.1. I will employ the same notation as in equation 2.9. The two-level AFC efficiency for this case was around  $\eta_{\text{sp}}^{\text{back}} = 40 \%$ . The dephasing caused by the storage in the spin-state for a time  $T_{\text{S}} = 3.5 \mu\text{s}$ , as said in the previous paragraph, is given by  $\eta_{\text{C}} =$

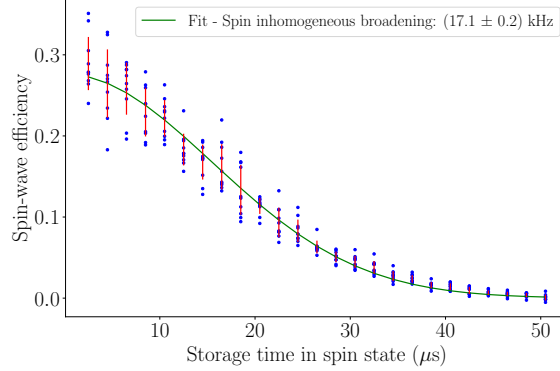


Figure 4.16: Decay of the spin-wave efficiency as a function of the storage time in the spin state, i.e. the separation  $T_S$  between the two CPs. The blue points are experimental points, whereas the red bars display one standard deviation around the mean of each set of points. The fit with a function of the kind  $\exp(-\frac{\pi^2 \gamma_{\text{inh}}^2 T_S^2}{2 \log(2)})$  provides a value for the spin inhomogeneity  $\gamma_{\text{inh}}$  of  $(17.1 \pm 0.2)$  kHz.

$\exp(-\frac{\pi^2 \gamma_{\text{inh}}^2 T_S^2}{2 \log(2)})$ , with  $\gamma_{\text{inh}} = 17.1$  kHz. From equation 2.9, assuming  $\eta_{\text{SW}} = 32.7\%$  as we reported in figure 4.15, we can thus infer the control pulses efficiency as  $\eta_T = \sqrt{\eta_{\text{SW}} / (\eta_{\text{sp}}^{\text{back}} \eta_C)} = 91.6\%$ .

We are currently performing measurements at the few photon level. The challenging task in this kind of measurements is filtering the amount of noise induced by the CP tails and by fluorescence. Usually, this issue makes experiments at the single photon level quite challenging. In figure 4.17, I am reporting one of our measurements. With an average mean photon number of 1.14 photons per pulse (1000 pulses over a measurement period of 5 ms per each cryostat cycle), the achieved efficiency was  $(21.7 \pm 0.9)\%$ . We estimated the SNR to be  $4.1 \pm 0.3$  and, from these values, we could calculate a  $\mu_1$  value (see section 5.4.1.2) of 0.28. The measurement time was 369 s. Similarly to the measurements presented in section 4.2.1, in this measurement we alternated our measurement cycles between three different

situations: the creation of an absorption feature blocking the cavity, to record the 40 % input (blue trace in figure 4.17); a noise recording without input, by sending no input and the two CPs (red trace in figure 4.17); and, finally, the real spin-wave storage, by sending both the input and the CPs and preparing the comb (black dashed trace in figure 4.17).

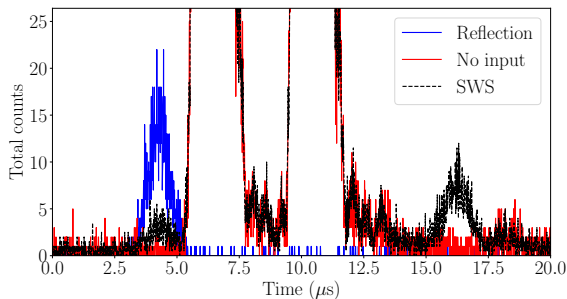


Figure 4.17: Example of a spin-wave storage measurement. Different cases are shown: when only the input pulse is sent, with no CPs and no comb (in blue), when only CPs are sent, with no input and no comb (in red), and when both input and CPs are sent, with the comb, i.e. the actual spin-wave storage experiment (in black, dashed) for  $11.5 \mu\text{s}$  storage time. The shown input pulse is 40 % of the original input sent to the cavity. The three different traces are explained in the text. Each of the input pulses ( $1000 \text{ s}^{-1}$ ) contains 1.14 photons. The efficiency recorded in this trial is  $(21.7 \pm 0.9) \%$ , with a SNR of  $4.1 \pm 0.3$ .

### 4.3 Discussion and outlook

In conclusion, we demonstrated the highest AFC efficiency up-to-date at the single-photon level. We were able to store weak coherent single pulses with up to 62 % device efficiency (section 4.2.1). Furthermore, we performed the most efficient storage of qubits in a solid-state quantum memory to date by storing weak coherent time-bin qubits with 52 % efficiency (section 4.2.2). In addition, we analyzed them by means of an AFC-based

unbalanced Mach-Zehnder interferometer, which demonstrated the high fidelity of our quantum memory, around 94.8%, which approached 100% when we correct it for the interferometer fidelity of 94.2%. Additionally, we managed to change the storage time of our memory and extend it up to 50  $\mu\text{s}$ , demonstrating cavity enhancement at different storage times (section 4.2.3). Moreover, we showed that slow light was affecting our experiment and decreasing our storage efficiency depending on the bandwidth of the light we wanted to store. Nonetheless, the efficiency was around 30% even for pulses as broad as 3.7 MHz and, at 1.8 MHz, which is the linewidth of the photons emitted by our single-photon source, we observed a 48% efficiency (section 4.2.4.2). Finally, we demonstrated that our cavity is suitable for spin-wave storage (section 4.2.5). We have demonstrated a cavity-enhanced spin-wave efficiency up to more than 32% at the classical level and up to  $(21.7 \pm 0.9)\%$  with weak coherent states. This latter result was achieved with 1.14 photons per pulse, and a SNR of  $4.1 \pm 0.3$ .

There were several limitations that affected our experiment, the main one being intra-cavity losses. As it is stated in section 4.1.2.1 and in reference [88], losses are very detrimental for the cavity-assisted AFC efficiency, especially when they become comparable to  $\tilde{d}$ . In terms of loss reduction in the current setup, we already installed AR-coated windows on the cryostat vacuum chamber, we removed the radiation shield windows and we used an AR-coated crystal. Eventually, a possible solution for this problem is using a coated crystal as a cavity, such that no intra-cavity losses are possible, like in references [87, 89]. The drawback of this solution lies in the fact that no single-pass measurements are possible, since the cavity cannot be temporarily removed as we do with the flip mirror inside the cavity. These measurements which are extremely useful for characterizing losses and reading the AFC we are preparing inside the crystal. Additionally, it is not clear how to apply spin-wave storage CPs in a cavity-coated crystal, given that the pulses are usually applied off-axis. A viable strategy would be installing the cavity inside the vacuum chamber of our cryostat. This would have the additional benefit of increasing the FSR of our cavity, since it would be much shorter, hence reducing drastically all the slow-light problems we encountered in section 4.2.4.1.

On top of the purely optical losses due to crystal interfaces, we have atomic losses, i.e. all the incoherent background absorption from the AFC that is not contributing to the later echo, which I previously referred to as  $d_0$  (in OD). To reduce this contribution, we aim at creating better combs that display little or no background absorption. I will deal later with comb creation issues. An alternative viable solution to the background absorption is using shorter crystals, thus decreasing the overall OD.

As far as the cavity is concerned, the efficiency can be further improved by increasing the reflectivity  $R_{\text{out}}$  of the output mirror. As shown in figure 2.14, there is a dramatic change in efficiency when this value is incremented: fixing our  $\tilde{d}$  to 0.45 and increasing the value of  $R_{\text{out}}$  from the current 97% to 99.98% lead to an increase in efficiency (in the lossless scenario) from 80.5% to 86.4%, assuming a square comb with  $\mathcal{F}_{\text{AFC}} = 6.5$ .

Another line of improvement would be reducing  $\tilde{d}$  and thus increasing the finesse of the cavity. To this aim, the reflectivity of the first mirror should be increased. For instance, targeting a  $\tilde{d} = 0.1$ , keeping  $R_{\text{out}} = 99.98\%$  and the same comb shape and finesse, leads to an impedance-matched condition fulfilled with  $R_{\text{in}} = 81.9\%$ . In the lossless scenario, this change makes 92% efficiency attainable. Increasing the finesse of the cavity has some drawbacks: an increased instability of the cavity and an increased sensitivity to intra-cavity losses. As far as the first issue is concerned, we would need to improve the passive stability of the cavity, for instance by installing the mirrors on a monolithic mount decoupled from the optical table by means of a Sorbothane® layer at the base, or on dampened posts. Furthermore, insulating the cavity path from external air currents might improve the stability as well.

Nonetheless, even with our current low finesse, we need to improve on the cavity passive and active stability, which was the main limitation to the duty cycle of our experiment. For the moment, the limited duty cycle was a minor issue, since our statistics was very good, but it will become more important as soon as we interface our cavity-assisted memory with a single-photon source. We employed a chop-lock scheme: the cavity is actively stabilized during the locking cycle and then left drifting passively during the measurement cycle (appendix section C.1.5.2). Previous im-

plementations of a continuous lock mechanism have failed for two main reasons: in the first place, the cavity-mode finesse of auxiliary laser beams at wavelength different from 606 nm is even smaller than the 606 nm light finesse, leading to broader cavity modes and reduced sensitivity to changes from the resonant position for 606 nm light; secondly, whenever we need to measure with single-photon detectors, we need to be able to filter this light out by means of filtering systems with high suppression ratio, but if the auxiliary light wavelength is very close to the main one—as it needs to be in order to be resonant with our cavity—then it becomes extremely challenging to filter the locking light and let the single-photon level light through.

Another problem we faced was mode-matching of the cavity. The main experimental issue was that, with our finesse, cavity modes consist of very broad Lorentzians. As such, aligning the cavity (the procedure is described in appendix section C.1.5.1) to reach the best possible configuration is not trivial, as most of the high order modes can be hidden inside the tails of these broad fundamental cavity modes. In addition, we also observed that to a condition of perfect alignment of the cavity, judged as such by the height and shape of transmitted modes and by the increased contrast of reflected modes, it does not necessarily correspond to a condition of good efficiency for the experiment. We attribute this mismatch to the aforementioned difficulty of reaching an objectively good alignment condition.

Experimentally, it was very challenging to create AFCs with the right absorption. On the one hand, we need to achieve the right average OD  $\tilde{d}$  to be able to impedance-match the cavity, so we only care about the ratio between the maximum AFC OD and its finesse  $\mathcal{F}_{\text{AFC}}$ . On the other hand,  $\mathcal{F}_{\text{AFC}}$  needs to be maximized in order to reach a value of  $\eta_{\text{deph}}$  as close as possible to 1, as stated in section 2.2.1. Maximizing the finesse while keeping a high OD is a challenging task since, in most cases, optically pumping away population from the minima to decrease the peak width affects the peaks as well because of power broadening (section 2.1.2.5), reducing their contrast with the background.

In the near future, we would like to perform storage of heralded single photons from a cavity-enhanced SPDC single photon source and, ideally,

single photon qubits. The single photon source we use in our group to interface with  $\text{Pr}^{3+}:\text{Y}_2\text{SiO}_5$  memories emits photons that are too broad for our cavity, around 2 MHz [63], and the pulses we can store in our memory must have a certain bandwidth, ideally around 1.2 MHz or lower, as just seen in section 4.2.4. Therefore, to this aim, we are currently building another narrow cavity-assisted single photon source based on SPDC, which will produce photons around 1 MHz linewidth. Despite the emitted photons have Lorentzian waveshapes rather than Gaussian ones, which implies that their tails are much longer and might not fit completely within the AFC, this should guarantee a good storage efficiency. This new source will be very similar to the one reported in reference [63], but with a narrower linewidth due to the higher finesse of the cavity, guaranteed by a ppKTP crystal which exhibits less losses than the PPLN crystal used in our current source. An experiment of single photon storage of this kind has already been performed in reference [89], as I stated in section 4.1.1. Yet, in that case, the efficiencies were much lower than the ones we are targeting.

Finally, we would also like to implement, for the first time, an impedance-matched cavity-assisted AFC-DLCZ experiment. As a matter of fact, the theory developed in the first theoretical paper [86] is symmetric, meaning that the cavity enhances the absorption efficiency of the AFC as much as it boosts the read-out efficiency from the same structure, as mentioned in section 3.3.2. Hence, it can be applied to the AFC-DLCZ protocol in order to obtain high efficiencies. An AFC-DLCZ experiment has already been shown in chapter 3 and the theory behind this protocol has been detailed in section 2.2.3.





# Chapter 5

## Quantum frequency conversion

### 5.1 Introduction

In this chapter, I will be speaking about our experiment of quantum frequency conversion. As introduced in chapter 1, quantum frequency conversion (QFC) is a technique aimed at converting photons coherently from a wavelength to a different wavelength without adding noise by means of non-linear effects. The purpose of this procedure is interfacing quantum nodes working at different wavelengths via flying qubits, typically photons, travelling through optical fibers at the telecom wavelength. QFC has been proven to preserve the entanglement between photons [157].

The purpose of the experiment was achieving the conversion of long photons, in the  $\mu\text{s}$  range, with high SNR. This would allow interfacing typical long DLCZ photons with telecom optical fibers and with different material systems, such as trapped ions, which can emit photons in this range (around  $20\ \mu\text{s}$  FWHM [158]). As stated in chapter 3, however, our latest AFC-DLCZ experiment had a very low heralding efficiency, 1.6 %, so converting these sparse photons is extremely challenging.

Quantum frequency conversion was first theoretically proposed in 1990 [159]

and, in 1992, the same author performed the first conversion experiment [160]. Since then, experimental techniques have been perfected, especially by means of waveguides prepared inside periodically poled non-linear crystals [18, 161–163]. These have allowed to reach efficiencies as high as 84 % (external efficiency<sup>1</sup>) [164] and, more recently, 57 % device efficiency<sup>1</sup>, with an impressive 96 % internal efficiency<sup>1</sup> [165]. Furthermore, quantum frequency conversion has already been employed to interface distant quantum memories [18, 166], and it is therefore one of the most mature quantum communication technologies.

In this chapter, I am going to report our experimental trials concerning QFC. In sections 5.2.1 and 5.2.2, I will treat the theory behind QFC and show which noise processes in the waveguide are affecting the converted signal. Then, in section 5.3, I will describe the two different waveguides employed in the experiment.

Later on, in section 5.4, I will report on the experimental results obtained with the two waveguides, highlighting the superiority of the second one in terms of conversion performances.

Finally, in section 5.5, I will discuss the results presented throughout this chapter and show future perspectives for this experiment.

Appendix D contains some details about the filtering cavity we are planning to use in the future to filter further the converted signal from the second waveguide.

My contribution to this work was to rebuild the experimental setup (previously used by Dr. Nicolas Maring), to take the measurements presented in sections 5.4.1 and 5.4.2.1 and to analyze data. The work was done in collaboration with Dr. Alessandro Seri and Dr. Sören Wengerowsky. A master student, Josep Maria Batllori Berenguer, participated in early measurements. Together with him, we also designed the filtering cavity presented in appendix D.

---

<sup>1</sup>The definitions for these different efficiencies will be given in section 5.2.3.

## 5.2 Theoretical background

To explain thoroughly how quantum frequency conversion works, I will need to introduce some fundamental topics pertaining to the non-linear optics field. The main references I employed were Boyd's book on non-linear optics [167] and five PhD theses [146, 168–171].

### 5.2.1 Three-wave mixing

An electric field  $\mathbf{E}(t)$  impinging on a dielectric material causes a response by it which is determined by the polarization vector  $\mathbf{P}(t)$ , as will be introduced in appendix section A.1.2. In linear optics, the relationship between these two quantities is approximated with a linear relationship of the form  $\mathbf{P}(t) = \epsilon_0 \chi^{(1)} \mathbf{E}(t)$ ; nevertheless, when we consider higher order terms, we can write the polarization components as:

$$P_i(t) = \epsilon_0 \left[ \sum_j \chi_{ij}^{(1)} E_j(t) + \sum_{j,k} \chi_{ijk}^{(2)} E_j(t) E_k(t) + \mathcal{O}(\mathbf{E}^3(t)) \right] \quad (5.1)$$

Equation 5.1 describes different phenomena, depending on where it is truncated. The first sum containing  $\chi^{(1)}$  is still describing linear optics and accounts for every effect described by the complex refractive index, e.g. absorption or refraction. The term containing  $\chi^{(2)}$  starts being relevant only for very strong electric fields and it is the quadratic term describing the interactions I will deal with in this chapter. The higher-order term of equation 5.1 will be disregarded, since they are not pertinent to this discussion. Therefore, the original vector  $\mathbf{P}(t)$  can be split into the linear component  $\mathbf{P}^L(t)$  and the second-order non-linear component  $\mathbf{P}^{NL}(t)$ :  $\mathbf{P}(t) = \mathbf{P}^L(t) + \mathbf{P}^{NL}(t)$ . Normally, equation 5.1 would couple all the components of the electric field to all the components of the polarization, since  $\chi_{ijk}^{(2)}$  is a component of a 3rd-rank tensor with 27 elements. Nonetheless, by means of symmetry considerations and considering lithium niobate ( $\text{LiNbO}_3$ ), it can be demonstrated [168, 172] that only the  $d_{33}$  plays an important role, due to the fact that it exceeds by one order of magnitude

the non-zero components of the  $\chi^{(2)}$  tensor. Therefore, the tensorial equation 5.1 for  $\mathbf{P}^{\text{NL}}(t)$  reduces to the scalar equation  $P_3^{\text{NL}}(t) = 2\epsilon_0 d_{33} E_3^2(t)$ .

Usually, two electric fields with respective frequencies  $\omega_s$  and  $\omega_p$  are combined inside the non-linear material, to have the total field:

$$\mathbf{E}(t) = \mathbf{E}_s(t)e^{-i\omega_s t} + \mathbf{E}_p(t)e^{-i\omega_p t} + c.c. \quad (5.2)$$

For reasons that will be cleared later, I labelled the two fields with s (signal) and p (pump). The propagation of this field in the material is related to the non-linear polarization through the scalar equation defined previously, which then holds for the third component of the sum of the two fields. Therefore, the third field  $\mathbf{E}_i(t)e^{-i\omega_i t}$  (where the subscript i stands for idler) will result from their sum—hence the name three-wave mixing for this process—and its third component can be inferred from:

$$\begin{aligned} P_3^{\text{NL}}(t) &= 2\epsilon_0 d_{33} E_{i_3}(t)^2 = \\ &2\epsilon_0 d_{33} [E_s^2 e^{-2i\omega_s t} + E_p^2 e^{-2i\omega_p t} + c.c. \\ &\quad + 2E_s E_p e^{-i(\omega_s + \omega_p)t} + c.c. \\ &\quad + 2E_s E_p^* e^{-i(\omega_s - \omega_p)t} + c.c. + \dots] \quad (5.3) \end{aligned}$$

This new field exhibits several frequency contributions: the second line of equation 5.3 describes the second-harmonic generation (SHG) process, where fields with twice the original frequency arise; the second line contains a phase with the sum of the original field frequencies, thus describing the sum-frequency generation (SFG); finally, the third line displays a phase with the difference between the two fields, accounting for difference-frequency generation (DFG). In our QFC experiment, SHG is only an additional source of noise, as I will mention in section 5.2.2. The relevant processes are SFG and DFG. We harness DFG in order to perform conversion of a signal field, with frequency  $\omega_s$ , to a converted (idler) field, with frequency  $\omega_i$ , by means of a strong pump field, with frequency  $\omega_p$ :

$$\omega_i = \omega_s - \omega_p \Rightarrow \frac{2\pi}{\lambda_i} = \frac{2\pi}{\lambda_s} - \frac{2\pi}{\lambda_p} \quad (5.4)$$

In particular, I will speak about conversion of visible 606 nm signal photons to the telecom regime, 1552 nm, by means of a infrared pump laser at 994 nm. Usually, the inverse process is also allowed in the same waveguide: the former idler photons can be up-converted by means a pump laser, performing SFG.

What is still missing is a quantitative prediction of the converted field, which will be the topic of the next section.

### 5.2.1.1 Phase-matching

So far, the only known information about the idler field is its frequency, which is either a sum or a difference of the mixing fields. In this thesis, I will not go into detail but, in order to make quantitative predictions about SFG–DFG, one can proceed by starting from equation 5.3 and solving the Maxwell equations linking the electric field to the polarization vector for the three electric fields; in order to do that, the amplitudes  $A_j(t)$ , with  $j = s, p, i$ , of the mixing fields must be used. A full treatment is provided in references [146, 167–170].

In solving this equations, the phase mismatch  $\Delta k = k_s \pm k_p - k_i$  (+ for SFG, – for DFG) plays a very important role. It represents the momentum conservation of the SFG–DFG process. As we will see, the conversion efficiency of the process depends crucially on this parameter.

In the regime where the pump is not depleted from the interaction and the signal is only partially depleted, the amplitude for the idler electric field can be expressed through an analytical form:

$$A_i(L) = \frac{2id_{33}\omega_i}{n_i c} A_s A_p^* \int_0^L e^{i\Delta k z} dz = \frac{2id_{33}\omega_i}{n_i c} A_s A_p^* \left( \frac{e^{i\Delta k L} - 1}{i\Delta k} \right) \quad (5.5)$$

under the assumptions that the crystal has a length  $L$  and that the index of refraction of the idler in the medium is  $n_i$ .

From this explicit form, a trend of the intensity of the idler field can be inferred, since it is proportional to the square modulus of  $A_i(L)$ :

$$I_i \propto |A_i(L)|^2 = L^2 \frac{\sin^2(\Delta k L/2)}{(\Delta k L/2)^2} \equiv L^2 \text{sinc}^2(\Delta k L/2) \quad (5.6)$$

The intensity of the idler field reaches a maximum for the phase-matching condition, i.e. when the difference between the field momenta vanishes:

$$\Delta k = 0 \quad (5.7)$$

Obviously, conservation of energy throughout the process (equation 5.4) should hold as well. Normally, these two conditions 5.4 and 5.7 are hardly met at the same time. Indeed, focusing on DFG, equation 5.7 can be re-written as:

$$\Delta k = \frac{1}{c}(n_s\omega_s - n_i\omega_i - n_p\omega_p) = 0 \quad (5.8)$$

with  $n_j$  respective indexes of refraction. If now the energy conservation 5.4 is plugged into equation 5.8, we can write:

$$\Delta k = \frac{1}{c}((n_s - n_i)\omega_i - (n_s - n_p)\omega_p) = 0 \quad (5.9)$$

In a normal dispersion regime, we have that  $n_s > n_i, n_p$ , so this last condition is never satisfied since  $\Delta k > 0$ . Alternatively, the birefringence of the material can be harnessed to ensure the phase-matching condition 5.7. Nonetheless, in the next section, I will focus on quasi-phase-matching, another method to approximate the phase-matching condition in many crystals.

### 5.2.1.2 Quasi-phase-matching

The quasi-phase matching technique (QPM) has been devised in order to cope with this non-null mismatch. It consists in shaping the permanent ferroelectric domains, which give rise to the non-linearity along the axis direction, in such a way that they periodically invert their direction [168]. Crystals engineered with this axis are defined as periodically poled (PP) crystals. This axis inversion causes the coefficient  $d_{33}$  defined in the previous section to change its sign periodically, compensating the wavevector mismatch. Figure 5.1 from reference [167] illustrates the effect of the periodical poling. It is apparent that the best regime is achieved in the case of

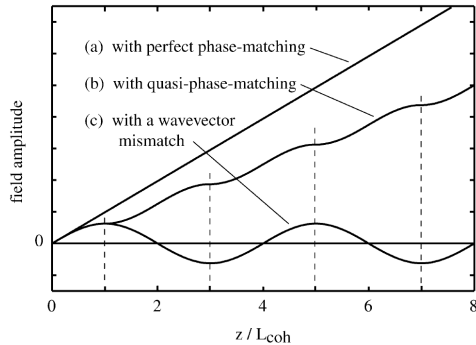


Figure 5.1: Field amplitude versus propagation length inside the medium, in units of  $L_{\text{coh}} = \pi/\Delta k$ . Curve (a) assumes the perfect mode-matching condition, predicting a linear growth of the output field amplitude. Curve (c) describes the case where the mismatch  $\Delta k \neq 0$  is not compensated, leading to an average zero amplitude. Finally, curve (b) predicts the behavior with quasi-phase-matching, showing the improvement with respect to the non-periodically-poled case. This figure is taken from reference [167].

phase-matching, but the quasi-phase-matching regime still provides a good output field amplitude.

The phase mismatch in the quasi-phase matching regime can be written as:

$$\Delta k_{\text{QPM}} = k_s - k_i - k_p - \frac{2\pi}{\Lambda} \quad (5.10)$$

where  $\Lambda$  is the poling period of the crystal axis direction  $d_{33}$ .

This poling period ensures that the wavevector mismatch vanishes. Changing the angle of the crystal and/or the temperature allows to change slightly the refractive index and thus the wavevectors and achieve a better quasi-phase-matching.

### 5.2.2 Noise processes

SFG and DFG are the processes we are interested in when dealing with quantum frequency conversion. As mentioned in the previous sections,



other processes arise from the interaction of the pump and the signal light with the non-linear material, and these processes constitute often a source of noise. As reported in reference [146], in a periodically poled lithium niobate (PPLN) waveguide, we experience three main kinds of noise:

- **Raman noise:** this type of noise is generated by the pump alone. It stretches for hundreds of nm around the pump wavelength  $\lambda_p$  [146, 171, 173, 174] and it generates both red-detuned Stokes photons ( $\lambda_{\text{Stokes}} > \lambda_p$ ) and blue-detuned Anti-Stokes photons ( $\lambda_{\text{Anti-Stokes}} < \lambda_p$ ). Nonetheless, the separation between our pump photons and our telecom photons is  $1552 \text{ nm} - 994 \text{ nm} = 558 \text{ nm}$ , therefore Raman photons are not falling within our converted signal spectrum;
- **SPDC noise:** this process happens because of small imperfections in the poling period of the crystal which cause the process to be weakly phase-matched for the pump beam [146, 174, 175]. The main effect is the splitting of pump photons into pairs of photons at longer wavelengths ( $\lambda_{\text{SPDC}} > \lambda_p$ ), potentially overlapping with both the signal and idler wavelengths in some cases [170]. Nonetheless, we only observe SPDC noise at the target converted wavelength of 1552 nm, linearly increasing with the pump power. Despite we do not observe direct SPDC noise at the signal wavelength, part of this noise is partially quasi-phase-matched for SFG and it is then up-converted to the 606 nm band by means of the pump beam; this makes the noise increase at the target wavelength sub-linear for conversion from 606 nm to 1552 nm, and quadratic for conversion from 1552 nm to 606 nm [146];
- **SHG noise:** the pump beam undergoes SHG as well, producing photons at twice its frequency. We can observe this noise by eye by injecting the pump inside our waveguide: the result is a strong blue light at 497 nm. As such, this light is unimportant when observing the converted telecom signal.

The first two noise sources are visually summarized in figure 5.2, taken from references [146, 174].

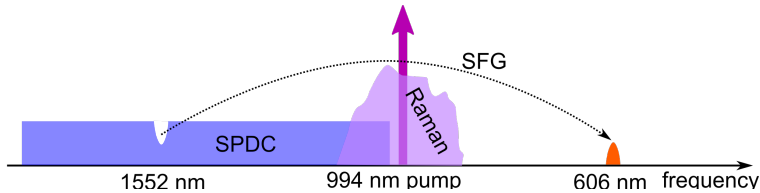


Figure 5.2: Noise processes involved in our QFC experiment. The SPDC noise pedestal stretches for hundreds of nm around the target 1552 nm wavelength. Part of this noise is back-converted to 606 nm because of SFG with the pump field. Finally, the Raman noise is not constant and falls into an interval of some tens of nm around the 994 nm pump wavelength. This figure has been reproduced from references [146, 174].

### 5.2.3 Measures of efficiency

Different efficiencies for the conversion process can be defined, depending on the context in which we are employing them.

The internal efficiency  $\eta_{\text{int}}$  is the bare conversion efficiency inside the non-linear crystal. It can be estimated by measuring the ratio between the measured output converted power  $P_{\text{out}}^i$  and the coupled input power  $P_{\text{in}}^s$  and compensating for all the measurable losses (coupling losses, absorption/transmission losses) and for the wavelength of the beams:

$$\eta_{\text{int}} = \frac{P_{\text{out}}^i}{P_{\text{in}}^s} \frac{\lambda^i}{\lambda^s} \quad (5.11)$$

This quantity can also be estimated by measuring the depletion of the signal beam, which is defined as:

$$\eta_{\text{int}} = 1 - \frac{P_{\text{out}}^s}{P_{\text{out}}^s(P=0)} \quad (5.12)$$

where  $P = 0$  indicates no pump power. Basically, the depletion efficiency can be calculated with a measurement of the output signal power when the pump is switched on and another one with the signal output power when

the pump is turned off. Since this ratio does not require a measurement of losses, it is usually the most practical way of estimating  $\eta_{\text{int}}$ .

A theoretical expression for the internal efficiency as a function of pump power  $P$  and waveguide length  $L$  can be expressed as [176]:

$$\eta_{\text{int}} = \sin^2(L\sqrt{\eta_n P}) \quad (5.13)$$

In this expression, there is a free parameter  $\eta_n$ , the so-called normalized efficiency. Its physical meaning is associated to how efficiently the waveguide can convert signal light in units of power and length squared: therefore, it is usually expressed in  $\% \text{ W}^{-1} \text{ cm}^{-2}$ .

The external efficiency  $\eta_{\text{ext}}$  is often defined as the efficiency from input to output of the waveguide, accounting for coupling losses  $\eta_{\text{coupl}}$  and absorption/transmission losses  $\eta_{\text{int-loss}}$  through the mode-matching lenses or the waveguide. As such, it is related to the previously defined internal efficiency through:

$$\eta_{\text{ext}} = \eta_{\text{int}}\eta_{\text{coupl}}\eta_{\text{int-loss}} \quad (5.14)$$

The device efficiency  $\eta_{\text{dev}}$ , finally, is usually the “fiber-to-fiber” efficiency, accounting for all the losses on the path:

$$\eta_{\text{dev}} = \eta_{\text{ext}}\eta_{\text{loss}} \quad (5.15)$$

### 5.3 Experimental setup

To perform our quantum frequency conversion experiments, we employed two different waveguides. The first one is the same employed in Maring’s PhD thesis [146]. It is a PPLN waveguide, 1.4 cm long, fabricated by HC Photonics. The second waveguide is a PPLN waveguide as well, 4.8 cm long, manufactured by NTT. I will speak about the older waveguide in section 5.3.1 and about the newer waveguide in section 5.3.2.

Two lasers were employed in the experiment: the signal laser at 606 nm and the pump laser at 994 nm. Both lasers will be described in appendix B.

The telecom detector employed for the single-photon-level measurements is a ID Quantique ID230 (20  $\mu\text{s}$  dead time, 10 % detection efficiency, around 5 Hz dark count rate).

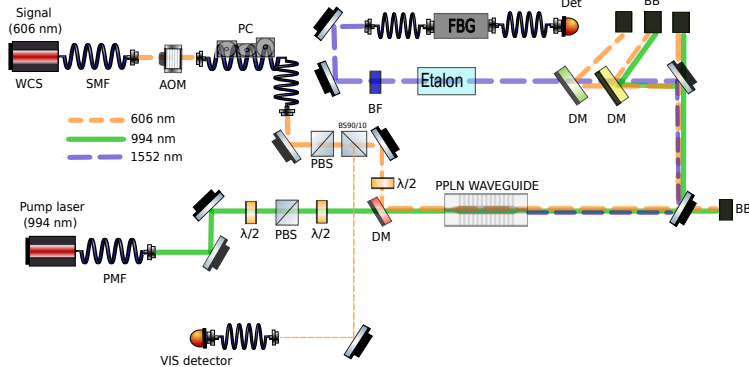


Figure 5.3: QFC setup. The 606 nm laser (orange beam) is diffracted by an AOM and coupled to a polarization controller (PC). The horizontal component is let through by a PBS, and split with a 90:10 BS in two separate beams: the 10% component is sent to a SPD (when dealing with weak coherent states), while the 90% component is transmitted, adjusted to match the right conversion polarization and sent to the waveguide. The 994 nm laser, whose polarization is adjusted to be matching the one of the waveguide through a HWP+PBS+HWP system, is transmitted by a dichroic mirror which instead reflects the signal light, and coupled into the waveguide. The in-coupling and out-coupling lenses are both by Thorlabs: the first one is a A110-TME-B lens, whereas the second one is a A110-TME-C lens. Inside the waveguide the signal light gets converted to 1552 nm through DFG. The light is then coupled out and sent to the filtering stages described in section 5.3.2.1.

### 5.3.1 First waveguide

The first waveguide is a HC Photonics ridge waveguide<sup>2</sup> embedded inside a lithium niobate crystal, and it was used in DFG and SFG experiments of our

<sup>2</sup>A ridge waveguide is a waveguide whose guiding structure is provided by a ridge, inside which the light is guided because of the difference in index of refraction between the ridge material and the air.

group [18, 177] with signals at respectively 606 nm or 1552 nm. The crystal dimensions were 14 mm (L) $\times$ 0.5 mm (W) $\times$ 1.5 mm (T). Only one waveguide was etched in this crystal.

The waveguide converts only a specific linear polarization component of the input beams, so for each laser we always need to use a PBS in order to clean and a half-wave plate in order to adjust the polarization.

In December 2020, we accidentally burned one of the facets of the waveguide, and we had it repaired by HC Photonics. After the repolishing procedure, the crystal length was reduced to 13.3 mm.

The crystal was glued on top of a copper mount with silver paste. The copper mount was attached to two Peltier stages, a more powerful one which was providing most of the heat and a weaker one, controlled by a home-made PID system, in order to keep the waveguide at temperatures around 65 °C. XYZ translators provided the capability of moving the aspherical lenses at the input and output of the waveguide in all the desired directions. The crystal itself could be translated, perpendicularly to the waveguides in the Y direction, through a coarse translator. The setup employed with this waveguide is visible in figure 5.3.

### 5.3.2 Second waveguide

The second PPLN waveguide was made by NTT, and was purchased because of the previous demonstrations of its high performances [178]. Our waveguide model is WS-0606-000-A-C-C-TEC and the chip dimensions are 48 mm (L) $\times$ 2 mm (W) $\times$ 0.5 mm (T). There are three pairs of ridge waveguides inside the crystal and the poling period is different for each pair: 10.2  $\mu\text{m}$  (first), 10.225  $\mu\text{m}$  (second) and 10.25  $\mu\text{m}$  (third). The core size of the waveguides is  $10 \mu\text{m}_{-1.5 \mu\text{m}}^{+1 \mu\text{m}} \times 11 \mu\text{m}_{-1.5 \mu\text{m}}^{+1 \mu\text{m}}$ . To stabilize the waveguide temperature, we purchased a programmable temperature controller (PTC10) from Stanford Research Systems, which provides a PID stabilization. The translation stage where this new waveguide chip is mounted on is exactly the same as the previous one's. Analogously to the old waveguide, in this waveguide the DFG process requires a specific polarization of the beams. A scheme of the waveguide is visible in figure 5.4, and the setup

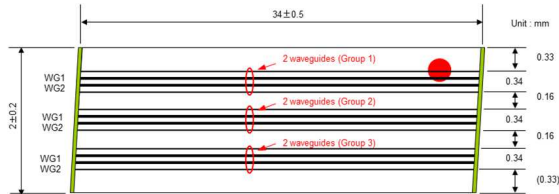


Figure 5.4: NTT waveguide scheme for our model WS-0606-000-A-C-C-TEC, taken from the manual. As it can be seen from the scheme, the chip contains three pairs of waveguides, each pair with  $0.34$  mm width and with  $0.16$  mm separation between each other.

in which the waveguide is being used is visible in figure 5.3 (where this waveguide was installed in the place of the old waveguide).

As I mentioned, the conversion efficiency of this latter waveguide has proven to be superior to the old waveguide one. This will be shown in detail in section 5.4.2.

### 5.3.2.1 Filtering stages

The filtering stages used to remove the residual pump and signal beams and to filter the telecom noise floor down are shown in figure 5.3, except for the second bandpass filter.

The common elements to both are a pair of dichroic mirrors, an etalon and two bandpass filters. The two dichroic mirrors are meant to filter the transmitted pump and signal out. The first two mirrors at the output of the waveguide are optimized for reflecting at telecom wavelength. Therefore, the remaining pump and signal beams undergo large transmission losses. The first dichroic mirror is a Thorlabs DMLP1180 mirror. From our characterization, its reflectivity for the  $994$  nm pump and  $606$  nm signal is respectively  $98.6\%$  and  $72\%$ , which implies that this mirror is meant to eliminate most of the pump signal. In series, a Thorlabs DMLP650 mirror is installed, in order to remove every residual beam but the idler. This mirror reflects  $98\%$  of the signal and  $0.4\%$  of the pump. Usually, we mea-

sure the depletion efficiency of our signal defined in section 5.2.3 by picking up the reflected signal beam from this mirror. These two mirrors globally transmit 95 % of the converted 1552 nm idler signal.

After the dichroic stage, an etalon (made by SLS Optics) is installed. This etalon has a FWHM of 210 MHz and a FSR of 4 GHz, with 95 % theoretical transmission, although we never reached anything higher than 82 % when measuring. The etalon is stabilized in temperature by a home-made PID. Then, two bandpass filters, a NIR01-1550/3-25 by Semrock centered at 1550 nm (transmission above 90 % within  $\pm 3$  nm) with around 8.8 nm FWHM bandwidth and a Thorlabs longpass filter FELH1450 with cut-off wavelength at 1450 nm, reduce further the telecom noise not centered around the wavelength of converted light. A fiber Bragg grating (FBG) is cascaded to the bandpass filters. This device is stabilized in temperature and has a bandwidth of 2.5 GHz, with a maximum 65 % transmission depending on the temperature it is stabilized at.

## 5.4 Experiment

In the following sections, the fundamental steps towards the conversion of  $\mu$ s-long photons with high SNR will be reported. We performed those steps with both waveguides, achieving much better results with the NTT one. This waveguide boosted the SNR we were able to attain, confirming the feasibility of interfacing a DLCZ-based quantum node with material nodes working at a different wavelength by converting photons with this specific quantum frequency converter.

### 5.4.1 HC Photonics waveguide

The first waveguide we employed was the one described in section 5.3.1. In his PhD thesis [146], Dr. Nicolas Maring, using the same device, reported a maximum internal conversion efficiency of 59 %, achieved with a coupled pump power of 415 mW. By fitting the internal efficiency as a function of the coupled pump power with the formula 5.13 reported in section 5.2.3, he obtained a conversion efficiency of  $(94 \pm 1) \% \text{ W}^{-1} \text{ cm}^{-2}$ . He commented

that this quantity cannot be estimated very precisely due to the change of phase-matching condition induced by the local heating caused by the pump power. To avoid that, small tweaks to the overall waveguide temperature or to the 606 nm light alignment into the waveguide have to be applied to compensate for this warming. In addition, the 606 nm light is multimode in this waveguide. Since the refractive index changes slightly with the temperature, the modal overlap between the 606 nm light and the 994 nm light changes, leading to a change in efficiency.

In the next section, we will see our achievements with this setup, shown in figure 5.3.

#### 5.4.1.1 Estimation of $\alpha$

As a first thing, we wanted to estimate the pump-induced noise affecting the conversion process. To this aim, we proceeded with a measurement of a parameter that we call  $\alpha$ , which estimates the linear trend of the telecom noise induced by the pump beam (mainly SPDC noise, as explained in section 5.2.2); this noise process starts saturating when approaching high pump powers because part of the telecom noise is converted to 606 nm, as mentioned in the same section.

I will be following the same treatment as in references [146, 179]. To measure this quantity, we installed the filtering stages of section 5.3.2.1, we injected only the pump beam inside the waveguide, and then calculated the signal that would have been measured directly at the output of the waveguide based on previously characterized absorption and coupling losses. Since no signal was coupled to the waveguide, the only output signal at 1552 nm was telecom SPDC noise. The losses experienced by the telecom beam were due to the partial transmission of all the stages crossed along its path: the transmission  $T_{\text{dichr}}$  of the dichroic mirrors, which was 95 %; the etalon transmission  $T_{\text{eta}}$ , which averaged out to 81.5 %; the fiber Bragg grating transmission  $T_{\text{FBG}}$ , around 61 %; and, finally, the fiber coupling  $\eta_{\text{fb}} = 76.5\%$  and the detector efficiency  $\eta_{\text{det}} = 10\%$ . Besides this,  $\alpha$  is estimated over 1 GHz and in  $\text{cm}^{-1}$ , to facilitate the comparison between different setups and devices. Since the narrowest bandwidth filter is the



etalon, whose bandwidth is 210 MHz, to normalize  $\alpha$  over 1 GHz, we divide the experimental value by the ratio  $\frac{\Delta_{\text{Eta}}}{\Delta_{\alpha}} = \frac{210 \text{ MHz}}{1000 \text{ MHz}} = 0.21$ . The last step is dividing it by the length of the waveguide  $L$ , which is 1.39 cm. Finally, we compute the amount of noise counts by recording time stamps, selecting a time window and considering the number of counts in that specific window.

To back-propagate the signal, this amount of detections must be divided by the product  $T_{\text{dichr}} \cdot T_{\text{eta}} \cdot T_{\text{FBG}} \cdot \eta_{\text{fib}} \cdot \eta_{\text{det}} \cdot \frac{\Delta_{\text{Eta}}}{\Delta_{\alpha}} \cdot N_{\text{trig}} \cdot \Delta t$ , where  $N_{\text{trig}}$  is the number of triggers, sent at 10 kHz rate, and  $\Delta t$  is the time window, normally 20  $\mu\text{s}$ .

Figure 5.5 displays the result of the measurement of the telecom noise rate as a function of coupled pump power. The purple dashed line, which is a linear fit to the first 3 out of 8 points, highlights that the trend is linear at the beginning, but then it saturates for high pump power due to the re-conversion of noise to 606 nm, thus the experimental points lie below this line. In the inset, another linear fit to three points recorded at low power is shown. Note that these points belong to another set of data. This fit provides a value of  $\alpha$ , over a 1 GHz interval, around  $\alpha = 58 \text{ kHz mW}^{-1} \text{ cm}^{-1}$ . This value is comparable to the value of  $\alpha$  reported by Dr. Nicolas Maring in his PhD thesis [146]<sup>3</sup>.

#### 5.4.1.2 SNR and $\mu_1$ vs input number of photons

One of the most useful figures of merit employed to estimate the quality of a frequency converter is  $\mu_1$ . As introduced in section 1.3.1,  $\mu_1$  is the mean number of photons to send as an input to the converter to get a signal with a SNR of 1 in output. In the case of heralded single photons coming from a DLCZ experiment, the probability of having a photon at the input of the frequency converter, conditioned on the detection of a Stokes photon, is given by the heralding efficiency of the source  $\eta_{\text{her}}$ . Simulating these photons with weak coherent states implies sending pulses with a mean

<sup>3</sup>In his case, this value was  $76 \text{ kHz mW}^{-1} \text{ cm}^{-1}$ . Nonetheless, he measures the pump coupled into the waveguide, rather than the pump in front of the waveguide, so his value accounts for the 75% pump transmission of the out-coupling C-coated lens. Indeed, the discrepancy between the two values is around 75%.

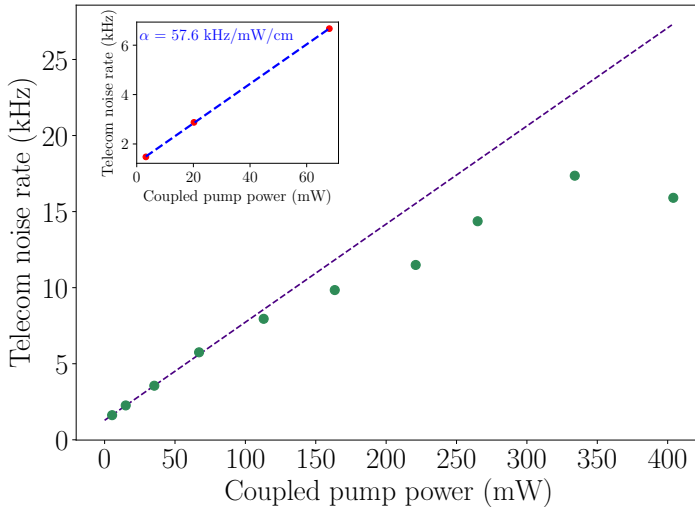


Figure 5.5: Rate of telecom noise as a function of the pump power for 8 different values of pump power. Note that the linear fit works very well for low pump powers, but fails to predict the saturation effect we observed for high pump powers. In the inset, a zoom on the low pump power region is shown. Note that the inset belongs to a different set of data. The linear fit highlights the linear behavior of the trend and enables to estimate the  $\alpha$  value. In this case, the fit yields a value of  $\alpha$  around  $58 \text{ kHz mW}^{-1} \text{ cm}^{-1}$  per GHz.

photon number  $\mu_{\text{in}}$  equal to the heralding efficiency  $\eta_{\text{her}}$ <sup>4</sup>.  $\mu_1$  can be written as

$$\mu_1 = \frac{\mu_{\text{in}}}{\text{SNR}} \quad (5.16)$$

Experimentally,  $\mu_1$  is measured by varying the input number of photons  $\mu_{\text{in}}$  in front of the waveguide and fitting them linearly, such as to obtain a

<sup>4</sup>Here we are in a regime where  $\eta_{\text{her}} \ll 1$ ; when this quantity approaches one, the multi-photon components of weak coherent states are not negligible anymore and thus this equivalence does not hold.

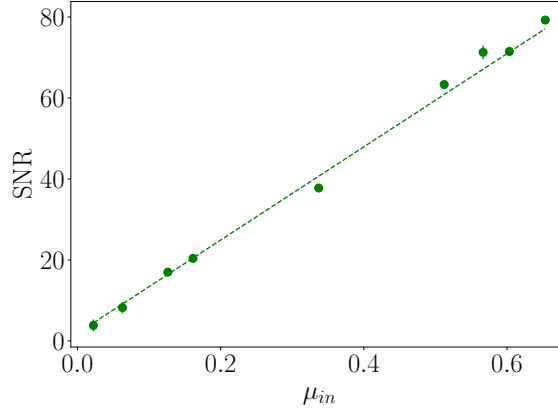


Figure 5.6: SNR as a function of the mean number of photons per pulse  $\mu_{in}$ . Pulses are 160 ns long and the time window covers the whole pulse (450 ns). From this curve, we inferred a  $\mu_1$  value of  $(8.7 \pm 0.3) \times 10^{-3}$ .

slope whose inverse is precisely  $\mu_1$ . In figure 5.6, I report this measurement performed with the older HC Photonics waveguide. The output photons were filtered by means of the filtering stages described in section 5.3.2.1. We were sending 160 ns-long Gaussian pulses (FWHM), considering a window as long as our entire pulse (450 ns). From this measurement, we inferred a  $\mu_1$  value of  $(8.7 \pm 0.3) \times 10^{-3}$  for our device. This certifies that our device is capable of operating in the quantum regime. Nevertheless, we need to be able to convert long pulses, and therefore to analyze the trend of  $\mu_1$  versus pulse length. This will be the topic of the next section.

#### 5.4.1.3 SNR and $\mu_1$ vs pulse length

What we were mostly interested in was the estimation of  $\mu_1$  as a function of pulse length, for a fixed number of photons per pulse. Enlarging the pulse length increases the noise, as we need to increase the signal window and more noise gets included, whereas the signal intensity stays constant. Obviously, the SNR also depends on the amount of filtering the output

undergoes and on the external conversion efficiency.

Our measurement of  $\mu_1$  as a function of the pulse duration can be seen in figure 5.7. To carry out this measurement, we sent Gaussian weak coherent pulses with less than one photon per pulse: this number was changing from case to case but we always re-normalized all the sets of measurements in order for them to be photon-number independent. The temporal pulse length was ranging from 160 ns to 4  $\mu$ s. The window considered encompassed the whole pulse. The filtering stages were the same mentioned in the previous section and in section 5.3.2.1. By fitting the experimental points with a line, we inferred a  $\mu_1$  value of 0.05/ $\mu$ s, which implies  $\mu_1 = 0.03$  for the typical duration of our DLCZ photons (700 ns). I will discuss this result in section 5.4.1.5.

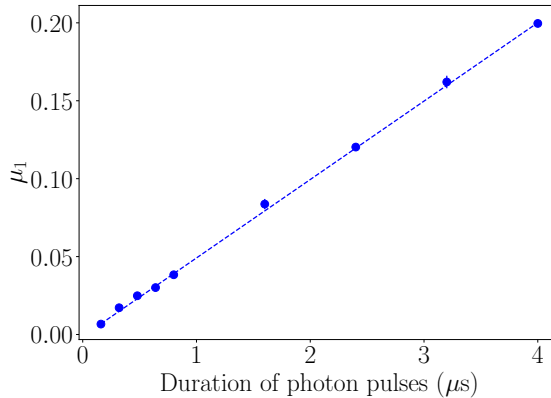


Figure 5.7:  $\mu_1$  as a function of the pulse length. The estimated value of  $\mu_1$  per second was 0.05/ $\mu$ s, calculated by fitting the experimental points (blue) with a line (dashed blue line). For a 700 ns-long pulse, which is the length of our DLCZ photons, this value yields  $\mu_1 = 0.03$ . The considered windows contain the whole pulses.

#### 5.4.1.4 Internal efficiency and $\mu_1$ vs pump power

To conclude the discussion about the old waveguide, we are missing the behavior of the conversion efficiency and the SNR when changing the pump power coupled inside it.

As already introduced in section 5.2.3, the internal efficiency depends on the pump power. Figure 5.8 shows this behavior for some points, and the fit predicting the saturation due to back-conversion I have been explaining throughout this chapter. The fit also predicts a value of  $\eta_m$  of  $61.4\% \text{ W}^{-1} \text{ cm}^{-2}$ . A growth in the internal efficiency  $\eta_{\text{int}}$  means a decrease in  $\mu_1$ . This can be seen in figure 5.9, where the behavior of  $\mu_1$  versus coupled pump power inside the waveguide is shown. To measure this curve, we sent 180 ns long weak coherent Gaussian 606 nm pulses, with around 0.023 photons per pulse. We estimated  $\mu_1$  by measuring the number of photons  $\mu_{\text{in}}$  in input, upon detection of 1/105 (including the 50% detection efficiency) of the light in front of the waveguide with a visible single-photon detector (Laser Component 100C-FC), and dividing this number by the SNR of the detected converted telecom photons.

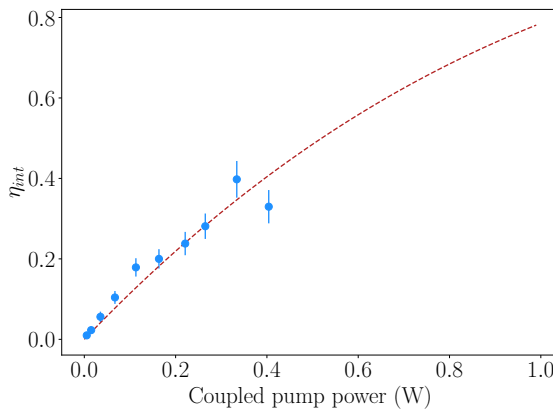


Figure 5.8:  $\eta_{\text{int}}$  as a function of the coupled pump power for some experimental points. The fit shows the expected saturation effect for high pump power, predicting a normalized efficiency of  $61.4\% \text{ W}^{-1} \text{ cm}^{-2}$ .

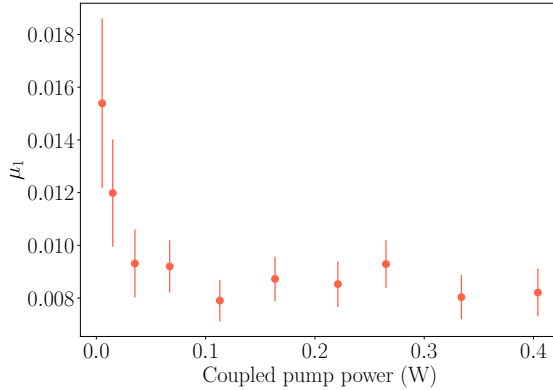


Figure 5.9:  $\mu_1$  as a function of increasing pump power.  $\mu_1$  was directly measured by estimating the number of 606 nm input photons in front of the waveguide ( $\mu_{\text{in}}$ ), and dividing this number by the SNR of the detected telecom counts.

#### 5.4.1.5 Discussion for the HC Photonics waveguide

In summary, the device efficiency  $\eta_{\text{dev}}$  achieved with this waveguide was about 9% (including all the filtering system), while the internal efficiency  $\eta_{\text{int}}$  was about 40%, measured via the depletion of the signal. By changing the duration of the input pulses to the converter, we carried out a measurement of  $\mu_1$  which yielded a value of  $0.05/\mu\text{s}$ . Hence, for the typical length of the single photons emitted by our AFC-DLCZ quantum memory (700 ns), the corresponding  $\mu_1$  value was about 0.03. This result is still too large to convert signals of about 0.016 photons per pulse with high SNR, corresponding to the 1.6% heralding efficiency of our DLCZ experiment reported in chapter 3. For photon durations of  $4\mu\text{s}$  (corresponding to a frequency bandwidth of 110 kHz, which may be accessible with trapped ions), the  $\mu_1$  was around 0.2. Even in the ideal case of unity memory read-out efficiency, the achieved  $\mu_1$  value would allow a maximum SNR of around 5 for  $4\mu\text{s}$  long photons. Therefore, the filtering and/or the conversion effi-

ciency must be improved. As I will show from section 5.4.2 on, we improved on both these parameters: this waveguide was outperformed by the newer NTT waveguide, so we switched to it for continuing the experiment.

### 5.4.2 NTT waveguide

The second waveguide is the one described in section 5.3.2. It is currently installed in the setup and was purchased in 2021. This waveguide outperformed the old HC Photonics one: we were able to observe internal conversion efficiencies above 80%, measured via depletion of the 606 nm signal. The device efficiency, with the filtering stages introduced in section 5.3.2.1, was of 27%. The measured normalized conversion efficiency  $\eta_n$  from formula 5.13 reported in section 5.2.3 was around  $(79.21 \pm 0.04) \% \text{W}^{-1} \text{cm}^{-2}$ , an improvement compared to the same efficiency measured for the old waveguide in section 5.4.1.4. This is shown in figure 5.10. The employed setup was basically the same one of figure 5.3, with the only replacement of the waveguide.

#### 5.4.2.1 SNR and $\mu_1$ vs input number of photons

As a first measurement, we repeated the measurement of section 5.4.1.2 with the new waveguide. This allowed us to estimate  $\mu_1$  for 180 ns-long Gaussian pulses. In figure 5.11, I am reporting the outcome of our measurement. This was performed by measuring the real  $\mu_{\text{in}}$  with a SPAD detector (the same used in chapter 4, PerkinElmer SPCM-AQR-16-FC), which was detecting 1/59 of the signal (excluding detection efficiency, which was around 60%), and dividing it by the SNR of the detected telecom photons. From this measurement, we extrapolated a  $\mu_1$  value of  $(1.1 \pm 0.5) \times 10^{-3}$ , which is almost 8 times lower than the measurement with the old waveguide reported in section 5.4.1.2. The filtering stages were the same reported in section 5.3.2.1.

We have not performed a measurement of  $\mu_1$  versus pulse length; however, we can infer the likely outcome from this measurement. Indeed,  $\mu_1 = (1.1 \pm 0.5) \times 10^{-3}$  for 180 ns-long pulses implies a value of  $\mu_1$  per

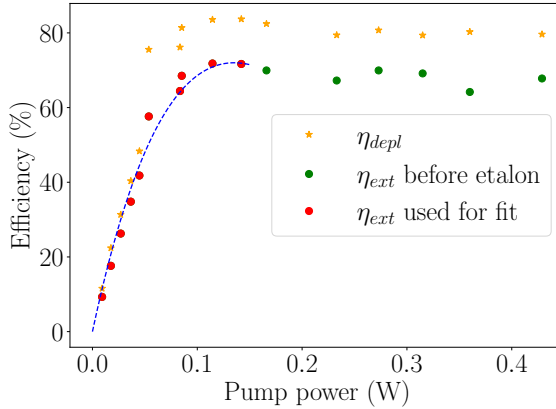


Figure 5.10:  $\eta_{depl}$  and two different  $\eta_{ext}$  as a function of the coupled pump power for some experimental points. The fit is performed on the first points of  $\eta_{ext}$ , for a better representation of the experimental data, and is predicting a normalized efficiency of  $(79.21 \pm 0.04) \% \text{ W}^{-1} \text{ cm}^{-2}$ .  $\eta_{depl}$  should coincide with  $\eta_{int}$ . We observe saturation to high pump powers in the experimental sets of efficiencies; however, we do not observe back-conversion and, as a consequence, a decrease in efficiency with high pump power.

pulse length of  $6.1 \times 10^{-3} \mu\text{s}^{-1}$ . With this value, the SNR of conversion for a  $1 \mu\text{s}$ -long single photon would be almost 164. Accounting for our low DLCZ heralding efficiency of 1.6%, mentioned in section 5.1 and in chapter 3, we can expect a SNR of  $1.6\% \times 164 = 2.6$ . This is already sufficient to generate quantum correlations between a converted telecom photon and a stored spin wave with our current experimental conditions. However, in practice, we need higher SNRs for applications in quantum communications and, to this aim, we will need an additional filtering stage, represented by the filtering cavity of appendix section D.1.1.



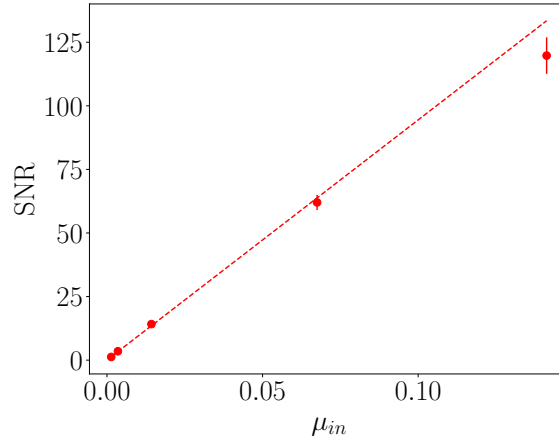


Figure 5.11: SNR as a function of the mean number of photons per pulse  $\mu_{in}$ . Pulses are 180 ns long and the window covers 2 FWHMs (360 ns). From this curve, we inferred a  $\mu_1$  value of  $(1.1 \pm 0.5) \times 10^{-3}$ .

## 5.5 Discussion and outlook

To sum up the results presented throughout this chapter, we were able to demonstrate the feasibility of an experiment of conversion of long weak coherent pulses mimicking the photons emitted by a AFC-DLCZ scheme. In particular, this has proven to be feasible with the NTT waveguide, where the current performances would already allow the observation of non-classical correlations, and where a factor 10 of improvement with respect to the current  $\mu_1$  value of  $6.1 \times 10^{-3} \mu\text{s}^{-1}$  is expected to come from the installation of a filter cavity, described in appendix section [D.1.1](#). In contrast, for the first waveguide,  $\mu_1$  was too low to allow for any additional filters to enhance the SNR.

This experiment demonstrates that interfacing a DLCZ experiment like the one described in chapter [3](#) of this thesis with the telecom band is feasible, thus providing a platform that can emit entangled pairs of photons, consisting of a visible photon and a telecom-fiber-compatible photon. Upon

up-conversion of this latter photon, interfacing a DLCZ experiment with trapped ions (which have a narrow bandwidth of the order of 100 kHz that is compatible with the linewidth of long DLCZ photons [101]) becomes feasible with current state-of-the-art waveguides, even in the case of heralding efficiencies as low as 1.6 %, like in our case. Certainly, a necessary step to achieve large conversion rates lies in the improvement of the DLCZ read-out efficiency, as mentioned in chapter 3 and in reference [100], and of conversion SNRs.

In conclusion, we have shown that a quantum interface enabling quantum correlations between a telecom photon and a solid-state emissive quantum memory is feasible. In addition, the results achieved show the feasibility of interfacing solid-state quantum memories and single trapped ions by way of a telecom photon.



## Chapter 6

# Conclusions and outlook

This chapter contains a summary of the results presented in chapters 3, 4 and 5, and a possible outlook for each of the experiments. The impedance-matched-cavity experiment is partially related to the AFC-DLCZ experiment, which is in turn strictly linked to the QFC experiment, so their outlooks will overlap.

### 6.1 Main results of the thesis

The first result we accomplished was the implementation of a multimode solid-state quantum memory working as a source of entangled photons, based on the AFC-DLCZ protocol implemented in a  $\text{Pr}^{3+}:\text{Y}_2\text{SiO}_5$  crystal. This system possesses the capability of storing the second photon of a pair and releasing it on-demand. This result was published in Physical Review Letters [53]. The main limitation of this experiment consisted in the limited read-out efficiency, as low as 1.6%, decreasing the countrate and limiting the applicability in a real quantum network scenario.

The main part of the thesis was then devoted to the realization of a cavity-enhanced high-efficiency quantum memory, by which we demonstrated the highest efficiency achieved so far with the AFC protocol. The storage efficiency for weak coherent single pulses was as high as 62% (the

previous record was 56 % [87]). Furthermore, our result was achieved for storage at the single photon level. With the same setup, we accomplished the most efficient storage of qubits in a solid-state quantum memory up-to-date, with a 52 % storage efficiency. We analyzed the fidelity of our quantum memory by measuring the output qubit state in different bases by means of an AFC-based unbalanced Mach-Zehnder interferometer and assessed a near-unity fidelity of our memory.

Finally, we proved the feasibility of a quantum frequency conversion experiment involving  $\mu\text{s}$ -long weak coherent pulses mimicking the single photons emitted in an AFC-DLCZ experiment. The achieved  $\mu_1$  of conversion was  $6.1 \times 10^{-3} \mu\text{s}^{-1}$  which, combined with the already mentioned heralding efficiency of our AFC-DLCZ experiment of 1.6 %, would permit us to convert 1  $\mu\text{s}$ -long photons with a SNR of 2.6. This value could be improved by using a narrower spectral filter, e.g. the filter cavity we built (described in appendix D), which would presumably yield an order of magnitude improvement. The results show the feasibility of converting photons from our AFC-DLCZ source to telecom wavelengths, and open prospects for interfacing our quantum memory with other quantum systems, e.g. single trapped ions, via a telecom photon.

## 6.2 Outlook

The accomplishments of the impedance-matched cavity experiment represent the state of the art for AFC storage. For the first time, the forward retrieval limit of 54 % of AFC is surpassed at the single photon level. The next steps we will be pursuing will be spin-wave storage at the single photon level, whose preliminary results were reported in section 4.2.5, and storage of single photons, emitted by an ultra-narrow single photon source that we are currently assembling, as anticipated in section 4.3.

The presented results permit us to envision possible improvements of this experiment. First, cavity losses and the limited bandwidth arising from slow light have to be addressed. As discussed in section 4.3, a relatively easy way of reducing transmission losses would be installing a >99 % reflecting

mirror. This comes at the price of reduced locking light, so we should use a more sensitive photodetector to perform the stabilization task. As far as intra-cavity losses are concerned, we could install our cavity inside the vacuum chamber of our cryostat, to have fewer interfaces inside the cavity path. At the same time, this solution would shorten the cavity, diminishing its FSR and decreasing our sensitivity to slow-light effects. A regime of lower losses also enables us to increase the targetable  $\tilde{d}$ , thus increasing the maximum efficiency. A different method for reducing the slow-light effect in our experiment would be reducing the overall OD by using a shorter crystal: as it can be seen from equation 4.5, the change in cavity FSR, and in turn in linewidth, depends on the time spent by the light inside the crystal. This time contains a term  $\alpha L_{\text{cr}}$ , which is the crystal OD. If we use the same parameters from section 4.2.4.1 but we assume  $L_{\text{cr}} = 2$  mm, the slow-light FSR increases to 13.9 MHz, which gives a linewidth of 2.1 MHz. Not only would this change lead to less sensitivity to absorption changes, but it would also diminish the comb background absorption. Nevertheless, once we opt for a certain value of  $\tilde{d}$ , we aim at the highest AFC finesse we can achieve with the available OD, and usually the procedure for addressing high finesse reduces further the comb OD. Hence, we might find out that the OD of a shorter crystal is not enough to guarantee the balance between the right  $\tilde{d}$  and a high  $\mathcal{F}_{\text{AFC}}$ .

Adopting all the aforementioned solutions would enable us to achieve the highest efficiency with the current parameters. If we assume some optimal parameters for the current cavity, such as  $R_{\text{out}} = 99.9\%$ ,  $\mathcal{F}_{\text{AFC}} = 10$ , and 1% double-pass losses, our achievable efficiency would reach 88%. This efficiency is very high, but we can aim at the  $> 90\%$  regime by decreasing our  $\tilde{d}$  and thus increasing the reflectivity of the first mirror. Indeed, by using the same parameters, but targeting the optimal value of  $\tilde{d} = 0.25$ , the efficiency would grow up to 90.6%. The resulting cavity would have a higher finesse, since  $R_{\text{in}} = R_{\text{out}} \exp(-2\tilde{d}) = 60.6\%$ , hence  $\mathcal{F}_{\text{cav}} = 12.5$ . In general, aiming at very low values of  $\tilde{d}$  would result in high finesse cavities, which would then be more affected by losses and stability issues.

Efficiency is not the only parameter we would like to improve. In our group, we are currently working on spatially multiplexed solid-state quan-

tum memories. We envision two different methods for spatial multiplexing the impedance-matched cavity memory. The first one is usually performed in cold atomic ensembles [44, 98], and consists in addressing different spatial points of the crystal: we could prepare AFCs in different positions of the same crystal, installing impedance-matched cavities around these points. A different approach, proposed in reference [180], addresses the orthogonality of spin-waves that we can write-in in the ensemble: by an appropriate choice of the control pulses of spin-wave storage, one could map several modes sent to the cavity into a superposition of orthogonal spin-waves. At a later time, a specific read-out for each of them, performed with the same choice as the write-in, would lead to re-emission of the same stored modes.

Storage time is another figure of merit of paramount importance in quantum memories. In principle, impedance-matched cavity quantum memories are compatible with the implementation of dynamical decoupling techniques to extend the storage time.

The impedance-matched experiment could be interfaced with our AFC-DLCZ experiment to enhance the read-out efficiency of the latter experiment. As stated in sections 3.3.2 and 4.3, the theoretical approach followed in reference [86] is time-reversible, meaning that both absorption efficiency and read-out efficiency are boosted. As such, we would expect our cavity to be extremely beneficial to a potential AFC-DLCZ scheme. The experiment requires no major amendments of the current setup, but the write and read beam should be counter-propagating (section 3.2.1.1).

As far as the AFC-DLCZ experiment is concerned, I have already highlighted the low 1.6% retrieval efficiency. The main causes for this low efficiency come from an imperfect AFC preparation, from the limited OD, from the spin decoherence affecting the stored spin-wave and from the background noise in the heralding photon. On the one hand, increasing the OD is equivalent to embedding the crystal in an impedance-matched cavity, as I have just said, with the advantage of potentially overcoming the 54% limitation. On the other hand, this experiment was carried out with the older 606 nm laser described in appendix section B.1.1, which also had a wider linewidth. Therefore, we are currently able to shape much better AFCs, with higher finesse and less absorption background.

Any improvements on the heralding efficiency of the AFC-DLCZ experiment would have repercussions on the QFC experiment. In this latter work, the main limitation is given by the low SNR with which photons are converted to the telecom band. The SNR can be enhanced either by increasing the signal or by decreasing the amount of noise falling within the signal window. We will pursue both approaches, starting from the reduction of noise via the filter cavity we installed in our setup (described in appendix D). With the help of this additional filtering stage, we are aiming at improving the SNR by a factor 10. As far as the signal is concerned, improvements in the heralding efficiency would be equivalent to an increase in the mean photon number per pulse  $\mu_{\text{in}}$ , thus yielding a better SNR, for the same pulse length.

It must be remarked that our AFC-DLCZ experiment already enables the distribution of entanglement over distances of a few kilometers, despite the low heralding efficiency. Moreover, the SNR obtained in our QFC experiment allows for preservation of quantum correlations between the heralded photon and the converted heralding photon of the entangled photon pair, even with the current read-out efficiency of the AFC-DLCZ experiment. Therefore, we can envision that, by combining the AFC-DLCZ with the impedance-matched cavity experiment, we can boost the heralding efficiency of the experiment, thus enhancing the SNR of conversion of the Anti-Stokes photon. The three experiments merged together could represent a highly efficient quantum node that can be interfaced with the telecom band thanks to our conversion capabilities, thus satisfying two of the main criteria listed in section 1.3. Furthermore, there is no intrinsic limitation to the extension of memory storage time, neither from the AFC-DLCZ experiment nor from the impedance-matched experiment, that is preventing us from extending it to the tens of ms regime.

The synergy of the combined AFC-DLCZ, QFC and impedance-matched-cavity experiments could concretely lead to an efficient AFC-based quantum node to be employed in future quantum networks. Whether this would be realistic or not depends mainly on the success of a cavity-assisted AFC-DLCZ experiment, which has never been performed before but is definitely within our reach in the next future.





# Appendix A

## Theory of two-pulse photon echoes

### A.1 Optical echoes

Throughout this section, I will be dealing with optical echoes. This topic has already been briefly illustrated in section 2.1.2.6, and here I will provide a full theoretical treatment. Optical echoes, also called photon echoes, are an example of how a physical system can spontaneously recover from a decay. The first description was provided for nuclear spins by Hahn [67], who described a method for magnetizing an ensemble of atoms with a first pulse and reverse the magnetization decay through a second pulse. This technique was applied a few years later to  $\text{Cr}^{3+}$  in ruby, leading to the first observation of optical echoes [181, 182].

The treatment I will be presenting throughout this section is following rigorously reference [183]. It is entirely based on basic quantum mechanics and does not require any advanced knowledge of solid-state physics. A semi-classical theory of light-matter interaction is assumed, where atoms are quantum objects, while light is a classical electromagnetic wave.

### A.1.1 Two-level atom interacting with light

The first result I want to derive, following reference [183], is an expression of the atomic states of a single atom after an optical pulse has been shone. To do so, we consider an atom placed at a position  $\mathbf{r}$ , with two possible states: a ground state  $|g\rangle$  with zero energy and an excited state  $|e\rangle$  with  $\hbar\omega$  energy. Both states are eigenstates of the Hamiltonian  $\hat{H}$  of the system. The pulse is an electromagnetic wave of the form:

$$E(\mathbf{r}, t) = \begin{cases} 0 & t < t_i \\ E_0 \cos(\omega_L t - \mathbf{k} \cdot \mathbf{r}) & t_i \leq t \leq t_i + t_p \\ 0 & t > t_i + t_p \end{cases} \quad (\text{A.1})$$

where  $\omega_L$  is close to the angular frequency  $\omega$  of the transition  $|g\rangle \rightarrow |e\rangle$ ,  $t_i$  is the starting time of the pulse and  $t_i + t_p$  the finishing time of the pulse. We restrict ourselves to the case  $t_p \gg \frac{2\pi}{\omega_L}$ , which is a fair assumption since, as we will see later,  $\frac{2\pi}{\omega_L} \sim 13$  fs for our system, while  $t_p \sim \mu\text{s}$ .

This pulse, impinging on the atom, will cause the atomic state to be in the superposition  $|\psi\rangle$ :

$$|\psi\rangle = \alpha(t) |g\rangle + \beta'(t) |e\rangle = \alpha(t) |g\rangle + \beta(t) e^{-i\omega t} |e\rangle \quad (\text{A.2})$$

where  $\alpha(t)$  and  $\beta'(t)$  are the time-dependent amplitudes of the states under the time evolution of the state in the Schrödinger picture: in this representation, only quantum states depend on time. However, in equation A.2, the free evolution factor  $e^{-i\omega t}$  induced by  $\hat{H}$  has been factorized, so that we are left with terms whose temporal evolution can only be induced by the pulse. This is equivalent to saying that the coefficients  $\alpha(t)$  and  $\beta(t)$  are now expressed in the interaction representation, that is, both observables and operators carry time dependence.

In order to lead to electric dipole transitions, the parity of  $|g\rangle$  and  $|e\rangle$  must be opposite, therefore the diagonal matrix elements of the operator  $\hat{d}$  between the two states vanish and only non-diagonal terms are left:

$$\langle g | \hat{d} | g \rangle = \langle e | \hat{d} | e \rangle = 0 \quad (\text{A.3})$$

$$\langle g | \hat{d} | e \rangle = \langle e | \hat{d} | g \rangle = d \quad (\text{A.4})$$

As a consequence, another term adds up to the previous Hamiltonian  $\hat{H}$ :

$$\hat{H}' = -E(\mathbf{r}, t)\hat{d} \quad (\text{A.5})$$

Ignoring the spontaneous emission, the Schrödinger equation for this system will read:

$$(\hat{H} + \hat{H}')|t\rangle = i\hbar \frac{d}{dt}|t\rangle \quad (\text{A.6})$$

Putting together all the equations from A.2 to A.6, explicit expressions for the eigenvalues  $\alpha(t)$  and  $\beta(t)$  of equation A.2 can be deduced:

$$\dot{\alpha}(t) = i\beta(t) \frac{E_0 d}{2\hbar} \left( e^{i[(\omega_L - \omega)t - \mathbf{k} \cdot \mathbf{r}]} + e^{-i[(\omega_L + \omega)t - \mathbf{k} \cdot \mathbf{r}]} \right) \quad (\text{A.7})$$

$$\dot{\beta}(t) = i\alpha(t) \frac{E_0 d}{2\hbar} \left( e^{-i[(\omega_L - \omega)t - \mathbf{k} \cdot \mathbf{r}]} + e^{i[(\omega_L + \omega)t - \mathbf{k} \cdot \mathbf{r}]} \right) \quad (\text{A.8})$$

The quantity  $E_0 d/\hbar$  is commonly known as *Rabi frequency*. It is a quantity associated with the strength of the light-matter interaction: the higher this frequency, the stronger the interaction. Generally, if the transition  $|g\rangle - |e\rangle$  is illuminated with resonant light that is strong enough to drive population, Rabi cycles, i.e. oscillations of population between the two levels, at the Rabi frequency will be observed.

In order to proceed with the integration of the two coupled differential equations A.7-A.8, we need to simplify these expressions by employing the rotating-wave approximation, i.e. neglecting terms where the sum  $\omega_L + \omega$  appears and retaining those of the kind  $\omega_L - \omega$  (see reference [184] for an explanation of this approximation), and assuming that the incident wave is perfectly resonant, such that  $\omega_L = \omega$ , then equations A.7 and A.8 become:

$$\dot{\alpha}(t) = i\beta(t) \frac{E_0 d}{2\hbar} e^{-i\mathbf{k} \cdot \mathbf{r}} \quad (\text{A.9})$$

$$\dot{\beta}(t) = i\alpha(t) \frac{E_0 d}{2\hbar} e^{i\mathbf{k} \cdot \mathbf{r}} \quad (\text{A.10})$$

whose solutions are straightforward:

$$\alpha(t) = A_1 \cos\left(\frac{E_0 d}{2\hbar} t\right) + A_2 \sin\left(\frac{E_0 d}{2\hbar} t\right) \quad (\text{A.11})$$

$$\beta(t) = B_1 \sin\left(\frac{E_0 d}{2\hbar} t\right) + B_2 \cos\left(\frac{E_0 d}{2\hbar} t\right) \quad (\text{A.12})$$

The boundary conditions permit to establish the values of  $\{A_i, B_i\}$ ,  $i = 1, 2$ : since we know the initial values  $\alpha(t_i)$  and  $\beta(t_i)$  at the beginning of the pulse, then these coefficients can be determined; defining the *pulse area*  $\theta$  as  $\frac{E_0 t_p d}{\hbar}$ , then the amplitudes after the effect of the pulse read:

$$\alpha(t_i + t_p) = \cos\left(\frac{\theta}{2}\right) \alpha(t_i) + i \sin\left(\frac{\theta}{2}\right) e^{-i\mathbf{k}\cdot\mathbf{r}} \beta(t_i) \quad (\text{A.13})$$

$$\beta(t_i + t_p) = i \sin\left(\frac{\theta}{2}\right) e^{i\mathbf{k}\cdot\mathbf{r}} \alpha(t_i) + \cos\left(\frac{\theta}{2}\right) \beta(t_i) \quad (\text{A.14})$$

Figure [A.1](#) provides an intuitive physical picture of the effect of a pulse on the atomic amplitudes: the ground (excited) state amplitude  $\alpha(t_i)$  ( $\beta(t_i)$ ) is transferred to the excited (ground) level with a factor containing the phase  $e^{i\mathbf{k}\cdot\mathbf{r}}$  ( $e^{-i\mathbf{k}\cdot\mathbf{r}}$ ) and the amplitude  $\sin\left(\frac{\theta}{2}\right)$  of the incident pulse, and this transfer is indicated by a red (blue) arrow pointing upwards (downwards).

### A.1.2 Free-induction decay

For the next step, we need to introduce the concept of polarization. The polarization in a macroscopic volume is defined as the electric dipole moment over the considered volume. To proceed with this treatment, we need to calculate the dipole moment induced on the atom by the impinging pulse, and this calculation can be carried out by evaluating the expectation value of the  $\hat{d}$  operator on the atomic state as in references [[185](#), [186](#)]. Using equations [A.3-A.4](#) and referring to the state [A.2](#), we can write:

$$\langle \psi(t) | \hat{d} | \psi(t) \rangle = d e^{-i\omega t} \beta(t) \alpha^*(t) + c.c. \quad (\text{A.15})$$

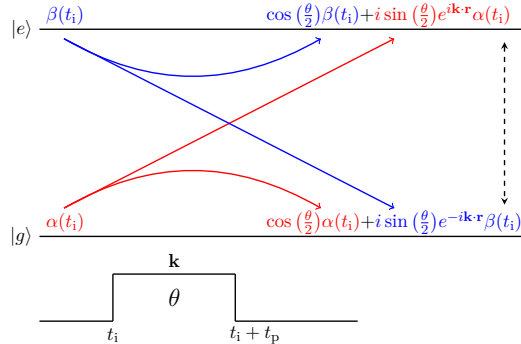


Figure A.1: Effect of an incoming pulse (shown under the level scheme) of wavevector  $\mathbf{k}$  and area  $\theta$ , shone from a time  $t_i$  until  $t_i + t_p$ , on two-level atom amplitudes. The initial ground (excited) state amplitude  $\alpha(t_i)$  ( $\beta(t_i)$ ), in red (blue), is conserved with a factor  $\cos(\theta/2)$  for the ground (excited) level and transferred to the excited (ground) state with a factor  $\sin(\theta/2)e^{i\mathbf{k}\cdot\mathbf{r}}$  ( $\sin(\theta/2)e^{-i\mathbf{k}\cdot\mathbf{r}}$ ). The dashed arrow indicates the coupled terms by equation A.15 to give the dipole moment A.16. This figure is taken from reference [183].

In principle, considering a pulse A.1 shone at  $t_i = t_0$ , the values of  $\alpha(t_0)$  and  $\beta(t_0)$  to be plugged into equation A.15 could be inferred from equations A.13-A.14. Nonetheless, these amplitudes are not the same for all the atoms in an ensemble; therefore, in order to ensure that their value can be generalized to the whole medium, we need to assume the following conditions:

1. all the atoms in the ensemble get excited at the same time. This is not a necessary assumption, since atoms excited later will re-emit later, but it simplifies the calculations;
2. no absorption or dispersion is experienced by the pulse propagating in the sample. Together with the first assumption, this makes it possible for all the atoms to sense the same pulse described in equation A.1;

3. the atoms are all resonant with the pulse [A.1](#), i.e. the transition is not inhomogeneously broadened (see section [2.1.2.3](#) for an explanation of the inhomogeneous broadening);
4. the irreversible decay mechanisms like spontaneous emission are slow compared to the excitation process.

Thanks to these hypotheses, equation [A.15](#) finally admits a solution that can be generalized to all the atoms. The coupled amplitudes that enter this calculation are linked by a double dashed arrow in figure [A.1](#). Assuming that the atoms are all relaxed to the ground state at a time  $t_0 = 0$  (hence,  $\alpha(t_0 = 0) = 1$  and  $\beta(t_0 = 0) = 1$ ), the explicit form of the expectation value [A.15](#) for the atomic system becomes:

$$\langle \psi(t_p) | \hat{d} | \psi(t_p) \rangle = \frac{1}{2} i d e^{-i\omega t_p} \sin(\theta) e^{i\mathbf{k}\cdot\mathbf{r}} + c.c. \quad (\text{A.16})$$

and the polarization of the ensemble, called  $N$  the number of atoms interacting with the pulse, is  $N$  times this dipole moment.

The dephasing of atomic dipoles after the pulse, causing the decay of polarization, is induced by the inhomogeneous broadening. Therefore, although we disregarded it during the excitation period by introducing our third hypothesis, we will need to consider its effect in this phase. As I treated in chapter [2](#), in crystals doped with rare-earth ions, the inhomogeneous broadening is typically caused by strain applied by the crystal lattice matrix to the ions. Nevertheless, the distribution function adopted by reference [\[183\]](#) is inspired to gases at room temperature, and we can adopt it with no loss of generality for what concerns the explanation of optical echoes. This function  $\rho(\Delta)$  can be written as:

$$\rho(\Delta) = \frac{\sqrt{\pi}}{\Delta_0} \exp\left(-\frac{\Delta^2}{\Delta_0^2}\right) \quad (\text{A.17})$$

where:  $\Delta$  is the frequency detuning due to the Doppler shift, leading to a resonance frequency of the atoms of  $\omega + \Delta$ ;  $\Delta_0 = \frac{\omega}{c} \sqrt{\frac{2k_B T}{M}}$  is a constant,

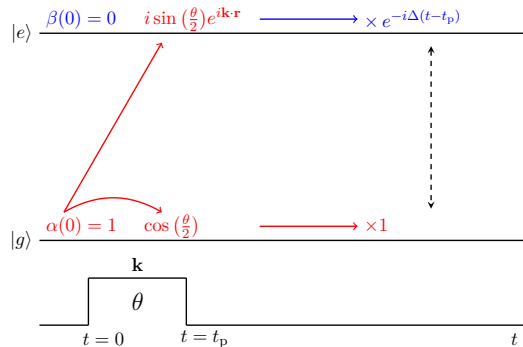


Figure A.2: Full evolution of an atomic system, whose transition is inhomogeneously broadened with central resonance frequency of  $\omega + \Delta$ , initially in the ground state and perturbed by a narrow pulse. The coefficients are now expressed in the interaction picture. This sketch represent the evolution following the situation depicted in figure A.1: the excited state amplitude is evolving, while the ground state one is unperturbed. This figure is taken from reference [183].

with frequency dimension, which takes into account the mass  $M$  of atoms and the temperature  $T$  of the ensemble ( $k_B$  is the Boltzmann constant).

This distribution allows us to calculate the next evolution of atoms. Taken  $\omega + \Delta$  as resonant frequency, then the energies of  $|g\rangle$  and  $|e\rangle$  are respectively 0 and  $\hbar(\omega + \Delta)$ . The time evolution of every atom is described by its Hamiltonian, which accounts for the interaction with the environment as well. The phase evolution of the excited state is then described by the factor  $e^{-i(\omega+\Delta)(t-t_p)}$ , while the ground state amplitude is not evolving.

Figure A.2 depicts this situation, illustrating the evolution of the state amplitudes due to the inhomogeneous broadening. The left side of the picture represents what was shown by figure A.1, but this time we adopted the interaction representation rather than the Schrödinger one because it enables easy generalizations of the current states. Therefore, the factor  $e^{-i(\omega+\Delta)(t-t_p)}$  in the Schrödinger picture corresponds to  $e^{-i\Delta(t-t_p)}$  in the interaction picture, analogously to equation A.2. It can be seen from fig-



ure A.2 that the excited state is acquiring a phase advance of  $\Delta(t - t_p)$  with respect to the ground state.

The representation of figure A.2 is so powerful that we can read the amplitude expressions for  $\alpha$  and  $\beta$  directly from the figure and infer the dipole moment by plugging them into equation A.15:

$$\langle \psi(t) | \hat{d} | \psi(t) \rangle = \frac{1}{2} i d e^{-i\omega t_p} \sin(\theta) e^{i\mathbf{k}\cdot\mathbf{r}} e^{-i\Delta(t-t_p)} + c.c. \quad (\text{A.18})$$

It is apparent from this last equation that the dephasing induced by the factor  $e^{-i\Delta(t-t_p)}$  scrambles the polarization of the ensemble, because  $\Delta$  is inhomogeneously distributed according to  $\rho(\Delta)$ . The overall polarization can be calculated by integrating equation A.18 over all possible frequencies, accounting for the number of atoms  $N$ .

$$P(\mathbf{r}, t) = \frac{i}{2} N d e^{-i\omega t} \sin(\theta) e^{i\mathbf{k}\cdot\mathbf{r}} \int_{-\infty}^{\infty} \rho(\Delta) e^{-i\Delta(t-t_p)} d\Delta + c.c. \propto e^{-\frac{\Delta_0^2(t-t_p)^2}{4}} \quad (\text{A.19})$$

where the last result is what emerges from the evaluation of the integral. The decay time of this factor is  $\sim \frac{2}{\Delta_0} \approx 1$  ns. Therefore, the polarization decay lasts on average less than a typical pulse length of some ns, and this phenomenon is usually called *free-induction decay*. It is important to remark that, in this simplified model, no decay of atomic dipole moments is allowed, due to the assumptions made at the beginning of this section. What is really decaying in this model are the phase coherences. Luckily, by shining a second pulse at a later time, even later than the free-induction decay, we can restore these coherences and lead to an echo emission, as it will be shown in the next section.

### A.1.3 Rephasing and echo emission

Finally, we shine a second pulse on the atomic ensemble, resonant with the transition as well. To adapt the notation and account for the second pulse, we will call  $\mathbf{k}$  the wavevector of the two pulses,  $\{t_{p_1}, t_{p_2}\}$  their respective durations and  $\{\theta_1, \theta_2\}$  their respective pulse areas. The distance  $\tau$  between the two pulses is usually in the  $\mu\text{s}$  regime, so that any free induction decay

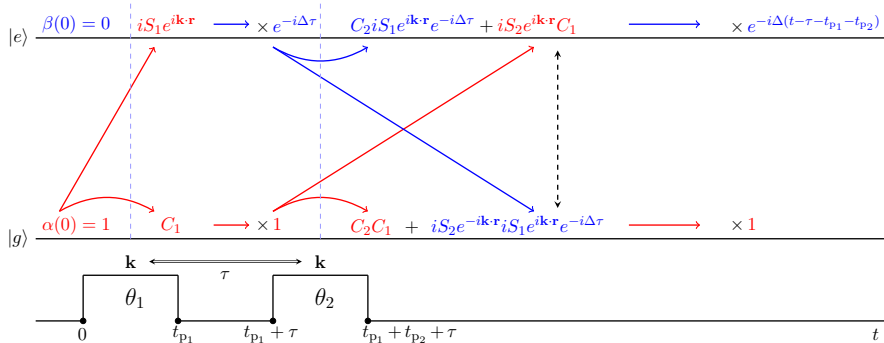


Figure A.3: Evolution of the atomic ensemble after two pulses (shown at the bottom) are shone on it. With respect to figures A.1 and A.2, we defined  $C_i \equiv \cos(\theta_i/2)$  and  $S_i \equiv \sin(\theta_i/2)$ ,  $i = 1, 2$ . The description and the salient points of the picture are provided in the text. This figure is taken from reference [183].

effect has disappeared. Just before the second pulse is shone, the ground state is not evolving, while the excited state is acquiring a phase  $e^{-i\Delta\tau}$  with respect to  $|g\rangle$  due to free evolution. This is clearly displayed in figure A.3. The most remarkable effect of the second pulse is that it induces a term on the excited level—coming from the ground state—that is not evolving with time (red arrow pointing upwards in figure A.3); on the other hand, it also transfers the free evolution term from the excited to the ground level (blue arrow pointing downwards in figure A.3). The ultimate effect of the second pulse is then creating a phase-advanced term on  $|g\rangle$ : this is the so-called *phase-reversal* effect of the pulse. It can be seen that, if we use equation A.15 to calculate the dipole moment at a time  $\tau$  after the second pulse, the dependence of this quantity on  $\Delta$  vanishes, since both amplitudes in both levels contain the term  $\exp(-i\Delta\tau)$ , and this holds for all the atoms in the sample: this implies that the polarization has rephased and thus we have the emission of the so-called *echo*. To find out the echo amplitude, we first proceed with computing this dipole moment at a time  $t > t_{p_1} + t_{p_2} + \tau$ , after the second pulse has acted. To perform this calculation, it suffices to

consider the terms linked by the dashed black arrow in figure A.3, as they are the only ones leading to an echo emission. The electric dipole moment will thus be:

$$\begin{aligned} \langle \psi(t) | \hat{d} | \psi(t) \rangle &= ide^{-i\omega t} S_2 e^{i\mathbf{k}\cdot\mathbf{r}} C_1 e^{-i\Delta(t-\tau-t_{p_1}-t_{p_2})} \\ &\quad \times (iS_2 e^{-i\mathbf{k}\cdot\mathbf{r}} iS_1 e^{i\mathbf{k}\cdot\mathbf{r}} e^{-i\Delta\tau})^* + c.c. = \\ &= -\frac{1}{2} ide^{-i\omega t} \sin(\theta_1) \sin^2\left(\frac{\theta_2}{2}\right) e^{i\mathbf{k}\cdot\mathbf{r}} e^{-i\Delta(t-2\tau-t_{p_1}-t_{p_2})} + c.c. \end{aligned}$$

where we defined  $C_i \equiv \cos(\theta_i/2)$  and  $S_i \equiv \sin(\theta_i/2)$ ,  $i = 1, 2$ . As anticipated, at a relative time  $\tau$  after the second pulse, corresponding to an absolute time of  $t = t_{p_1} + t_{p_2} + 2\tau$ , the dependence on  $\Delta$  of the dipole moment disappears.

Then, we repeat the same procedure as in equation A.19 to find the polarization of the medium:

$$P_{\text{echo}}(\mathbf{r}, t) = -\frac{i}{2} N d e^{-i\omega t} \sin(\theta_1) \sin^2\left(\frac{\theta_2}{2}\right) e^{i\mathbf{k}\cdot\mathbf{r}} e^{-\Delta_0^2(t-2\tau-t_{p_1}-t_{p_2})^2/4} + c.c. \quad (\text{A.20})$$

This describes the time and the duration of the echo: it consists in a pulse of duration  $\sim 4\Delta_0^{-1}$  emitted at a time  $\sim 2\tau$  after the first pulse. More details about how this echo is changed when the inhomogeneous broadening is considered can be found in references [183, 186]. Under the assumptions that the medium does not re-absorb completely the echo, and that diffraction effects are negligible, the polarization described in equation A.20 gives rise to a plane-wave echo with intensity:

$$I \propto |P(\mathbf{r}, t_e)|^2 \propto N^2 d^2 \sin^2(\theta_1) \sin^4(\theta_2/2) \quad (\text{A.21})$$

The maximum of this intensity is reached when  $\theta_1 = \frac{\pi}{2}$  and  $\theta_2 = \pi$ .

The two pulses can be at different angles, e.g. the second pulse can have a slight angle  $\phi$  with respect to the first one: in this case, the echo intensity is reduced because of lack of phase-matching (see section 5.2.1.1), but the echo is still emitted at an angle  $2\phi$  with respect to the first pulse.

Finally, in the case of a more detailed description accounting for all the decay processes we neglected (e.g. spontaneous emission, relaxation, collisions in gas), equation [A.20](#) must be adapted phenomenologically by including some decreasing exponential factors.



## Appendix B

# Experimental tools and techniques

In this chapter, I will introduce some experimental devices and procedures that are common to the following chapters. In particular, I will deal with the lasers (section B.1) and the cryostats (section B.2) we employ in our labs, and I will speak about how to experimentally prepare an atomic frequency comb, whose theory has been introduced in section 2.2, in a  $\text{Pr}^{3+}:\text{Y}_2\text{SiO}_5$  crystal (section B.3.1). Finally, I will present our use of the two-pulse photon echo technique, treated in appendix section A.1, to estimate the  $T_2$  (section 2.1.2.2) of our crystal.

### B.1 Lasers

#### B.1.1 606 nm laser

To perform optical pumping inside the  $\text{Pr}^{3+}:\text{Y}_2\text{SiO}_5$  crystals and to probe them, we use a Toptica tapered amplifier (TA) SHG Pro laser system. This laser generates narrow light centered around the 605.977 nm (494.726 THz)

wavelength<sup>1</sup> via the second-harmonic generation (SHG) non-linear process, which I will briefly mention also in section 5.2.1. A master diode laser emits light at 1212 nm, which is amplified by a TA and then injected in a bow-tie ring cavity. Inside the cavity, a non-linear crystal is present, which enables the second harmonic generation process (section 5.2.1): two photons at 1212 nm are converted into a photon with half the original wavelength, in this case 606 nm. The cavity forces the light to interact multiple times with the crystal, thus boosting the conversion efficiency. With this procedure, we have almost 1 W of visible power available for our purposes.

We used two different generations of this laser system: the older one was employed for the DLCZ experiment in chapter 3, whereas a newer laser was purchased in 2020 and it was used to perform the experiments in chapters 4 and 5.

Despite this laser system is reaching very narrow linewidths—what Topica guarantees is under 500 kHz in principle—the produced light is not narrow enough for our purposes. To this aim, we purchased an optical ultrastable Fabry-Pérot cavity from Stable Laser Systems, whose modes are used to lock the frequency of the 1212 nm light by means of the Pound-Drevel-Hall (PDH) method [187]. The free spectral range of this cavity is 1.5 GHz, which means that we are able to scan the wavelength of the 606 nm laser in steps of 3 GHz. This cavity enables us to reach laser linewidths around 3 kHz.

#### **B.1.1.1 Modulation of light**

Obtaining the spectral features I will speak about in section B.3.2 requires a very precise modulation of the light, with a sub-MHz precision. To this end, we employ acousto-optic modulators (AOMs), which are driven by an arbitrary waveform generator (Signadyne/Keysight). The maximum shift the AOMs can provide is 200 MHz. To be able to sweep the light frequency without changing the path alignment, we employ a double-pass configuration, in which the diffracted modes crosses the same AOM twice,

---

<sup>1</sup>This frequency corresponds to the central frequency of the inhomogeneously broadened  $\text{Pr}^{3+}:\text{Y}_2\text{SiO}_5$  transition we want to address, as stated in section 2.1.2.1.

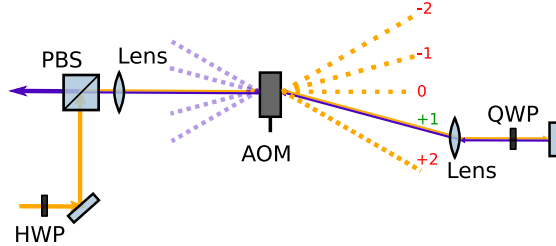


Figure B.1: Example of a double-pass configuration AOM. From the bottom left, a vertically-polarized beam is coupled via a PBS into the AOM path. Here it gets focused and it gets diffracted (dashed orange beams) by the AOM (the angle of diffraction is emphasized in the picture). Each diffracted beam has a frequency shift  $\Delta\nu$  that is voltage-dependent. So, the shifts will be  $0, \pm\Delta\nu$  ( $\pm 1$  in the figure),  $\pm 2\Delta\nu$  ( $\pm 2$  in the figure), and so on. Usually, we are interested in the  $+1$  shift, therefore we discard all the other diffraction orders using a pinhole (not shown in the picture). The  $+1$  order is collimated and its polarization is rotated in double-pass by a QWP set at  $22.5^\circ$ , so to get a horizontally-polarized beam. The  $+1$  order is bounced back to the AOM, where it gets diffracted again (dashed blue beams), and its  $+1$  order is counterpropagating with respect to the original input beam (solid blue beam), and it is thus transmitted by the PBS (top left). The total effect is having a  $2\Delta\nu$ -frequency-shifted output beam from the AOM path.

thus experiencing twice the frequency shift but maintaining the same path in any case [188]. An illustration of this technique is provided by figure B.1.

### B.1.2 994 nm laser

As a pump laser for the quantum frequency experiment reported in chapter 5, we used a Toptica TA-pro highly tunable laser. The laser is composed of two main stages: a tunable master diode laser and a tapered amplifier (TA). The diode laser can output laser beams ranging from 934 nm to 995 nm. The emitted power changes with the wavelength, with a peak of



emission at 987 nm. At the limit wavelength of 994 nm we are interested in, the emission power is low. The tapered amplifier can enhance the amount of emitted power, and at 994 nm we can expect a maximum power around 30 mW output from the TA. The main parameters dictating the emission wavelength of the TA-pro are the current supplied to the diode and its temperature. In addition to that, we can change the position of the grating in front of it for a coarser tuning, or the position of the piezo of the laser cavity for a finer tuning.

This power is too small for our conversion experiment, for which powers of the order of  $10^2$  mW need to be coupled inside the waveguide. For this reason, cascaded to the TA-pro, we installed a further Toptica BoosTA pro tapered amplifier. This tapered amplifier outputs around 1.6 W.

The output mode from tapered amplifiers is usually elliptical in shape. In order to make it Gaussian, cylindrical lenses are used. Usually, the shape of the output beams is never perfectly Gaussian, so their coupling to single mode fibers (SM-fibers) is never optimal. To couple into the BoosTA pro a beam that is as Gaussian as possible, we couple the output of the TA pro in a PM-fiber and then we out-couple it before the second tapered amplifier. This is shown in figure B.2. This ensures that the input beam to the tapered amplifier is Gaussian.

Since the output beam is too big to be coupled inside a fiber, we further use a telescope to diminish the beam size and we couple it to a PM-fiber bringing the beam all the way to the quantum frequency conversion setup, shown in figure 5.3.

## B.2 Cryostat

We need to cool our  $\text{Pr}^{3+}:\text{Y}_2\text{SiO}_5$  crystals to cryogenic temperatures in order to benefit from their coherence properties described in chapter 2. Our cryostat is a closed-cycle helium cryostat from Montana Instruments. It manages to cool our crystals down to a temperature around to 3 K, with a stability of 10 mK. It possesses 5 optical windows, 4 side ones and a top one, all with 30 mm diameter round apertures.



Figure B.2: Box enclosing the TA pro laser and the BoosTA pro tapered amplifier. The first PM-fiber above the TA pro serves the purpose of bringing its output to the external tapered amplifier, while the other one brings the output of the BoosTA pro to the quantum frequency conversion experiment setup.

Two cooling stages are meant to refrigerate the platform where our crystals are located. Stage 1 is the warmer one, and it gets down to 40 K. It is thermally linked to a radiation shield which prevents external radiation from leaking inside. A thermometer is connected to this element and enables us to read its temperature.

Stage 2 is the colder one. It is connected to the so-called cold finger, inside which the helium expands when pumped inside by the compressor. This stage temperature is around 2.7 K, and we can read it thanks to the thermometer attached to it.

The platform, where the crystals are attached, is thermally linked to this last stage. This stage also has its own thermometer. Our Montana cryostat offers the possibility of installing an additional user thermometer.

A typical cooldown procedure from environmental temperature proceeds as follows:

- Vacuum is generated inside the vacuum chamber by means of an in-built pump. Air is removed until the internal pressure reaches 2 Torr.

This step might fail if the vacuum chamber is not properly sealed;

- The compressor starts pumping helium. Stage 2 temperature drops faster than the platform temperature to trap potential impurities that might be left inside the vacuum chamber, so that the platform is in principle preserved from condensation effects on it. Stage 1 follows immediately after it;
- the cooldown typically achieves  $T_{\text{Stage 2}}=2.7\text{ K}$ ,  $T_{\text{Stage 1}}=27\text{ K}$  and  $T_{\text{Platform}}=3.4\text{ K}$ .

The compressor—by compressing and expanding the helium—causes vibrations which are detrimental for our experiments. A careful study of the vibrations induced by the compressor is presented in the next section. To avoid these noise-related issues, we synchronize our experimental sequence with the cryostat cycle: the cryostat has a BNC port from which a TTL is output, which is produced by a built-in Hall probe sensor that is accommodated on top of the cold head. Therefore, since the cryostat cycle has an 1 s period, we have to repeat the whole AFC preparation every second.

Throughout my PhD, we used two distinct cryostats of the same model. The first one was used for the DLCZ experiment of chapter 3, but was then devoted to a different experiment. Hence, we bought a second-hand one from another ICFO group to perform the cavity experiment of chapter 4.

### **B.2.1 Cryostat noise**

As I have just mentioned, the cryostat has a 1 s cycle. However, our duty cycle is limited to a small portion of this cycle, because at some specific times vibrations hit the crystal, causing strain-induced random frequency shifts of the transitions that broaden the absorption peaks. One way of tackling this issue is having the crystals sitting on spring mounts, as the one I will present in the next section. However, it is usually convenient to prepare the comb and perform measurements during some specific times when vibrations are low. Figure B.3 displays the described cycle. This measurement is referred to the newer cryostat. The noise is quantified

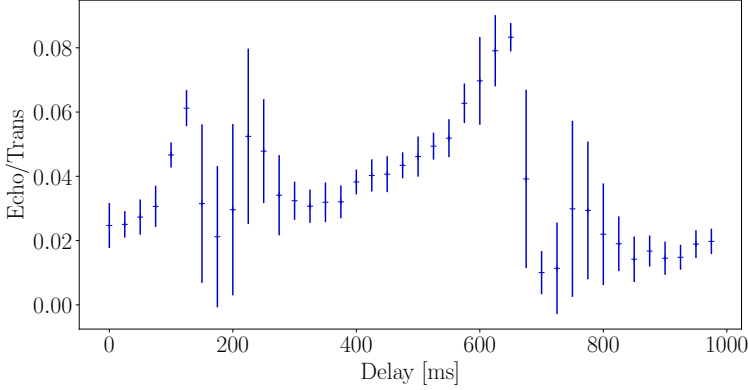


Figure B.3: Ratio between the AFC echo and the transmission through the transparency window, in single-pass, as a function of the delay between the beginning of the cryostat cycle and the start of the sequence. The regions with the most intense noise are the ones with higher standard deviation, 200 ms-300 ms and 700 ms-800 ms intervals. The AFC storage time is 10  $\mu$ s.

estimating the ratio between the AFC echo and the transmission through the transparency window when no AFC is prepared inside the crystal<sup>2</sup>. The noisy regions appear as an increased standard deviation of this ratio, since the vibrations are making the echo change dramatically in size, and they are limited approximately to the 200 ms-300 ms region and to the 700 ms-800 ms region. All the timings are referred to the starting point of the cryostat TTL, which we define as the starting point of our cycle. A behavior of the AFC efficiency in multi-pass configuration, i.e. with a cavity around the crystal, will be shown in appendix section C.1.4.

<sup>2</sup>This ratio differs from the AFC efficiency estimation, since the efficiency is estimated by calculating the ratio between the echo area and the input area when the input polarization is set to non-interacting and a pit is prepared in the memory.

## B.2.2 Crystals and mounts

I have spoken about the optical properties of the  $\text{Pr}^{3+}:\text{Y}_2\text{SiO}_5$  crystals we use in chapter 2. In the experiments described in chapters 3 and 4, we used two  $\text{Pr}^{3+}:\text{Y}_2\text{SiO}_5$  crystals, a memory crystal (MC) and an interferometric filter crystal (IFC). Both crystals have sizes 6 mm (width)  $\times$  4 mm (height)  $\times$  3 mm (depth). Their doping concentration is around 0.05 % of praseodymium ions (as mentioned in sections 2.1 and 2.1.2.1). In order to assess the thermalization of these crystals, we always check their coherence time, with the procedure described in section B.3.1. The thermalization mainly depends on the cooling power of our cryostat, on the shielding from black-body radiation and on the thermal contact between the copper mount we use and the crystals. To glue the crystals to the mount, we use a special varnish (GE Low Temperature Varnish by Oxford Instruments), and we ensure that the crystals are adhering well to the copper by applying a slight pressure. In general, to avoid any stress-induced shift of their inhomogeneous line, we never have the crystals undergo constant pressure during the varnish drying period. Nevertheless, it was also tried to tie the crystal to the mount with aluminum foil to improve its thermal link to the copper mount, as I will mention in appendix section C.1.1, and no evidence of inhomogeneous shift was found: the measurement of the inhomogeneous line reported in figure C.1 was meant to verify precisely that.

We have two different kinds of copper mounts: a stiff copper mount and a spring copper mount. The first one was used in DLCZ experiment of chapter 3 and in most part of the experiment of chapter 4 except sections 4.2.1 and 4.2.5. The spring mount can dampen vibrations very effectively, as the spring are meant to decouple, vibration-wise, the upper part where the crystals sit from the bottom part which is sensing the noise induced by the cryostat compressor. However, one of the drawbacks is that it generally thermalizes worse than the monolithic mount, and for this reason copper foils are installed on the two sides of the upper part to link it to the lower part. The monolithic mount is shown in the first picture (from left) of picture B.4, while the spring mount is displayed in the second picture.

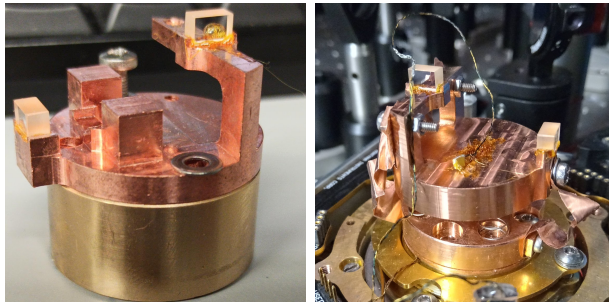


Figure B.4: Monolithic mount (on the left) and spring mount (on the right). The memory crystal is the one accommodated on the suspended arm, while the filter crystal is the lower one, orthogonally addressed with respect to the memory one. The crystals are pasted with varnish to the mount (orange substance below the crystals). Both kinds of mounts are fixed to a lower cylinder, connected in turn to the cryostat platform. The upper part of the spring mount has copper foils bridging it with the lower part in order to ensure a good thermal link. The springs are 1 cm long, and have a elastic constant of  $0.125 \text{ N m}^{-1}$  for a diameter of 0.3 mm ( $0.059 \text{ N m}^{-1}$  for a diameter of 0.25 mm).

## B.3 Experimental techniques

In this section, I will report about some experimental procedures we normally employ in our lab and that are useful to know to better understand our experimental work.

### B.3.1 Two-pulse photon echo measurement

In section 2.1.2.6 and appendix A, I have introduced the theory behind two-pulse photon echo (TPE) technique. The reverse of the dephasing induced by the two pulses that was described applies only for the dephasing caused by the inhomogeneous broadening. As mentioned at the end of appendix section A.1.3 and in reference [109], many other factors play a role in the decay of atoms, and act randomly in time. Therefore, if we start

increase the delay between the pulses, the likelihood that decays or losses of coherence happen during the induced dephasing time (between  $t_{p_1}$  and  $t_{p_1} + \tau$ , to use the same notation as appendix section A.1.3) or during the rephasing time (between  $t_{p_1} + t_{p_2} + \tau$  and  $t_{p_1} + t_{p_2} + 2\tau$ ) increases, and the intensity of the final echo will decrease. Thus, we use this phenomenon to measure the optical coherence time  $T_2$  of our ensemble by distancing the two pulses more and more in time, to extract the echo intensity at different times. This measurement is extremely sensitive to the number of excited ions. This amount of ions depends on the Rabi frequency defined in appendix section A.1.1, which in turn depends on the power of the exciting beam, on its waist and on the number of available ions in the ground state. When too many ions get excited, they experience instantaneous spectral diffusion (defined in section 2.1.2.2), which limits the achievable coherence time. Given all these parameters, our measurement of the coherence time is therefore rather a lower limit to the coherence time and serves to verify the thermalization in comparison to other cool-downs and other experimental conditions. Referring to the setup depicted in figure 4.3, we always perform the TPE measurement with the cavity beam, set at about 1 mW (as measured in front of the vacuum chamber of our cryostat) and with a waist inside the cavity of  $75 \mu\text{m}$  (appendix section C.1.2). The measurement is performed in a single-pass fashion by re-routing the light to a detector with a flip mirror before the second cavity mirror. Unlike what I described in appendix section A.1.3, when we implement this protocol experimentally, we use two Gaussian pulses with the same area and same duration (860 ns). We first prepare a controlled absorption feature with a given OD, which we probe with the two pulses.

The result of a measurement of the coherence time of the memory crystal from the experiment in chapter 4 is depicted in figure B.5. As mentioned, the echo is clearly decaying in the scanned interval (ranging from  $12 \mu\text{s}$  to  $50 \mu\text{s}$ ). The  $T_2$  values we usually obtain fall in the range  $30 \mu\text{s}$ - $80 \mu\text{s}$ , and are strongly affected by the vibrations of our cryostat and by the quality of thermal links between its platform and the samples. In particular, this test can be used for an assessment of the thermalization of our crystal. For the reported measurement, the sample was not sitting on a spring-dampened

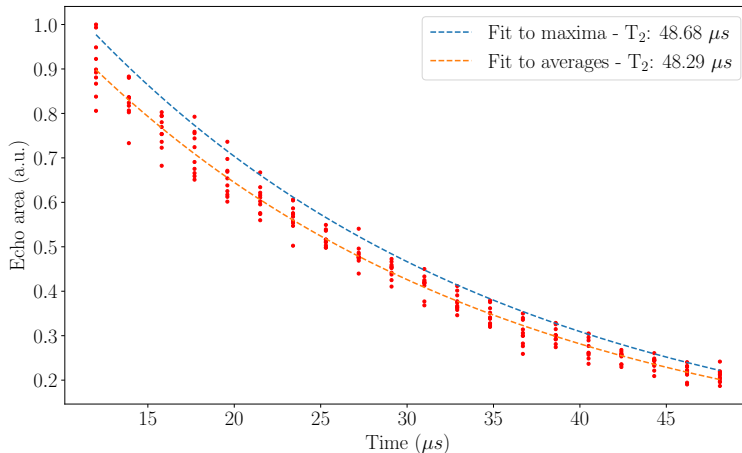


Figure B.5: Example of a  $T_2$  measurement by employing the TPE technique. Two strong pulses, with pulse areas  $\pi/2$  and  $\pi$ , are shone on the ensemble. Their separation  $\tau$  increases in 20 steps, from  $12\ \mu\text{s}$  to  $50\ \mu\text{s}$ . For each step, 10 echo traces are recorded. The plots shows two fits, both with the decreasing exponential law  $A \exp(-t/B)$ , where  $t$  is time and  $A$  and  $B$  are respectively the initial amplitude and the wanted  $T_2$ , performed on the means of the values and on the maxima of the values. Unless differently stated, I always quote the value of  $T_2$  extracted from the fit to the maxima. The sequence was synchronized to the cryostat cycle.

mount, thus being affected by vibrations coupling through the stiff copper mount attached to the platform of our cryostat. If we dampen vibrations and if the sample is at the correct temperature, we can achieve values around  $80\ \mu\text{s}$ . Much higher values were obtained in our group with low excitation intensities (using low powers and large beam waists), up to  $116\ \mu\text{s}$ , compatible with what has been measured in the literature previously [116].



### B.3.2 AFC preparation

The AFC has been described theoretically in section 2.2, and now I will describe its experimental preparation. The steps of this technique will be illustrated with figures that we obtained by an optical-pumping simulator programmed by a former member of our group, Dr. Bernardo Casabone.

As shown in section 2.1.2.4, nine frequency classes of ions arise from the crystal matrix strain experienced by the ions. The initial situation of these classes in terms of population and transition intensities is summarized in figure B.6, where we have not performed any optical pumping yet, while the uppermost plot of figure B.11 shows the initial OD spectrum.

To create an atomic frequency comb on the  $\pm 1/2g \rightarrow \pm 3/2e$  means that we need to be able to address univocally this specific transition of one class of ions. To this aim, we perform optical pumping to progressively shift all the addressable classes, except one desired class, outside of the spectrum of interest. This procedure is called *class cleaning*.

The comb creation procedure is usually divided into four steps:

1. the creation of a transparency window that we call *pit*;
2. the controlled repopulation of this transparency window with an absorption feature;
3. the creation of a comb on top of this absorption feature: this step is different depending on whether we are using the hole-burning technique or the coherent method to shape the AFC. We will see the difference between these two procedures in the comb paragraph.
4. the cleaning of the  $3/2g$  level following the creation of the comb in order to have a single-class comb and provide an empty level for spin-wave storage. The previous step and this last step are performed alternately and iteratively.

These steps are preceded by a cleaning affecting all the levels of interest, when we wipe out any remains of the spectral structures prepared previously. We do so by shining a pulse centered at the pit frequency, chirped by 120 MHz around it, at maximum power, 20 mW.

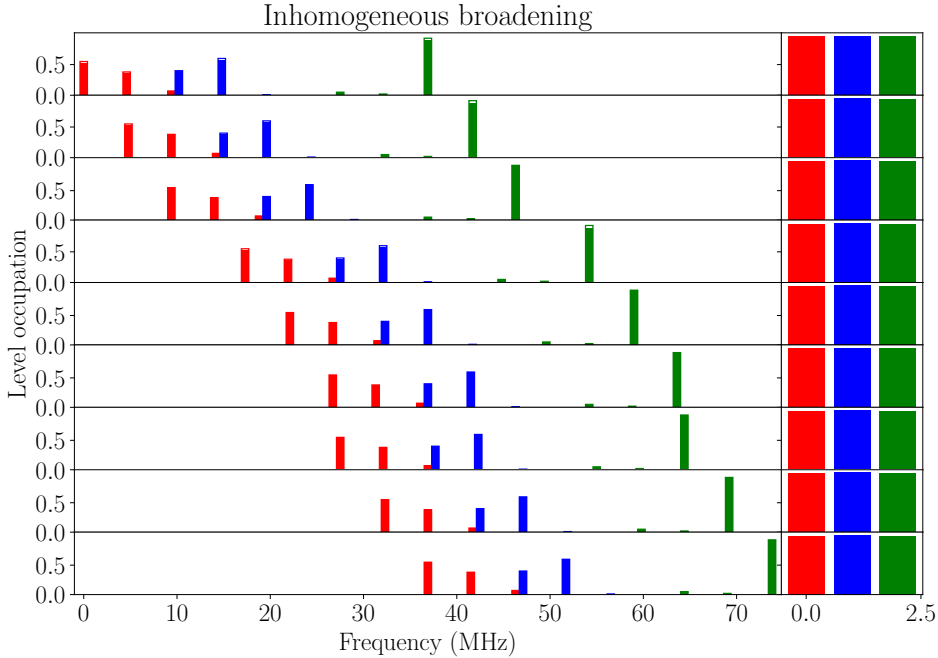


Figure B.6: Level occupations as a function of frequency for the nine classes of ions shown in figure 2.6 when no optical pumping has been performed, i.e. with the pristine inhomogeneously broadened line. I followed the same convention used in section 2.1.2.4, where the transitions starting from  $\pm 1/2g$  are red, from  $\pm 3/2g$  are blue, from  $\pm 5/2g$  are green. The left side of the plot shows the nine classes of ions (nine rows), with the transitions  $\pm 1/2g \rightarrow \pm 1/2g, \pm 3/2g, \pm 5/2g$  (first three red rectangles of each row),  $\pm 3/2g \rightarrow \pm 1/2g, \pm 3/2g, \pm 5/2g$  (second three blue rectangles of each row) and  $\pm 5/2g \rightarrow \pm 1/2g, \pm 3/2g, \pm 5/2g$  (third three green rectangles of each row). Their height indicates the strength of the transition, while their filling indicates the amount of population left in the starting level. Their separation in MHz is shown on the x axis. The overall occupation of the three ground levels is summed up on the right side, where the height of rectangles is proportional to the population of each level. As this plot is representing the initial situation, there is total balance between all level populations.

### B.3.2.1 Pit preparation

The first step consists in creating a transparency window where the optical depth is close to zero. To perform the optical pumping required for the creation of this feature, a strong chirped laser pulse is sent resonantly with the six transitions involving  $\pm 1/2g$  and  $\pm 3/2g$  of figure 2.4. This pulse is applied repeatedly so to empty completely those two ground levels. At the end of this burning procedure, a 16 MHz broad window is created. The width of the broadest pit that can be created is given by the difference of the sum of separations of ground levels and the sum of separations of excited states; in  $\text{Pr}^{3+}:\text{Y}_2\text{SiO}_5$ , this is equivalent to 18.1 MHz [110]. Performing this procedure implies that only four classes of ions are left to interact with. Figure B.7 shows the result of the pit preparation on the occupation level of the nine classes of ions. The effect on the OD of the ensemble can be seen in the second plot from above of figure B.11.

The creation of a spectral hole of 16 MHz changes the absorption in the medium within the transparency region and hence the group velocity of light, as I treated in section 4.2.4.

### B.3.2.2 Broad spectral feature preparation

The pit preparation depletes  $\pm 1/2g$  and  $\pm 3/2g$  levels and, as a consequence, fills  $\pm 5/2g$ , as discussed in section 2.1.2.5. The so-called *burn-back pulse* addresses the  $\pm 5/2g \rightarrow \pm 5/2e$  transition, which has the strongest dipole moment among the 9 transitions (see table 2.1), to transfer some population back to the  $\pm 1/2g$  and  $\pm 3/2g$  levels. Differently from the pit preparation, the chirp and amplitude of this pulse are carefully tuned such that the re-filling of these levels happens in a controlled way: the absorption structures formed on these ground levels have a custom width and OD. Depending on the technique we use to burn the comb, this absorption feature has different characteristics. There are two different techniques to accomplish this result, as we will see in the next section: the hole-burning technique [51, 189] and the coherent technique [51]. In the experiments reported in this thesis, both have been employed, in different cases: the hole-burning

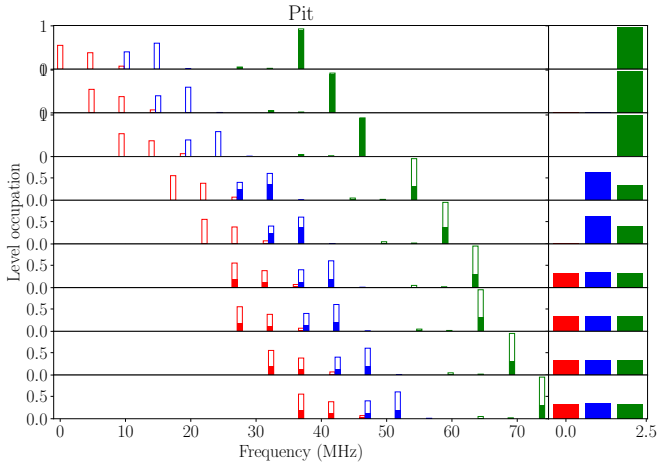


Figure B.7: Evolution of the level occupations of figure B.6 after a pit has been created on the  $\pm 1/2g$  and  $\pm 3/2g$  levels. As it is apparent from the figure, within the 16 MHz of the pit, we are now interacting only with the first 4 classes.

procedure has been used with combs whose storage time was lower than  $4\ \mu\text{s}$ ; the coherent technique, instead, has been shown to be more effective when dealing with combs whose storage time exceeds  $4\ \mu\text{s}$ , like the ones we prepared for the different storage times of section 4.2.3. For employing the hole-burning technique, we repopulate this transition in a comb-like manner, with a coarse spectral feature that already resembles an AFC; for the coherent technique, we opt for preparing a single square spectral feature to target with the pulses we create the comb with. For the comb-like pedestal, we address the reservoir transition  $\pm 5/2g \rightarrow \pm 5/2e$  with 5 adiabatic secant pulses [190], each with  $40\ \mu\text{s}$  duration and repeated 100 times, for a total preparation time of 20 ms.

Addressing the  $\pm 5/2g$  level eliminates another class, leaving three classes with which the interaction is possible. In figure B.8, the effect on the population of the transitions is shown, and the third plot of figure B.8 shows

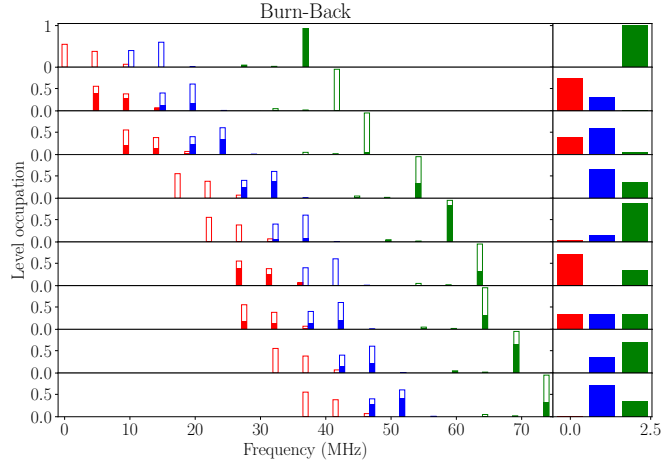


Figure B.8: Evolution of the level occupations after an absorption feature has been burnt back onto the transparency window by addressing the  $\pm 5/2g \rightarrow \pm 5/2e$  transition. The number of addressed classes reduces to 3.

the burnt-back features. In both the illustrated cases, the monolithic absorption feature has been simulated, i.e. the single square one.

### B.3.2.3 Comb preparation

The last step consist in creating a comb on  $\pm 1/2g \rightarrow \pm 3/2e$  starting from the absorption feature. Independently of which of the two methods of comb creation is used, the resulting AFC must be a single-class feature. This is achieved by eliminating the two left classes from the transparency window spectrum. This elimination is carried out by cleaning the  $\pm 3/2g \rightarrow \pm 3/2e$  transition. This cleaning step is iterated together with the comb-burning technique so to get a comb on the  $\pm 1/2g \rightarrow \pm 3/2e$  and to leave as little population as possible on the  $3/2g$  level. The cleaning effect on the level occupation is shown in figure B.9, whereas its effect on the OD is shown in the fourth plot of figure B.11.

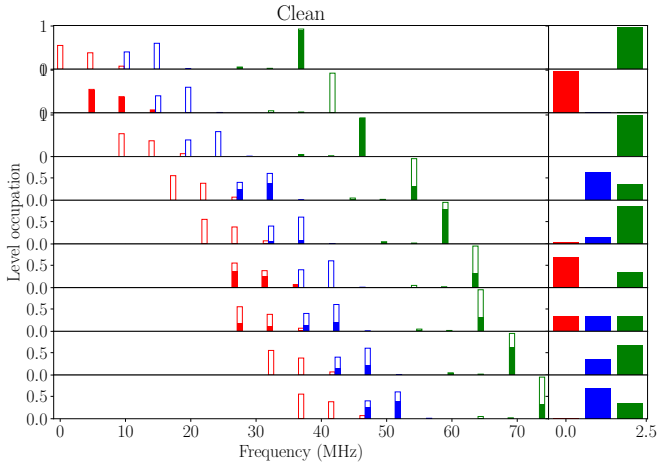


Figure B.9: Evolution of the level occupations after the  $\pm 3/2g$  level has been cleaned thoroughly. The number of addressed classes reduces to 1.

**Hole-burning technique** The hole-burning technique [51, 189] consists in tailoring the comb by shining several pulses resonant with the  $\pm 1/2g \rightarrow \pm 3/2e$  transition in order to create holes inside the burned-back absorption feature. As already mentioned, to facilitate this operation, we are repopulating the transparency window in a controlled way with a “comb”-like structure.

Following this controlled optical repopulation, we shine 6 adiabatic pulses whose spectral distance between each other is  $\Delta$  and whose spectral extension is approximately  $\Delta - \gamma$ . This extension is achieved by chirping the pulses. The preparation time for this comb is equivalent to the product between the number of series of pulses that we send, the number of pulses we shine and the duration of a single pulse. Typical figures for  $2\ \mu\text{s}$ , which is one of the storage times that we addressed in the experiment of chapter 4, are 225 series of 6 pulses with  $120\ \mu\text{s}$ , yielding a 162 ms preparation time. Note that the minimum duration for each single pulse is set by the peak separation: in the  $2\ \mu\text{s}$  case, the separation between the peaks

is 500 kHz and the peak width  $\gamma$  is 77 kHz (assuming  $\mathcal{F}_{\text{AFC}} = 6.5$ , which is a reasonable experimental value as mentioned in section 4.1.2.1), and this sets a minimal preparation time  $\tau_{\text{prep}}$  for each peak of 13  $\mu\text{s}$ ; to avoid being in this regime, we should always aim at  $\gamma \gg \frac{1}{\tau_{\text{prep}}}$ , which is our situation. Since this is a serial method, the preparation time can also be defined as:

$$\frac{1}{\tau} = \frac{N}{T_{\text{prep}}} = \frac{B}{T_{\text{prep}} \Delta} \quad (\text{B.1})$$

where, following the conventions of reference [51], I have called  $B$  the total bandwidth of the AFC (usually 4 MHz) and  $N$  the number of AFC peaks. Therefore, for a given preparation time  $T_{\text{prep}}$  and a given comb, the Fourier limitation of a preparation pulse is bound to be the one fixed by equation B.1.

This technique has been applied in shaping the 1.5  $\mu\text{s}$  and 2  $\mu\text{s}$  combs. In our group, this technique has been experimentally shown not to be optimal for making combs with storage times longer than 4  $\mu\text{s}$ . For this reason, we resorted to the coherent technique for shaping all the longer storage time combs.

I chose to picture the hole-burning procedure rather than the coherent one, which would be less easy to implement with our simulator. Figure B.10 shows the effect of 7 hole-burning pulses shone on the absorption feature created earlier. As anticipated, some of the classes eliminated with the previous procedures go back to being available again, therefore the cleaning procedure must be alternated to the comb preparation until a comb is formed on the  $\pm 1/2g$  from the first class and at the same time the  $\pm 3/2g$  is depleted on the same class. This repopulation of this latter level is also apparent from the last plot of figure B.11, where an absorption feature has re-grown where the cleaning pulse was shone.

**Coherent technique** The coherent technique [51] employs only one waveform, unlike the hole-burning procedure, shaped like the FFT of the desired “negative AFC”, i.e., the part to be removed from the single absorption feature to get the desired AFC. This pulse contains all the Fourier components

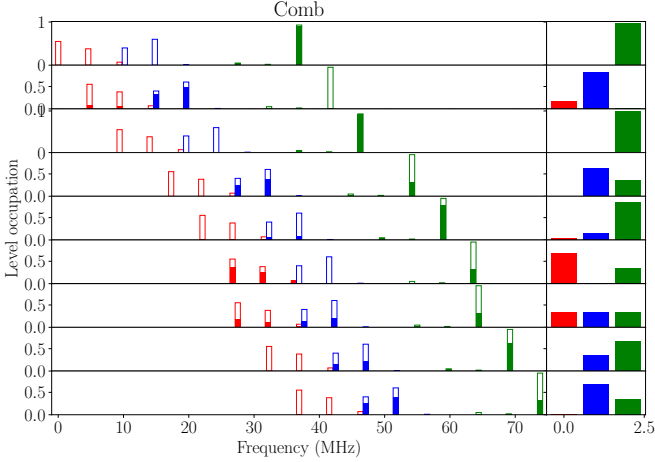


Figure B.10: Evolution of the level occupations after a comb has been shaped onto the  $\pm 1/2g$  level absorption feature by shining 7 pulses on it (hole-burning technique). The number of addressed classes increases, so we have to loop the cleaning procedure of figure B.9 repeatedly with the comb-creation procedure until we obtain a single-class comb.

of this structure and has the advantage of reaching the Fourier limit defined in equation B.1 with a single preparation round:  $\frac{1}{\tau} = \frac{1}{T_{\text{prep}}}$ . In this case, as the frequency periodicity of the AFC is embedded in the preparation pulse and does not depend on the features of the pre-existing absorption structure on the  $\pm 1/2g \rightarrow \pm 3/2e$  transition, we simply create a square absorption feature with no periodicity.

This different scaling as a function of  $\Delta$  and  $B$  makes this method insensitive to the echo storage time, while the hole-burning method gets slower and slower as the peak width shrinks, according to equation B.1. Therefore, this technique is the most suitable to prepare combs from 8  $\mu\text{s}$  up to 50  $\mu\text{s}$  storage time, which are the typical storage times of the experiment of section 4.2.3.



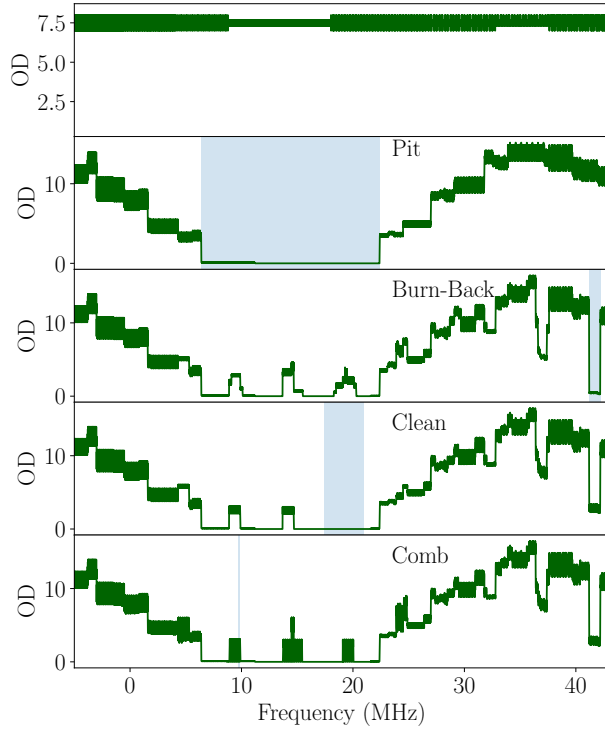


Figure B.11: Simulated inhomogeneous spectrum in a 48 MHz window in the case of: starting situation, when no optical pumping is performed (first plot); transparency window of 16 MHz, created by shining the blue semi-transparent pulse shown (second plot); absorption feature burnt-back inside the pit, where the burning back pulse is shown as well addressing a side transition (third plot); a cleaned spectrum (fourth plot); comb, where only the last of seven shone tooth-shaping pulses is shown (fifth plot). It is evident that, if we want to have a single-class comb, we need to repeat the cleaning procedure iteratively with the comb creation until the  $\pm 3/2g \rightarrow \pm 3/2e$  transition is cleaned (i.e. the absorption feature at the cleaning frequency in the last plot). This simulation has been performed by taking into consideration  $5 \times 10^4$  ions distributed over 200 MHz of spectrum and by assuming a laser linewidth of 10 kHz.

# Appendix C

## Further details for Chapter 4

### C.1 Details of the setup

In this section, I will provide additional details about the setup for the experiment reported in chapter 4.

#### C.1.1 Crystals

For our experiments, we used two  $\text{Pr}^{3+}:\text{Y}_2\text{SiO}_5$  crystals, a memory crystal (MC) and an interferometric filter crystal (IFC), described in appendix section B.2.2. The sizes of the two crystals are the same, 6 mm (width)  $\times$  4 mm (height)  $\times$  3 mm (depth), and they are accommodated on the same copper mount. In a first phase of the experiment (section 4.2.1), we employed the spring mount described in appendix section B.2.2. For the experiments in sections 4.2.2, 4.2.3 and 4.2.4.2, we switched to the monolithic mount (described in the same section as before), because there seemed to be a lack of crystal thermalization. At some point, we tied the memory crystal to its mount with some aluminum tape, to ensure even better thermal conduction, and we were afraid this strain could shift the center of the inhomogeneously broadened line. Thus, we proceeded to perform an inhomogeneous broadening measurement, reported in figure C.1, where we observed no spectral shift.

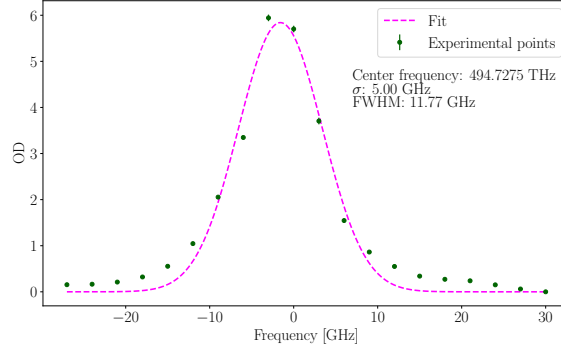


Figure C.1: Measurement of the inhomogeneously broadened line of the memory crystal. The green points are the experimental measurements, while the magenta dotted line is a Gaussian fit to those points. The fit predicts a FWHM of the broadened transition of 11.77 GHz.

### C.1.2 Laser beams

The laser we employed was the Toptica tapered amplifier (TA) SHG Pro laser described in appendix section B.1.1. In the same section, I described how we can use AOMs to create different beams at different frequencies. As mentioned in section 4.2, we have five different beams that are used to address the ions, coming from four different AOM channels. I will provide a description for each one of them. Note that all the AOMs we are using employ the double-pass configuration described in appendix section B.1.1.1, so all the frequency shifts I will quote must be multiplied by 2 to obtain the real shift of the beams. The AOM scheme is pictured in figure C.2.

**Memory preparation beam** The memory preparation beam is used to optically pump the memory crystal to create the desired features (see appendix section B.3.2). Its AOM is aligned to operate around 160.65 MHz, i.e., the first diffracted mode is shifted from the central frequency by this amount (in single pass). In the setup in figure 4.3, this beam is represented by the red dashed line, and 20 mW are typically out-coupled after the fiber;

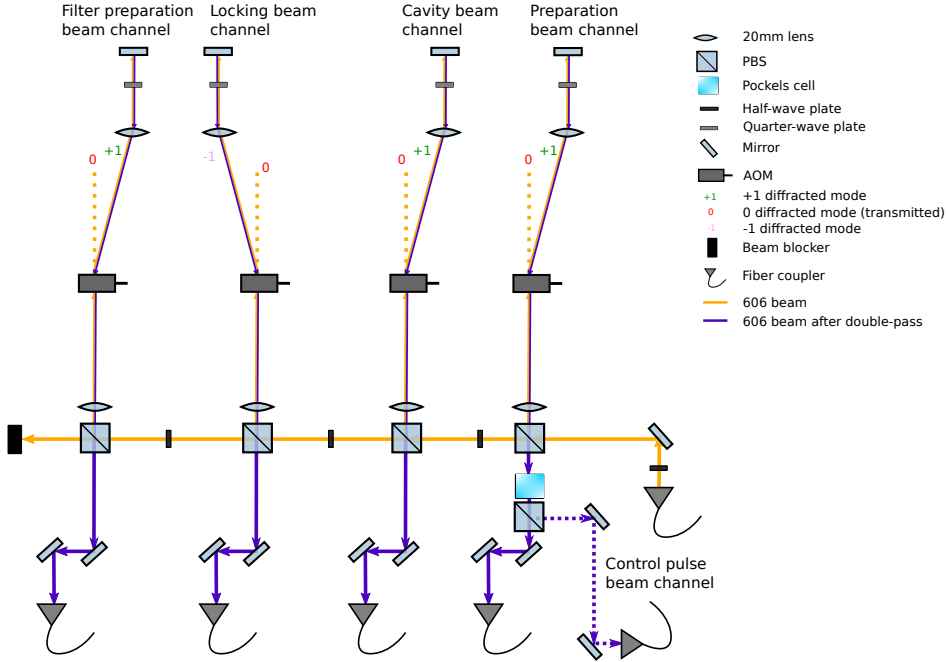


Figure C.2: Sketch of the AOM scheme we employed in our experiment. A strong 606 nm laser is injected from the bottom right coupler into 4 different AOM channels, all of them working in a double-pass configuration. The preparation channel is used also to produce control pulses for spin-wave storage: in that case, its polarization is changed with a Pockels cell to couple them into a different coupler. All the paths are aligned on the +1 diffracted mode of AOMs, except the locking beam path, which is coupled to the -1 mode.

in the spin-wave storage experiment reported in section 4.2.5, this value was increased up to 46 mW, because the same AOM channel was used to produce spin-wave control pulses with approximately the same power; however, it was still employed at around 20 mW for tailoring spectral structures. The

coupler focus is set in such a way to have a beam waist at the center of the memory crystal of  $300\ \mu\text{m}$ . This beam waist ensures the overlap between the spatial region prepared by the preparation beam and the cavity beam, in order for this last beam to always interact with a prepared spectral structure. Its polarization is first cleaned by means of a PBS—although this light travels through a polarization-maintaining (PM) fiber—and then is set parallel to the D2 axis of the crystal by means of a half-wave plate (HWP). As we have seen in section 2.1.2.1, this polarization is the one interacting the most with the  $\text{Pr}^{3+}$  ions; therefore, from now on, I will refer to this polarization as the interacting one. In this specific case, it coincides with the vertical polarization.

**Control pulse beam** The same AOM used for the memory preparation beam is employed to generate control pulses for the spin-wave storage experiment reported in section 4.2.5. In this case, the polarization of light is turned back to vertical thanks to a Pockels cell, clearly visible in figure C.2, and coupled to a different coupler. This beam has a typical power of 50 mW and a waist of  $150\ \mu\text{m}$  at the memory crystal.

**Cavity beam** The cavity beam is employed for sending pulses to the memory and to probe the spectral features we prepare. In the second case, we usually block the cavity by lifting the flip mirror just before the second cavity mirror and steer the beam onto the preparation/transmission detector, in order to be able to observe the prepared spectral features inside the crystal in single-pass. This is accomplished by sending a 4 ms-long square chirped pulse and detecting its transmission through the crystal. Its AOM frequency is 160.65 MHz, as the preparation one, and it is controlled by the same waveform generator. The power we route into this path is usually around  $160\ \mu\text{W}$  after the PBS. For a photon echo measurement (appendix sections A.1 and B.3.1), we increase the power to 1 mW, measured before the vacuum chamber. For most of our applications, we set this beam to the interacting polarization by tuning the half-wave plate before the BS. The beam waist of this beam is  $570\ \mu\text{m}$  before the mode-matching lens, and it

is bound to be  $75\ \mu\text{m}$  inside the cavity, which is the intrinsic waist of the cavity (see section C.1.3).

This same beam is used to probe the filter crystal, in reflection. When this procedure is carried out, we usually block the cavity after the first mirror, such to observe the 40% reflection from the first mirror, and we couple the reflection output of the BS into the single-mode fiber going to the filter crystal. After the fiber, its polarization is restored to the interacting one, and, after interacting with the filter, it is recoupled into a SM fiber, to be detected with a APD (in the case of classical pulses) or a SPAD (in the case of weak coherent states).

**Locking beam** This beam is the only one whose AOM is controlled by a voltage-controlled oscillator (VCO), the only beam set to the diffracted mode minus one, as clearly highlighted in figure C.2—this means that its central frequency is  $-160.65\ \text{MHz}$ , so  $-642.60\ \text{MHz}$  shifted (real shift) with respect to the other memory crystal beams—and the only one usually set to the non-interacting polarization, i.e., parallel to the  $D_1$  axis defined in section 2.1.2.1. Since we use this beam to stabilize the cavity, as I will describe in section C.1.5.2, we want this beam to interact as little as possible with the memory crystal, otherwise any changes affecting the crystal (e.g. vibrations) could have repercussions on the cavity stability. As such, its spatial features such as its beam waist and its position are the same as the cavity beam. Its transmission is monitored in transmission from the cavity by means of the transmission photodetector PDB450A from Thorlabs. The power of this beam does not have to be precise, since we only need to detect some light in transmission. However, we usually set it in the interval  $13\ \mu\text{W}$ – $20\ \mu\text{W}$ , as measured after the PBS. The VCO drives it with a frequency of  $160.5\ \text{MHz}$ , and it only switches the beam on and off, because we do not need to modulate it. This beam is employed in the cavity stabilization procedure explained in section C.1.5.2.

**Filter preparation beam** Similarly to the memory preparation beam, this beam is employed to tailor the inhomogeneously broadened line of

Beam	AOM Freq.	Waist	Driver	Power
Memory preparation	160.65 MHz	300 $\mu\text{m}$	SD-PXE-AOU-H0002	20 mW
Cavity	160.65 MHz	75 $\mu\text{m}$	SD-PXE-AOU-H0002	160 $\mu\text{W}$
Locking	-160.5 MHz	75 $\mu\text{m}$	VCO	13 $\mu\text{W}$
Filter preparation	160.65 MHz	310 $\mu\text{m}$	SD-PXE-AOU-H0002	10 mW
Control pulse	160.65 MHz	150 $\mu\text{m}$	SD-PXE-AOU-H0002	50 mW

Table C.1: Summary of the relevant characteristics of the five beams described in section C.1.2. The beam waist value is the value at the center of the respective crystals. In case of different power values, only the minimum ones reported in section C.1.2 were considered.

the filter crystal. It is controlled by the same RF generator and set at 160.65 MHz. Its polarization is interacting and its output power from the fiber is usually set at 10 mW and its radius is around 320  $\mu\text{m}$ , reaching a waist of 310  $\mu\text{m}$  in the crystal. Analogously to the memory preparation beam, this waist permits the overlap with the filter probing beam, i.e. the cavity beam reflected by the first cavity mirror and coupled into a SM fiber.

### C.1.3 Cavity

Some details about our cavity have been introduced in section 4.2, and throughout this section I am going to provide additional ones. The impedance-matched cavity is built with two 1/2-inch plano-concave curved mirrors, mounted on precision mounts. Both are installed on Thorlabs pillars sitting on the optical table and clamped to it. The second mirror is glued to a piezo actuator which is in turn glued to a piezo mount in teflon. This piezo can be driven to expand and shrink, in order to be able to scan the length of the cavity by some micrometers. Our cavity is asymmetrical, with respective radii of  $r_{\text{in}}=125$  mm for the input mirror and  $r_{\text{out}}=100$  mm for the output mirror. The reflectivity of the second mirror is  $R_{\text{out}}=97\%$ , so some of the light is transmitted when the cavity is on resonance and can be observed by means of a photodetector. If we fix the average optical depth of our atomic frequency comb to  $\tilde{d}=0.45$ , then, from the impedance-matching

condition 2.13, we have  $R_{\text{in}} = R_{\text{out}} e^{-2\bar{d}} \approx 40\%$ . The length of the cavity is fixed by setting the angle between the preparation beam and the cavity beam to  $5^\circ$ : once this condition is fixed, the minimum length of the cavity that ensures its stability is  $L = 208$  mm, which is a suitable length to fit the vacuum chamber between the two mirrors and still be able to align it or insert flip mirrors into the cavity path. The stability of this cavity is given by  $g_1 \cdot g_2 = 0.72$ , where  $g_i = 1 - \frac{L}{r_i}$  [191]. The beam waist of a beam coupled to the TEM00 mode of this resonator is found at 117.8 mm (90.6 mm) from the first (second) mirror. Its dimension at this point is  $75 \mu\text{m}$ , while the beam spot size is respectively  $312 \mu\text{m}$  ( $245 \mu\text{m}$ ) at the first (second) mirror.

The free spectral range (FSR) of the empty cavity only depends on its length, and it is  $\text{FSR} = \frac{c}{2L} = 719$  MHz. The finesse of the cavity  $\mathcal{F}_{\text{cav}}$  only depends on mirror reflectivities and intra-cavity losses and it is given by  $\mathcal{F}_{\text{cav}} = \frac{\pi \sqrt[4]{R_{\text{in}} R_{\text{out}}}}{1 - \sqrt{R_{\text{in}} R_{\text{out}}}} \approx 6.5$  (in the lossless case). The linewidth of the empty cavity is finally the ratio between these two last quantities:  $\gamma_{\text{cav}} = \frac{\mathcal{F}_{\text{cav}}}{\text{FSR}} \approx 111$  MHz. In section 4.2.4, I reported on how manipulating the absorption of the ions of the crystal sitting inside the cavity produces a virtual enlargement of the cavity and hence a reduction of its FSR.

### C.1.4 Cryostation and noise

To perform this experiment, we are using the last cryostat described in appendix section B.2. I have already shown the effect of the cryostat noise on the AFC echo in single-pass in figure B.3. We did not know whether the cavity was going to affect our noisy regions, therefore we repeated this investigation with the cavity echo. Figure C.3 mimics figure B.3, and we can observe that no substantial change, in the qualitative behaviour, is observed with respect to the single-pass case.

A more thorough analysis is shown in figure C.4. Here both the positions of the input pulse with respect to the end of the AFC preparation and the position of the sequence in the cryostat cycle are scanned, with a resolution of 4.5 ms and 40 steps for the first delay and 40 steps for the second delay. In the end, a color plot is constructed by calculating the echo efficiency for each position.



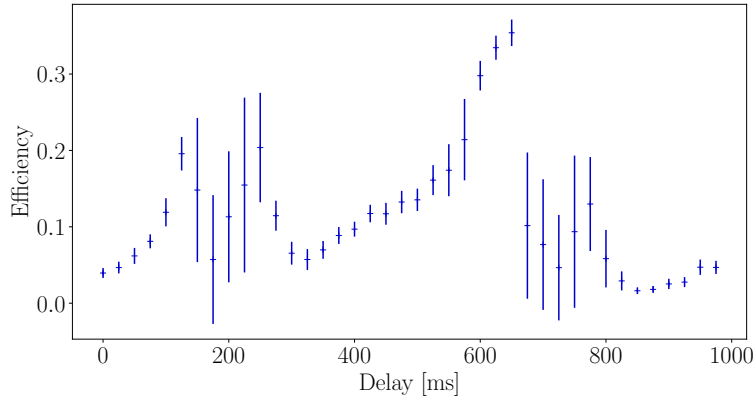


Figure C.3: AFC efficiency in cavity as a function of the delay between the beginning of the cryostat cycle and the start of the sequence. The regions with the most intense noise are the ones with higher standard deviation, 200 ms-310 ms and 730 ms-830 ms intervals. The AFC storage time is 10  $\mu$ s.

## C.1.5 Cavity alignment and stabilization

### C.1.5.1 Aligning the cavity

As introduced in section C.1.3, our impedance-matched cavity is mounted on two pillars clamped onto the optical table. In order to align it, we drive the piezo on the back of the second mirror with a triangle wave to change the length of the cavity and observe the cavity modes in transmission. In figure C.5, an example of what we observe on the oscilloscope is reported. The piezo is driven by an Arduino Due microcontroller, whose digital-to-analog converter output is connected to the piezo amplifier, from 0.5 V to 2.5 V in around 10 ms, and this signal is then amplified by means of a PiezoMaster VP7206 amplifier to the range 88 V to 141 V and eventually supplied to the piezo actuator.

In figure C.5, the Lorentzian modes out of the cavity are shown in blue. It is apparent that they are quite broad and they display some deviations from the Lorentzian shape close to the minima. This behavior conceals

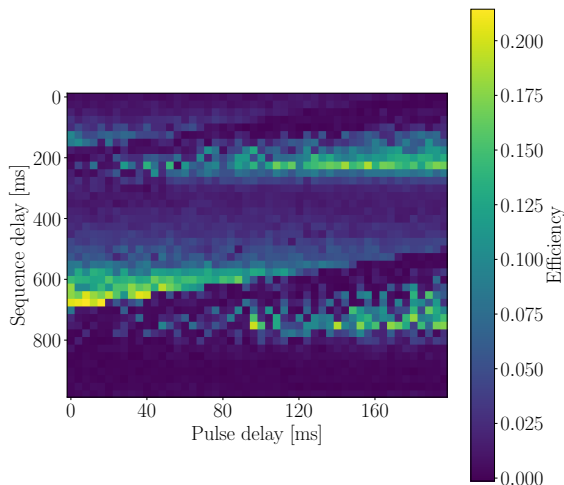


Figure C.4: AFC efficiency in cavity when delaying both the input pulse to the AFC with respect to the AFC preparation and the sequence inside the cryostat cycle. The AFC storage time is  $10\ \mu\text{s}$ .

the imperfection of our alignment procedure and does not allow to reach a perfect alignment only by assessing the shape of the modes.

The alignment procedure of the cavity beam on the cavity involves adjusting several degrees of freedom of the setup, the main one being the vertical and horizontal tilts of the two cavity mirrors and of the two input mirrors the beam is impinging on. Additionally to that, we can change the position of the mode-matching lens, a lens of 15 cm focal length put at 7.3 cm from the first cavity mirror. In terms of focus, also the focus of the coupler outcoupling the cavity beam can be modified. These procedures are performed iteratively to achieve a condition close to the one showed in figure C.5.

For the locking beam, the only degrees of freedom we can optimize are the tilts of its input mirrors and the focus of its outcoupler, because all the other elements are in common with the cavity beam. The alignment procedure for the locking beam should accomplish an overlap between it

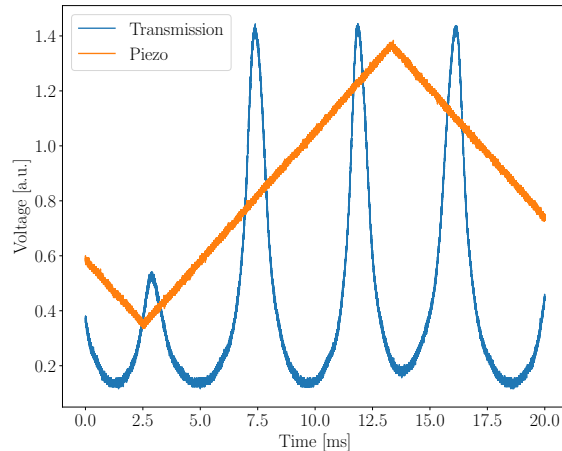


Figure C.5: Plot of the cavity modes and of the ramp signal supplied to the piezo. The piezo signal trace has been re-scaled to have the same height as the modes, but was originally ranging from 0.5 V to 2.5 V.

and the cavity beam, with its same beam waist and divergence, such that the two beams have the same alignment into the cavity.

### C.1.5.2 Stabilizing the cavity

Our impedance-matched cavity mirrors, as described at the beginning of this appendix, are clamped to the optical table separately. As such, both of them are independently affected by noise coupled to the optical table or by air movements in the lab. One example of this noise is vibrations coming from the compressor, which I describe thoroughly in appendix section B.2.1 and section C.1.4. The effect of these environmental factors is bringing the cavity out of resonance. So, we need an active stabilization mechanism to be able to restore it into the resonant configuration.

To fulfill this task, we use an auxiliary beam with respect to the cavity beam, that is, the locking beam mentioned in the previous section. This beam is shone through the same spatial path as the cavity beam, and it is

partially transmitted by the second mirror. We pick up this light by means of the transmission detector shown in figure 4.3, and its output is fed to the Arduino Due. The strength of this transmitted signal can be maximized to keep the cavity on resonance. We can distinguish three phases of the locking mechanism:

1. Arduino tries to shrink and enlarge the piezo, to find which of the two directions yields a better transmission;
2. Then, it pushes the piezo in that direction, until it reaches the maximum;
3. Finally, it wiggles the piezo around the maximum position, but always ensuring that the transmission does not drop. If something pushes the cavity off-resonance, the whole procedure starts over.

The algorithm is very basic because, as I have just described, it does not look for the global maximum in transmission, nor has it the capability to understand in which direction to move the piezo prior to scanning it, like the Pound-Drever-Hall locking system mentioned in appendix section B.1.1 has. Nevertheless, considering the high degree of passive stability of our cavity and the fact that no modulation of the light is required in our case, this logic is satisfying our demands. A trace of the cavity transmission is shown in figure C.6. In the first phase, encompassed by the Arduino TTL, the cavity is actively stabilized for 450 ms. For the left 550 ms, the cavity has no active stabilization, but nonetheless remains in resonance. The small drop shown in the free-drifting phase is 24% of the whole fringe (which is the blue shaded area between the maximum transmission, in green, and the minimum transmission, in dark red), which shows that our cavity is resilient enough against external perturbations.

In the actual experiment, employing this method of stabilization for the whole experimental cycle is not feasible. Indeed, when we send weak coherent light to the cavity, we connect single photon detectors to the reflection path (see figure 4.3); but this path is shared with the locking light, which has a power on the order of  $\mu\text{W}$ , which would be coupled to the detectors

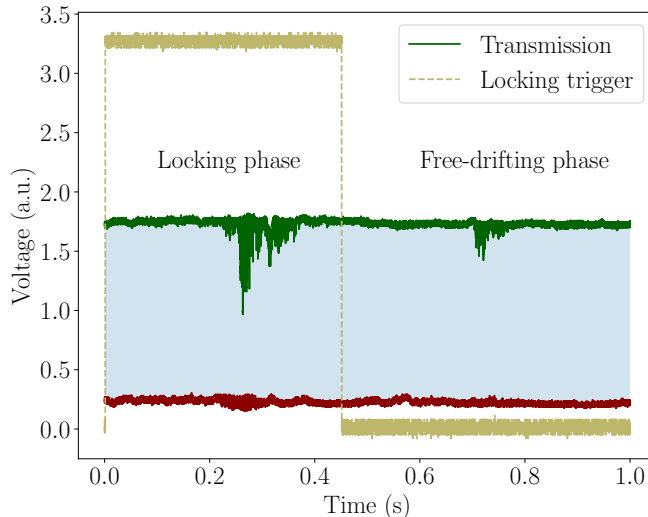


Figure C.6: Typical locking cycle of our cavity. After a first 450 ms-long locking phase, when Arduino is actively maximizing the transmission (in dark green) of non-interacting polarization light through the cavity (high TTL), the active locking is suspended and the cavity is free-drifting for 550 ms. The small decrease in transmission around 750 ms is around 24% of the difference between the maximum transmission and the minimum transmission (in dark red).

and damage them. In these circumstances, locking the cavity and performing measurements at the same time is impossible. Therefore, we divide the experiment into two distinct phases:

1. During the first phase, lasting approximately from 190 ms to 400 ms (depending on the specific performed experiment), the VCO switches the locking AOM on, so the locking light is circulating into the setup; during this period, mechanical shutters on the detector path are in the closed position to protect the detector. We use this period of time to prepare the AFC (see appendix section B.3.2) inside the crystal,

since the preparation beam is off-axis;

2. In the second phase (whose length changes depending on the experiment we are performing, but it is usually ranging from 10 ms to some hundreds of ms), the locking AOM is turned off and the shutter on the locking path is switched to close. In order to block potential leakage through the AOM, the preparation shutter is also closed, although no pulse is coming from that AOM. The detector path is now free and weak coherent states are sent to the cavity and retrieved in reflection.

The entire procedure is repeated once per second, synchronized with the cryostat cycle.

As I mentioned in section C.1.2, the locking light is detuned by  $-642.60$  MHz with respect to our cavity light interacting with the comb. As such, the length of the cavity yielding maximum transmission for it does not correspond to the same length for which the cavity light has the maximum interaction with the comb, since the cavity FSR is 720 MHz. Therefore, in order to overcome this limitation, our locking logic stabilizes the cavity to the maximum locking light transmission position; then, after the lock has finished working, it shifts the piezo very slowly to another position, the one which guarantees an input beam mode to be at the spectral position of the comb. The offset of the piezo voltage with respect to the resonant position is adjusted empirically by us by turning a potentiometer which changes the voltage supplied by the Arduino to the piezo. The best method we devised in order to choose this position is sending a bright pulse to the AFC and maximizing its echo intensity by fine-tuning the position of the potentiometer.

At the end of the cycle, the piezo is slowly brought again back to the locking light resonance position, and the locking mechanism starts acting again on the piezo to maximize the transmission.

The whole experimental cycle is sketched in figure C.7. The locking period covers approximately all the phase up to the Wait time.

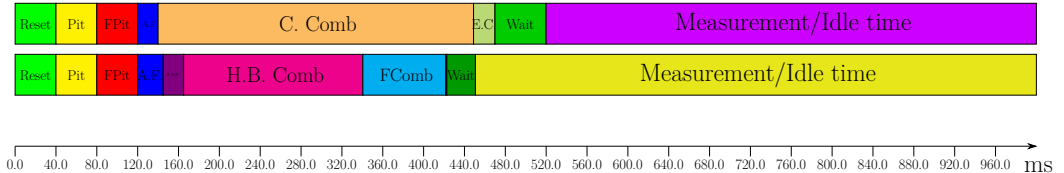


Figure C.7: Sketch of the sequence timings for preparing a comb via the coherent technique (first row) or with the hole-burning technique (second row), with scaled durations. The first 4 steps are common to both techniques: after resetting the ion ensemble by shining a strong chirped laser on it, a pit in the memory (*Pit*) and in the filter crystal (*FPit*) are prepared, followed by the preparation of an absorption feature (*A.F.*) in the memory. **Coherent comb:** with the coherent comb, we never need a comb in the filter crystal (which is only needed for the AFC interferometer of section C.2, when the memory comb is a hole-burned one), so we proceed by preparing a comb in the memory (*C. Comb.*), with an extra clean phase (*E.C.*); after a waiting time (*Wait*), meant to wait for the shutters to close or open and to the AOMs to switch on or off completely, we can finally measure (*Measurement/Idle time*).

**Hole-burned comb:** in this case, an absorption feature in the filter is prepared (*F.A.F.*, *filter absorption feature*), and hole-burned combs are prepared both in the memory (*H.B. Comb*) and in the crystal (*FComb*). The rest of the cycle is the same as with the coherent comb.

## C.2 Analysis of the AFC interferometer

In section 4.2.2, I have showed how we analyzed the visibility and the fidelity of our qubits stored in our quantum memory, and I called it system fidelity. This does not account for the fidelity of the AFC-based unbalanced Mach-Zehnder interferometer, through which we can calculate the fidelity of our quantum memory. As I already described in chapter 4, every other cryostat cycle we prepared a saturated absorption feature inside the memory, such that the cavity was stopped. Therefore, only the reflected qubits were crossing the interferometer, and we used them to estimate the interfer-

ometer visibility and fidelity. In figure C.8, interference fringes for the interferometer are visible, together with their visibilities. The fringe visibilities are  $V_{0^\circ}^{\text{interf}} = (91.6 \pm 2.4) \%$ ,  $V_{45^\circ}^{\text{interf}} = (88.5 \pm 2.7) \%$ ,  $V_{90^\circ}^{\text{interf}} = (83.6 \pm 3.1) \%$  and  $V_{135^\circ}^{\text{interf}} = (82.6 \pm 3.2) \%$ ; repeating the same procedure adopted for the qubit visibility, we estimated a visibility of  $V_{\text{avg}}^{\text{interf}} = (86.6 \pm 2.8) \%$ ; this, together with the fidelity in the computational basis  $F_{\text{poles}}^{\text{interf}} = (96.0 \pm 0.3) \%$ , yields an interferometer fidelity of  $F^{\text{interf}} = (94.2 \pm 1.0) \%$ .

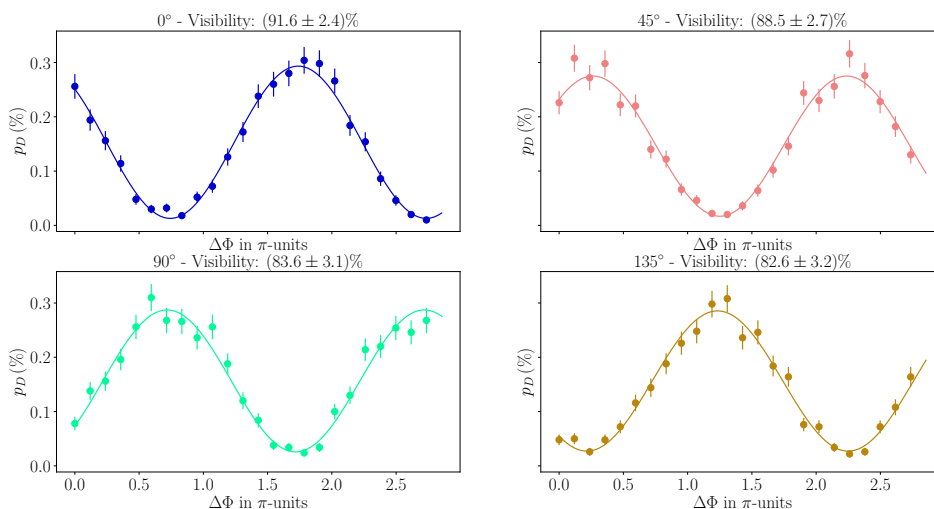


Figure C.8: Interference fringes for different measurement bases obtained by sending only the reflected pulses from the first cavity mirror to the interferometer. The plots show the detection probability per trial ( $p_D$ ) versus the comb phase change, expressed in units of  $\pi$ . These measurements were recorded with 2000 qubits per second. The detection window for this analysis was 1  $\mu\text{s}$ .

The whole procedure for the memory and for the interferometer is summarized in figure C.9; in particular, the characterization is visible in the lower sketch of the same figure.



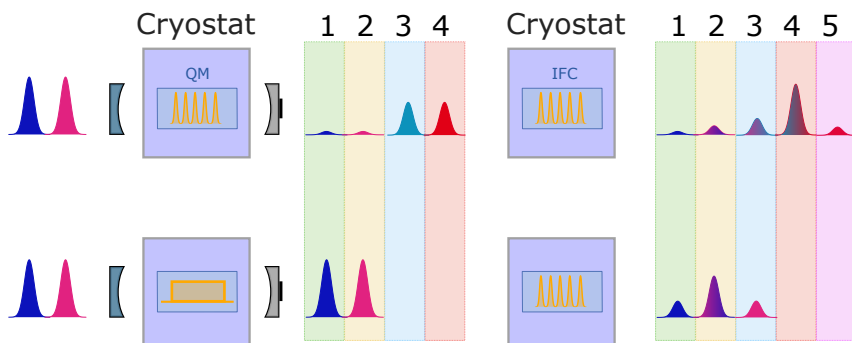


Figure C.9: Sketch of the two different cases. **Upper sketch:** the prepared qubit (blue and magenta pulses on the left, where  $|e\rangle$  is blue and  $|l\rangle$  magenta) is absorbed by the AFC in the memory (QM) embedded in the cavity, and gives rise to two echoes. Its reflected components from the cavity are respectively shown in time-bins 1 and 2 (green and yellow), while its echoes are contained in bins 3 and 4 (light blue and light red). The size of each bin is  $1\ \mu\text{s}$ . After crossing the interferometric filter crystal (IFC), 5 temporal bins will be occupied: both reflections and echoes from the cavity will be either transmitted or stored and re-emitted from the  $1\ \mu\text{s}$  AFC. Since the separation between the qubit components is also  $1\ \mu\text{s}$ , interference will occur in bins 1–4. We are interested in the interference between the echoes from the memory crystal, contained in bin 4. **Lower sketch:** the cavity is blocked by a high OD absorption feature, so the input pulses are reflected from the cavity and no echo is emitted by the memory. Interference in the filter crystal only occurs in bin 2 between the reflected  $|e\rangle$  and  $|l\rangle$ .

# Appendix D

## Further details for Chapter 5

### D.1 Details of the setup

In this section, I will provide additional details about the new setup that includes the filtering cavity for the experiment reported in chapter 5.

#### D.1.1 Filtering cavity

The filtering cavity was designed by Josep Maria Batllori Berenguer, a master student of our group. All the relevant quantities about Fabry-Perot cavities I will mention are explained in detail in appendix section C.1.3. The cavity is a Fabry-Perot cavity, 12.1 cm long, therefore its FSR (from equation 4.3 with  $n_g = 1$ ) is 1.24 GHz. The two plano-concave (100 mm curvature) cavity mirrors have a reflectivity at 1552 nm of about 96.9%, yielding a cavity finesse of 99.8. From these values, we can calculate a filter cavity bandwidth as  $\frac{1.24\text{GHz}}{99.8} \approx 12.4\text{MHz}$ .

In figure D.1, we can see the spectra of the etalon, the Semrock bandpass filter, the FBG and our filter cavity. We can notice that the overlap is very narrow.

We have actually installed the cavity and figure D.2 shows the setup built around it. A temperature controller stabilizes the cavity temperature around 25 °C, and this temperature is often tweaked manually by us to

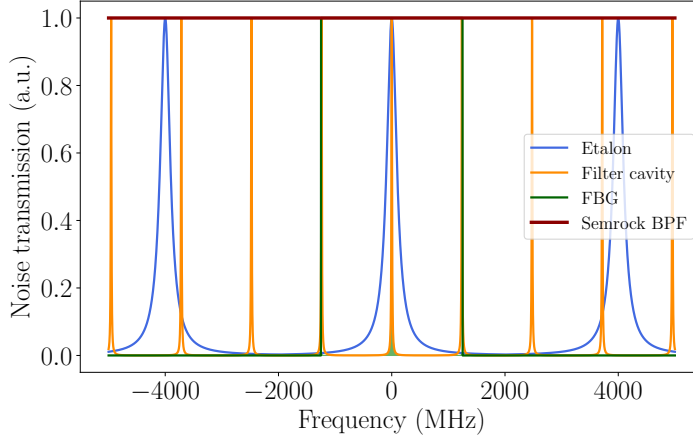


Figure D.1: Spectra of the filters introduced throughout this section: the etalon, the Semrock band-pass filter (Semrock BFG), the fiber Bragg grating (FBG), and the filter cavity. The spectra are shown in a 10 MHz interval around the 0. The central green shaded area represents the spectral overlap of these 4 filters.

bring the cavity back into the frequency range that the piezo can span. The signal is coupled through the planar facet of the first mirror, which is AR-coated ( $< 0.2\%$  reflection), via a 250 mm lens at 20 cm from the cavity center. The cavity stabilization is performed in a very similar fashion as the one used in the experiment reported in chapter 4 and detailed in appendix section C.1.5.2: the locking mechanism is alternating between active stabilization and measurement time (passive stability). To implement it, two synchronized chopper wheels are installed in the setup: the first one either lets a classical 606 nm laser beam through or blocks it. The second chopper wheel either blocks the detector path when the first one is “open” or lets light pass. When the classical 606 nm light is passing through the waveguide, it gets converted to 1552 nm (the pump beam at 994 nm is always on) and is coupled to the filter cavity, but it does not reach the detector because the second chopper wheel is blocking it. The converted signal is

observed with a photodetector in transmission and fed-back to an Arduino Due micro-controller, which can move the cavity piezo and stabilize the cavity around the maximum transmission. When the strong 606 nm path is blocked, only weak coherent light is propagating into the waveguide. In this phase, we rely on the passive stability of the cavity, and the only actively stabilized parameter is the cavity temperature. Weak coherent states get converted and filtered and they can reach the detector because the path is free.

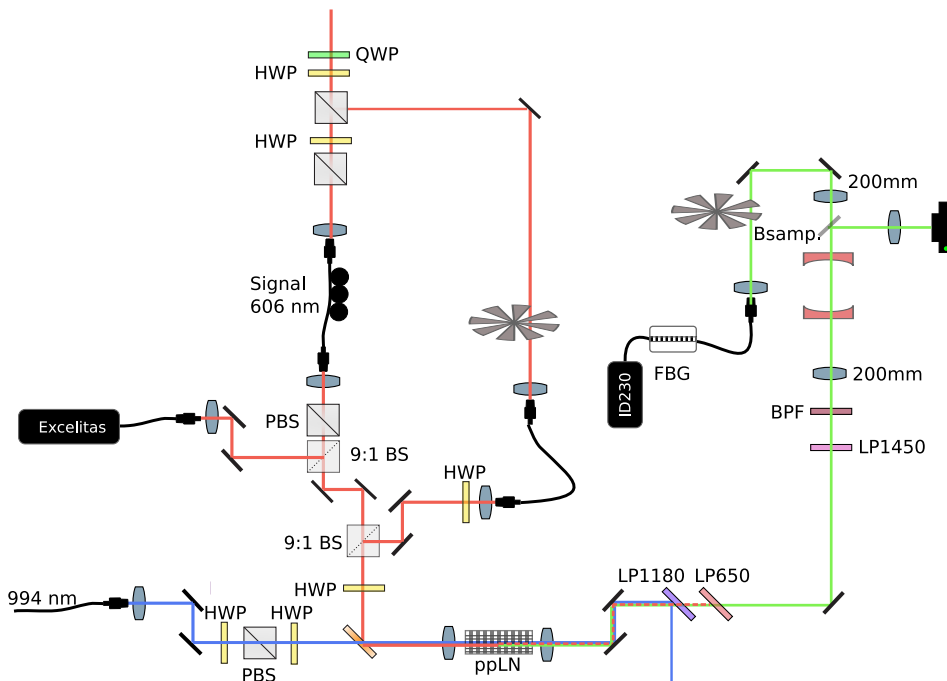


Figure D.2: QFC new setup. Its full explanation is provided in the main text. The main differences with respect to the old setup are concerned with the use of the new NTT waveguide and with the filtering stages, where a new filtering cavity is added and chopping wheels are used to prevent the cavity locking light from reaching the single-photon detectors.



# Bibliography

- <sup>1</sup>N. Gisin, G. Ribordy, W. Tittel, and H. Zbinden, “Quantum cryptography”, [Reviews of Modern Physics](#) **74**, 145–195 (2002) (cit. on pp. [2](#), [5](#)).
- <sup>2</sup>F. Xu, X. Ma, Q. Zhang, H.-K. Lo, and J.-W. Pan, “Secure quantum key distribution with realistic devices”, [Reviews of Modern Physics](#) **92**, 025002 (2020) (cit. on p. [2](#)).
- <sup>3</sup>Y. Cao, Y. Zhao, Q. Wang, J. Zhang, S. X. Ng, and L. Hanzo, “The Evolution of Quantum Key Distribution Networks: On the Road to the Qinternet”, [IEEE Communications Surveys & Tutorials](#) **24**, 839–894 (2022) (cit. on p. [2](#)).
- <sup>4</sup>C. L. Degen, F. Reinhard, and P. Cappellaro, “Quantum sensing”, [Reviews of Modern Physics](#) **89**, 035002 (2017) (cit. on p. [2](#)).
- <sup>5</sup>S. Pirandola, B. R. Bardhan, T. Gehring, C. Weedbrook, and S. Lloyd, “Advances in photonic quantum sensing”, [Nature Photonics](#) **12**, 724–733 (2018) (cit. on p. [2](#)).
- <sup>6</sup>M. A. Nielsen and I. L. Chuang, *Quantum Computation and Quantum Information: 10th Anniversary Edition*, Dec. 2010 (cit. on p. [3](#)).
- <sup>7</sup>W. K. Wootters and W. H. Zurek, “A single quantum cannot be cloned”, [Nature](#) **299**, 802–803 (1982) (cit. on p. [3](#)).
- <sup>8</sup>C. Simon, G. Weihs, and A. Zeilinger, “Optimal Quantum Cloning via Stimulated Emission”, [Physical Review Letters](#) **84**, 2993–2996 (2000) (cit. on p. [5](#)).

- <sup>9</sup>N. Gisin, “How far can one send a photon?”, *Frontiers of Physics* **10**, 100307 (2015) (cit. on p. 5).
- <sup>10</sup>H.-J. Briegel, W. Dür, J. I. Cirac, and P. Zoller, “Quantum Repeaters: The Role of Imperfect Local Operations in Quantum Communication”, *Physical Review Letters* **81**, 5932–5935 (1998) (cit. on p. 5).
- <sup>11</sup>L.-M. Duan, M. D. Lukin, J. I. Cirac, and P. Zoller, “Long-distance quantum communication with atomic ensembles and linear optics”, *Nature* **414**, 413–418 (2001) (cit. on pp. 7, 12, 37, 48).
- <sup>12</sup>N. Sangouard, C. Simon, H. de Riedmatten, and N. Gisin, “Quantum repeaters based on atomic ensembles and linear optics”, *Reviews of Modern Physics* **83**, 33–80 (2011) (cit. on pp. 7, 48, 66).
- <sup>13</sup>M. Lettner, M. Mücke, S. Riedl, C. Vo, C. Hahn, S. Baur, J. Bochmann, S. Ritter, S. Dürr, and G. Rempe, “Remote Entanglement between a Single Atom and a Bose-Einstein Condensate”, *Physical Review Letters* **106**, 210503 (2011) (cit. on p. 8).
- <sup>14</sup>M. Körber, O. Morin, S. Langenfeld, A. Neuzner, S. Ritter, and G. Rempe, “Decoherence-protected memory for a single-photon qubit”, *Nature Photonics* **12**, 18–21 (2018) (cit. on p. 8).
- <sup>15</sup>Y.-W. Cho, G. T. Campbell, J. L. Everett, J. Bernu, D. B. Higginbottom, M. T. Cao, J. Geng, N. P. Robins, P. K. Lam, and B. C. Buchler, “Highly efficient optical quantum memory with long coherence time in cold atoms”, *Optica* **3**, 100–107 (2016) (cit. on pp. 8, 12, 15).
- <sup>16</sup>Y. Wang, J. Li, S. Zhang, K. Su, Y. Zhou, K. Liao, S. Du, H. Yan, and S.-L. Zhu, “Efficient quantum memory for single-photon polarization qubits”, *Nature Photonics* **13**, 346–351 (2019) (cit. on pp. 8, 12).
- <sup>17</sup>Y.-F. Hsiao, P.-J. Tsai, H.-S. Chen, S.-X. Lin, C.-C. Hung, C.-H. Lee, Y.-H. Chen, Y.-F. Chen, I. A. Yu, and Y.-C. Chen, “Highly Efficient Coherent Optical Memory Based on Electromagnetically Induced Transparency”, *Physical Review Letters* **120**, 183602 (2018) (cit. on pp. 8, 12, 15).

- <sup>18</sup>N. Maring, P. Farrera, K. Kutluer, M. Mazzer, G. Heinze, and H. de Riedmatten, “Photonic quantum state transfer between a cold atomic gas and a crystal”, *Nature* **551**, 485–488 (2017) (cit. on pp. 8, 15, 57, 100, 110).
- <sup>19</sup>B. Julsgaard, J. Sherson, J. I. Cirac, J. Fiurášek, and E. S. Polzik, “Experimental demonstration of quantum memory for light”, *Nature* **432**, 482–486 (2004) (cit. on p. 8).
- <sup>20</sup>K. F. Reim, J. Nunn, V. O. Lorenz, B. J. Sussman, K. C. Lee, N. K. Langford, D. Jaksch, and I. A. Walmsley, “Towards high-speed optical quantum memories”, *Nature Photonics* **4**, 218–221 (2010) (cit. on p. 8).
- <sup>21</sup>K. F. Reim, P. Michelberger, K. C. Lee, J. Nunn, N. K. Langford, and I. A. Walmsley, “Single-Photon-Level Quantum Memory at Room Temperature”, *Physical Review Letters* **107**, 053603 (2011) (cit. on p. 8).
- <sup>22</sup>M. Hosseini, G. Campbell, B. M. Sparkes, P. K. Lam, and B. C. Buchler, “Unconditional room-temperature quantum memory”, *Nature Physics* **7**, 794–798 (2011) (cit. on p. 8).
- <sup>23</sup>W. L. Yang, Z. Q. Yin, Y. Hu, M. Feng, and J. F. Du, “High-fidelity quantum memory using nitrogen-vacancy center ensemble for hybrid quantum computation”, *Physical Review A* **84**, 010301 (2011) (cit. on p. 8).
- <sup>24</sup>G. D. Fuchs, G. Burkard, P. V. Klimov, and D. D. Awschalom, “A quantum memory intrinsic to single nitrogen–vacancy centres in diamond”, *Nature Physics* **7**, 789–793 (2011) (cit. on p. 8).
- <sup>25</sup>D. Kielpinski, V. Meyer, M. A. Rowe, C. A. Sackett, W. M. Itano, C. Monroe, and D. J. Wineland, “A Decoherence-Free Quantum Memory Using Trapped Ions”, *Science* **291**, 1013–1015 (2001) (cit. on p. 8).
- <sup>26</sup>T. E. Northup and R. Blatt, “Quantum information transfer using photons”, *Nature Photonics* **8**, 356–363 (2014) (cit. on p. 8).
- <sup>27</sup>Y. Wang, M. Um, J. Zhang, S. An, M. Lyu, J.-N. Zhang, L.-M. Duan, D. Yum, and K. Kim, “Single-qubit quantum memory exceeding ten-minute coherence time”, *Nature Photonics* **11**, 646–650 (2017) (cit. on p. 8).



- <sup>28</sup>S. Chen, Y.-A. Chen, T. Strassel, Z.-S. Yuan, B. Zhao, J. Schmiedmayer, and J.-W. Pan, “Deterministic and Storable Single-Photon Source Based on a Quantum Memory”, [Physical Review Letters](#) **97**, 173004 (2006) (cit. on p. 8).
- <sup>29</sup>D. N. Matsukevich, T. Chanelière, S. D. Jenkins, S.-Y. Lan, T. A. B. Kennedy, and A. Kuzmich, “Deterministic Single Photons via Conditional Quantum Evolution”, [Physical Review Letters](#) **97**, 013601 (2006) (cit. on p. 8).
- <sup>30</sup>P. Kok, W. J. Munro, K. Nemoto, T. C. Ralph, J. P. Dowling, and G. J. Milburn, “Linear optical quantum computing with photonic qubits”, [Reviews of Modern Physics](#) **79**, 135–174 (2007) (cit. on p. 8).
- <sup>31</sup>F. Bussi eres, N. Sangouard, M. Afzelius, H. de Riedmatten, C. Simon, and W. Tittel, “Prospective applications of optical quantum memories”, [Journal of Modern Optics](#) **60**, 1519–1537 (2013) (cit. on pp. 8, 10).
- <sup>32</sup>M. Hosseini, B. M. Sparkes, G. H etet, J. J. Longdell, P. K. Lam, and B. C. Buchler, “Coherent optical pulse sequencer for quantum applications”, [Nature](#) **461**, 241–245 (2009) (cit. on pp. 8, 11).
- <sup>33</sup>M. P. Hedges, J. J. Longdell, Y. Li, and M. J. Sellars, “Efficient quantum memory for light”, [Nature](#) **465**, 1052–1056 (2010) (cit. on pp. 8, 11, 12, 15).
- <sup>34</sup>S. A. Moiseev and S. Kr oll, “Complete Reconstruction of the Quantum State of a Single-Photon Wave Packet Absorbed by a Doppler-Broadened Transition”, [Physical Review Letters](#) **87**, 173601 (2001) (cit. on p. 8).
- <sup>35</sup>B. Kraus, W. Tittel, N. Gisin, M. Nilsson, S. Kr oll, and J. I. Cirac, “Quantum memory for nonstationary light fields based on controlled reversible inhomogeneous broadening”, [Physical Review A](#) **73**, 020302 (2006) (cit. on p. 8).
- <sup>36</sup>O. Kocharovskaya and Y. I. Khanin, “Population trapping and coherent bleaching of a three-level medium by a periodic train of ultrashort pulses”, [Journal of Experimental and Theoretical Physics](#) **63**, 945 (1986) (cit. on pp. 8, 12).

- <sup>37</sup>H. Xia, S. J. Sharpe, A. J. Merriam, and S. E. Harris, “Electromagnetically induced transparency in atoms with hyperfine structure”, *Physical Review A* **56**, R3362–R3365 (1997) (cit. on pp. 8, 12).
- <sup>38</sup>K. Heshami, D. G. England, P. C. Humphreys, P. J. Bustard, V. M. Acosta, J. Nunn, and B. J. Sussman, “Quantum memories: emerging applications and recent advances”, *Journal of Modern Optics* **63**, 2005–2028 (2016) (cit. on pp. 8, 10).
- <sup>39</sup>N. Sinclair, E. Saglamyurek, H. Mallahzadeh, J. A. Slater, M. George, R. Ricken, M. P. Hedges, D. Oblak, C. Simon, W. Sohler, and W. Tittel, “Spectral Multiplexing for Scalable Quantum Photonics using an Atomic Frequency Comb Quantum Memory and Feed-Forward Control”, *Physical Review Letters* **113**, 053603 (2014) (cit. on pp. 9, 14, 83).
- <sup>40</sup>T.-S. Yang, Z.-Q. Zhou, Y.-L. Hua, X. Liu, Z.-F. Li, P.-Y. Li, Y. Ma, C. Liu, P.-J. Liang, X. Li, Y.-X. Xiao, J. Hu, C.-F. Li, and G.-C. Guo, “Multiplexed storage and real-time manipulation based on a multiple degree-of-freedom quantum memory”, *Nature Communications* **9**, 3407 (2018) (cit. on pp. 9, 14).
- <sup>41</sup>E. Saglamyurek, M. Grimau Puigibert, Q. Zhou, L. Giner, F. Marsili, V. B. Verma, S. Woo Nam, L. Oesterling, D. Nippa, D. Oblak, and W. Tittel, “A multiplexed light-matter interface for fibre-based quantum networks”, *Nature Communications* **7**, 11202 (2016) (cit. on p. 9).
- <sup>42</sup>A. Seri, D. Lago-Rivera, A. Lenhard, G. Corrielli, R. Osellame, M. Mazzer, and H. de Riedmatten, “Quantum Storage of Frequency-Multiplexed Heralded Single Photons”, *Physical Review Letters* **123**, 080502 (2019) (cit. on pp. 9, 11, 14).
- <sup>43</sup>S.-Y. Lan, A. G. Radnaev, O. A. Collins, D. N. Matsukevich, T. a. B. Kennedy, and A. Kuzmich, “A Multiplexed Quantum Memory”, *Optics Express* **17**, 13639–13645 (2009) (cit. on p. 9).
- <sup>44</sup>Y.-F. Pu, N. Jiang, W. Chang, H.-X. Yang, C. Li, and L.-M. Duan, “Experimental realization of a multiplexed quantum memory with 225 individually accessible memory cells”, *Nature Communications* **8**, 15359 (2017) (cit. on pp. 9, 48, 128).

- <sup>45</sup>R. Chrapkiewicz, M. Dąbrowski, and W. Wasilewski, “High-Capacity Angularly Multiplexed Holographic Memory Operating at the Single-Photon Level”, *Physical Review Letters* **118**, 063603 (2017) (cit. on pp. 9, 48).
- <sup>46</sup>L. Tian, Z. Xu, L. Chen, W. Ge, H. Yuan, Y. Wen, S. Wang, S. Li, and H. Wang, “Spatial Multiplexing of Atom-Photon Entanglement Sources using Feedforward Control and Switching Networks”, *Physical Review Letters* **119**, 130505 (2017) (cit. on p. 9).
- <sup>47</sup>I. Usmani, M. Afzelius, H. de Riedmatten, and N. Gisin, “Mapping multiple photonic qubits into and out of one solid-state atomic ensemble”, *Nature Communications* **1**, 12 (2010) (cit. on p. 9).
- <sup>48</sup>M. Bonarota, J.-L. L. Gouët, and T. Chanelière, “Highly multimode storage in a crystal”, *New Journal of Physics* **13**, 013013 (2011) (cit. on p. 9).
- <sup>49</sup>C. Clausen, I. Usmani, F. Bussièrès, N. Sangouard, M. Afzelius, H. de Riedmatten, and N. Gisin, “Quantum storage of photonic entanglement in a crystal”, *Nature* **469**, 508–511 (2011) (cit. on pp. 9, 11, 14, 48, 57).
- <sup>50</sup>M. Gündoğan, P. M. Ledingham, K. Kutluer, M. Mazzera, and H. de Riedmatten, “Solid State Spin-Wave Quantum Memory for Time-Bin Qubits”, *Physical Review Letters* **114**, 230501 (2015) (cit. on pp. 9, 14, 53).
- <sup>51</sup>P. Jobez, N. Timoney, C. Laplane, J. Etesse, A. Ferrier, P. Goldner, N. Gisin, and M. Afzelius, “Towards highly multimode optical quantum memory for quantum repeaters”, *Physical Review A* **93**, 032327 (2016) (cit. on pp. 9, 15, 35, 156, 159, 160).
- <sup>52</sup>K. Kutluer, M. Mazzera, and H. de Riedmatten, “Solid-State Source of Nonclassical Photon Pairs with Embedded Multimode Quantum Memory”, *Physical Review Letters* **118**, 210502 (2017) (cit. on pp. 9, 15, 47, 48, 51, 61–63).

- <sup>53</sup>K. Kutluer, E. Distante, B. Casabone, S. Duranti, M. Mazzerà, and H. de Riedmatten, “Time Entanglement between a Photon and a Spin Wave in a Multimode Solid-State Quantum Memory”, *Physical Review Letters* **123**, 030501 (2019) (cit. on pp. 9, 16, 40, 47, 50, 52, 54, 56, 59–61, 64, 125).
- <sup>54</sup>C. Laplane, P. Jobez, J. Etesse, N. Gisin, and M. Afzelius, “Multimode and Long-Lived Quantum Correlations Between Photons and Spins in a Crystal”, *Physical Review Letters* **118**, 210501 (2017) (cit. on pp. 9, 15, 48, 62).
- <sup>55</sup>C. Simon, H. de Riedmatten, M. Afzelius, N. Sangouard, H. Zbinden, and N. Gisin, “Quantum Repeaters with Photon Pair Sources and Multimode Memories”, *Physical Review Letters* **98**, 190503 (2007) (cit. on pp. 9, 48).
- <sup>56</sup>S. Massar and S. Popescu, “Optimal Extraction of Information from Finite Quantum Ensembles”, *Physical Review Letters* **74**, 1259–1263 (1995) (cit. on p. 10).
- <sup>57</sup>M. Rančić, M. P. Hedges, R. L. Ahlefeldt, and M. J. Sellars, “Coherence time of over a second in a telecom-compatible quantum memory storage material”, *Nature Physics* **14**, 50–54 (2018) (cit. on p. 10).
- <sup>58</sup>I. Usmani, C. Clausen, F. Bussièrès, N. Sangouard, M. Afzelius, and N. Gisin, “Heralded quantum entanglement between two crystals”, *Nature Photonics* **6**, 234–237 (2012) (cit. on pp. 11, 14).
- <sup>59</sup>Y.-L. Hua, T.-S. Yang, Z.-Q. Zhou, J. Wang, X. Liu, Z.-F. Li, P.-Y. Li, Y. Ma, C. Liu, P.-J. Liang, J. Hu, X. Li, C.-F. Li, and G.-C. Guo, “Storage of telecom-C-band heralded single photons with orbital-angular-momentum encoding in a crystal”, *Science Bulletin* **64**, 1577–1583 (2019) (cit. on p. 11).
- <sup>60</sup>M. F. Askarani, A. Das, J. H. Davidson, G. C. Amaral, N. Sinclair, J. A. Slater, S. Marzban, C. W. Thiel, R. L. Cone, D. Oblak, and W. Tittel, “Long-Lived Solid-State Optical Memory for High-Rate Quantum Repeaters”, *Physical Review Letters* **127**, 220502 (2021) (cit. on pp. 11, 15).

- <sup>61</sup>X. Liu, J. Hu, Z.-F. Li, X. Li, P.-Y. Li, P.-J. Liang, Z.-Q. Zhou, C.-F. Li, and G.-C. Guo, “Heralded entanglement distribution between two absorptive quantum memories”, *Nature* **594**, 41–45 (2021) (cit. on p. 11).
- <sup>62</sup>D. Rieländer, K. Kutluer, P. M. Ledingham, M. Gündoğan, J. Fekete, M. Mazzera, and H. de Riedmatten, “Quantum Storage of Heralded Single Photons in a Praseodymium-Doped Crystal”, *Physical Review Letters* **112**, 040504 (2014) (cit. on p. 11).
- <sup>63</sup>D. Lago-Rivera, S. Grandi, J. V. Rakonjac, A. Seri, and H. de Riedmatten, “Telecom-heralded entanglement between multimode solid-state quantum memories”, *Nature* **594**, 37–40 (2021) (cit. on pp. 11, 14, 15, 84, 97).
- <sup>64</sup>J. V. Rakonjac, D. Lago-Rivera, A. Seri, M. Mazzera, S. Grandi, and H. de Riedmatten, “Entanglement between a Telecom Photon and an On-Demand Multimode Solid-State Quantum Memory”, *Physical Review Letters* **127**, 210502 (2021) (cit. on pp. 11, 15).
- <sup>65</sup>M. Hosseini, B. M. Sparkes, G. Campbell, P. K. Lam, and B. C. Buchler, “High efficiency coherent optical memory with warm rubidium vapour”, *Nature Communications* **2**, 174 (2011) (cit. on pp. 12, 15).
- <sup>66</sup>M. Cao, F. Hoffet, S. Qiu, A. S. Sheremet, and J. Laurat, “Efficient reversible entanglement transfer between light and quantum memories”, *Optica* **7**, 1440–1444 (2020) (cit. on pp. 12, 15).
- <sup>67</sup>E. L. Hahn, “Spin Echoes”, *Physical Review* **80**, 580–594 (1950) (cit. on pp. 12, 36, 131).
- <sup>68</sup>Y. O. Dudin, L. Li, and A. Kuzmich, “Light storage on the time scale of a minute”, *Physical Review A* **87**, 031801 (2013) (cit. on p. 12).
- <sup>69</sup>G. Heinze, C. Hubrich, and T. Halfmann, “Stopped Light and Image Storage by Electromagnetically Induced Transparency up to the Regime of One Minute”, *Physical Review Letters* **111**, 033601 (2013) (cit. on pp. 12, 15, 37, 62).

- <sup>70</sup>M. Hain, M. Stabel, and T. Halfmann, “Few-photon storage on a second timescale by electromagnetically induced transparency in a doped solid”, [New Journal of Physics](#) **24**, 023012 (2022) (cit. on pp. 12, 15).
- <sup>71</sup>K. Kutluer, M. F. Pascual-Winter, J. Dajczgewand, P. M. Ledingham, M. Mazzer, T. Chanelière, and H. de Riedmatten, “Spectral-hole memory for light at the single-photon level”, [Physical Review A](#) **93**, 040302 (2016) (cit. on p. 12).
- <sup>72</sup>A. Kuzmich, W. P. Bowen, A. D. Boozer, A. Boca, C. W. Chou, L.-M. Duan, and H. J. Kimble, “Generation of nonclassical photon pairs for scalable quantum communication with atomic ensembles”, [Nature](#) **423**, 731–734 (2003) (cit. on pp. 13, 16, 55).
- <sup>73</sup>C. H. van der Wal, M. D. Eisaman, A. André, R. L. Walsworth, D. F. Phillips, A. S. Zibrov, and M. D. Lukin, “Atomic Memory for Correlated Photon States”, [Science](#) **301**, 196–200 (2003) (cit. on p. 13).
- <sup>74</sup>C. W. Chou, H. de Riedmatten, D. Felinto, S. V. Polyakov, S. J. van Enk, and H. J. Kimble, “Measurement-induced entanglement for excitation stored in remote atomic ensembles”, [Nature](#) **438**, 828–832 (2005) (cit. on p. 13).
- <sup>75</sup>C.-W. Chou, J. Laurat, H. Deng, K. S. Choi, H. de Riedmatten, D. Felinto, and H. J. Kimble, “Functional Quantum Nodes for Entanglement Distribution over Scalable Quantum Networks”, [Science](#) **316**, 1316–1320 (2007) (cit. on p. 13).
- <sup>76</sup>Z.-S. Yuan, Y.-A. Chen, B. Zhao, S. Chen, J. Schmiedmayer, and J.-W. Pan, “Experimental demonstration of a BDCZ quantum repeater node”, [Nature](#) **454**, 1098–1101 (2008) (cit. on p. 13).
- <sup>77</sup>X.-J. Wang, S.-J. Yang, P.-F. Sun, B. Jing, J. Li, M.-T. Zhou, X.-H. Bao, and J.-W. Pan, “Cavity-Enhanced Atom-Photon Entanglement with Sub-second Lifetime”, [Physical Review Letters](#) **126**, 090501 (2021) (cit. on pp. 13, 15).

- <sup>78</sup>P. Farrera, G. Heinze, B. Albrecht, M. Ho, M. Chávez, C. Teo, N. Sangouard, and H. de Riedmatten, “Generation of single photons with highly tunable wave shape from a cold atomic ensemble”, *Nature Communications* **7**, 13556 (2016) (cit. on pp. 13, 16).
- <sup>79</sup>P. M. Ledingham, W. R. Naylor, J. J. Longdell, S. E. Beavan, and M. J. Sellars, “Nonclassical photon streams using rephased amplified spontaneous emission”, *Physical Review A* **81**, 012301 (2010) (cit. on pp. 13, 37).
- <sup>80</sup>S. E. Beavan, M. P. Hedges, and M. J. Sellars, “Demonstration of Photon-Echo Rephasing of Spontaneous Emission”, *Physical Review Letters* **109**, 093603 (2012) (cit. on p. 13).
- <sup>81</sup>K. R. Ferguson, S. E. Beavan, J. J. Longdell, and M. J. Sellars, “Generation of Light with Multimode Time-Delayed Entanglement Using Storage in a Solid-State Spin-Wave Quantum Memory”, *Physical Review Letters* **117**, 020501 (2016) (cit. on pp. 13, 15, 48).
- <sup>82</sup>H. de Riedmatten, M. Afzelius, M. U. Staudt, C. Simon, and N. Gisin, “A solid-state light–matter interface at the single-photon level”, *Nature* **456**, 773–777 (2008) (cit. on p. 13).
- <sup>83</sup>M. Afzelius, C. Simon, H. de Riedmatten, and N. Gisin, “Multimode quantum memory based on atomic frequency combs”, *Physical Review A* **79**, 052329 (2009) (cit. on pp. 13, 31, 33, 35, 43, 48, 57, 65, 78).
- <sup>84</sup>M. Afzelius, I. Usmani, A. Amari, B. Lauritzen, A. Walther, C. Simon, N. Sangouard, J. Minář, H. de Riedmatten, N. Gisin, and S. Kröll, “Demonstration of Atomic Frequency Comb Memory for Light with Spin-Wave Storage”, *Physical Review Letters* **104**, 040503 (2010) (cit. on pp. 14, 36).
- <sup>85</sup>P. Jobez, C. Laplane, N. Timoney, N. Gisin, A. Ferrier, P. Goldner, and M. Afzelius, “Coherent Spin Control at the Quantum Level in an Ensemble-Based Optical Memory”, *Physical Review Letters* **114**, 230502 (2015) (cit. on p. 14).

- <sup>86</sup>M. Afzelius and C. Simon, “Impedance-matched cavity quantum memory”, *Physical Review A* **82**, 022310 (2010) (cit. on pp. 14, 35, 41–43, 63, 65, 67, 97, 128).
- <sup>87</sup>M. Sabooni, Q. Li, S. Kröll, and L. Rippe, “Efficient Quantum Memory Using a Weakly Absorbing Sample”, *Physical Review Letters* **110**, 133604 (2013) (cit. on pp. 14, 15, 67, 68, 71, 86, 87, 94, 126).
- <sup>88</sup>P. Jobez, I. Usmani, N. Timoney, C. Laplane, N. Gisin, and M. Afzelius, “Cavity-enhanced storage in an optical spin-wave memory”, *New Journal of Physics* **16**, 083005 (2014) (cit. on pp. 14, 34, 67, 69, 71, 94).
- <sup>89</sup>J. H. Davidson, P. Lefebvre, J. Zhang, D. Oblak, and W. Tittel, “Improved light-matter interaction for storage of quantum states of light in a thulium-doped crystal cavity”, *Physical Review A* **101**, 042333 (2020) (cit. on pp. 14, 67, 68, 94, 97).
- <sup>90</sup>A. Ortu, J. V. Rakonjac, A. Holzäpfel, A. Seri, S. Grandi, M. Mazzera, H. de Riedmatten, and M. Afzelius, “Multimode capacity of atomic-frequency comb quantum memories”, *Quantum Science and Technology* **7**, 035024 (2022) (cit. on p. 14).
- <sup>91</sup>M. Businger, L. Nicolas, T. S. Mejia, A. Ferrier, P. Goldner, and M. Afzelius, “Non-classical correlations over 1250 modes between telecom photons and 979-nm photons stored in 171Yb3+:Y2SiO5”, *Nature Communications* **13**, 6438 (2022) (cit. on p. 14).
- <sup>92</sup>Z.-Q. Zhou, Y.-L. Hua, X. Liu, G. Chen, J.-S. Xu, Y.-J. Han, C.-F. Li, and G.-C. Guo, “Quantum Storage of Three-Dimensional Orbital-Angular-Momentum Entanglement in a Crystal”, *Physical Review Letters* **115**, 070502 (2015) (cit. on p. 14).
- <sup>93</sup>A. Ortu, A. Holzäpfel, J. Etesse, and M. Afzelius, “Storage of photonic time-bin qubits for up to 20 ms in a rare-earth doped crystal”, *npj Quantum Information* **8**, 1–7 (2022) (cit. on pp. 14, 15, 37).
- <sup>94</sup>Y. Ma, Y.-Z. Ma, Z.-Q. Zhou, C.-F. Li, and G.-C. Guo, “One-hour coherent optical storage in an atomic frequency comb memory”, *Nature Communications* **12**, 2381 (2021) (cit. on pp. 14, 15, 37, 62).



- <sup>95</sup>E. Saglamyurek, N. Sinclair, J. Jin, J. A. Slater, D. Oblak, F. Bussi eres, M. George, R. Ricken, W. Sohler, and W. Tittel, “Broadband waveguide quantum memory for entangled photons”, [Nature](#) **469**, 512–515 (2011) (cit. on pp. 14, 48).
- <sup>96</sup>M. I. G. Puigibert, M. F. Askarani, J. H. Davidson, V. B. Verma, M. D. Shaw, S. W. Nam, T. Lutz, G. C. Amaral, D. Oblak, and W. Tittel, “Entanglement and nonlocality between disparate solid-state quantum memories mediated by photons”, [Physical Review Research](#) **2**, 013039 (2020) (cit. on p. 14).
- <sup>97</sup>J. V. Rakonjac, G. Corrielli, D. Lago-Rivera, A. Seri, M. Mazzera, S. Grandi, R. Osellame, and H. de Riedmatten, “Storage and analysis of light-matter entanglement in a fiber-integrated system”, [Science Advances](#) **8**, eabn3919 (2022) (cit. on p. 15).
- <sup>98</sup>P. Vernaz-Gris, K. Huang, M. Cao, A. S. Sheremet, and J. Laurat, “Highly-efficient quantum memory for polarization qubits in a spatially-multiplexed cold atomic ensemble”, [Nature Communications](#) **9**, 363 (2018) (cit. on pp. 15, 128).
- <sup>99</sup>C. Laplane, P. Jobez, J. Etesse, N. Timoney, N. Gisin, and M. Afzelius, “Multiplexed on-demand storage of polarization qubits in a crystal”, [New Journal of Physics](#) **18**, 013006 (2015) (cit. on p. 15).
- <sup>100</sup>K. Kutluer, “Quantum memory protocols for photonic solid-state devices”, [TDX \(Tesis Doctorals en Xarxa\)](#) (2017) (cit. on pp. 15, 18, 20, 22, 23, 36, 123).
- <sup>101</sup>V. Krutyanskiy, M. Meraner, J. Schupp, V. Krcmarsky, H. Hainzer, and B. P. Lanyon, “Light-matter entanglement over 50 km of optical fibre”, [npj Quantum Information](#) **5**, 1–5 (2019) (cit. on pp. 16, 123).
- <sup>102</sup>W. M. Haynes, D. R. Lide, and T. J. Bruno, eds., *CRC Handbook of Chemistry and Physics*, Ninety-seventh (CRC Press, Boca Raton, July 2016) (cit. on p. 18).

- <sup>103</sup>H. de Riedmatten and M. Afzelius, “Quantum Light Storage in Solid State Atomic Ensembles”, in *Engineering the Atom-Photon Interaction: Controlling Fundamental Processes with Photons, Atoms and Solids*, edited by A. Predojević and M. W. Mitchell, Nano-Optics and Nanophotonics (Springer International Publishing, Cham, 2015), pp. 241–273 (cit. on p. 18).
- <sup>104</sup>P. Goldner, A. Ferrier, and O. Guillot-Noël, “Rare Earth-Doped Crystals for Quantum Information Processing”, in *Handbook on the Physics and Chemistry of Rare Earths*, Vol. 46, edited by J.-C. G. Bünzli and V. K. Pecharsky (Elsevier, Jan. 2015), pp. 1–78 (cit. on pp. 18, 20).
- <sup>105</sup>R. M. Macfarlane and R. M. Shelby, “Coherent Transient and Holeburning Spectroscopy of Rare Earth Ions in Solids”, in *Modern Problems in Condensed Matter Sciences*, Vol. 21, edited by A. A. Kaplyanskii and R. M. Macfarlane, Spectroscopy of Solids Containing Rare Earth Ions (Elsevier, Jan. 1987), pp. 51–184 (cit. on pp. 18, 20, 21, 23, 25, 28).
- <sup>106</sup>B. G. Wybourne and W. F. Meggers, “Spectroscopic Properties of Rare Earths”, *Physics Today* 18, 70–72 (1965) (cit. on pp. 18, 20, 21, 23).
- <sup>107</sup>G. Liu, “Electronic Energy Level Structure”, in *Spectroscopic Properties of Rare Earths in Optical Materials*, edited by R. Hull, J. Parisi, R. M. Osgood, H. Warlimont, G. Liu, and B. Jacquier, Springer Series in Materials Science (Springer, Berlin, Heidelberg, 2005), pp. 1–94 (cit. on pp. 18, 22, 23).
- <sup>108</sup>L. Allen and J. H. Eberly, *Optical Resonance and Two-level Atoms* (Courier Corporation, Jan. 1987) (cit. on pp. 18, 24).
- <sup>109</sup>A. Seri, “A multimode solid-state quantum memory for single photons”, TDX (Tesis Doctorals en Xarxa) (2019) (cit. on pp. 18, 20, 23, 37, 63, 151).
- <sup>110</sup>M. Gündoğan, “Solid-state quantum memory for photonic qubits”, TDX (Tesis Doctorals en Xarxa) (2015) (cit. on pp. 18, 21, 23, 83, 156).

- <sup>111</sup>M. Lovrić, “Hyperfine characterisation and enhanced optical to spin storage in rare earth ion doped crystals”, [10.17877/DE290R-3279](#) (2012) (cit. on p. 18).
- <sup>112</sup>A. J. Freeman and R. E. Watson, “Theoretical Investigation of Some Magnetic and Spectroscopic Properties of Rare-Earth Ions”, [Physical Review](#) **127**, 2058–2075 (1962) (cit. on p. 19).
- <sup>113</sup>R. W. Equall, Y. Sun, R. L. Cone, and R. M. Macfarlane, “Ultraslow optical dephasing in  $\text{Eu}^{3+}:\text{Y}_2\text{SiO}_5$ ”, [Physical Review Letters](#) **72**, 2179–2182 (1994) (cit. on p. 18).
- <sup>114</sup>M. Nilsson, L. Rippe, S. Kröll, R. Klieber, and D. Suter, “Hole-burning techniques for isolation and study of individual hyperfine transitions in inhomogeneously broadened solids demonstrated in  $\text{Pr}^{3+}:\text{Y}_2\text{SiO}_5$ ”, [Physical Review B](#) **70**, 214116 (2004) (cit. on pp. 23, 28).
- <sup>115</sup>A. M. Fox and M. Fox, *Quantum Optics: An Introduction* (OUP Oxford, Apr. 2006) (cit. on p. 24).
- <sup>116</sup>R. W. Equall, R. L. Cone, and R. M. Macfarlane, “Homogeneous broadening and hyperfine structure of optical transitions in  $\text{Pr}^{3+}:\text{Y}_2\text{SiO}_5$ ”, [Physical Review B](#) **52**, 3963–3969 (1995) (cit. on pp. 25, 30, 153).
- <sup>117</sup>E. S. Maniloff, F. R. Graf, H. Gygax, S. B. Altner, S. Bernet, A. Renn, and U. P. Wild, “Power broadening of the spectral hole width in an optically thick sample”, [Chemical Physics](#) **193**, 173–180 (1995) (cit. on p. 30).
- <sup>118</sup>M. L. Citron, H. R. Gray, C. W. Gabel, and C. R. Stroud, “Experimental study of power broadening in a two-level atom”, [Physical Review A](#) **16**, 1507–1512 (1977) (cit. on p. 30).
- <sup>119</sup>N. V. Vitanov, B. W. Shore, L. Yatsenko, K. Böhmer, T. Halfmann, T. Riekens, and K. Bergmann, “Power broadening revisited: theory and experiment”, [Optics Communications](#) **199**, 117–126 (2001) (cit. on p. 30).
- <sup>120</sup>J. Nunn, K. Reim, K. C. Lee, V. O. Lorenz, B. J. Sussman, I. A. Walmsley, and D. Jaksch, “Multimode Memories in Atomic Ensembles”, [Physical Review Letters](#) **101**, 260502 (2008) (cit. on p. 33).

- <sup>121</sup>M. Bonarota, J. Ruggiero, J. -. L. Gouët, and T. Chanelière, “Efficiency optimization for atomic frequency comb storage”, *Physical Review A* **81**, 033803 (2010) (cit. on pp. 33, 34).
- <sup>122</sup>N. Sangouard, C. Simon, M. Afzelius, and N. Gisin, “Analysis of a quantum memory for photons based on controlled reversible inhomogeneous broadening”, *Physical Review A* **75**, 032327 (2007) (cit. on p. 35).
- <sup>123</sup>B. S. Ham, M. S. Shahriar, M. K. Kim, and P. R. Hemmer, “Frequency-selective time-domain optical data storage by electromagnetically induced transparency in a rare-earth-doped solid”, *Optics Letters* **22**, 1849–1851 (1997) (cit. on p. 36).
- <sup>124</sup>E. Fraval, M. J. Sellars, and J. J. Longdell, “Method of Extending Hyperfine Coherence Times in  $\text{Pr}^{3+}:\text{Y}_2\text{SiO}_5$ ”, *Physical Review Letters* **92**, 077601 (2004) (cit. on p. 36).
- <sup>125</sup>E. Fraval, M. J. Sellars, and J. J. Longdell, “Dynamic Decoherence Control of a Solid-State Nuclear-Quadrupole Qubit”, *Physical Review Letters* **95**, 030506 (2005) (cit. on p. 36).
- <sup>126</sup>E. Fraval, M. J. Sellars, A. Morrison, and A. Ferris, “Pr–Y interaction in  $\text{Pr}^{3+}:\text{Y}_2\text{SiO}_5$ ”, *Journal of Luminescence, Proceedings of the 8th International Meeting on Hole Burning, Single Molecule, and Related Spectroscopies: Science and Applications* **107**, 347–350 (2004) (cit. on p. 36).
- <sup>127</sup>S. E. Beavan, E. Fraval, M. J. Sellars, and J. J. Longdell, “Demonstration of the reduction of decoherent errors in a solid-state qubit using dynamic decoupling techniques”, *Physical Review A* **80**, 032308 (2009) (cit. on p. 36).
- <sup>128</sup>K. Holliday, M. Croci, E. Vauthey, and U. P. Wild, “Spectral hole burning and holography in an  $\text{Y}_2\text{SiO}_5:\text{Pr}^{3+}$  crystal”, *Physical Review B* **47**, 14741–14752 (1993) (cit. on p. 36).
- <sup>129</sup>G. Heinze, C. Hubrich, and T. Halfmann, “Coherence time extension in  $\text{Pr}^{3+}:\text{Y}_2\text{SiO}_5$  by self-optimized magnetic fields and dynamical decoupling”, *Physical Review A* **89**, 053825 (2014) (cit. on p. 36).

- <sup>130</sup>A. Seri, A. Lenhard, D. Rieländer, M. Gündoğan, P. M. Ledingham, M. Mazzerà, and H. de Riedmatten, “Quantum Correlations between Single Telecom Photons and a Multimode On-Demand Solid-State Quantum Memory”, [Physical Review X](#) **7**, 021028 (2017) (cit. on p. 36).
- <sup>131</sup>A. Holzäpfel, J. Etesse, K. T. Kaczmarek, A. Tiranov, N. Gisin, and M. Afzelius, “Optical storage for 0.53 s in a solid-state atomic frequency comb memory using dynamical decoupling”, [New Journal of Physics](#) **22**, 063009 (2020) (cit. on p. 37).
- <sup>132</sup>P. Sekatski, N. Sangouard, N. Gisin, H. de Riedmatten, and M. Afzelius, “Photon-pair source with controllable delay based on shaped inhomogeneous broadening of rare-earth-metal-doped solids”, [Physical Review A](#) **83**, 053840 (2011) (cit. on pp. 37, 39).
- <sup>133</sup>B. Albrecht, “Quantum control of single spin excitations in cold atomic quantum memories”, [TDX \(Tesis Doctorals en Xarxa\)](#) (2015) (cit. on p. 38).
- <sup>134</sup>H. J. Kimble, “The quantum internet”, [Nature](#) **453**, 1023–1030 (2008) (cit. on p. 48).
- <sup>135</sup>M. Afzelius, N. Gisin, and H. de Riedmatten, “Quantum memory for photons”, [Physics Today](#) **68**, 42–47 (2015) (cit. on p. 48).
- <sup>136</sup>D. N. Matsukevich, T. Chanelière, M. Bhattacharya, S.-Y. Lan, S. D. Jenkins, T. A. B. Kennedy, and A. Kuzmich, “Entanglement of a Photon and a Collective Atomic Excitation”, [Physical Review Letters](#) **95**, 040405 (2005) (cit. on p. 48).
- <sup>137</sup>H. de Riedmatten, J. Laurat, C. W. Chou, E. W. Schomburg, D. Felinto, and H. J. Kimble, “Direct Measurement of Decoherence for Entanglement between a Photon and Stored Atomic Excitation”, [Physical Review Letters](#) **97**, 113603 (2006) (cit. on p. 48).
- <sup>138</sup>S. Chen, Y.-A. Chen, B. Zhao, Z.-S. Yuan, J. Schmiedmayer, and J.-W. Pan, “Demonstration of a Stable Atom-Photon Entanglement Source for Quantum Repeaters”, [Physical Review Letters](#) **99**, 180505 (2007) (cit. on p. 48).

- <sup>139</sup>R. Inoue, N. Kanai, T. Yonehara, Y. Miyamoto, M. Koashi, and M. Kozuma, “Entanglement of orbital angular momentum states between an ensemble of cold atoms and a photon”, *Physical Review A* **74**, 053809 (2006) (cit. on p. 48).
- <sup>140</sup>P. Farrera, G. Heinze, and H. de Riedmatten, “Entanglement between a Photonic Time-Bin Qubit and a Collective Atomic Spin Excitation”, *Physical Review Letters* **120**, 100501 (2018) (cit. on p. 48).
- <sup>141</sup>R. Riedinger, S. Hong, R. A. Norte, J. A. Slater, J. Shang, A. G. Krause, V. Anant, M. Aspelmeyer, and S. Gröblacher, “Non-classical correlations between single photons and phonons from a mechanical oscillator”, *Nature* **530**, 313–316 (2016) (cit. on p. 48).
- <sup>142</sup>P. M. Ledingham, W. R. Naylor, and J. J. Longdell, “Experimental Realization of Light with Time-Separated Correlations by Rephasing Amplified Spontaneous Emission”, *Physical Review Letters* **109**, 093602 (2012) (cit. on p. 48).
- <sup>143</sup>J. D. Franson, “Bell inequality for position and time”, *Physical Review Letters* **62**, 2205–2208 (1989) (cit. on p. 56).
- <sup>144</sup>P. Jobez, “Stockage multimode au niveau quantique pendant une milliseconde”, PhD thesis (University of Geneva, 2015) (cit. on pp. 57, 78).
- <sup>145</sup>J. F. Clauser, M. A. Horne, A. Shimony, and R. A. Holt, “Proposed Experiment to Test Local Hidden-Variable Theories”, *Physical Review Letters* **23**, 880–884 (1969) (cit. on p. 58).
- <sup>146</sup>N. Maring, “Quantum frequency conversion for hybrid quantum networks”, *TDX (Tesis Doctorals en Xarxa)* (2018) (cit. on pp. 62, 101, 103, 106–108, 112–114).
- <sup>147</sup>M. Zhong, M. P. Hedges, R. L. Ahlefeldt, J. G. Bartholomew, S. E. Beavan, S. M. Wittig, J. J. Longdell, and M. J. Sellars, “Optically addressable nuclear spins in a solid with a six-hour coherence time”, *Nature* **517**, 177–180 (2015) (cit. on p. 62).

- <sup>148</sup>M. Sabooni, S. T. Kometa, A. Thuresson, S. Kröll, and L. Rippe, “Cavity-enhanced storage—preparing for high-efficiency quantum memories”, *New Journal of Physics* **15**, 035025 (2013) (cit. on pp. 66–68, 86, 87).
- <sup>149</sup>M. Sabooni, Q. Li, L. Rippe, R. K. Mohan, and S. Kröll, “Spectral Engineering of Slow Light, Cavity Line Narrowing, and Pulse Compression”, *Physical Review Letters* **111**, 183602 (2013) (cit. on pp. 66–68, 86, 87).
- <sup>150</sup>I. Marcikic, H. de Riedmatten, W. Tittel, H. Zbinden, and N. Gisin, “Long-distance teleportation of qubits at telecommunication wavelengths”, *Nature* **421**, 509–513 (2003) (cit. on p. 82).
- <sup>151</sup>M. Gündoğan, P. M. Ledingham, A. Almasi, M. Cristiani, and H. de Riedmatten, “Quantum Storage of a Photonic Polarization Qubit in a Solid”, *Physical Review Letters* **108**, 190504 (2012) (cit. on p. 83).
- <sup>152</sup>A. E. Siegman, *Lasers* (University Science Books, 1986) (cit. on p. 86).
- <sup>153</sup>A. Walther, A. Amari, S. Kröll, and A. Kalachev, “Experimental super-radiance and slow-light effects for quantum memories”, *Physical Review A* **80**, 012317 (2009) (cit. on p. 87).
- <sup>154</sup>R. N. Shakhmurov, A. Rebane, P. Mégret, and J. Odeurs, “Slow light with persistent hole burning”, *Physical Review A* **71**, 053811 (2005) (cit. on p. 87).
- <sup>155</sup>S. P. Horvath, C. Shi, D. Gustavsson, A. Walther, A. Kinos, S. Kröll, and L. Rippe, “Slow light frequency reference cavities—proof of concept for reducing the frequency sensitivity due to length fluctuations”, *New Journal of Physics* **24**, 033034 (2022) (cit. on p. 87).
- <sup>156</sup>J.-C. Diels and W. Rudolph, *Ultrashort Laser Pulse Phenomena* (Elsevier, Sept. 2006) (cit. on p. 88).
- <sup>157</sup>S. Ramelow, A. Fedrizzi, A. Poppe, N. K. Langford, and A. Zeilinger, “Polarization-entanglement-conserving frequency conversion of photons”, *Physical Review A* **85**, 013845 (2012) (cit. on p. 99).

- <sup>158</sup>V. Krutyanskiy, M. Galli, V. Krcmarsky, S. Baier, D. A. Fioretto, Y. Pu, A. Mazloom, P. Sekatski, M. Canteri, M. Teller, J. Schupp, J. Bate, M. Meraner, N. Sangouard, B. P. Lanyon, and T. E. Northup, *Entanglement of trapped-ion qubits separated by 230 meters*, Aug. 2022 (cit. on p. 99).
- <sup>159</sup>P. Kumar, “Quantum frequency conversion”, *Optics Letters* **15**, 1476–1478 (1990) (cit. on p. 99).
- <sup>160</sup>J. Huang and P. Kumar, “Observation of quantum frequency conversion”, *Physical Review Letters* **68**, 2153–2156 (1992) (cit. on p. 100).
- <sup>161</sup>S. Ates, I. Agha, A. Gulinatti, I. Rech, M. T. Rakher, A. Badolato, and K. Srinivasan, “Two-Photon Interference Using Background-Free Quantum Frequency Conversion of Single Photons Emitted by an InAs Quantum Dot”, *Physical Review Letters* **109**, 147405 (2012) (cit. on p. 100).
- <sup>162</sup>X. Fernandez-Gonzalvo, G. Corrielli, B. Albrecht, M. li Grimau, M. Cristiani, and H. de Riedmatten, “Quantum frequency conversion of quantum memory compatible photons to telecommunication wavelengths”, *Optics Express* **21**, 19473–19487 (2013) (cit. on p. 100).
- <sup>163</sup>A. Dréau, A. Tchebotareva, A. E. Mahdaoui, C. Bonato, and R. Hanson, “Quantum Frequency Conversion of Single Photons from a Nitrogen-Vacancy Center in Diamond to Telecommunication Wavelengths”, *Physical Review Applied* **9**, 064031 (2018) (cit. on p. 100).
- <sup>164</sup>A. Samblowski, C. E. Vollmer, C. Baune, J. Fiurášek, and R. Schnabel, “Weak-signal conversion from 1550 to 532 nm with 84% efficiency”, *Optics Letters* **39**, 2979–2981 (2014) (cit. on p. 100).
- <sup>165</sup>T. van Leent, M. Bock, R. Garthoff, K. Redeker, W. Zhang, T. Bauer, W. Rosenfeld, C. Becher, and H. Weinfurter, “Long-Distance Distribution of Atom-Photon Entanglement at Telecom Wavelength”, *Physical Review Letters* **124**, 010510 (2020) (cit. on p. 100).
- <sup>166</sup>Y. Yu, F. Ma, X.-Y. Luo, B. Jing, P.-F. Sun, R.-Z. Fang, C.-W. Yang, H. Liu, M.-Y. Zheng, X.-P. Xie, W.-J. Zhang, L.-X. You, Z. Wang, T.-Y. Chen, Q. Zhang, X.-H. Bao, and J.-W. Pan, “Entanglement of two quan-



- tum memories via fibres over dozens of kilometres”, *Nature* **578**, 240–245 (2020) (cit. on p. 100).
- <sup>167</sup>R. W. Boyd, *Nonlinear Optics* (Academic Press, Mar. 2020) (cit. on pp. 101, 103–105).
- <sup>168</sup>M. Bock, “Polarization-preserving quantum frequency conversion for trapped-atom based quantum networks”, [10.22028/D291-35322](https://doi.org/10.22028/D291-35322) (2020) (cit. on pp. 101, 103, 104).
- <sup>169</sup>A. Lenhard, “Quantum photonic interfaces between atomic and telecommunication wavelengths”, [10.22028/D291-23046](https://doi.org/10.22028/D291-23046) (2015) (cit. on pp. 101, 103).
- <sup>170</sup>J. S. Pelc, *Frequency Conversion of Single Photons: Physics, Devices, and Applications*, tech. rep. (STANFORD UNIV CA, July 2012) Chap. Technical Reports (cit. on pp. 101, 103, 106).
- <sup>171</sup>S. Zaske, “Quantum frequency down-conversion of single photons in nonlinear optical waveguides”, [10.22028/D291-22872](https://doi.org/10.22028/D291-22872) (2013) (cit. on pp. 101, 106).
- <sup>172</sup>I. Shoji, T. Kondo, A. Kitamoto, M. Shirane, and R. Ito, “Absolute scale of second-order nonlinear-optical coefficients”, *JOSA B* **14**, 2268–2294 (1997) (cit. on p. 101).
- <sup>173</sup>J. S. Pelc, L. Ma, C. R. Phillips, Q. Zhang, C. Langrock, O. Slattery, X. Tang, and M. M. Fejer, “Long-wavelength-pumped upconversion single-photon detector at 1550 nm: performance and noise analysis”, *Optics Express* **19**, 21445–21456 (2011) (cit. on p. 106).
- <sup>174</sup>N. Maring, D. Lago-Rivera, A. Lenhard, G. Heinze, and H. de Riedmatten, “Quantum frequency conversion of memory-compatible single photons from 606 nm to the telecom C-band”, *Optica* **5**, 507–513 (2018) (cit. on pp. 106, 107).
- <sup>175</sup>J. S. Pelc, C. Langrock, Q. Zhang, and M. M. Fejer, “Influence of domain disorder on parametric noise in quasi-phase-matched quantum frequency converters”, *Optics Letters* **35**, 2804–2806 (2010) (cit. on p. 106).

- <sup>176</sup>R. V. Roussev, C. Langrock, J. R. Kurz, and M. M. Fejer, “Periodically poled lithium niobate waveguide sum-frequency generator for efficient single-photon detection at communication wavelengths”, *Optics Letters* **29**, 1518–1520 (2004) (cit. on p. 108).
- <sup>177</sup>P. Farrera, N. Maring, B. Albrecht, G. Heinze, and H. de Riedmatten, “Nonclassical correlations between a C-band telecom photon and a stored spin-wave”, *Optica* **3**, 1019–1024 (2016) (cit. on p. 110).
- <sup>178</sup>P. C. Strassmann, A. Martin, N. Gisin, and M. Afzelius, “Spectral noise in frequency conversion from the visible to the telecommunication C-band”, *Optics Express* **27**, 14298–14307 (2019) (cit. on p. 110).
- <sup>179</sup>R. Ikuta, T. Kobayashi, S. Yasui, S. Miki, T. Yamashita, H. Terai, M. Fujiwara, T. Yamamoto, M. Koashi, M. Sasaki, Z. Wang, and N. Imoto, “Frequency down-conversion of 637 nm light to the telecommunication band for non-classical light emitted from NV centers in diamond”, *Optics Express* **22**, 11205–11214 (2014) (cit. on p. 113).
- <sup>180</sup>A. N. Vetlugin and I. V. Sokolov, “Multivariate quantum memory as controllable delayed multi-port beamsplitter”, *Europhysics Letters* **113**, 64005 (2016) (cit. on p. 128).
- <sup>181</sup>N. A. Kurnit, I. D. Abella, and S. R. Hartmann, “Observation of a Photon Echo”, *Physical Review Letters* **13**, 567–568 (1964) (cit. on p. 131).
- <sup>182</sup>I. D. Abella, N. A. Kurnit, and S. R. Hartmann, “Photon Echoes”, *Physical Review* **141**, 391–406 (1966) (cit. on p. 131).
- <sup>183</sup>A. V. Durrant, J. Manners, and P. M. Clark, “Understanding optical echoes using Schrodinger’s equation: I. Echoes excited by two optical pulses”, *European Journal of Physics* **10**, 291–297 (1989) (cit. on pp. 131, 132, 135–137, 139, 140).
- <sup>184</sup>R. Loudon, “The Quantum Theory of Light”, *American Journal of Physics* **42**, 1041–1042 (1974) (cit. on p. 133).
- <sup>185</sup>M. Sargent Iii, *Laser Physics* (CRC Press, Mar. 2018) (cit. on p. 134).
- <sup>186</sup>L. Allen and J. H. Eberly, *Optical Resonance and Two-Level Atoms* (Courier Corporation, May 2012) (cit. on pp. 134, 140).

- <sup>187</sup>E. D. Black, “An introduction to Pound–Drever–Hall laser frequency stabilization”, *American Journal of Physics* **69**, 79–87 (2001) (cit. on p. 144).
- <sup>188</sup>E. A. Donley, T. P. Heavner, F. Levi, M. O. Tataw, and S. R. Jefferts, “Double-pass acousto-optic modulator system”, *Review of Scientific Instruments* **76**, 063112 (2005) (cit. on p. 145).
- <sup>189</sup>M. Gündoğan, M. Mazzera, P. M. Ledingham, M. Cristiani, and H. de Riedmatten, “Coherent storage of temporally multimode light using a spin-wave atomic frequency comb memory”, *New Journal of Physics* **15**, 045012 (2013) (cit. on pp. 156, 159).
- <sup>190</sup>L. Rippe, M. Nilsson, S. Kröll, R. Klieber, and D. Suter, “Experimental demonstration of efficient and selective population transfer and qubit distillation in a rare-earth-metal-ion-doped crystal”, *Physical Review A* **71**, 062328 (2005) (cit. on p. 157).
- <sup>191</sup>B. E. A. Saleh and C. T. Malvin, “Resonator Optics”, in *Fundamentals of Photonics* (John Wiley & Sons, Ltd, 1991) Chap. 9, pp. 310–341 (cit. on p. 169).